Author:
Pomery, Gabby J

Title:
Understanding the impact of non-local contributions to B 0 K *0 transitions

Understanding the impact of non-local contributions to $\bar{B}^0 \to \bar{K}^{*0}\mu^+\mu^-$ transitions

by

Gabriela Johanna Pomery

A thesis submitted to the University of Bristol for the degree of Doctor of Philosophy

in the
Faculty of Science
School of Physics

September 2019

Abstract

The impact of the non-local contributions to $\bar{B}^0 \to \bar{K}^{*0}\mu^+\mu^-$ decays has been assessed through creating a framework suitable to perform a five dimensional, unbinned, maximum likelihood fit to the data collected by the LHCb experiment. Both $\bar{B}^0$ and B^0 decays are treated equally in this analysis, thus providing a sample rich in $\bar{B}^0(B^0) \to \bar{K}^{*0}(K^{*0})\mu^+\mu^-$ candidates. The data analysed corresponds to the full Run 1 dataset which equates to an integrated luminosity of 3 fb^{-1}, and the 2016 dataset from Run 2 that amounts to an integrated luminosity of 1.67 fb^{-1}.

The model considers all possible hadronic contributions that contribute to $\bar{B}^0 \to \bar{K}^{*0}\mu^+\mu^-$ decays, in the invariant dilepton mass squared (q^2) region of $1.0 < q^2 < 18.0$ GeV$^2/c^4$. No previous analyses have been published that determine the impact of the non-local contributions in $\bar{B}^0 \to \bar{K}^{*0}\mu^+\mu^-$ decays. Therefore, for the first time, the analysis presented in this thesis tries to understand these contributions.

Recent results published from LHCb reveal anomalous results seen in $b \to s\ell^+\ell^-$ transitions. Possible explanations include New Physics, at the TeV scale, or hadronic resonances interfering with the penguin component and causing a sizeable effect that appears like New Physics. This analysis through a fit to the data will determine the latter, demonstrating how the effects seen could be due to our lack of understanding of the non-local contributions.

Declaration of authorship

I, Gabriela Johanna Pomery, declare that the work in this dissertation was carried out in accordance with the requirements of the University's Regulations and Code of Practice for Research Degree Programmes and that it has not been submitted for any other academic award. Except where indicated by specific reference in the text, the work is the candidate's own work. Work done in collaboration with, or with the assistance of, others, is indicated as such. Any views expressed in the dissertation are those of the author.

Signed: _____

Date: _____

Acknowledgements

To what has been a rocky but enjoyable PhD. To all those who have been there for me, when I needed them the most. Whether is it has been through supporting me, making me laugh, or by just being there. The Bristol Particle Physics group has been my home for the past 5 years, where I have made so many friends and met some truly inspirational people. I will miss you all.

I would like thank my supervisor Kostas Petridis. You have taken the time to really educate me on not only b-physics, but all things physics related. You allowed me to be part of a project that I have truly enjoyed from the start and am going to be sad to leave.

I owe a huge debt of gratitude to the members of the Bristol LHCb group. I am grateful in the way you have all listened to my ideas, commented on my talks and made me feel truly part of the group.

A special thank you to Martisse Foster, for always being there and listening to me when I have felt I needed to confide in someone. You are a treasure to the Bristol group and I appreciate all you have done for me over the years.

To the class of 2015, Alex Titterton, Joe Taylor and Stoyan Trilov. I am grateful to be finishing at the same time as some really lovely people. I will miss the banter, and the general antics.

To my friends and family, you have been there behind the scenes. You have always pushed me to strive for bigger things, but also to just simply enjoy life. I thank you all so much. And of course to Hank and Maggie the dogs, for when work has been stressful, making it feel like nothing has happened by getting so excited when I come in the door.

Author's contribution

The author's contributions are detailed by the following list,

- Chapter 3: The model and results from it that are presented in this chapter, were constructed and made by the author. Many of the figures have been published in a peer reviewed journal, written by the author, Ref [1].
- Chapter 4: The data analysed in this chapter was collected using the LHCb detector, by the LHCb collaboration. The simulation samples were produced by the LHCb simulation group. Both the data and simulated sampled had the LHCb software applied to it. The software was written by subgroups of the collaboration. All remaining studies on the data and simulation in this chapter were the authors own work.
- Chapter 5: The results documented in this chapter are the result of the authors own work.
- Chapter 6: The studies and results presented in this chapter are the result of the authors own work.
- Appendix B: The studies documented in this appendix chapter are the results of the authors work from her time at the Large Hadron Collider, where the author tested prototype mirrors for the LHCb RICH 1 upgrade. These studies are a separate entity and do not contribute to the topic of the analysis. They are included to fully document the author's work over the duration of her PhD.

Contents

List of Figures

List of Tables

Abbreviations

ATLAS	A Toriodial LHC ApparatuS
BDT	Boosted Decision Tree
BSM	Beyond Standard Model
B2XMuMu	trigger line for any decay that proceeds via $B \to X\mu^+\mu^-$
CCD	Charged coupling device
CFRP	Carbon fibre Reinforced Polymer
CMS	Compact Muon Solenoid
CKM	Cabbibo-Kobayashi-Maskawa (matrix)
CoM	center of mass
CP	charge-parity
D_0	diameter of the smallest circle that encases 95% of the light produced by a source on a optical mirror.
DIRA	direction of the mother particle
DLL	difference in log likelihood between two particle hypotheses
$\mathbf{DLL}_{K\pi}$	the DLL of the kaon and pion hypotheses
$\mathbf{DLL}_{\mu\pi}$	the DLL of the muon and pion hypotheses
ECAL	Electron Calorimeter
EFT	Effective field theory
FCCC	Flavour changing charged currents
FCNC	Flavour changing neutral currents
FD	flight distance
GEC	the number of hits in the SPD
GIM	Glashow-Iliopoulos-Maiani (mechanism)
HCAL	Hadronic Calorimeter
HLT	High Level Trigger
HPD	Hybrid Pixel Detector
IP	impact parameter
IT	Inner Tracker
LCSR	Light Cone Sum Rules
LEP	Large Electron-Position collider
LFU	Lepton Flavour Universality
LHC	Large Hadron Collider

LHCb	Large Hadron Collider beauty
`L0`	Level zero hardware trigger
`L0Calorimeter`	calorimeter trigger stream at level zero
`L0DiMuon`	dimuon trigger stream at level zero
`L0Electron`	electron trigger stream at level zero
`L0Photon`	photon trigger stream at level zero
`L0Muon`	muon trigger stream at level zero
LS	Long shutdown
MC	Monte Carlo
MVA	Multivariate analysis
NNLO	Next-to-next-to-leading order
NP	New Physics
OPE	Operator expansion product
OT	Outer Tracker
PDF	Probability Distribution function
PID	Particle identification
PS	Proton Synchrotron or Pre-Shower (depending on context)
PSB	Proton Synchrotron Booster
p_T	transverse momentum
PV	Primary vertex
q^2	invariant mass squared for the dimuon system
QCD	Quantum Chromodynamics
RICH	Ring Imaging Cherenkov (detector)
SM	Standard Model of Particle Physics
SPD	Scintillating Pad detector
SPS	Super Proton Synchrotron
SV	Secondary vertex
TT	Tracker Turicensis
UT	Upstream Tracker
VELO	VErtex LOcator
θ_c	cherenkov angle
θ_ℓ	angle between the direction of the positively (negatively) charged muon in the dimuon rest frame and the direction of the dimuon in the rest frame of the $\bar{B}^0/B^0$
θ_K	angle between the direction of the kaon in the $\bar{K}^{*0}/K^{*0}$ rest frame, and the direction of the $\bar{K}^{*0}/K^{*0}$ in the $\bar{B}^0/B^0$ rest frame
ϕ	angle between the plane containing the two muons (μ^+, μ^-) and the plane containing the $K^-\pi^+$/ $K^+\pi^-$ from the $\bar{K}^{*0}/K^{*0}$
cos θ_ℓ	cosine of the angle θ_ℓ
cos θ_K	cosine of the angle θ_K

Chapter 1

Theoretical overview of rare $b \to s\ell^+\ell^-$ decays

The decay $\bar{B}^0 \to \bar{K}^{*0}\mu^+\mu^-$ is a rare Flavour Changing Neutral Current (FCNC) transition in the Standard Model (SM). These transitions are GIM, CKM and mass suppressed in the SM and therefore can only occur at loop-level. The flavour aspect of the SM describes FCNC processes. Section 1.1 describes flavour in the Standard Model. It is the suppression that makes the decay $\bar{B}^0 \to \bar{K}^{*0}\mu^+\mu^-$ intriguing to study as it is sensitive to possible New Physics (NP) contributions. These NP contributions can enter virtually at loop or tree level, modifying the decay rate and the distribution of the decay products. An effective field theory approach is often used to model both contributions from the SM and NP, in a framework denoted the operator-product expansion (OPE). The effective theory approach and its application to $b \to s\ell^+\ell^-$ decays is presented in Section 1.2. Explicitly, the OPE for $\bar{B}^0 \to \bar{K}^{*0}\mu^+\mu^-$ decays is provided in Section 1.3. In recent years, a series of anomalous results, all associated with $b \to s\ell^+\ell^-$ transitions have shown to exhibit tensions with the SM. A discussion of these anomalies and their current status is given in Section 1.4.1. One possible explanation of the anomalous results in $b \to s\ell^+\ell^-$ transitions is that it is an effect of the "charm loop". The charm loop is the name given to the hadronic resonant contributions that can proceed via $b \to s\ell^+\ell^-$ decays, where the two leptons are obtained from the decay of a quark

and antiquark pair ($q\bar{q} \to \ell^+\ell^-$). These transitions are several orders of magnitude larger than the penguin decay, and therefore if these contributions interfere with the penguin decay ($\bar{B}^0 \to \bar{K}^{*0}\mu^+\mu^-$) they can cause sizeable effects that might appear as NP contributions. More information regarding the charm loop is provided in Section 1.4.2. In this thesis, an angular analysis of the decay $\bar{B}^0 \to \bar{K}^{*0}\mu^+\mu^-$ is performed, in order to measure how the charm loop interferes with the penguin decay $\bar{B}^0 \to \bar{K}^{*0}\mu^+\mu^-$ and determine the effect it has on the angular distribution. A complete anatomy of the $\bar{B}^0 \to \bar{K}^{*0}\mu^+\mu^-$ decay, its angular distribution and the impact of long-distance effects are given in Section 1.3. This chapter concludes with a discussion of the current experimental and theoretical status of $\bar{B}^0 \to \bar{K}^{*0}\mu^+\mu^-$.

1.1 The Standard Model from a flavour perspective

The discussion presented in this section was written in reference to [5–7]. Any additional references are explicitly noted in the text.

Particle physics is built upon elementary particles and their interactions. The SM is the framework used to describe such interactions. Explicitly, the SM is a quantum field theory that follows the symmetry group $SU(3)_c \otimes SU(2)_L \otimes U(1)_Y$. Each component of the symmetry group describes a different sector. The $SU(3)_c$ symmetry group is associated to the theory of quantum chromodynamics (QCD), and defines the strong interaction which is mediated through 8 gluonic fields. Only particles that are colour charged can couple to these fields and feel the strong force. The second component, $SU(2)_L \otimes U(1)_Y$ is the group that describes the electroweak interactions. Explicitly, this group unifies the electromagnetic interaction and the weak interaction, and therefore is mediated through 4 mediators; γ, $W^\pm$ and Z, where γ is the photon, and $W^\pm, Z$ are massive gauge bosons. Fermions are spin $\frac{1}{2}$ particles that can be grouped into elementary particles called quarks and leptons, where each have different properties. All fermions experience the electroweak force, but only quarks experience the strong force as they are colour charged. The quarks and leptons form one part of the flavour structure in the SM. In particular the quarks and leptons are arranged into three families (generations)

	Generation	Particle	Q	Y_W	T^3
Leptons	1	ν_{eL}	0	-1	$\frac{1}{2}$
		e_L	-1	-1	$-\frac{1}{2}$
		e_R	-1	-2	0
	2	$\nu_{\mu L}$	0	-1	$\frac{1}{2}$
		μ_L	-1	-1	$-\frac{1}{2}$
		μ_R	-1	-2	0
	3	$\nu_{\tau L}$	0	-1	$\frac{1}{2}$
		τ_L	-1	-1	$-\frac{1}{2}$
		τ_R	-1	-2	0
Quarks	1	d_L	$-\frac{1}{3}$	$\frac{1}{3}$	$-\frac{1}{2}$
		d_R	$-\frac{1}{3}$	$-\frac{2}{3}$	0
		u_L	$\frac{2}{3}$	$\frac{1}{3}$	$\frac{1}{2}$
		u_R	$\frac{2}{3}$	$\frac{4}{3}$	0
	2	s_L	$-\frac{1}{3}$	$\frac{1}{3}$	$-\frac{1}{2}$
		s_R	$-\frac{1}{3}$	$-\frac{2}{3}$	0
		c_L	$\frac{2}{3}$	$\frac{1}{3}$	$\frac{1}{2}$
		c_R	$\frac{2}{3}$	$\frac{4}{3}$	0
	3	b_L	$-\frac{1}{3}$	$\frac{1}{3}$	$-\frac{1}{2}$
		b_R	$-\frac{1}{3}$	$-\frac{2}{3}$	0

Table 1.1: The elementary fermions in the Standard Model. The fermions are defined as either quarks or leptons, and are assigned a generation. For every particle the subscript L or R, defines whether the particle is left- or right-handed. Other properties given are the electric charge Q, weak hypercharge Y_W and weak isospin T^3 [8].

as shown by Table 1.1. Table 1.1 also provides for each particle, the electric charge Q, weak isospin T^3 and weak hypercharge Y_W. Weak isospin is the quantum number used for the weak interaction, while weak hypercharge is the quantum number relating, electric charge to weak isospin via the relation, $Y_W = 2(Q - T^3)$. The SM despite its complexity can be expressed fully by the following renormalisable Lagrangian;

$$\mathcal{L}_{\text{SM}} = \mathcal{L}_{\text{kinetic}} + \mathcal{L}_{\phi} + \mathcal{L}_{\text{Gauge}} \tag{1.1}$$

The first term $\mathcal{L}_{\text{kinetic}}$, in Equation 1.1, is the kinetic term and takes the form,

$$\mathcal{L}_{\text{kinetic}} = i\bar{\psi}\gamma^{\mu}\mathcal{D}_{\mu}\psi \tag{1.2}$$

where, the term $\mathcal{D}_{\mu}$ is the covariant derivative and is defined as,

$$\mathcal{D}_{\mu} = \partial_{\mu} - ig\frac{1}{2}\overrightarrow{\tau}\cdot\overrightarrow{W}_{\mu} - ig^{'}\frac{1}{2}Y_{\mu}B_{\mu} - ig^{''}\frac{1}{2}\overrightarrow{\lambda}\cdot\overrightarrow{G}_{\mu} \tag{1.3}$$

where g^{i} denotes a coupling constant that multiplies each gauge field in the covariant derivative. The first term is the gauge field for the $U(1)_{Y}$ symmetry group, the second for $SU(2)_{L}$, and the last for $SU(3)_{c}$. The second term $\mathcal{L}_{\text{Gauge}}$, in Equation 1.1, corresponds to the Lagrangian of the gauge fields and is defined as,

$$\mathcal{L}_{\text{Gauge}} = -\frac{1}{4}F_{\mu\nu}F^{\mu\nu} \tag{1.4}$$

where, $F^{\mu\nu}$ is the field tensor of a given symmetry group. The component $\mathcal{L}_{\phi}$ in the SM Lagrangian (see Equation 1.1), is the term related to the Higgs interaction after spontaneous symmetry breaking. The origin of mass in the SM comes from introducing the Higgs boson. Explicitly, by adding $\mathcal{L}_{\phi}$ one can give mass to the fermions and W, Z bosons. The complex scalar field ϕ in the SM is represented by the following complex doublet,

$$\begin{pmatrix} \phi^{+} \\ \phi^{0} \end{pmatrix} \tag{1.5}$$

The doublet obeys the Higgs Lagrangian $\mathcal{L}_{\phi}$ which is defined as such,

$$\mathcal{L}_{\phi} = (\mathcal{D}^{\mu}\phi)^{\dagger}(\mathcal{D}_{\mu}\phi) - V(\phi)^{\dagger} + \mathcal{L}_{\text{Yukawa}} \tag{1.6}$$

In Equation 1.6, the first term is the Higgs kinetic term, the second term, $V(\phi)$ is the Higgs potential which has the form,

$$V(\phi) = \mu^2(\phi^\dagger\phi) + \lambda(\phi^\dagger\phi)^2 \tag{1.7}$$

and finally, $\mathcal{L}_{\text{Yukawa}}$ are the Yukawa terms that correspond to the Higgs interactions with fermionic fields. This term is discussed in detail later on in this Chapter. The potential, $V(\phi)$, has a minimum that is non-zero when $\mu^2 < 0$ and $\lambda > 0$, giving rise to a non-zero vacuum expectation value (vev). The minimum at $\phi \equiv \phi_0$, is given as,

$$|\phi_0| = \frac{\mu}{\sqrt{2\lambda}} = \frac{\nu}{\sqrt{2}} \tag{1.8}$$

where, $\nu \equiv \frac{\mu}{\sqrt{\lambda}}$ and is the vev of the Higgs potential. An $SU(2)$ rotation of ϕ_0 gives rise to degenerate minimum of the Higgs potential. To break the degeneracy, one applies a unitary gauge transformation that spontaneously breaks the electroweak symmetry. The gauge transformation gives the solution,

$$\langle\phi\rangle = \frac{1}{\sqrt{2}}\begin{pmatrix} 0 \\ \nu \end{pmatrix} \tag{1.9}$$

Radial fluctuations of $\langle\phi\rangle$ generate the Higgs boson H. The Higgs field is then defined by the following perturbation of $\langle\phi\rangle$,

$$\langle\phi\rangle_{pert} = \frac{1}{\sqrt{2}}\begin{pmatrix} 0 \\ \nu + H \end{pmatrix} \tag{1.10}$$

By introducing the Higgs field, the mass terms for the gauge bosons can be introduced. In particular, the masses of the gauge bosons can be obtained from the kinetic component of $\mathcal{L}_\phi$ (See Equation 1.6). Substituting the perturbation of the Higgs potential $\langle\phi\rangle_{pert}$, into the Higgs kinetic term yields the following,

$$
\begin{aligned}
(\mathcal{D}^{\mu}\phi)^{\dagger}(\mathcal{D}_{\mu}\phi) = \Bigg[\frac{1}{\sqrt{2}}[\Bigg(\partial^{\mu} - ig\frac{1}{2}\overrightarrow{\tau}\cdot\overrightarrow{W}^{\mu} - ig^{'}\frac{1}{2}YB^{\mu}\Bigg)\begin{pmatrix}0\\ \nu+H\end{pmatrix}\Bigg]^{\dagger} \\
\times\Bigg[\frac{1}{\sqrt{2}}\Bigg(\partial_{\mu} - ig\frac{1}{2}\overrightarrow{\tau}\cdot\overrightarrow{W}_{\mu} - ig^{'}\frac{1}{2}YB_{\mu}\Bigg)\begin{pmatrix}0\\ \nu+H\end{pmatrix}\Bigg]
\end{aligned}
\tag{1.11}
$$

Expanding out Equation 1.11 one obtains the following,

$$
(\mathcal{D}^{\mu}\phi)^{\dagger}(\mathcal{D}_{\mu}\phi) = \frac{\nu^2}{8}\Bigg(g^2(W_1+W_2)^2 + (-gW_3 + YB_{\mu})^2\Bigg) + ... \tag{1.12}
$$

The masses of the gauge bosons can now be directly extracted, where

$$
m_W = \frac{g\nu}{2}, \qquad m_Z = \frac{\nu}{2}\sqrt{g^2+g^{'2}}, \qquad m_Z cos(W) = m_W \tag{1.13}
$$

In addition to the gauge bosons, the Higgs boson also provides the fermions with their masses. This is achieved through the component $\mathcal{L}_{\text{Yukawa}}$, which reiterating from earlier is the Yukawa term. The Yukawa term are expressions that contain the interactions between scalar fields and dirac fields. The generalised Yukawa Lagrangian for a single generation is given by Equation 1.14.

$$
\mathcal{L}_{\text{Yukawa}} = \lambda_e\bar{E}_L\phi E_R - \lambda_u\bar{Q}_L\phi^c u_R - \lambda_d\bar{Q}_L\phi d_R \tag{1.14}
$$

The first term in Equation 1.14 is the leptonic component, and the remaining terms are the quark terms. Moreover, $Q_L = \begin{pmatrix}u_L\\ d_L\end{pmatrix}$, is a quark $SU(2)$ doublet, $\phi^c = i\sigma_2\phi^*$, and L/R denotes left or right handed helicity. Substituting in the minimum solution from spontaneous symmetry breaking (SSB) (see Equation 1.9), one can determine the mass of the fermions in a single generation. As an illustration, the mass of the electron is derived,

$$\begin{aligned}
\mathcal{L}_{\mathrm{e}}^{Yukawa} &= -\lambda_e \bar{E}_L \phi E_R \\
&= -\lambda_e \Big[\bar{e_L} \phi e_R + \bar{e_R} \phi e_L \Big] \\
&= -\frac{\lambda_e}{\sqrt{2}} \Big[(\bar{\nu}, \bar{e}) \begin{pmatrix} 0 \\ \nu \end{pmatrix} e_R + \bar{e_R} (0, \nu) \begin{pmatrix} \nu \\ e \end{pmatrix}_L \Big] \\
&= -\frac{\lambda_e}{\sqrt{2}} \Big[\nu \bar{e_L} e_R + \nu \bar{e_R} e_L \Big] \\
&= -\frac{\nu \lambda_e}{\sqrt{2}} \bar{e} e
\end{aligned} \tag{1.15}$$

The term $\frac{\nu\lambda_e}{\sqrt{2}}$ is the mass of the electron. The same derivation can be applied to the quarks, and consequently the masses of the first generation fermions are given as,

$$m_e = \frac{\nu \lambda_e}{\sqrt{2}}, \qquad m_u = \frac{\nu \lambda_u}{\sqrt{2}}, \qquad m_d = \frac{\nu \lambda_d}{\sqrt{2}} \tag{1.16}$$

The mass terms are independent of generation and so the only difference is λ for all quarks and leptons, where $\lambda_{i=u,d,s,c,t,b,e,\mu,\tau}$. Moreover, the Yukawa terms can be extended further for quarks, taking into account couplings between different generations. The requirement is a modification to the quark component of the Yukawa Lagrangian (Equation 1.14), where the singlets u_R, d_R and doublet Q_L, become triplets in flavour, as illustrated below.

$$Q_{L,i} = \begin{pmatrix} U_{L,i} \\ D_{L,i} \end{pmatrix} = \left(\begin{pmatrix} u_L \\ c_L \\ t_L \end{pmatrix} \begin{pmatrix} d_L \\ s_L \\ b_L \end{pmatrix} \right), \quad u_{R,i} = (u_R, c_R, t_R), \quad d_{R,i} = (d_R, s_R, b_R) \tag{1.17}$$

The resulting Yukawa term for the quarks becomes,

$$\mathcal{L}_q^{Yukawa} = Y_{ij}^d \bar{Q}_{Lz} \phi D_{Rj} + Y_{i,j}^u \bar{Q}_{Lz} \phi^{*c} U_{Rj} \tag{1.18}$$

where i, j are the indices in space, z is the flavour index and $Q_{L,z}$ is defined in Equation 1.17. The terms in front $Y_{ij}^{u,d}$ have evolved from merely being constants when there is a single generation, to becoming a 3×3 matrix when one considers all generations. This matrix need not be diagonal as the states (u_L, c_L, t_L) and (d_L, s_L, b_L) are flavour eigenstates and not mass eigenstates. One can diagonalise the matrices $Y_{i,j}^{u,d}$ by performing a transformation through 4 unitary matrices, $V_{L,R}^{u,d}$ as defined in Equation 1.19,

$$\begin{aligned} V_L^d Y^d V_R^d &= \overrightarrow{M_d} \\ V_L^u Y^u V_R^u &= \overrightarrow{M_u} \end{aligned} \tag{1.19}$$

where $M_{d,u}$ are diagonal matrices. The states $U_{L,R}^{u,d}$ can also be transformed into another basis through these 4 unitary matrices,

$$\begin{aligned} U_L^{'} &= V_L U_L \\ U_R^{'} &= V_R U_R \\ D_L^{'} &= V_L D_L \\ D_R^{'} &= V_R D_R \end{aligned} \tag{1.20}$$

This means the whole Lagrangian as defined in Equation 1.18 can be transformed. Moreover, these transformations need to be invariant under the electroweak symmetry group. This is because U_L, D_L are states that appear in the charge coupling of the W boson, $\mathcal{L}_{\text{cc}}$, given by Equation 1.21.

$$\mathcal{L}_{\text{cc}} = -\frac{g}{\sqrt{2}} \underbrace{(u_L, d_L, t_L)}_{\bar{U_L}} W_\mu^+ \gamma^\mu \underbrace{\begin{pmatrix} d_L \\ s_L \\ b_L \end{pmatrix}}_{D_L} + hc \tag{1.21}$$

To transform Equation 1.21 into a physical, mass basis the 4 unitary matrices are utilised again.

$$\begin{aligned}\mathcal{L}_{\mathrm{cc}} &= -\frac{g}{\sqrt{2}}\left(\bar{U_L}' V_L^u D_L' V_L^{d\dagger} W_\mu^+ \gamma^\mu\right) \\ &= -\frac{g}{\sqrt{2}}\left(\bar{U_L}' (V_L^u V_L^{d\dagger}) D_L' W_\mu^+ \gamma^\mu\right)\end{aligned} \tag{1.22}$$

The term $V_L^u V_L^{d\dagger}$ in Equation 1.22 is a 3 $\times$ 3 matrix unitary matrix called the CKM matrix, V_{CKM}. V_{CKM} takes the generalised form as given by Equation 1.23. It should be mentioned that the CKM matrix can take a different form where it is parametrised in a hierarchial structure in terms of the parameter λ, where λ=0.22 [9]. This parametrisation is known as the Wolfenstein parametrisation. V_{CKM} under this parametrisation is given by Equation 1.24.

$$V_{\mathrm{CKM}} = \begin{pmatrix} V_{ud} & V_{us} & V_{ub} \\ V_{cd} & V_{cs} & V_{cb} \\ V_{td} & V_{ts} & V_{tb} \end{pmatrix} \tag{1.23}$$

$$V_{\mathrm{CKM}} = \begin{pmatrix} 1-\lambda^2/2 & \lambda & A\lambda^3(\rho - i\eta) \\ -\lambda & 1-\lambda^2/2 & A\lambda^2 \\ A\lambda^3(1-\rho-i\eta) & -A\lambda^2 & 1 \end{pmatrix} \tag{1.24}$$

The CKM matrix includes all coefficients corresponding to the interactions and mixing between quarks. The coefficients have been studied by various experiments over the years, and the precision on these terms has constantly improved. Equation 1.24 with λ=0.22 gives an approximation to the size of the CKM matrix elements. Table 1.2 shows the measured values for the magnitudes of the CKM matrix elements from the latest results. The CKM matrix play an important part in how flavour changing neutral currents are introduced in the SM. This is described in detail in the next section.

CKM Matrix element	Value
$\mid V_{ud} \mid$	0.974
$\mid V_{us} \mid$	0.223
$\mid V_{ub} \mid$	3.75×10^{-3}
$\mid V_{cd} \mid$	0.225
$\mid V_{cs} \mid$	0.974
$\mid V_{cb} \mid$	0.042
$\mid V_{td} \mid$	8.71×10^{-3}
$\mid V_{ts} \mid$	0.042
$\mid V_{tb} \mid$	0.999

Table 1.2: CKM matrix element size with the values taken from Ref [9].

1.1.1 Flavour changing neutral currents in the SM

In the previous section, it was demonstrated that the CKM matrix permits flavour changing charged current (FCCC) interactions, which are mediated through a W boson. This was shown by Equations 1.21 and 1.22. However, for flavour changing neutral current transitions, the same result cannot be obtained. This is demonstrated by the following example. The Lagrangian for a neutral current transition of a u-quark is given as,

$$\mathcal{L}_{NC} = ig(\bar{u}_{Lj} Z_\mu \gamma^\mu u_{Lj}) \tag{1.25}$$

Transforming this expression into the physical, mass basis, using the CKM matrix, the following expression is obtained,

$$\begin{aligned} \mathcal{L}_{NC} &= ig(\bar{u}_{Lj} V_L^u V_L^{u\dagger} Z_\mu \gamma^\mu u_{Lj}) \\ &= ig(\bar{u}_{Lj} \delta Z_\mu \gamma^\mu u_{Lj}) \\ &= ig(\bar{u}_{Lj} Z_\mu \gamma^\mu u_{Lj}) \end{aligned} \tag{1.26}$$

The property that the CKM matrix is unitary results in the same initial configuration, demonstrating that at tree level FCNC processes are forbidden. Hence, this means that only FCCC processes can change quark flavour at tree level. This phenomena is also known as the GIM mechanism. In order for FCNC processes to occur they must happen

at second order through loop level processes. Rare $b \to s\ell^+\ell^-$ decays are examples of FCNC processes. As an example, Figure 1.1 shows the Feynman diagrams for the rare $b \to s\ell^+\ell^-$ decay, $\bar{B}^0 \to \bar{K}^{*0}\mu^+\mu^-$. Figure 1.1 (a) shows the electroweak penguin process and Figure 1.1 (b) shows the box process. These processes are suppressed and occur with a much lower branching fraction than tree level processes, which makes them difficult to study. Nevertheless, they are an interesting probe for BSM physics. Rare $b \to s\ell^+\ell^-$ decays are FCNC transitions that can be susceptible to NP effects. The next section is dedicated to discussing rare $b \to s\ell^+\ell^-$ decays.

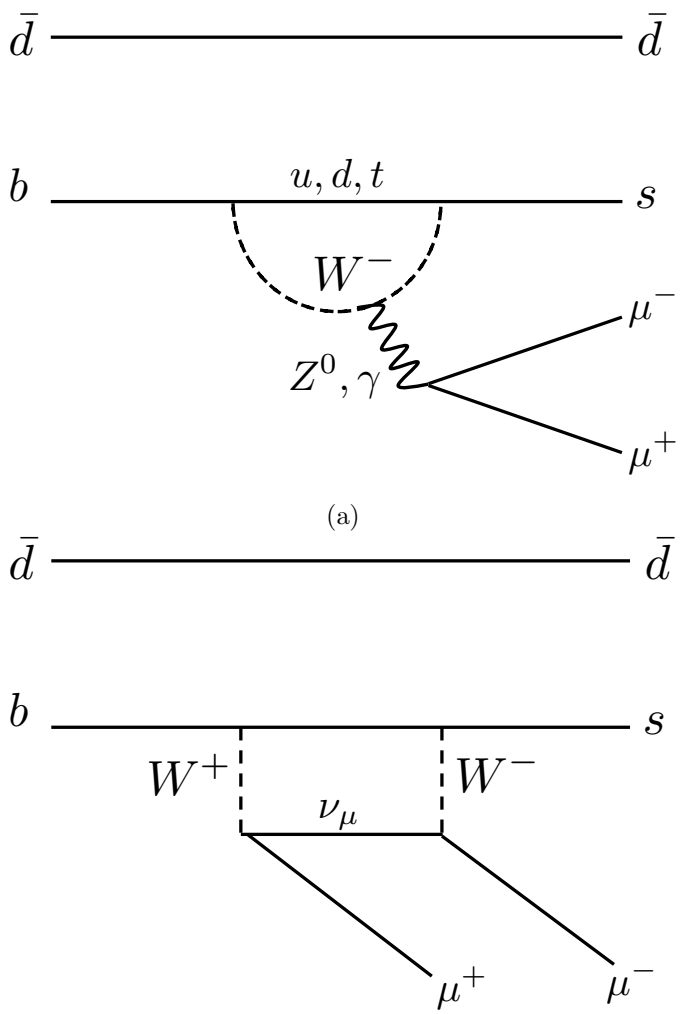

Figure 1.1: Feynman diagram showing the electroweak penguin (a) and box (b) processes for $\bar{B}^0 \to \bar{K}^{*0}\mu^+\mu^-$

1.2 Rare $b \to s\ell^+\ell^-$ decays

Rare $b \to s\ell^+\ell^-$ decays are particularly interesting to study because they can be susceptible to NP contributions that enter at the loop level through virtual loops. The NP contributions can modify the structure and angular distribution and decay rate. Nevertheless, before one can understand the distributions of rare $b \to s\ell^+\ell^-$ transitions and possible NP contributions that enter, a framework is needed to model the transitions themselves. This section describes the treatment of $b \to s\ell^+\ell^-$ transitions though an effective field theory framework.

1.2.1 An effective field theory approach

Particle physics aims to test the SM and search for possible NP beyond the SM (BSM). Many studies that aim to investigate phenomena BSM, rely on measuring a physical quantity through a framework which includes alternative NP models. Effective field theory (EFT) is a branch of quantum field theory that aims to describe and separate physical effects in terms of a given energy scale μ. There are many advantages of adopting such an EFT approach. For instance, it is model independent, no assumptions are made about the NP models included and the low energy effects are handled effectively. Nevertheless, there are disadvantages to such an approach. One problem that can arise is in how well one can factorise the physical effects according to the energy scale μ. If one can not factorise the effects, then it will impact the modelling. Another disadvantage is that the parametrisation of hadronic effects can introduce terms called Form Factors, which are low energy QCD effects that are difficult to determine precisely. Regardless of this, the effective theory approach is adequate for the study of B hadrons and in particular for $b \to s\ell^+\ell^-$ transitions where the effective field theory approach is expressed in terms of an Operator Product Expansion (OPE). The OPE for $b \to s\ell^+\ell^-$ transitions is described subsequently.

1.2.2 Operator Expansion Product

The OPE is an EFT tool that performs a summation over physical effects that have been separated according to a scale μ. It has been seen to be a powerful tool for many processes [10], making it appropriate for the modelling of $b \to s\ell^+\ell^-$ transitions. This section provides an overview of the OPE and its structure. The explicit form of the OPE for $\bar{B}^0 \to \bar{K}^{*0}\mu^+\mu^-$ decays is provided in Section 1.3.1. To begin, the first stage of the OPE is to split the physical processes according to the scale μ. Explicitly, the physical processes are split into two categories; short- and long-distance effects. Short distance effects are high energy effects such as weak physics interactions and NP contributions. They are described by scalar couplings, also known as Wilson Coefficients, C. Physical effects are categorised as short distance effects if the particles involved have a mass greater than μ. These short distance effects consequently are seen as effects in one or more Wilson Coefficients. The Wilson Coefficients form the perturbative section of the OPE, which makes them easy to calculate in physics models that contain SM or BSM processes. However, they can be difficult to determine experimentally. In contrast to the short distance effects, the long distance effects are low energy phenomena such as QCD effects. In order to model these long distance effects, various operators, $\mathcal{O}$ are introduced that incorporate effects below the scale of μ. These operators, $\mathcal{O}$, can be difficult to calculate as the physical processes are often non-pertubative. Furthermore, for every $\mathcal{O}_i$, where i is a given index, there is a corresponding Wilson Coefficient. This one-to-one relation means one can directly sum over an index i to produce a total OPE including all physics contributions. The result is an effective Hamiltonian $\mathcal{H}_{\text{eff}}$. The exact form of $\mathcal{H}_{\text{eff}}$ evaluated at the given scale μ and expressed in terms of a matrix element transitioning from an initial state (i) to a final state (f), is given by Equation 1.27.

$$\langle f|\mathcal{H}_{\text{eff}}|i\rangle = \sum_i = C_i(\mu)\langle f|\mathcal{O}_i|i\rangle|_\mu \tag{1.27}$$

This expression includes contributions from the SM physics and possible NP. Explicitly, once can separate the Wilson Coefficients into terms associated with contributions from

NP and contributions from the SM, as illustrated by Equation 1.28.

$$C_i = C_i^{\mathrm{SM}} + C_i^{\mathrm{NP}} \tag{1.28}$$

This is important when performing experimental measurements as any deviation from the SM Wilson Coefficient could imply possible NP. Moreover, the operators $\mathcal{O}_i$, encode the Lorentz structure of the coupling and therefore, if a deviation is seen in a particular Wilson Coefficient, it can reveal the coupling of the NP by noting the corresponding operators of that Wilson Coefficient.

1.3 The $\bar{B}^0 \to \bar{K}^{*0}\mu^+\mu^-$ decay

The $\bar{B}^0 \to \bar{K}^{*0}\mu^+\mu^-$ decay is an example of a $b \to s\ell^+\ell^-$ transition. It can be studied under the OPE framework and is an important decay for NP searches.

1.3.1 The effective Hamiltonian for $\bar{B}^0 \to \bar{K}^{*0}\mu^+\mu^-$

The complete effective Hamiltonian that describes rare $b \to s\ell^+\ell^-$ transitions such as $\bar{B}^0 \to \bar{K}^{*0}\mu^+\mu^-$ is given by Equation 1.29 [11].

$$\mathcal{H}_{\mathrm{eff}} = \frac{4G_F}{\sqrt{2}}\Big(V_{tb}V_{ts}^*\mathcal{H}_{\mathrm{eff}}^{(t)} + V_{ub}V_{us}^*\mathcal{H}_{\mathrm{eff}}^{(u)}\Big) \tag{1.29}$$

where

$$\mathcal{H}_{\mathrm{eff}}^{(t)} = C_1\mathcal{O}_1^c C_i + C_2\mathcal{O}_2^c + \sum_{i=3}^{6} C_i\mathcal{O}_i + \sum_{i=7,8,9,10,P,S} (C_i\mathcal{O}_i + C_i'\mathcal{O}_i') \tag{1.30}$$

$$\mathcal{H}_{\mathrm{eff}}^{(u)} = C_1(\mathcal{O}_1^c - \mathcal{O}_1^u) + C_2(\mathcal{O}_2^c - \mathcal{O}_2^u) \tag{1.31}$$

Equation 1.29 illustrates how the effective Hamiltonian is expressed in terms of 12 short distance Wilson Coefficients C_i and 12 long distance operators $\mathcal{O}_i$. Despite the significant number of operators that contribute to this decay, many of them are suppressed or constrained by experimental measurements [11]. The $\mathcal{O}_{1,2}^{c,u}$ terms in $\mathcal{H}_{\text{eff}}^{(u)}$ involve charm- and up-quark contributions that are doubly Cabbibo suppressed and are therefore ignored [11]. Likewise, the scalar and pseudo-scalar operators $\mathcal{O}_{P,S}$ are also highly suppressed and can be ignored. A detailed description of these operators can be found in Ref [11]. Through cancelling several operators this leaves three operators that are sizeable enough to contribute to $b \to s\ell^+\ell^-$ decays. These operators are $\mathcal{O}_7$, $\mathcal{O}_9$, $\mathcal{O}_{10}$ and their chiral partners, $\mathcal{O}_7^{'}$, $\mathcal{O}_9^{'}$, $\mathcal{O}_{10}^{'}$, defined as follows,

$$\mathcal{O}_7 = \frac{e}{g^2} m_b (\bar{s}\sigma_{\mu\nu} P_R b) F^{\mu\nu} \qquad \mathcal{O}_7^{'} = \frac{e}{g^2} m_b (\bar{s}\sigma_{\mu\nu} P_L b) F^{\mu\nu} \tag{1.32}$$

$$\mathcal{O}_9 = \frac{e^2}{g^2} (\bar{s}\gamma_\mu P_L b)(\bar{\mu}\gamma^\mu \mu) \qquad \mathcal{O}_9^{'} = \frac{e^2}{g^2} (\bar{s}\gamma_\mu P_R b)(\bar{\mu}\gamma^\mu \mu) \tag{1.33}$$

$$\mathcal{O}_{10} = \frac{e^2}{g^2} (\bar{s}\gamma_\mu P_L b)(\bar{\mu}\gamma^\mu \gamma_5 \mu) \qquad \mathcal{O}_{10}^{'} = \frac{e^2}{g^2} (\bar{s}\gamma_\mu P_R b)(\bar{\mu}\gamma^\mu \gamma_5 \mu) \tag{1.34}$$

In Equations 1.32, 1.33, 1.34, e denotes the electromagnetic coupling constant, g the strong coupling constant, m_b is the mass of the b quark, $\sigma_{\mu\nu}$ are the Pauli-spin matrices, $F^{\mu\nu}$ is the electromagnetic field tensor and $P_{L/R}$ are the left/right chirality projections. Each operator corresponds to a different process. $\mathcal{O}_7$ is the electromagnetic operator and is associated with penguin diagrams that proceed via a photon current as illustrated by Figure 1.2. Both $\mathcal{O}_9$ and $\mathcal{O}_{10}$ are semileptonic operators. Specifically, $\mathcal{O}_9$ is the vector operator, while $\mathcal{O}_{10}$ is the axial-vector operator. Bubble diagrams of the processes for the operators $\mathcal{O}_{7,9,10}$ are given in Figure 1.2. As mentioned earlier in Section 1.2.2, the OPE and therefore the effective Hamiltonian is a function of a scale μ. The Wilson Coefficients are calculated at $\mu = m_W$ before evolving down to the scale $\mu = m_b$, where terms are expanding out perturbatively. This results in adding many terms to the

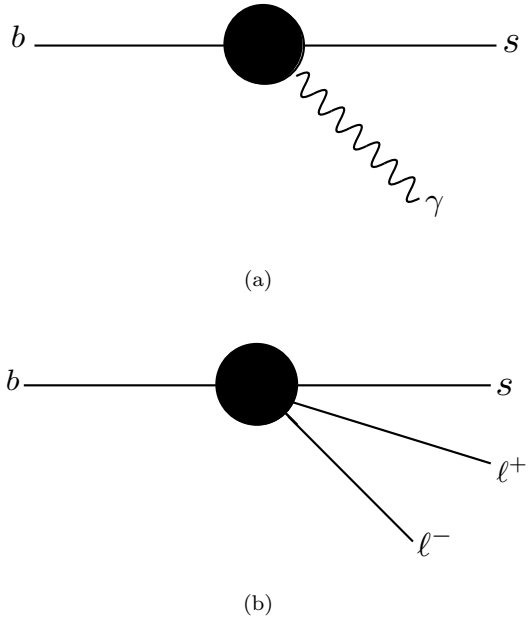

Figure 1.2: Bubble diagrams demonstrating the operators that significantly contribute to $b \to s\ell^+\ell^-$ processes. (a) describes the electromagnetic operator $\mathcal{O}_7$ which describes processes that proceed via a photon current and (b) describes the operators $\mathcal{O}_9$ and $\mathcal{O}_{10}$ that describe processes involving a vector current.

Wilson Coefficients and therefore one cannot assume one specific contribution to a given Wilson Coefficient. To deal with these additional next-to-next-to-leading order terms (NNLO) the Wilson Coefficients are often expressed as "effective Wilson Coefficients". Only Wilson Coefficients $C_{7,9,10}$ are significant to $b \to s\ell^+\ell^-$ transitions. Therefore, the effective Wilson Coefficients that are the focus of in this analysis are $C^{\text{eff}}_{7,9,10}$, $C'^{\text{eff}}_{7,9,10}$ which are shown by Equation 1.35.

$$\begin{aligned} C_7^{\text{eff}} &= \frac{4\pi}{\alpha_s} C_7 - \frac{1}{3} C_3 - \frac{4}{9} C_4 - \frac{20}{3} C_5 - \frac{80}{9} C_6 \\ C_9^{\text{eff}} &= \frac{4\pi}{\alpha_s} C_9 + Y(q^2) \\ C_{10}^{\text{eff}} &= \frac{4\pi}{\alpha_s} C_{10} \\ C'^{\text{eff}}_{7,910} &= \frac{4\pi}{\alpha_s} C'_{7,910} \end{aligned} \tag{1.35}$$

In Equation 1.35 one can clearly see the mixing between Wilson Coefficients. For example, C_7^{eff} is a combination of $C^{\text{SM}}_{3,4,5,6,7}$. The term $Y(q^2)$ is a collection of Wilson Coefficients that span several terms and includes the contributions from non-local effects.

Wilson Coefficient	Value
C_9^{eff}	4.27
$C_9^{\prime\text{eff}}$	0
C_{10}^{eff}	-4.16
$C_{10}^{\prime\text{eff}}$	0
C_7^{eff}	-0.304
$C_7^{\prime\text{eff}}$	-0.006

Table 1.3: The main SM Wilson coefficients C_i^{eff} that enter into the $\bar{B}^0 \to \bar{K}^{*0}\mu^+\mu^-$ decay. The Wilson coefficients have been calculated to NNLL, at the scale $\mu = m_b$, [11].

A detailed discussion of this term is given in Section 1.4.2. The values of the NNLO Wilson Coefficients for $b \to s\ell^+\ell^-$ transitions is given by Table 1.3. Each Wilson Coefficient that contributes to $\bar{B}^0 \to \bar{K}^{*0}\mu^+\mu^-$ controls the behaviour in a certain region of the q^2 spectrum. This is illustrated in the differential decay rate in Figure 1.3. In Figure 1.3, there is a rise < 1.0 GeV$^2/c^4$, which corresponds to the photon pole and originates from C_7 transitions. C_7 dominates in this region, however as q^2 increases this Wilson Coefficient interferes with the Wilson Coefficient C_9. In the middle of the q^2 range, near the dominant J/ψ and $\psi(2S)$ resonances, C_9 dominates. Beyond the J/ψ and $\psi(2S)$ resonances, effects from C_{10} enter and dominate. It is evident that the Wilson Coefficients heavily influence the shape of the q^2 spectrum and therefore are important to $\bar{B}^0 \to \bar{K}^{*0}\mu^+\mu^-$.

1.3.2 Form factors

In $\bar{B}^0 \to \bar{K}^{*0}\mu^+\mu^-$ decays, there are six form factors $F(q^2) = V$, A_1, A_{12}, T_1, T_2, T_{23} that describe the $\bar{B} \to \bar{K}^*$ matrix elements for the main contributing operators for $b \to s\ell^+\ell^-$ transitions. One thing that makes these form factors difficult to determine precisely is that they can only be calculated by a non-perturbative approach [11]. There are two methods implemented to calculated the form factors: Light Cone Sum Rules (LCSR) and Lattice QCD. More detail about these methods can be found in Refs [11, 13, 14]. In this analysis, which aims to determine the impact of the non-local charm loop in $\bar{B}^0 \to \bar{K}^{*0}\mu^+\mu^-$ decays across the full q^2 spectrum, a parameterisation of the form

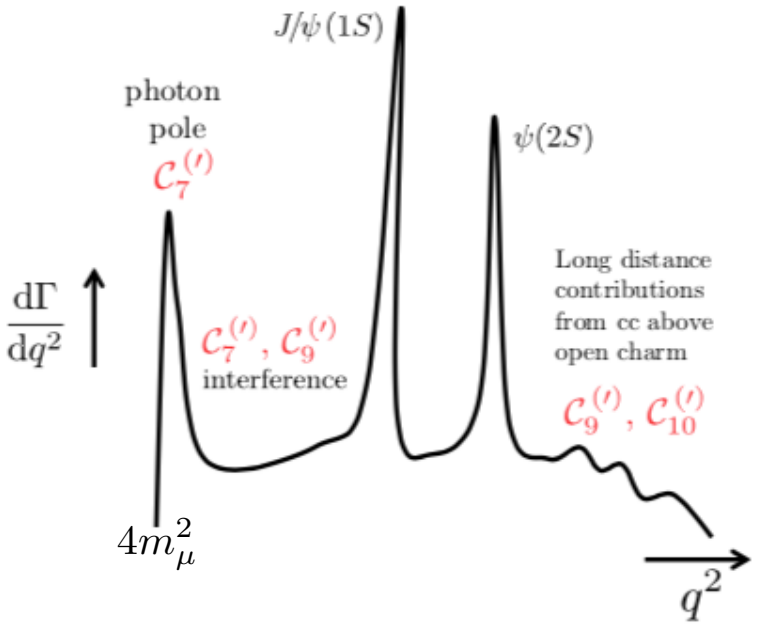

Figure 1.3: The differential decay rate for $\bar{B}^0 \to \bar{K}^{*0}\mu^+\mu^-$ as a function of q^2 and illustrating the regions of the dimuon, invariant mass-squared spectrum that are susceptible to different Wilson Coefficients. The diagram is orignally taken from Ref [12]

factors across the full kinematic range is required. To achieve this, the parameterisation as given in Ref [13] is adopted. In Ref [13], the form factors have been calculated using both the LCSR and Lattice QCD, before interpolating between the two to achieve a continuous distribution for the form factors across the full q^2 spectrum. The six form factors are then written as follows,

$$F^i(q^2) = \frac{1}{1 - q^2/m_{R_i}^2} \sum_{k=0}^{2} a_k^i [z(q^2) - z(0)]^k \tag{1.36}$$

where

$$z(t) = \frac{\sqrt{t_+ - t_-} - \sqrt{t_+ - t_0}}{\sqrt{t_+ - t_-} + \sqrt{t_+ - t_0}} \tag{1.37}$$

In Equation 1.36 and Equation 1.37, $t_\pm = (m_B \pm m_{K*})^2$, $t_0 = t_+(1 - \sqrt{1 - t_-/t_+})$, m_{R_i} are the masses of the excited B_s states as given in Ref [13], a_i are the parameters obtained from fitting a $z-$expansion to a given form factor. The $z-$expansion up to an order of $z = 2$ can sufficiently describe the form factors. This means for each form factor

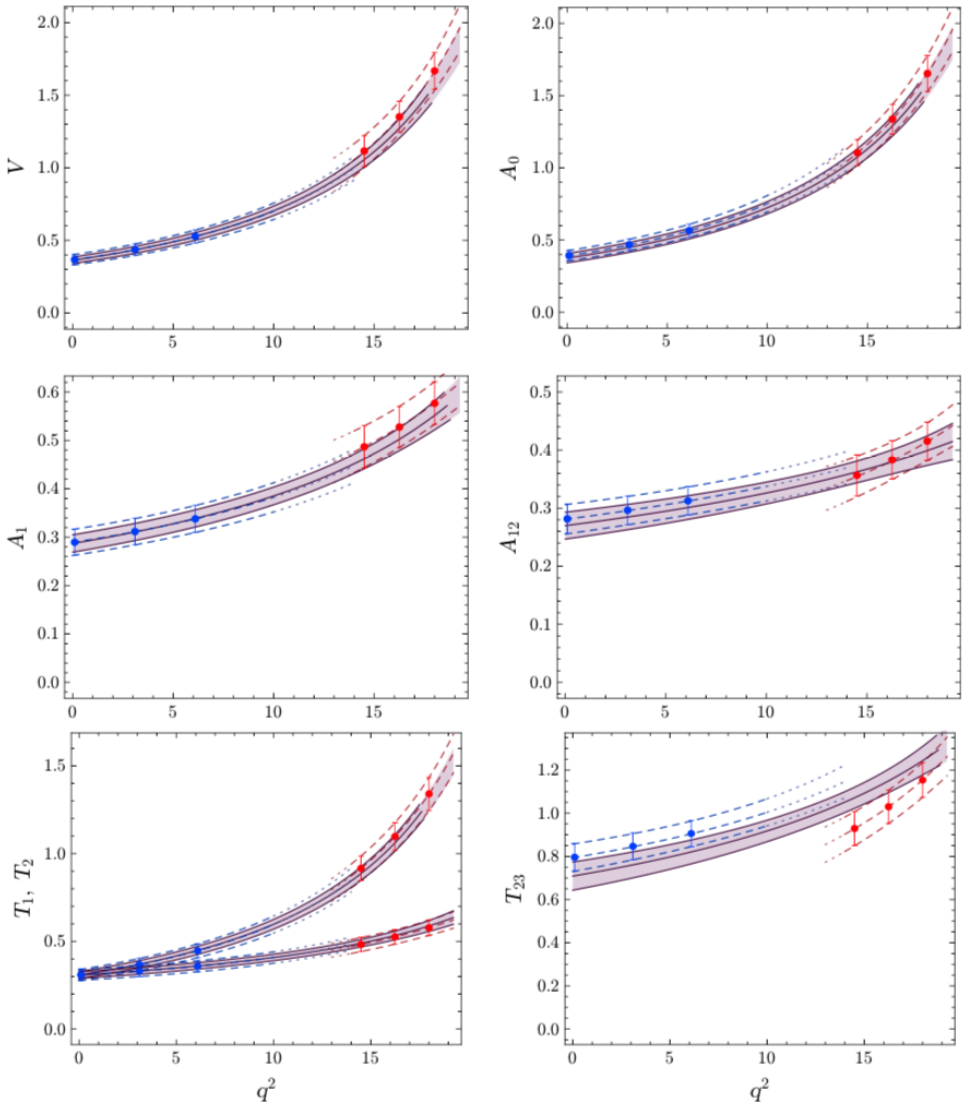

Figure 1.4: The $\bar{B} \to \bar{K}^*$ form factors, which have been obtained from combining both the Lattice QCD, and LCSR results. The LCSR data points are indicated by the blue points, the Lattice QCD data points by the red points and the combined fit using a z-expansion parametrisation which is truncated after the second order is illustrated by the grey band Ref [13].

F^i there are three fit parameters α_0^i, α_1^i, α_2^i. The values of these parameters and their correlations are taken from Ref [13]. An illustration of the form factors across the full q^2 range is given in Figure 1.4. The form factors generally agree with the data within their errors, apart from T_{23}, which shows slight deviation at both low and high q^2, where the data points lie outside the uncertainty bands. The authors in Ref [13] suggest that these deviations will disappear with improved measurements of the form factors, which should be done if we are to improve our modelling of decays that contain $B \to K^*$ form factors.

1.3.3 The $\bar{B}^0 \to \bar{K}^{*0}\mu^+\mu^-$ helicity amplitudes

The decay amplitudes in the transversity basis form the foundation of the angular distrsibution for $\bar{B}^0 \to \bar{K}^{*0}\mu^+\mu^-$ decays. In this section only the P-wave amplitudes are discussed. The impact of an S-wave contribution is described later in Chapter 4. The $\bar{K}^*$ is a vector meson that can be polarized. As a consequence, there exist longitudinal A_0, or transverse polarisations, for which for the latter can be either parallel $A_\parallel$ or perpendicular $A_\perp$. Each of these amplitude states can exist for both left and right handed chirality L, R. This means in total there are 6 complex transversity amplitudes that fully describe the P-wave state of $\bar{B}^0 \to \bar{K}^{*0}\mu^+\mu^-$ decays. The exact expressions for these amplitudes, assuming a narrow $\bar{K}^*$ are as follows,

$$\mathcal{A}_0^{\mathrm{L,R}}(q^2) = -8N\frac{m_B m_{K^*}}{\sqrt{q^2}}\left\{(C_9 \mp C_{10})A_{12}(q^2) + \frac{m_b}{m_B + m_{K^*}}C_7 T_{23}(q^2)\right\}, \tag{1.38}$$

$$\mathcal{A}_\parallel^{\mathrm{L,R}}(q^2) = -N\sqrt{2}(m_B^2 - m_{K^*}^2)\left\{(C_9 \mp C_{10})\frac{A_1(q^2)}{m_B - m_{K^*}} + \frac{2m_b}{q^2}C_7 T_2(q^2)\right\}, \tag{1.39}$$

$$\mathcal{A}_\perp^{\mathrm{L,R}}(q^2) = N\sqrt{2\lambda}\left\{(C_9 \mp C_{10})\frac{V(q^2)}{m_B + m_{K^*}} + \frac{2m_b}{q^2}C_7 T_1(q^2)\right\}, \tag{1.40}$$

where m_B, m_{K^*} and m_ℓ are the masses of the B-meson, K^*-meson, and lepton, and λ, β_ℓ, and N are defined as,

$$\lambda = m_B^4 + m_{K^*}^4 + q^4 - 2(m_B^2 m_{K^*}^2 + m_{K^*}^2 q^2 + m_B^2 q^2) \tag{1.41}$$

$$\beta_\ell = \sqrt{1 - 4m_\ell^2/q^2} \tag{1.42}$$

$$N = V_{tb}V_{ts}^{*}\sqrt{\frac{G_F^2\alpha^2}{3\times 2^{10}\pi^5 m_B^3}q^2\lambda^{1/2}\beta_\mu}\,. \tag{1.43}$$

1.3.4 Defining the angular basis and helicity angles

The decay $\bar{B}^0 \to \bar{K}^{*0}(K^-\pi^+)\mu^+\mu^-$ is a four body pseudoscalar to vector transition, that can fully be characterized by four degrees of freedom. These four degrees of freedom can be split into three angles cos θ_ℓ, cos θ_K and ϕ, and q^2 , where as mentioned previously q^2 is the dimuon invariant mass squared. It should be noted that the $\bar{K}^{*0}$ can also denote a scalar or vector resonance. This means that when considering a general $\bar{K}_J^{*0}$ state the additional dimension of the invariant mass of the $K^-\pi^+$ system is required. The definition of the decay angles is provided in a given helicity basis [11]. The angular basis is either written using either the theorists or experimentalists convention. The experimentalist convention is also referred to as the LHCb convention amongst the LHCb collaboration. It is important to be clear about what angular convention is used and how one can translate from one basis to another. The predominant basis which is also adopted for this analysis is the experimentalists basis. This basis is the same basis as used by previous analyses presented in Refs [4, 15, 16]. cos θ_ℓ is defined as the cosine of the angle (θ_ℓ), between the direction of the positively (negatively) charged muon in the dimuon rest frame and the direction of the dimuon in the rest frame of the $\bar{B}^0(B^0)$. This angle describes only the muons and is defined differently for $\bar{B}^0$ and B^0. Explicitly, Equation 1.44 shows cos θ_ℓ for $\bar{B}^0$ and Equation 1.45 shows cos θ_ℓ for B^0.

$$\cos\theta_\ell = -\frac{\vec{p}_{\mu^-}^{\,\mu\mu}\cdot\vec{p}_B^{\,\mu\mu}}{|\vec{p}_{\mu^-}^{\,\mu\mu}||\vec{p}_B^{\,\mu\mu}|} \tag{1.44}$$

$$\cos\theta_\ell = -\frac{\vec{p}_{\mu^+}^{\,\mu\mu}\cdot\vec{p}_B^{\,\mu\mu}}{|\vec{p}_{\mu^+}^{\,\mu\mu}||\vec{p}_B^{\,\mu\mu}|} \tag{1.45}$$

In both these equations and all subsequent equations for the other angles, p_a^b is the momentum of particle a in the rest frame of particle b. To support this, Figure 1.5 presents an illustration of the definition of θ_ℓ in the experimentalists convention for

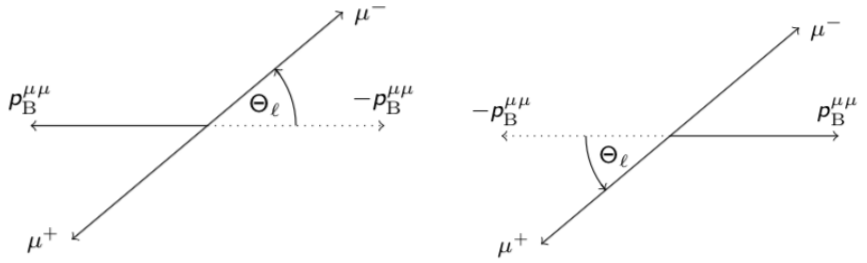

(a) θ_L for the $\bar{B}^0$ decay (b) θ_ℓ for the B^0 decay

Figure 1.5: θ_ℓ defined for (a) the $\bar{B}^0$ decay and (b) the B^0 decay [17].

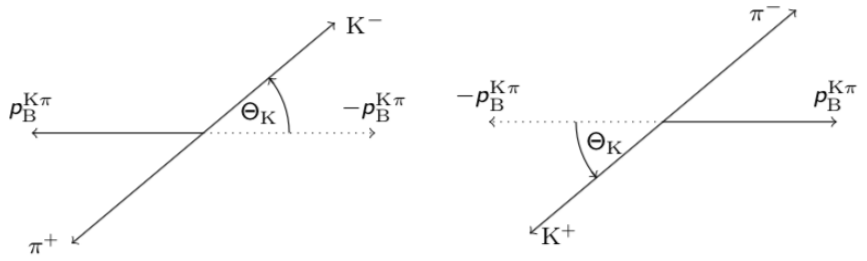

(a) θ_K for the $\bar{B}^0$ decay (b) θ_K for the B^0 decay

Figure 1.6: θ_K defined for (a) the $\bar{B}^0$ decay and (b) the B^0 decay [17].

both $\bar{B}^0$ and B^0. Moving on, cos θ_K is the cosine of the angle θ_K, which is defined as the angle between the direction of the kaon in the $\bar{K}^{*0}/K^{*0}$ rest frame, and the direction of the $\bar{K}^{*0}/K^{*0}$ in the $\bar{B}^0/B^0$ rest frame. The exact definition of cos θ_K is given by Equation 1.46 and is the same for both $\bar{B}^0$ and B^0. An illustration of θ_K is provided by Figure 1.6 which shows θ_K defined for both $\bar{B}^0$ and B^0, under the experimentalists convention.

$$\cos\theta_K = -\frac{\vec{p}_K^{K\pi} \cdot \vec{p}_B^{K\pi}}{|\vec{p}_K^{K\pi}||\vec{p}_B^{K\pi}|} \tag{1.46}$$

Finally, ϕ is defined as the angle between the plane containing the two muons (μ^+, μ^-) and the plane containing the $K^-\pi^+$/ $K^+\pi^-$ from the $\bar{K}^{*0}/K^{*0}$. The definition of ϕ given a $\bar{B}^0 \to \bar{K}^{*0}\mu^+\mu^-$ transition is shown by Equation 1.47. The definition of the mirrored decay $B^0 \to K^{*0}\mu^+\mu^-$ is also given by Equation 1.48.

$$\begin{aligned} \cos(\phi) &= -\vec{n}^{\,B}_{K\pi} \cdot \vec{n}^{\,B}_{\mu^-\mu^+} \\ \sin(\phi) &= (\vec{n}^{\,B}_{K\pi} \times \vec{n}^{\,B}_{\mu^-\mu^+}) \cdot \frac{\vec{p}^{\,B}_{K\pi}}{|\vec{p}^{\,B}_{K\pi}|} \end{aligned} \tag{1.47}$$

$$\begin{aligned} \cos\phi &= \vec{n}^{\,B}_{K\pi} \cdot \vec{n}^{\,B}_{\mu^-\mu^+} \\ \sin\phi &= (\vec{n}^{\,B}_{K\pi} \times \vec{n}^{\,B}_{\mu^-\mu^+}) \cdot \frac{\vec{p}^{\,B}_{K\pi}}{|\vec{p}^{\,B}_{K\pi}|} \end{aligned} \tag{1.48}$$

In these equations $\vec{n}$ denotes the unit normal vector. An illustration of ϕ is provided by Figure 1.7 which shows ϕ defined for both $\bar{B}^0$ and B^0, under the LHCb convention. As mentioned earlier the angles have been given in the experimentalists convention. For completeness, the theorists convention is given in Appendix A.1 and more information regarding this convention can be found in Ref [11, 18].

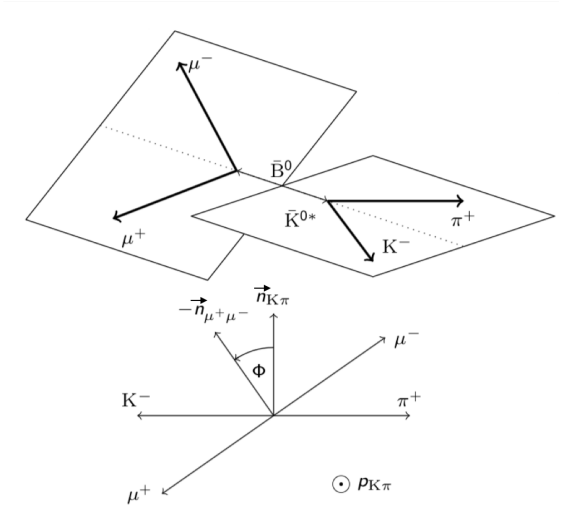

(a) ϕ defined for the $\bar{B}^0$ decay

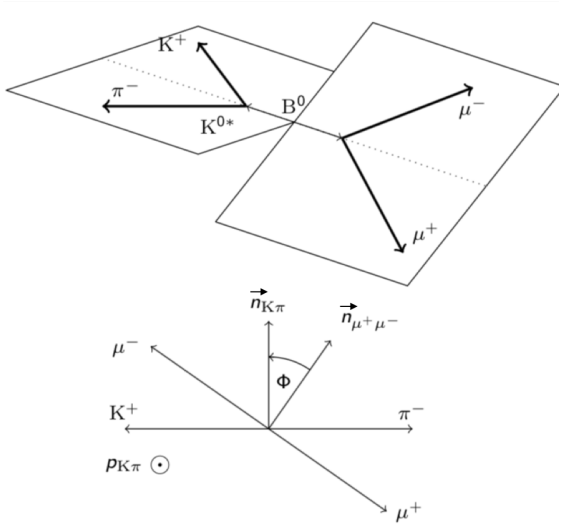

(b) ϕ defined for the B^0 decay

Figure 1.7: ϕ defined for (a) the $\bar{B}^0$ decay and (b) the B^0 decay [17].

1.3.5 The $\bar{B}^0 \to \bar{K}^{*0}\mu^+\mu^-$ angular distribution

The angular distribution for $\bar{B}^0 \to \bar{K}^{*0}\mu^+\mu^-$ in a P-wave system, is defined explicitly as,

$$\begin{aligned}\frac{\mathrm{d}^4\Gamma[\bar{B}^0 \to \bar{K}^{*0}\mu^+\mu^-]}{\mathrm{dcos}\,\theta_\ell\,\mathrm{dcos}\,\theta_K\,\mathrm{d}\phi\,\mathrm{d}q^2} = \frac{9}{32\pi}[&J_{1s}\sin^2\theta_K + J_{1c}\cos^2\theta_K + J_{2s}\sin^2\theta_K\cos2\theta_\ell \\ &+J_{2c}\cos^2\theta_K\cos2\theta_\ell + J_3\sin^2\theta_K\sin^2\theta_\ell\cos2\phi \\ &+J_4\sin2\theta_K\sin2\theta_\ell\cos\phi + J_5\sin2\theta_K\sin\theta_\ell\cos\phi \\ &+J_{6s}\sin^2\theta_K\cos\theta_\ell + J_7\sin2\theta_K\sin\theta_\ell\sin\phi \\ &+J_8\sin2\theta_K\sin2\theta_\ell\sin\phi + J_9\sin^2\theta_K\sin^2\theta_\ell\sin2\phi]\end{aligned} \tag{1.49}$$

Equation 1.49 demonstrates how the angular distribution is formed out of 11 angular coefficients, J. Each angular coefficient as shown in Equation 1.50 is formed from bilinear combinations of the transversity amplitudes and therefore can give direct information about the amplitudes. The angular coefficients contain the q^2 dependence of the angular distribution. The angular dependence (cos θ_K, cos θ_ℓ, ϕ) is introduced through the spherical harmonics that multiply each J_i [19].

$$
\begin{aligned}
J_{1s}(q^2) = \frac{(2+\beta_\mu^2)}{4}\Big[|A_\perp^L|^2 + |A_\parallel^L|^2 + (L \to R)\Big] + \frac{4m_\mu^2}{q^2} Re(A_\perp^L A_\perp^{R*} + A_\parallel^L A_\parallel^{R*}) \\
J_{1c}(q^2) = |A_0^L|^2 + |A_0^R|^2 + \frac{4m_\mu^2}{q^2}\Big[2\mathrm{Re}(A_0^L A_0^{R*})\Big] \\
J_{2s}(q^2) = \frac{\beta_\mu^2}{4}\Big[|A_\perp^L|^2 + |A_\parallel^L|^2 + (L \to R)\Big] \\
J_{2c}(q^2) = -\beta_\mu^2\Big[|A_0^L|^2 + (L \to R)\Big] \\
J_3(q^2) = \frac{\beta_\mu^2}{2}\Big[|A_\perp^L|^2 - |A_\parallel^L|^2 + (L \to R)\Big] \\
J_4(q^2) = \frac{\beta_\mu^2}{\sqrt{2}}\Big[\mathrm{Re}(A_0^L A_\parallel^{L*}) + (L \to R)\Big] \\
J_5(q^2) = \sqrt{q}\beta_\mu\Big[\mathrm{Re}(A_0^L A_\perp^{L*}) - (L \to R)\Big] \\
J_{6s}(q^2) = 2\beta_\mu\Big[\mathrm{Re}(A_\parallel^L A_\perp^{L*}) - (L \to R)\Big] \\
J_7(q^2) = \sqrt{q}\beta_\mu\Big[\mathrm{Im}(A_0^L A_\parallel^{L*}) - (L \to R)\Big] \\
J_8(q^2) = \beta_\mu^2\Big[\mathrm{Im}(A_0^L A_\perp^{L*}) + (L \to R)\Big] \\
J_9(q^2) = \beta_\mu^2\Big[\mathrm{Im}(A_\parallel^{L*} A_\perp^L) + (L \to R)\Big]
\end{aligned}
\tag{1.50}
$$

The continuous distribution of the J terms and the angles, result in the angular distribution being identical for B^0 and $\bar{B^0}$. This is important as one can sum up the decay rates (Γ,$\bar{\Gamma}$) to determine a new set of observables known as CP-even (S_i) and CP-odd (A_i) observables. For completeness, it should be mentioned that in the literature the CP-even observables are also referred to as CP-averaged observables. The CP-even observables are given by Equation 1.51 and the CP-odd observables are given by Equation 1.52.

$$
S_i = (J_i + \bar{J}_i) \Big/ \frac{d(\Gamma + \bar{\Gamma})}{dq^2} \tag{1.51}
$$

$$
A_i = (J_i - \bar{J}_i) \Big/ \frac{d(\Gamma + \bar{\Gamma})}{dq^2} \tag{1.52}
$$

The main motivation to study these CP-even and odd observables is that not only do they offer a theoretically clean way of studying $\bar{B}^0 \to \bar{K}^{*0}\mu^+\mu^-$ as a result of the cancellation of theoretical uncertainties, but they can be used to separate CP-conserving

and violating effects [11]. As mentioned previously, the form factors provide a source of uncertainty in the EFT approach used to treat $\bar{B}^0 \to \bar{K}^{*0}\mu^+\mu^-$ decays. In light of this, one can form a set of new optimised observables, $P_i^{(\prime)}$ where i=1-6,8, which have been calculated from the CP-even observables such that the form factor uncertainties cancel to first order. The optimised observables are,

$$\begin{aligned} P_1 &= \frac{2S_3}{1-F_L} \\ P_2 &= \frac{2}{3}\frac{A_{\rm FB}}{(1-F_L)} \\ P_3 &= \frac{-S_9}{(1-F_L)} \\ P_4^{\prime} &= \frac{S_4}{\sqrt{F_L(1-F_L)}} \\ P_5^{\prime} &= \frac{S_5}{\sqrt{F_L(1-F_L)}} \\ P_6^{\prime} &= \frac{S_7}{\sqrt{F_L(1-F_L)}} \\ P_8^{\prime} &= \frac{S_8}{\sqrt{F_L(1-F_L)}} \end{aligned} \tag{1.53}$$

where F_L is the longitudinal, polarisation fraction defined as $F_L \equiv S_{1c}$, and $A_{\rm FB}$ is the forward-backward asymmetry for the dimuons defined as, $A_{\rm FB} \equiv \frac{3}{4}S_{6s}$. These optimised observables have been studied extensively and more information on them can be found in Refs [4, 15, 20–22]. It should be mentioned that in some theoretical interpretations the definition of the optimised observables are different [20]. For this analysis, the form adopted for the angular observables is the same as Equation 1.53, which has been used in previous analyses [4, 16].

1.4 Investigating New Physics with $\bar{B}^0 \to \bar{K}^{*0}\mu^+\mu^-$ and other rare $b \to s\ell^+\ell^-$ decays

This section deals with how experiments can investigate NP with these decays and in particular the decay $\bar{B}^0 \to \bar{K}^{*0}\mu^+\mu^-$. This section lays the foundation for the analysis

provided in this thesis.

1.4.1 The $b \to s\ell^+\ell^-$ anomalies

Discrepencies between measured $b \to s\ell^+\ell^-$ decays and the SM predictions were first seen by LHCb in Run 1 (2011-2012) of the LHC. Since then experiments including CMS and Belle have studied theses discrepencies and their findings are generally consistent with the deviations seen by the LHCb experiment. This suggests that the deviations are not caused by detector effects, posing the question of what is causing these deviations from the SM in $b \to s\ell^+\ell^-$decays. It has been shown that the anomalies can be grouped into three categories. The three categories are: measurements of the differential branching fractions, angular analyses and tests of lepton universality. The differential branching fraction results show deviations between the measured differential branching fraction and the predicted SM differential branching fraction [4, 23–25]. In all the branching fraction measurements the results are lower than the predictions from the SM. Angular analyses are analyses performed on the angular structure of the decay to measure a number of angular observables. These analyses are often favoured as once can determine the complete anatomy of a decay from its rich amplitude structure. Several analyses performed at LHCb have deviations in the angular observables when compared to SM predictions [4, 25–27]. Finally, the last set of anomalous results fall into the category of lepton universality tests. The SM predicts the coupling of gauge bosons to leptons is universal and independent of the flavour of a given lepton. To test this, ratios are measured between transitions where the only difference is the leptons in the final state. These tests are often favoured as they are free from hadronic uncertainties, which cancel in the ratio. If there is universality between leptons then these ratios are 1. However, the LHCb experiment has measured deviations from unity in several channels [28, 29]. The complete list of anomalies seen in $b \to s\ell^+\ell^-$ transitions by LHCb is given in Table 1.4. One such anomalous result that gained significant attention were the discrepancies in the angular analysis of $\bar{B}^0 \to \bar{K}^{*0}\mu^+\mu^-$, measured by the LHCb experiment [4, 15]. Deviations were seen in the angular observables, F_L, $A_{\rm FB}$ and $P_5^{'}$, which were earlier defined in Section 1.3.5. The latest result presented in Ref

Angular analyses	Branching Fractions	Lepton flavour universality tests
$B^0 \to K^{*0}\mu^+\mu^-$	$B^0 \to K^{*0}\mu^+\mu^-$	$B^0 \to K^{*0}\ell^+\ell^-$
$B^0 \to K^{*0}e^+e^-$	$B^+ \to K^{(*)+}\mu^+\mu^-$	$B^+ \to K^+\ell^+\ell^-$
$\Lambda_b \to \Lambda\mu^+\mu^-$	$\Lambda_b \to \Lambda\mu^+\mu^-$	
$B_s \to \phi\mu^+\mu^-$	$B_s \to \phi\mu^+\mu^-$	

Table 1.4: The $b \to s\ell^+\ell^-$ transitions that have through experimental results show tensions with the SM. The anomalous results fall into the categories Angular analyses, Branching Fractions and Lepton flavour universality tests. All analyses have been performed by the LHCb experiment.

[4] investigated the angular observables with more data (3fb^{-1}) and reported a 3.4σ tension between the measured angular distribution for $\bar{B}^0 \to \bar{K}^{*0}\mu^+\mu^-$ and the SM predictions. This tension is interpreted as a shift in the real component of the vector Wilson Coefficient C_9. In light of this result, the angular analysis of $\bar{B}^0 \to \bar{K}^{*0}\mu^+\mu^-$ was repeated using data from other LHC experiments; CMS and ATLAS, as well as from the b-factory experiment Belle. Figure 1.8 shows the distribution of the form factor independent observable $P_5^{'}$ as a function of q^2 with the data from LHCb, CMS, ATLAS and Belle. For completeness, the SM prediction from two different groups; DHMV [30] and ASZB [13, 31], is included. The results revealed all experiments exhibit a disagreement with the SM in the q^2 region of 4.0 - 6.0 GeV^2/c^4, where the level of disagreement varies with the experiment. In light of the $\bar{B}^0 \to \bar{K}^{*0}\mu^+\mu^-$ anomaly many theorists attempted to quantify the result and determine if there were any connections to the other $b \to s\ell^+\ell^-$ anomalies [31–34]. Specifically, this is achieved by taking the results from branching fraction measurements, angular analyses and lepton universality tests, and performing global fits to the Wilson Coefficients. The central idea behind global fits is to take experimental results and combine them with theoretical uncertainties, whilst taking into account correlations between observables and bins. A fit is then performed and contours of possible regions of parameter space for the Wilson Coefficients are obtained. Conventionally, the contours are obtained for the Wilson Coefficients C_9 and C_{10}, and all other Wilson Coefficients are assumed to have the SM values. Moreover, the contours are produced as shifts to the SM values of the Wilson Coefficients. This allows a direct determination of the size of the shift to the Wilson Coefficients as well as the direction of the possible NP. Figure 1.9 illustrates a example fit to the real components of the Wilson Coefficients C_9 and C_{10}, when including results from the $b \to s\mu\mu$ analyses

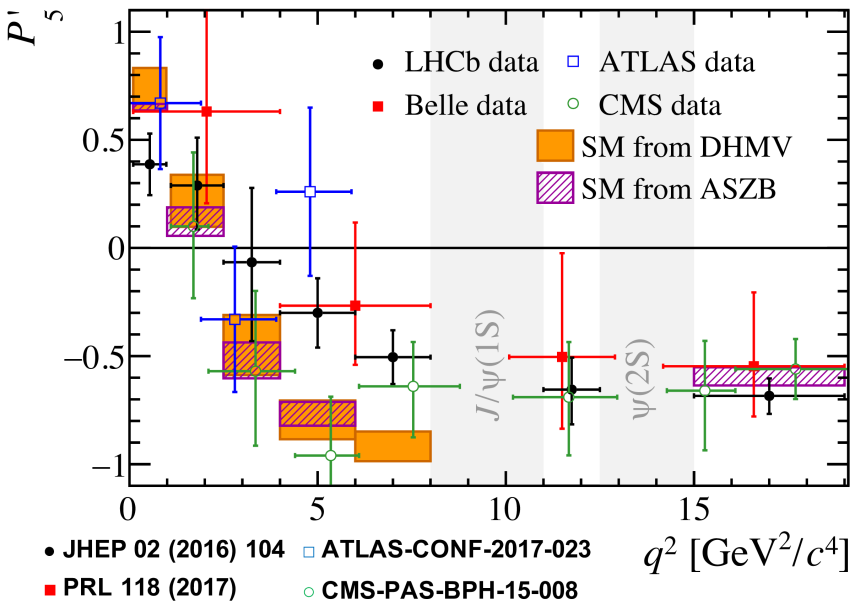

Figure 1.8: The observable $P_5^{'}$ as a function of q^2. The experimental results are shown for the LHCb experiment(solid, black data points), the Belle experiment (solid red, square data points), the ATLAS experiment (blue, square data points) and the CMS experiment (green, circle data points.) The theoretical predictions from two separate authors are shown, DHMV (yellow, square points)[30] and ASZB (hatched,purple points) [13].

and lepton flavour universality tests [35]. The fit in Figure 1.9 reveals a $\sim 5\sigma$ tension with the SM when combining all the lepton flavour universality (LFU) tests, branching fraction measurements and results of angular analyses. The best fit point is at Re(C_9^{μ}) $\sim$ -1.0 and Re(C_{10}^{μ}) $\sim$ 0.25. This implies a new vector coupling that is non-universal and at the TeV scale. In fact many NP models have been postulated to explain these deviations. Ideas have included a new massive vector gauge boson ($Z^{'}$) [36, 37], effects from B mixing [38], or leptoquarks [39–41]. Leptoquarks are defined as particles that have characteristics of both quarks and leptons, allowing them to interact with both fundamental particles. While the leptoquark explanation might be preferred, there is no evidence to pinpoint this as the definite cause. Others have postulated that perhaps the origin of the deviations are not from NP effects but the result of our limited knowledge of the hadronic effects. This suggestion is the motivation for the analysis presented in this thesis and is discussed in Section 1.4.2. The list of possible reasons for the deviation motivates more analyses with more data to identify the origins of the anomalies.

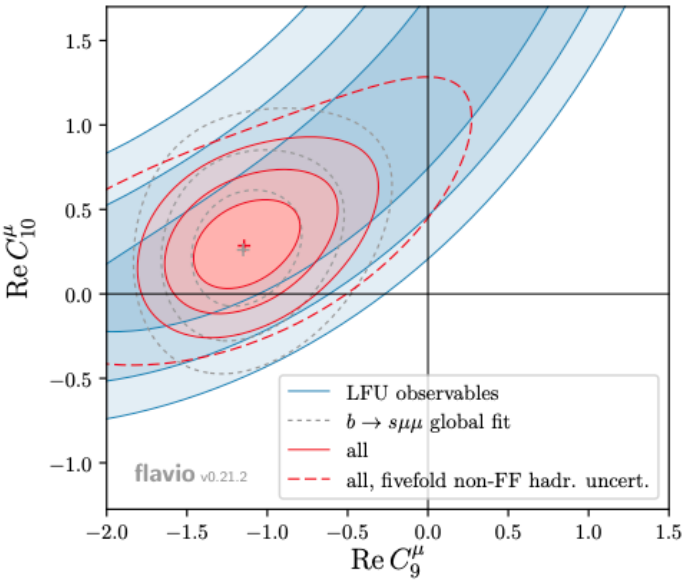

Figure 1.9: Allowed shifts to the $\mathrm{Re}(C_9^{\mu})$ and $\mathrm{Re}(C_{10}^{\mu})$, produced from global fits to the LFU observables and $b \to \mu\mu$ results. [35].

1.4.2 Impact of non-local contributions to $\bar{B}^0 \to \bar{K}^{*0}\mu^+\mu^-$

There is debate amongst the experimental and theoretical community to whether the anomalies seen in $b \to s\ell^+\ell^-$ transitions and in particular $\bar{B}^0 \to \bar{K}^{*0}\mu^+\mu^-$ are truly the result of NP contributions. An alternative suggestion is that perhaps these deviations are a result of our understanding of the hadronic resonant contributions. In the SM, $b \to s\ell^+\ell^-$ transitions proceed through either an electroweak penguin or box diagram. However, these short-distance processes are not the only processes that can achieve this same final state. The same final state can be obtained from any $b \to sq\bar{q}$ transition, where $q\bar{q}$ is a quark-antiquark pair. The $q\bar{q}$ quark-antiquark pair is a bound state and forms a hadronic resonance, that can decay to two leptons. In this thesis, the name given to all possible $b \to sq\bar{q}$ processes that might enter is the *non-local contributions*. Figure 1.10, shows an example of one such process, where the final state in a $b \to s\mu^+\mu^-$ decay, can be achieved through a $c\bar{c}$ resonance that enters through a loop and decays to two muons. The decay rates for these non-local contributions are several orders of magnitude greater than the penguin transition [42, 43]. As a consequence of this, it means that the non-local contributions have the capability of interfering with the short-distance amplitudes, changing the angular distribution through modifying the effective Wilson Coefficients and as a result mimicking possible NP. In $\bar{B}^0 \to \bar{K}^{*0}\mu^+\mu^-$, any decay that

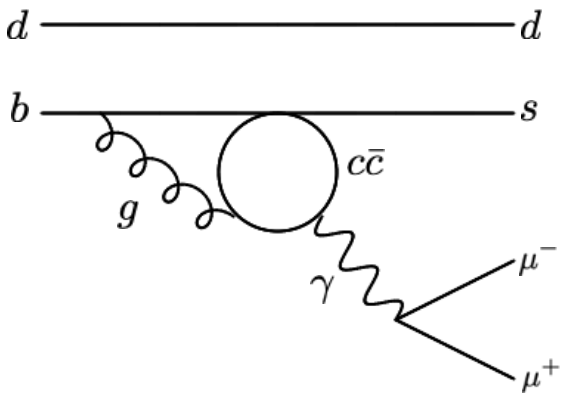

Figure 1.10: Feynman diagram for a $b \to \mu^+\mu^-$ transition that proceeds through a $c\bar{c}$ resonance, decaying to two muons. The loop which introduces a $c\bar{c}$ resonance is known as the "charm loop".

proceeds via a $\bar{B} \to \bar{K}^{*0}X$ transition, where X is a $J^{PC} = 1^{--}$ state, can contribute and interfere with the $\bar{B}^0 \to \bar{K}^{*0}\mu^+\mu^-$ decay. There are several $J^{PC} = 1^{--}$ states, which span the whole q^2 spectrum. At low q^2, contributions from the $\rho(770)$ and $\phi(1020)$, can be seen. As q^2 increases, these contributions are followed by the J/ψ and $\psi(2S)$, which are sizeable contributions. Beyond these resonances and above the $D\bar{D}$ threshold are states such as the $\psi(3770)$, $\psi(4040)$ and $\psi(4160)$. A complete list of the resonances is given in Ref [44]. Figure 1.11 shows the $\bar{B}^0 \to \bar{K}^{*0}\mu^+\mu^-$ differential decay rate as a function of q^2, across the whole q^2 spectrum. The solid, blue line is the differential decay rate containing both the penguin and non-local contributions. The broad states shown in this Figure are emphasised in Figure 1.12, which shows the differential decay rate for $\bar{B}^0 \to \bar{K}^{*0}\mu^+\mu^-$ above the $D\bar{D}$ threshold. In this Figure, one can clearly see the higher states that include the $\psi(3770)$, $\psi(4040)$ and the $\psi(4160)$.

The LHCb collaboration has measured the interference between short- and long-distance contributions in the $B^+ \to K^+\mu^+\mu^-$ decay [45]. The measurement was performed using 3fb^{-1} of data corresponding to Run 1 of the LHC. To perform the fit, a model was constructed that included resonant contributions as relativistic Breit-Wigners. As the K^+ is a pseudo-scalar, the fit was performed to the q^2 distribution of this decay and a single phase per resonance was defined. The results revealed that the interference was small. Nevertheless, the conclusions cannot be applied to the $\bar{B}^0 \to \bar{K}^{*0}\mu^+\mu^-$ decay, as the structure is very different. The fit for $\bar{B}^0 \to \bar{K}^{*0}\mu^+\mu^-$ transitions is 4 dimensional (q^2, cos θ_K, cos θ_ℓ, ϕ), in comparison to the fit for $B^+ \to K^+\mu^+\mu^-$

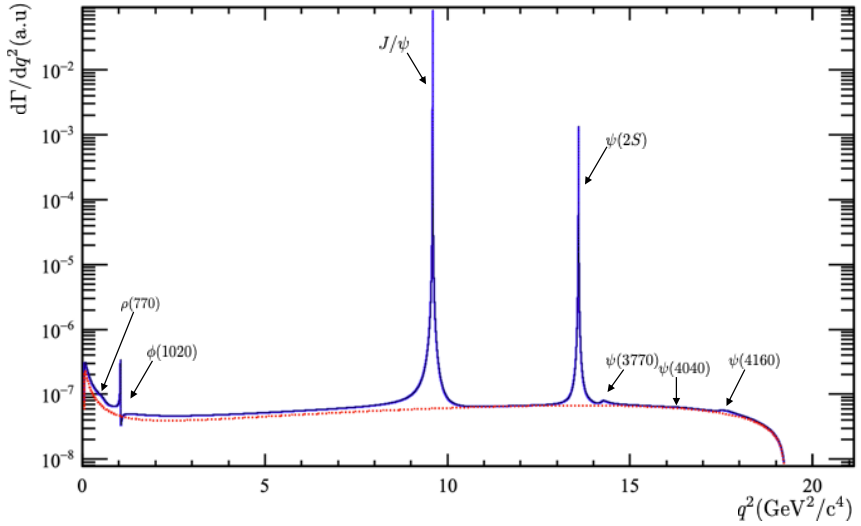

Figure 1.11: The differential decay rate for $\bar{B}^0 \to \bar{K}^{*0}\mu^+\mu^-$ as a function of q^2 including all the $c\bar{c}$ resonances with quantum numbers $J^{PC} = 1^{--}$ and produced with the model described in Chapter 3 (solid, blue line). For completeness the penguin only distribution, also produced using the model in Chapter 3, is given and illustrated by the red, dashed line.

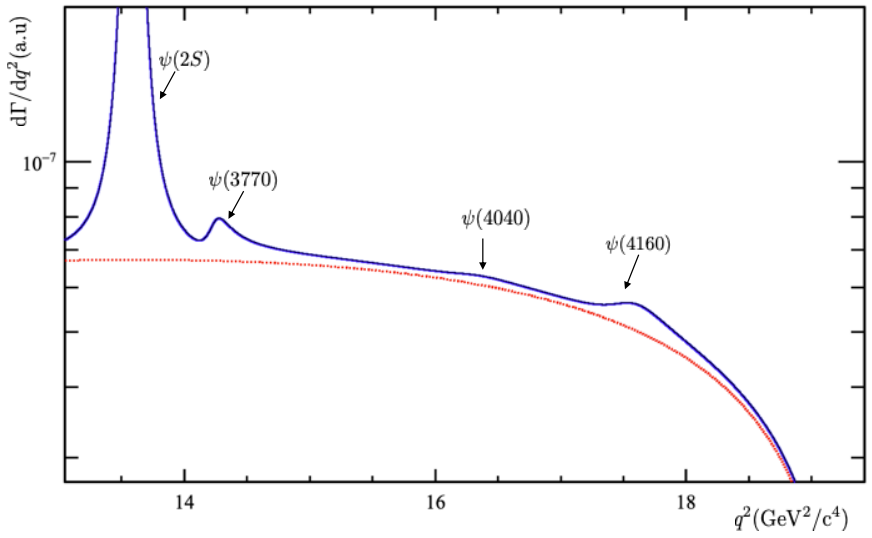

Figure 1.12: The differential decay rate for $\bar{B}^0 \to \bar{K}^{*0}\mu^+\mu^-$ as a function of q^2, illustrating the higher q^2 resonances above the $D\bar{D}$ threshold. The penguin only distribution is given by the red, dashed line and the distribution including the $c\bar{c}$ resonances is given by the solid, blue line. Both distributions have been produced by the model Chapter 3.

transitions, where there is only one dimension, q^2. Moreover, $\bar{B}^0 \to \bar{K}^{*0}\mu^+\mu^-$ is formed out of three transversity amplitudes, instead of one for the $B^+ \to K^+\mu^+\mu^-$ decay, which means there are three relative phases to fit for. No previous measurements have been performed by LHCb to measure the non-local charm loop in $\bar{B}^0 \to \bar{K}^{*0}\mu^+\mu^-$ transitions. This motivates the need to perform the analysis that is described in this thesis.

1.4.3 The experimental status of $\bar{B}^0 \to \bar{K}^{*0}\mu^+\mu^-$

The decay $\bar{B}^0 \to \bar{K}^{*0}\mu^+\mu^-$ has proven to be a significant channel to study in light of the discrepancies seen in its angular observables with Run 1 data collected by the LHCb experiment [4]. Since the results of this analysis were revealed it has been evident that more data is needed to understand the anomalous results. With the Large Hadron Collider (see Chapter 2 for more information) now providing more data from additional running periods, the analysis can be repeated by the LHCb experiment. Currently, the LHCb experiment is repeating the analysis of Ref [4] using the combination of both Run 1 (3fb^{-1}) and 1.7fb^{-1} of data taken in 2016 during Run 2. This updated analysis will be a binned analysis across the q^2 region of $0.1 < q^2 < 19.0\ \text{GeV}^2/c^4$ and will aim to determine the same angular observables as those measured in Ref [4]. The outcome of this analysis will determine whether the $\bar{B}^0 \to \bar{K}^{*0}\mu^+\mu^-$ anomaly persists with more data. Prior to this analysis, no measurements had been made of the interference between short-distance effects and the non-local contributions in $\bar{B}^0 \to \bar{K}^{*0}\mu^+\mu^-$ transitions. The analysis presented in this thesis aims to measure the effect of the non-local contributions, by directly fitting for the phases of the $c\bar{c}$ resonances, through an empirical model. Other analyses are attempting to build alternative models to determine the charm loop [3]. Nevertheless, this analysis is currently the only analysis that includes a complete model that accounts for all resonant contributions, across the full q^2 distribution with detector and additional effects/contributions included. The significance of this measurement of the phase difference in $\bar{B}^0 \to \bar{K}^{*0}\mu^+\mu^-$ is that from the results it will either rule out or provide further evidence that the charm loop is causing the anomalous results in $b \to s\ell^+\ell^-$ transitions.

Chapter 2

The LHCb experiment at the LHC

The LHCb experiment is one of the four main experiments at the Large Hadron Collider (LHC), based at the research facility CERN. The aim of this experiment is to study processes involving beauty- and charm- hadrons, referred to as b- and c-hadrons respectively. Precise measurements of rare b-hadron decays such as $\bar{B}^0 \to \bar{K}^{*0}\mu^+\mu^-$ require large samples of b-hadrons. The LHC is an ideal environment to study rare b-hadron decays due to the vast number of b-hadrons that are produced from collisions involving proton beams (pp beams).

The LHC is presented in Section 2.1. Section 2.2 presents a detailed description of the LHCb detector; its structure, how it is optimised to study $\bar{B}^0 \to \bar{K}^{*0}\mu^+\mu^-$ decays, and the future of the experiment.

2.1 The LHC

Particle accelerators are powerful machines that can be used to test the SM and investigate physics beyond it. The LHC is one such particle accelerator. The design and structure of the LHC makes it one of the most powerful and largest accelerators to date. The collider with a circumference of 27 km is located in an underground tunnel, near Geneva on the

border between France and Switzerland. The tunnel itself was previously occupied by the LEP experiment. Two proton beams traverse the ring in opposite directions such that they collide at a given centre of mass energy. For Run 1, the centre of mass energy was $\sqrt{s}$ = 7-8 TeV and for Run 2 it was $\sqrt{s}$ = 13 TeV. To achieve this large centre of mass energy, a series of steps are implemented before the protons enter the main LHC ring. Protons begin by being produced in the linear accelerator at CERN called the "Linac 2". The Linac 2 system provides the protons with energy as they move through this accelerator, and by the time the protons have traversed the full accelerator they have an energy of 50 MeV. These 50 MeV protons are then sent to the Proton Synchrotron Booster (PSB), which is the first synchrotron in the CERN complex. In the PSB, protons are accelerated to 1.46 GeV, before they are fed into the Proton Synchrotron (PS). The Proton Synchrotron is the second synchrotron in the CERN complex. It further accelerates protons, before they can reach the next system, which is the Super Proton Synchotron (SPS). The SPS accelerates the protons to 450GeV. Next, these 450GeV protons enter the LHC. Once the protons enter the LHC they are further accelerated and focussed until the pp interactions reach the desired centre of mass energy of 13 TeV. The exact structure of the CERN complex with its various substructures is presented in Figure 2.1. The LHC has been running since 2009 with two periods: Run 1 (2009-2012) that saw the LHC collide the proton beams with a bunch crossing of 50 ns, and Run 2 (2015-2018) which saw the LHC run with a bunch crossing time of 25 ns. During these data taking periods the LHCb experiment collected a total integrated luminosity of 3 fb^{-1} in Run 1 (1 fb^{-1} in 2011, 2 fb^{-1} in 2012), and 5 fb^{-1} of integrated luminosity in Run 2. Data collected from both Run 1 and part of Run 2 are used in this analysis.

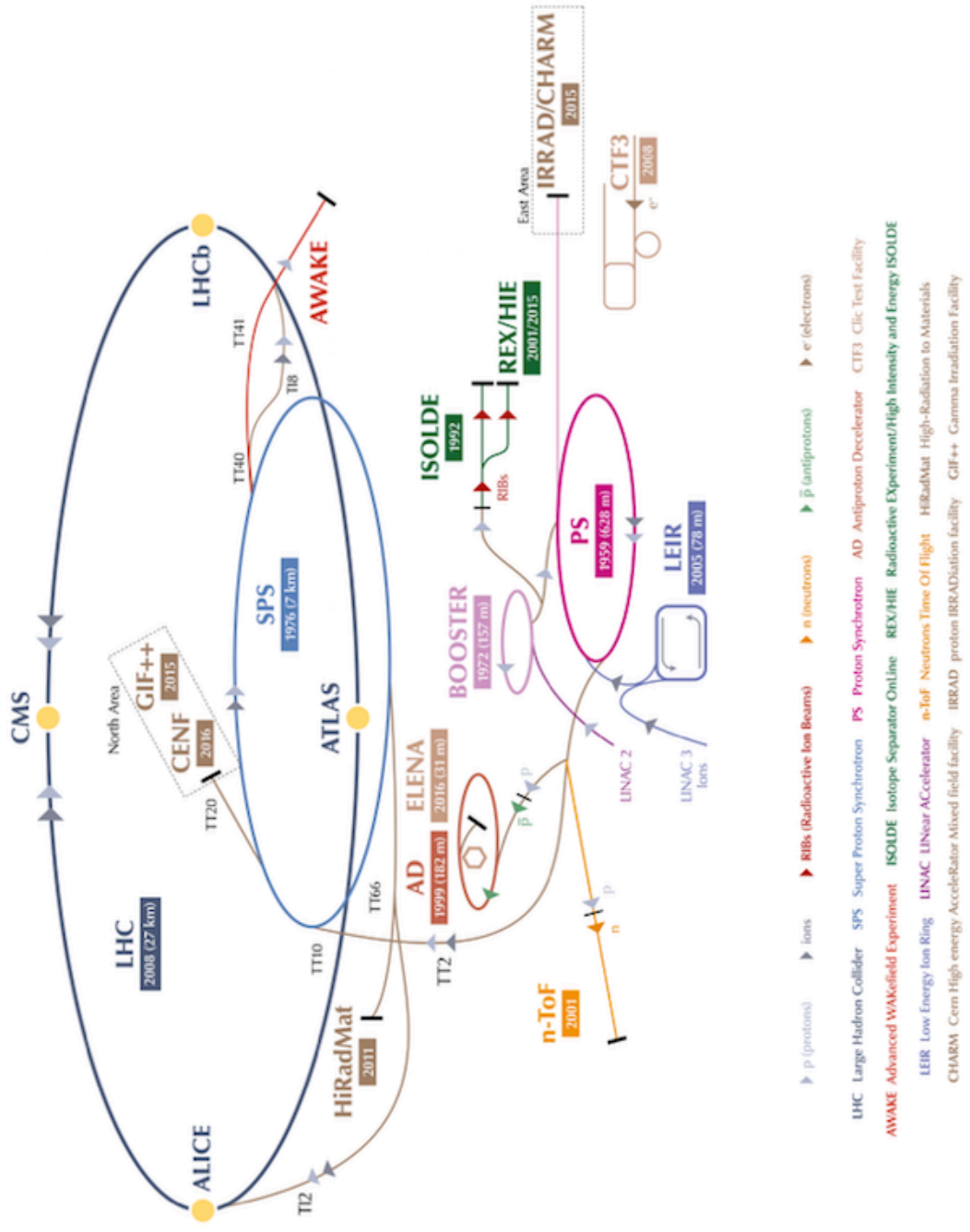

Figure 2.1: The CERN complex [46].

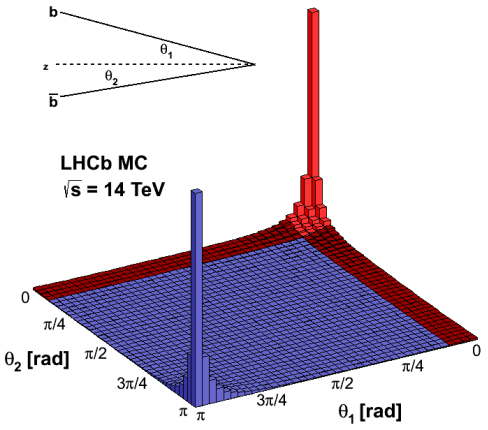

Figure 2.2: The production of $b\bar{b}$ quark-pairs as a function of the opening angle from simulations of the LHCb detector at $\sqrt{s}$= 14TeV. The opening angle is denoted by θ_1 for the b quark and θ_2 for the $\bar{b}$ quark. The red segment denotes the events selected by the LHCb detector acceptance and the blue denotes the events that are not within the LHCb acceptance [48].

2.2 The LHCb detector

The LHCb detector is optimised for precision measurements involving decays of b- and c-hadrons. The design of the LHCb experiment is different to the general purpose detectors at the LHC, that are designed to surround the pp interaction point. Instead, the LHCb detector is a forward, single-armed spectrometer with an angular acceptance of $10 < \theta < 250$ mrad. The angular acceptance of the LHCb detector is often expressed in terms of the pseudorapidity, η, where pseudorapidity is a way of expressing the polar angle θ between the momentum of the particle and the axis of the beam (Eq 2.1 [47]),

$$\eta = -\ln\left(\tan\frac{\theta}{2}\right) \tag{2.1}$$

The angular acceptance range in terms of pseudorapididty is $2 < \eta < 5$ for the LHCb detector. The $b\bar{b}$ quark-pairs are produced within the angular acceptance of the LHCb detector. These $b\bar{b}$ quark-pairs are often collinear, travel in either the positive or negative directions and have a small opening angle, where the latter is shown by Figure 2.2. A cross-section of the detector is shown in Figure 2.3 and illustrates the various components that combine to form the full detector. The pp interaction is surrounded by the VErtex

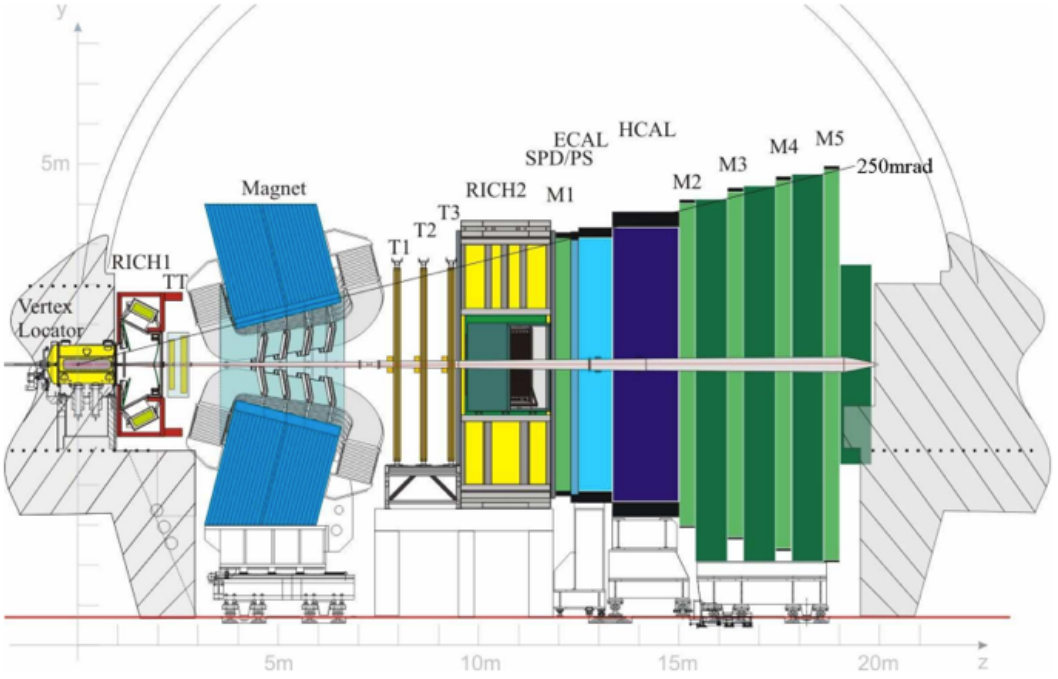

Figure 2.3: Schematic of the LHCb detector [49].

LOcator (VELO). Section 2.2.1 presents the VELO, discussing how it reconstructs the primary and secondary vertices. The next component is the first of two Ring-Imaging Cherenkov systems dedicated to particle identification. The first RICH system is denoted RICH 1 and the second RICH system is denoted RICH 2. These systems are critical in identifying the K and π in $\bar{B}^0 \to \bar{K}^{*0}\mu^+\mu^-$ decays. Section 2.2.2 discusses the RICH detectors. Tracking stations and a magnet are inserted between the RICH detectors. The magnet bends the trajectories of charged particles and the tracking stations reconstruct the tracks of individual particles. Both these components are discussed in Section 2.2.3. The energy of electrons and photons is measured in the Electromagnetic Calorimeter (ECAL) and the energy of hadrons is measured in the Hadronic Calorimeter (HCAL). Both the ECAL and the HCAL are discussed in detail in Section 2.2.4. The rare decay $\bar{B}^0 \to \bar{K}^{*0}\mu^+\mu^-$ contains muons in the final state. Therefore to fully reconstruct the four body system that characterises this decay it is essential that the muons are identified and their momenta are measured precisely. The muon system at LHCb fulfils this purpose and is described in Section 2.2.5.

The general purpose detectors at the LHC are dependent on running with a high luminosity. However, unlike these detectors, the LHCb detector can be operated at a

lower luminosity and still study a vast physics programme. The LHCb detector runs at a luminosity of $4 \times 10^{32} \text{cm}^2\text{s}^{-1}$ to produce on average, 1.5 interactions per bunch crossing. The experiment requires a trigger system to reduce the data size to manageable level. The trigger system of the LHCb experiment is described in Section 2.2.6. Simulation is used widely in particle physics and at LHCb. The simulation used in the LHCb experiment is described in Section 2.2.7.

The LHC has completed its second physics running period and now is entering its second long shut down (LS2) commencing from December 2018 until 2021, in preparation for Run 3. During the LS2, the LHCb detector along with the other detectors at the LHC, will be upgraded. The performance and upgrade of the LHCb detector are described in Section 2.2.8.

2.2.1 The VErtex LOcator

Precision flavour physics at LHCb is built on reconstructing the individual components of the decay, along with the decay vertex of the b- and c-hadrons. The b- and c-hadrons originate from the primary vertex (PV). The b- and c-hadrons decay in the LHCb detector. The secondary vertex is constructed out of the decay products of b- and c-hadrons. The VErtex LOcator (VELO) is the innermost tracking system of the LHCb detector and is used to identify the primary vertices and the secondary vertices. The b-hadrons produced within the LHCb acceptance, travel on average 1 cm before decaying. This means that one can identify the b-hadrons through the displaced vertex. The VELO is built up from arranging semicircular modules that combine together to cover the full acceptance. There are 42 semicircular modules arranged on two module supports. Figure 2.4 shows one support with the 21 individual modules it holds on it. Each semicircular module has many finely grained silicon strips arranged radially (r) and angularly (ϕ). Figure 2.5 illustrates two semicircular modules that come together in the VELO, along with their geometry.

During a physics run, the VELO is situated 7 mm from the beam; resulting in the LHCb detector being the closest detector to the beam at the LHC. One caveat to this is that during injection the beam will expand. This means the module supports

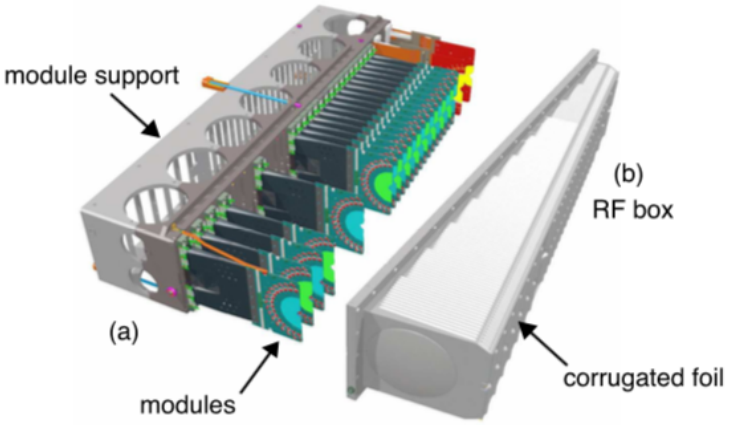

Figure 2.4: A individual module of the VELO with 21 semicircular modules arranged on it, along with the RF box which encloses the modules [49].

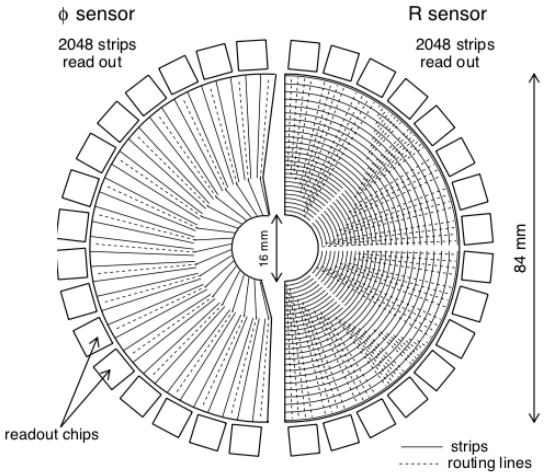

Figure 2.5: Illustration of the two semicircular modules that form the VELO in terms of their radial (R) and angular (ϕ) geometry [50].

cannot be fixed, and instead must be retractable to avoid damage to the semicircular modules during injection. As a consequence each module must be aligned and constantly monitored for any changes in position during each run. The VELO must be able to reconstruct additional properties associated to the decay to a high precision. This is demonstrated in Figure 2.6 which shows explicitly the tracks of the particles involved in the $\bar{B}^0 \to \bar{K}^{*0}\mu^+\mu^-$ decay and the various parameters of the decay. In particular, the flight distance (FD) is the distance the daughter flies from the PV. D_{rec} is the reconstructed direction of the $\bar{B}^0$. The impact parameter (IP) is the shortest distance between the PV and the reconstructed track of the parent particle calculated from the decay products. All these parameters need to be measured with a good resolution, such

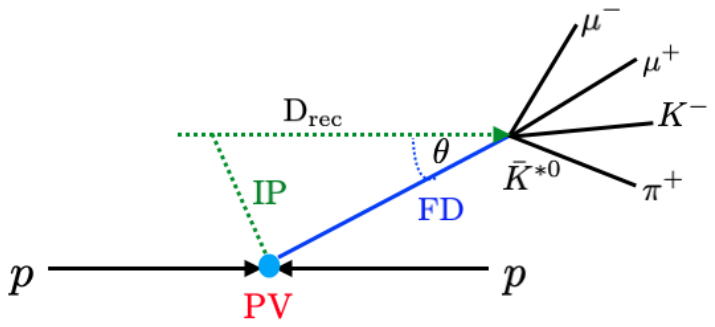

Figure 2.6: Schematic of the $\bar{B}^0 \to \bar{K}^{*0}\mu^+\mu^-$ decay. The individual particles that form the decay are indicated along with kinematic properties of the decay.

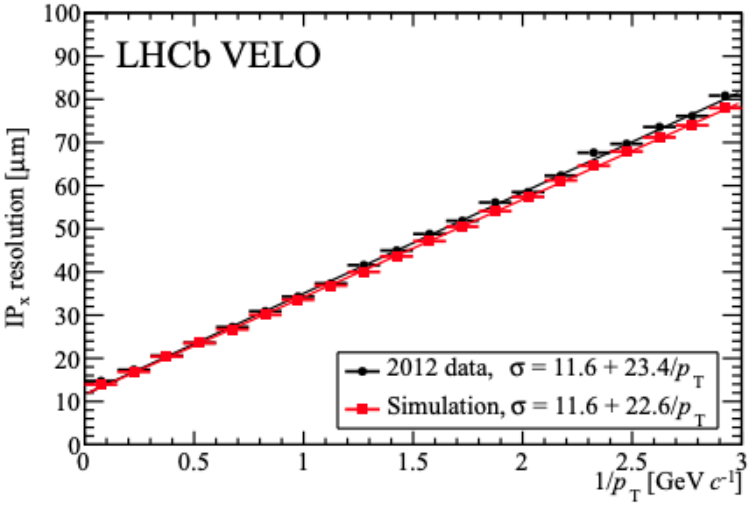

Figure 2.7: The IP_x resolution as a function of $1/p_T$, where p_T is the transverse momentum. The red data points correspond to the simulation and the black points correspond to the data. [51]

that the events can be used for physics. For the IP resolution, the value reported is 35 μm for particles with a momentum greater than 1.0 GeV/c. This is demonstrated in Figure 2.7 [51]. The primary vertex resolution is 13 μm for transverse plane and 71 μm in the z direction (beam axis). These values are reported for vertices that have 25 tracks [51]. For all tracks originating from the primary vertex the VELO has a 98% track reconstruction efficiency [51].

2.2.2 Ring-Imaging Cherenkov (RICH) system

The most abundant particles produced at the LHC are pions, π, followed by kaons, K, and protons, p. Many rare decays contain hadrons in their final state. The decay

$\bar{B}^0 \to \bar{K}^{*0}\mu^+\mu^-$ is an example with the $\bar{K}^{*0}$ decaying to a K^- π^+ combination. The identification of charged hadrons at the LHCb experiment is performed by the Ring Imaging Cherenkov (RICH) detectors. There are two RICH detectors at LHCb that are used to identify charged particles through the process of Cherenkov radiation. Cherenkov radiation is electromagnetic radiation produced when a charged particle travels in a material or medium with a speed greater than the speed of light in the material. When a particle traverses either of the RICH detectors, it emits Cherenkov photons in a cone. This cone geometry means for each particle, one can measure the Cherenkov angle (θ_C), which is the angle at which photons are emitted from relative to the particles direction. The Cherenkov angle is related to the velocity of the particle illustrated by Equation 2.2 [52], where η is the refractive index and $\beta = \frac{v}{c}$ where v is the velocity of the particle and c is the speed of light.

$$cos(\theta_c) = \frac{1}{\eta\beta} \tag{2.2}$$

Rewriting Equation 2.2 in terms of the momentum, we obtain the following,

$$cos\theta_c = \frac{\sqrt{mc^2 + p^2}}{\eta p} \tag{2.3}$$

where p is momentum of the particle and m is the mass of the particle. The momentum is directly related to the Cherenkov angle. Therefore by measuring the Cherenkov angle one can obtain a measurement of the particle's momentum. Figure 2.8 shows the relationship between the Cherenkov angle and the momentum spectrum for different particles in the RICH system. It is these distributions in Figure 2.8 that allow one to identify the different particles traversing the RICH 1 system. The medium of the RICH detectors is selected carefully to optimise the particle identification performance. The RICH 1 system is the first RICH detector and is situated between the VELO and the first tracking station the Tracker Turicensis (TT). Figure 2.9 is a schematic of the RICH 1 detector. RICH 1 is a smaller Cherenkov detector, with coverage of 25-300 mrad. RICH 1 is optimised to identify low momentum particles within the range of 2-40 GeV/c, using a gas radiator, C_4F_{10}, (as shown in Figure 2.9) which has a refractive index of 1.0014 at 400 nm [53]. It should be acknowledged that during Run 1, RICH 1 also used an aerogel, that was later removed for Run 2. The reason why the aerogel was removed was because

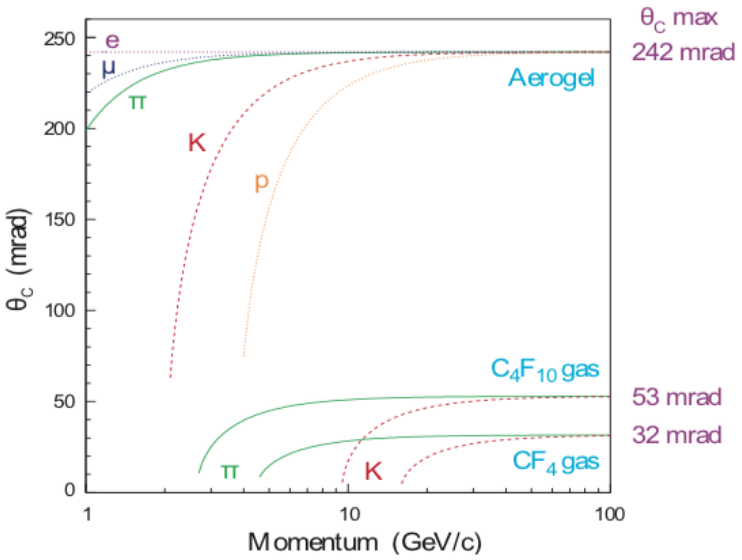

Figure 2.8: Cherenkov angle θ_c as a function of momentum, for the radiators in both RICH 1 and RICH 2 detector [49].

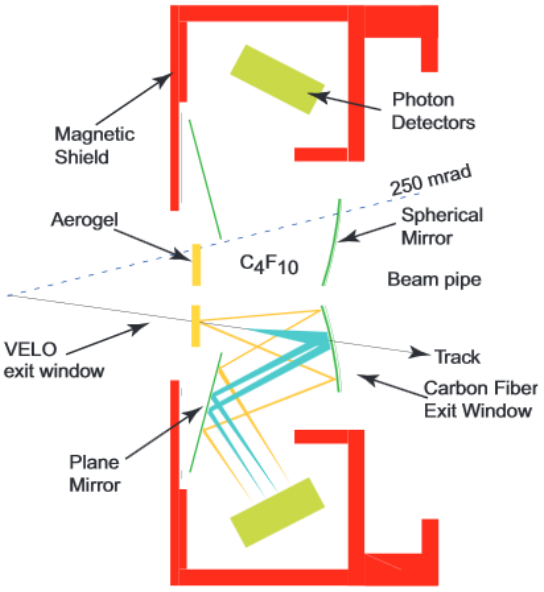

Figure 2.9: Schematic of the RICH 1 detector [49].

if could not be used for particle identification of kaons below the Cherenkov threshold as the aerogel provided a high multiplicity environment for kaons below the Cherenkov threshold [54]. The RICH 1 system is located before the magnet, as otherwise the low momentum particles such as those from $D^{*+} \to D^0\pi^+$ decays would be deflected out of the detector acceptance. The RICH 2 detector is upstream from the magnet and other tracking stations, but before the calorimeters, as demonstrated in Figure 2.3,. The RICH

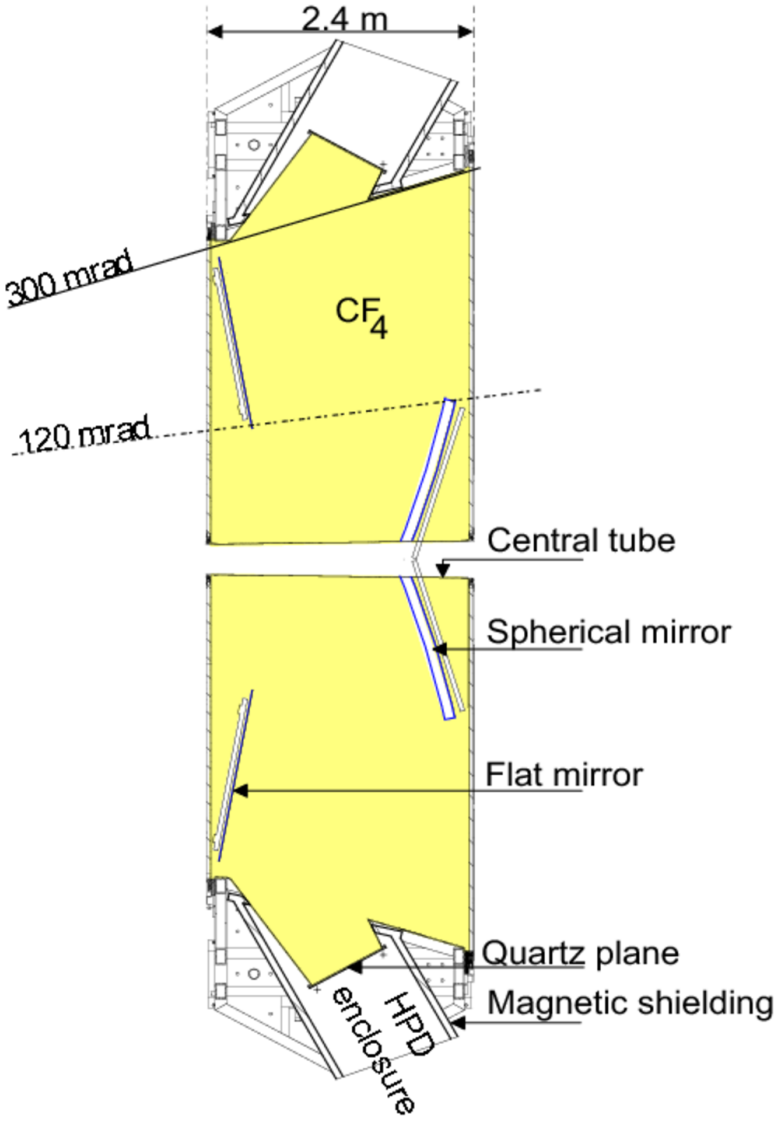

Figure 2.10: Schematic of the RICH 2 detector [49].

2 detector as shown in Figure 2.10 is used to identfy particles with a momentum range of 15-100 GeV/c, using a gas radiator, CF_4, which has a refractive index of 1.005 at a wavelength of 400 nm [53]. In comparison to the RICH 1 detector, the RICH 2 detector has a smaller acceptance range of 15-120 mrad. The RICH 2 detector can operate with a lower acceptance because the higher momenta particle have had their tracks bent into the acceptance, by the magnet. Together the RICH detectors can detect particles across a large momentum range, allowed by the LHCb experiment.

For accurate particle identification, it is important to have a good Cherenkov angle resolution. For RICH 1 the Cherenkov angle resolution is 1.65 mrad, while for RICH 2 it is 0.67 mrad [54]. Moreover, it is important that the RICH detectors can capture the

ring of light emitted from the particle to determine the momentum. To achieve this the RICH detectors have an optical detection system. The optical systems for RICH 1 and RICH 2 work on the same principle. The initial cone produced by the primary particle is focussed onto a spherical mirror. Once the light hits the spherical mirror it is reflected onto a flat mirror, which then reflects the light to the Hybrid Pixel Detectors (HPDs). Once, the photons are detected by the HPDs, the Cherekov ring is imaged and a photon distribution is produced. As an example, Figure 2.11 shows imaged Cherenkov rings from the RICH 1 detectors. The LHCb collaboration compare the photon distribution to the expected distribution for different particles. The difference in log likelihood (DLL) between two particle hypotheses is calculated, and used to identify the particle type for a given track. Equation 2.4 illustrates the DLL for the $K\pi$ system that forms the $\bar{K}^{*0}$

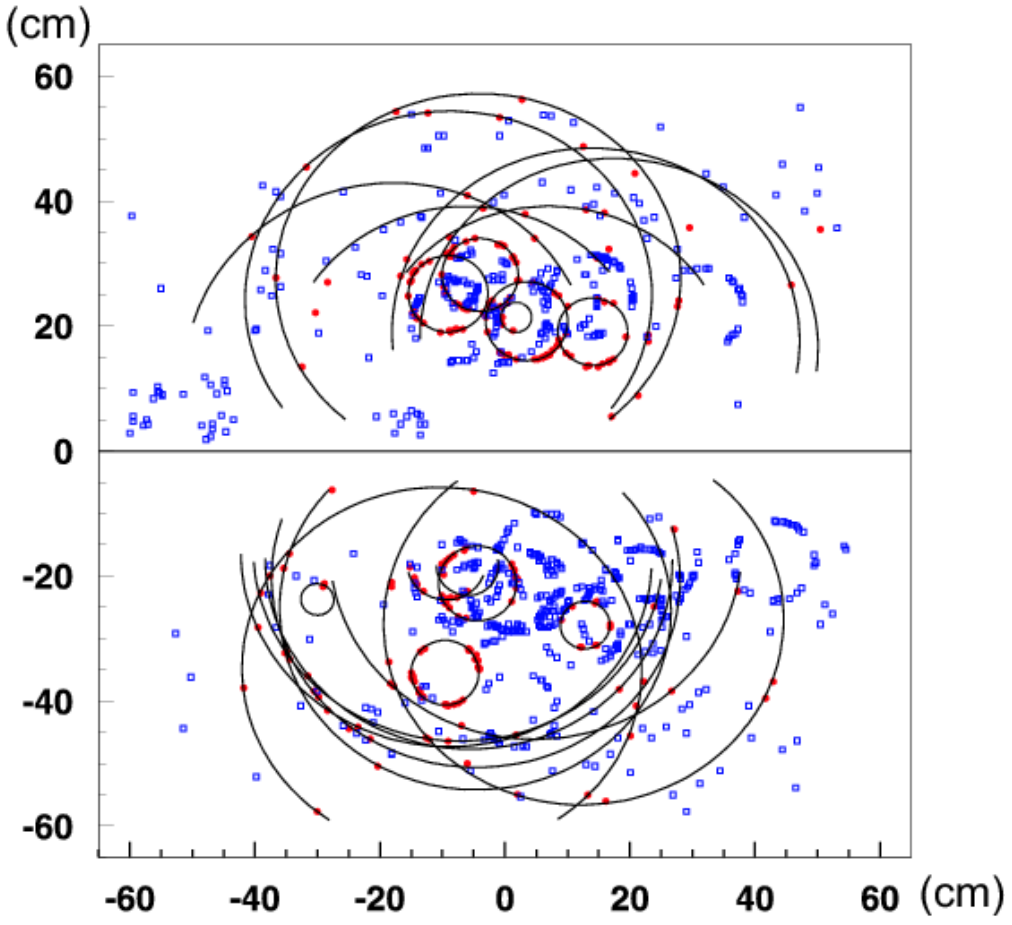

Figure 2.11: Cherenkov rings imaged from the RICH 1 detector [55]. The blue, hollow, points show the hits and the red points are points that are classified on the rings. All the rings are shown by the black curves. The small rings are formed from C_7F_{10} hits and the large rings are from hits in the aerogel.

in $\bar{B}^0 \to \bar{K}^{*0}\mu^+\mu^-$.

$$\mathrm{DLL}_{K\pi} = \log\mathcal{L}(\theta, p_K) - \log\mathcal{L}(\theta, p_\pi) \tag{2.4}$$

As the RICH measures K, π, and p the DLL can be computed for all combinations. Figure 2.12 shows the PID efficiencies as a function of track momentum. The efficiencies are shown in this figure for two different DLL values. The DLL is implemented as a cut that changes the PID efficiencies for different particles that transverse the RICH detectors. To conclude, the RICH subsystems in their design/operation form a powerful tool in particle identification and combinatorial background reduction for the LHCb experiment.

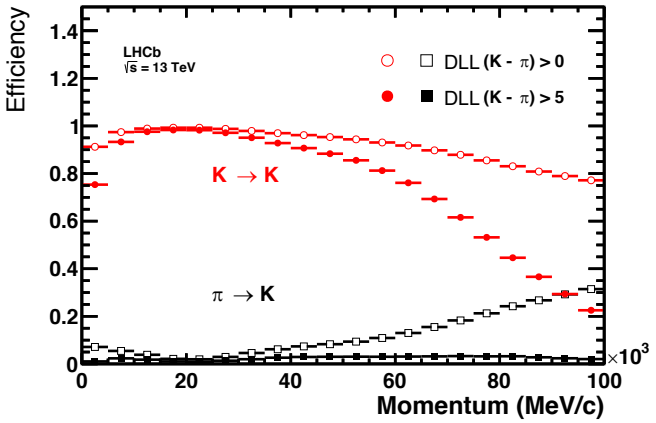

(a)

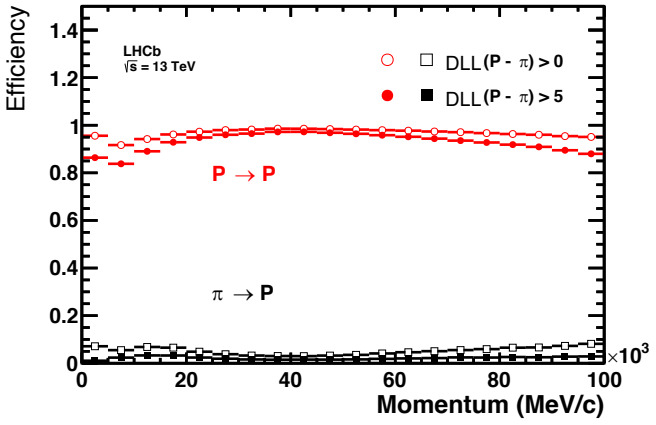

(b)

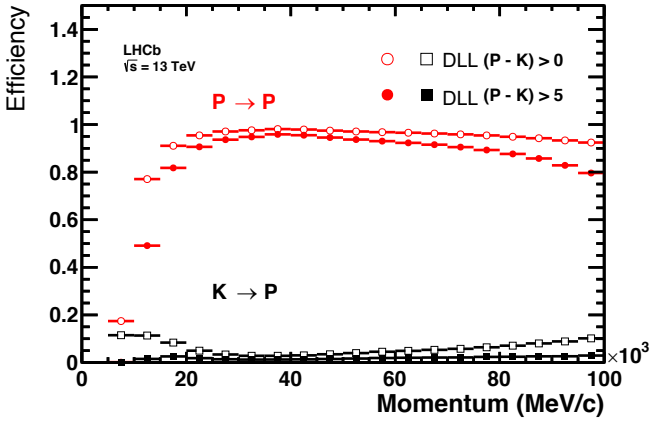

(c)

Figure 2.12: The PID efficiencies curves as a function of track momentum using 2015 data. (a) shows the K efficiency and the π misidentification rate, (b) shows the p efficiency and π misdentification rate, and (c) shows the p efficiency and K misdentification rate. The plots are taken from Ref[56]. The red data points are the original efficiencies and rates and the solid/empty square markers are the efficiencies after imposing two different cuts on the difference in log likelihood.

2.2.3 The magnet and tracking stations

The LHCb detector has a dipole magnet to bend the tracks of charged particles. The magnet has two identical coils which produce a bending power of 4 Tm over a 10 m baseline [49]. The magnet is situated downstream from the VELO and RICH 1 system, and sandwiched between the tracking stations. The magnetic field generated causes positively charged particles to move in one direction, while the negatively charged particles move in the opposite direction. By studying the curvature of the tracks one can then deduce the momentum of the particle.

As mentioned previously, the magnet is positioned between the tracking stations. The Tracker Turicensis (TT) is the first tracking station at the LHCb experiment and is located in front of the magnet. There are three other tracking stations, T1−T3, that are located behind the magnet. Each station (T1−T3) is modular and is divided into an inner and outer component known as the Inner Tracker (IT) and Outer Tracker (OT). Each component uses different technologies to measure the tracks of particles. The IT is formed out of silicon microstrips. Silicon gives good resolution on the hits and therefore the tracks of the particles. The IT is not the only tracking system that utilises silicon technology. The TT is formed purely from 183 μm pitch, silicon microstrips. The TT has a modular design of four individual layers, inclined at four different angles [0°,+5°,−5°,0°] [57]. The IT and TT form the Silicon Tracker (ST) at LHCb. As silicon is expensive, the whole tracking system cannot be made purely out of silicon. The OT uses straw tubes with a pitch of 5 mm. The larger pitch and different technology cause the OT to have a larger resolution than the IT and TT. Nevertheless, all resolutions are within the LHCb physics requirments. During Run 1 the TT had a hit position resolution of 53.4 μm, the IT of 54.9 μm and the OT of 205 μm [58]. The tracking systems are all required to have a good hit efficiency to maximise the efficiencies of the tracking algorithms. The hit efficiency for the TT is 99.7%, 99.8% for the IT and 99.2% for the OT [58]. For the hit resolution and efficiencies, all values quoted refer to Run 1. These values are consistent with the values in Run 2.

Particle tracks are reconstructed using a tracking algorithm. The algorithm searches for hits in the all the tracking stations (VELO, TT, IT and OT), and by

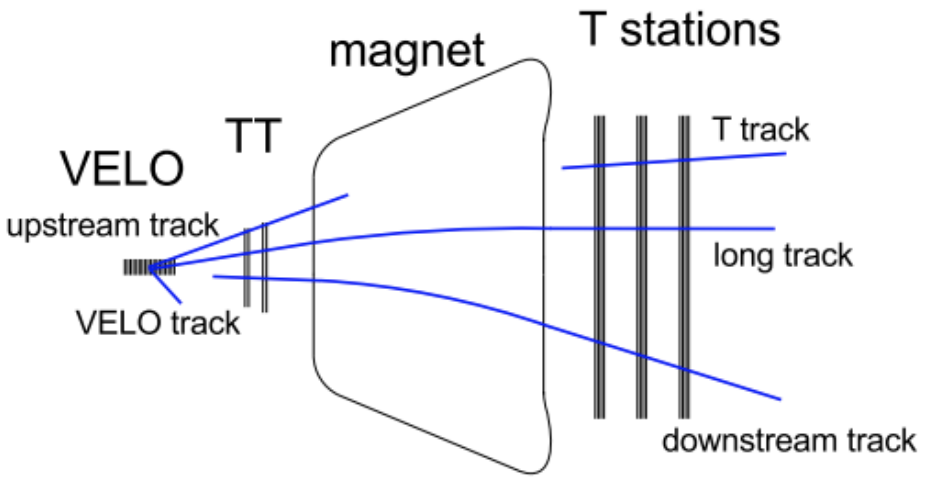

Figure 2.13: The different reconstructed tracks passing through the tracking stations and magnet in the LHCb detector [59].

connecting the tracks determines a particle's trajectory in the tracking stations. A particle may not traverse all the tracking stations, and instead only pass through some of the tracking stations. This could be because the particle does not have enough energy to traverse all the tracking stations, or it could be a particle that has been produced from another particle decaying in the tracking stations. The tracking algorithm takes these factors into account, and is optimised to search for all possible tracks that can occur. Figure 2.13 shows the different reconstructed tracks that can be apparent in the tracking stations. A T track only has hits in the T1-3 stations. A VELO track only has hits in the VELO detector. Moreover, an upstream track has hits in the VELO as well as the TT. A long track has hits in all the tracking stations, and finally a downstream track has hits in all tracking stations apart from the VELO. Once a track has been reconstructed its track momentum and track momentum resolution is determined. The momentum resolution is determined by using $J/\psi \to \mu^+\mu^-$ decays, as the muons in the final state traverse all the tracking stations before they are detected in the muon stations. The other advantage of using this channel to determine the momentum resolution is that, because the muon can have both large and small momenta, the momentum resolution can be determined across a vast momentum range. The momentum resolution as a function of momentum using this approach is shown in Figure 2.14.

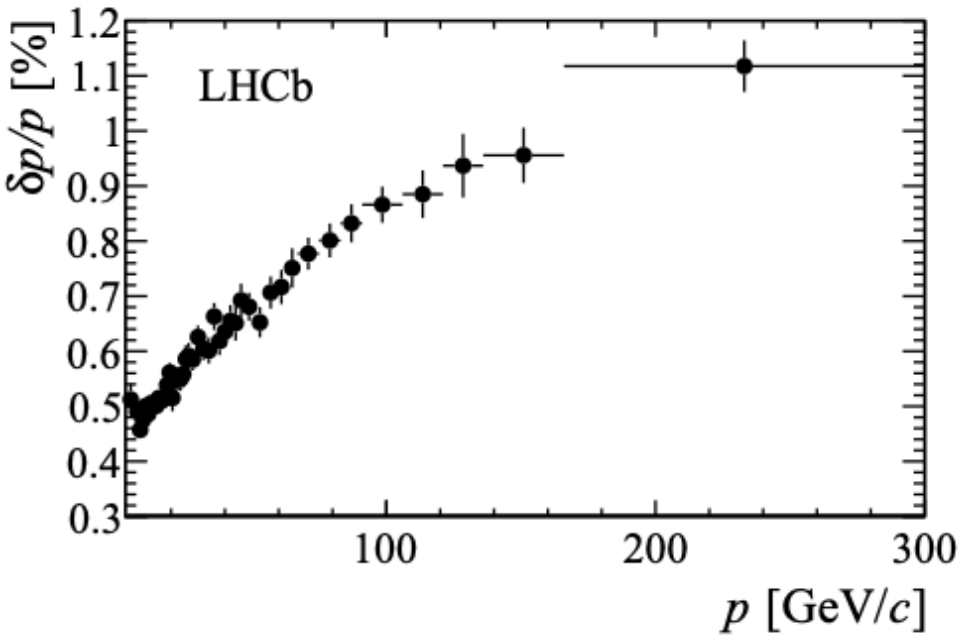

Figure 2.14: The momentum resolution as a function of momentum obtained from $J/\psi \to \mu^+\mu^-$ decays [60].

2.2.4 The calorimeters

Two calorimeters are deployed at the LHCb detector: the Electromagnetic Calorimeter (ECAL) and the Hadronic Calorimeter (HCAL). The ECAL is a heterogeneous lead/ scintillator sampling calorimeter, employed to measure the energy of photons and electrons. It is located after the RICH 2 but before the HCAL as shown in Figure 2.3. Two extra components are implemented just before the ECAL. These are the Scintillating Pad detector (SPD) and the Pre-Shower (PS) system. The SPD separates electrons from photons, as the scintillator in the active volume can detect charged particles. On the other hand, the PS is used to identify exactly what electromagnetic particle is traversing its active volume, again through scintillation. Both the SPD and PS are important components in the LHCb detector, as they provide the calorimeters with additional information that helps with background rejection. For example, they can help reduce backgrounds from π^0 decays. Once the particles have been identified by the SPD and the PS, their energies are determined by the ECAL with an energy resolution of 10% $/\sqrt{\mathrm{E(GeV)}} \oplus 1\%$ [49].

The HCAL is a iron/scintillator sampling calorimeter, that aims to measure the

energy of hadrons with an energy resolution of $(69 \pm 5)\%/\sqrt{\mathrm{E(GeV)}} \oplus (9 \pm 2)\%$ [49].

2.2.5 The muon system

The muon system for the LHCb detector is designed to deal with the high flux and identify muons produced from B decays successfully with a good precision. There are five, rectangular muon stations, M1-M5, that provide an acceptance of 300 mrad horizontally and 200 mrad vertically [61]. Each station is arranged in four regions (R1-R4). A schematic of the muon stations is shown by Figure 2.15 and a detailed view of a single muon station is shown in Figure 2.16.

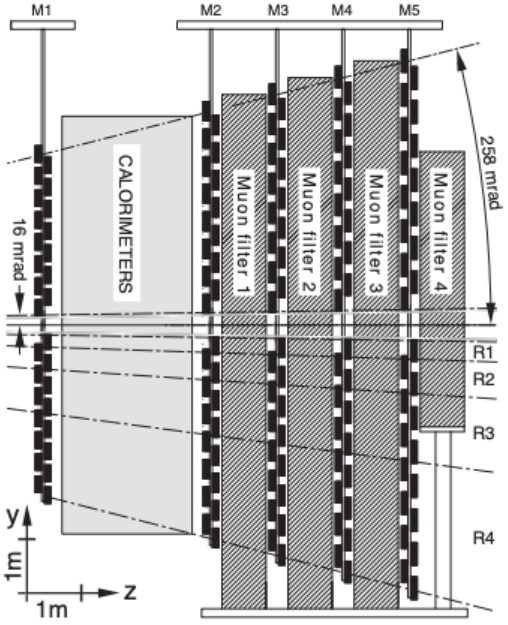

Figure 2.15: The LHCb muon system [62].

The muon station M1, is located upstream from the calorimeters, while the other stations are located downstream, as shown by Figure 2.3. This helps identify and measure muons that have energies less than 3 GeV/c and therefore would be absorbed in the calorimeters. Moreover, M1 uses gas electron multipliers to deal with the high volume of muons at all energies. Meanwhile, M2-M5 use multiwire proportional chambers due to the lower flux of muons with energies greater than 3 GeV/c. The momentum ranges of the muons is a fundamental component of the criteria needed for muon identification.

Moreover, the muon stations and the LHCb detector have been designed to help

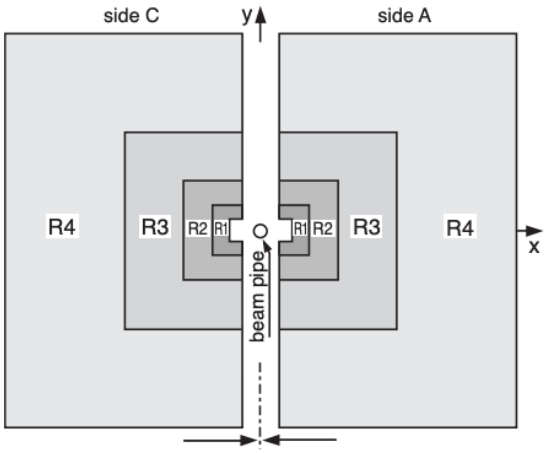

Figure 2.16: Schematic of a muon station at LHCb, indicated how the stations is arranged out of 4 separate regions (R1-R4) [62].

Momentum ranges	Muon stations with hits
3 GeV/c < p < 6 GeV/c	M2 and M3
6 GeV/c < p < 10 GeV/c	M2 and M3 and (M4 or M5)
p > 10 GeV/c	M2 and M3 and M4 and M5

Table 2.1: The criteria for the `IsMuon` boolean at LHCb that is based on the momentum of the muons and the hits in the different muon stations.

reduce backgrounds from both hadrons and muonic backgrounds that are from outside the detector. Explicitly, this is done by shielding the muon stations. M1 and M2 have different shielding to the other muon stations, because of where they are situated in LHCb. M1 is shielded by the RICH 2 detector, and M2 is shielded by the calorimeters. For the other muon stations (M3-5) iron shielding is placed in between the stations. The shielding for the muon stations can be seen in the schematic in Figure 2.15. At the LHCb experiment the identification of a muon is achieved by the following. Firstly, a criterion, `IsMuon` is applied. The `IsMuon` boolean is used to identify muons through hits in the various muon stations. The exact criteria for the `IsMuon` boolean at LHCb is provided in Table 2.1 [63].

Next, the particle identification (PID) variable, $\mathrm{DLL}_{\mu\pi}$, is computed using information from the muon stations, RICH systems and calorimeters. $\mathrm{DLL}_{\mu\pi}$ is defined as the difference in log-likelihood between the muon and pion hypotheses, and is given by the following,

$$\mathrm{DLL}_{\mu\pi} = \log\mathcal{L}(\theta_c, p, D^2|\mu) - \log\mathcal{L}(\theta_c, p, D^2|\pi) \tag{2.5}$$

where, θ_c is the Cherenkov angle as measured by the RICH systems. D^2 is the average squared distance between the hits in the muon stations and the track determined from extrapolating the track in the tracking stations to the muon stations [63]. The muon system is operated closely with the trigger system to ensure a reliable trigger for the B physics programme at LHCb. In the first stage of the trigger, 20% of its firmware is dedicated to muon information [64]. This is often referred to as the `L0Muon` trigger and is described in Section 2.2.6.

2.2.6 Trigger system for the LHCb detector

High energy particle accelerators produce many events through interactions in the beam. The greater the number of events, the more data there is to analyse in the physics programme. Nevertheless, the number of events processed is proportional to the computing power required to process these events. Often there is a limit on the amount of data that can be processed in a given time. This means that the events need to be filtered, to ensure the data samples are rich in interesting events. This is the role of the trigger. The LHCb trigger systems are implemented in both software and hardware, with the purpose of rigorously reducing the data rate, to have an enriched sample of $b\bar{b}$ candidates. Over both Run 1 and Run 2, the LHCb trigger has reduced the 40 MHz data rate, to 3.5kHz in 2011, 5kHz in 2012 and 12.5kHz in 2015 onwards. The trigger rates for each data taking year were different due to changes in the data aquistition (DAQ) and improvements in the collision rates in each running period [65]. The most significant changes were seen in the online calibration and alignment. Figure 2.17 presents the trigger for three separate data taking periods of the LHCb experiment. This section gives a detailed account of the hardware and software triggers at the LHCb experiment in terms of; the structure of the triggers, changes that have occurred over the running periods and how the triggers are important to $\bar{B}^0 \to \bar{K}^{*0}\mu^+\mu^-$ transitions.

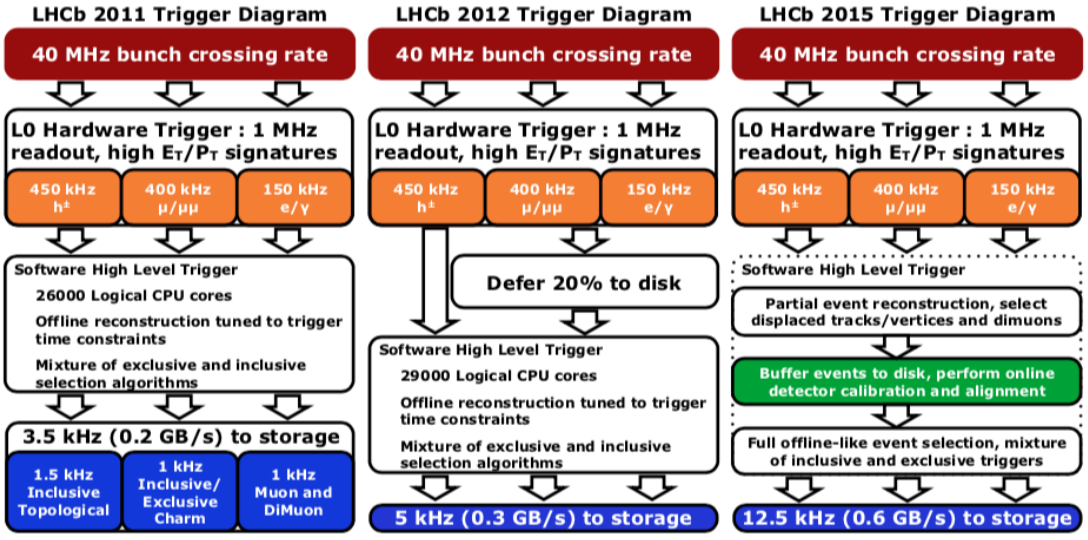

Figure 2.17: The LHCb trigger system illustrated for years 2011, 2012 and 2015 [65].

2.2.6.1 The hardware trigger

The hardware trigger referred to as the Level0 (`L0`) trigger is the first trigger in the LHCb trigger system. Synchronised with the LHCb clock and with a latency of 4μs, the `L0` trigger uses information obtained from the calorimeters and muon chambers, to accept or reject events. The calorimeters and muon chambers are the only systems that can harvest the information needed to reduce the input rate of 40 MHz to 1 MHz before the software trigger. The 1 MHz of data processed is split into three categories; hadrons (450kHz bandwidth), muons (400kHz badnwidth) and electrons/photons (150kHz bandwidth) as displayed by Figure 2.17. These subtriggers are also denoted `L0Calorimeter` for the hadrons, `L0Muon` for the muons and `L0Electron`/ `L0Photon` for electrons/photons. The `L0Calorimeter` and `L0Muon` are given a larger event processing rate because the predominant decay products from b hadrons at LHCb are muons and other hadrons. The `L0Muon` has been optimised so that it is 95% efficient at detecting muons in the LHCb experiment. It is divided into two algorithms; `L0Muon` and `L0DiMuon`, that place stringent criteria on single and pairs of muons. The motivation to include a `L0DiMuon` line for Run 2 was because the majority of hadrons decay to two muons or have pairs of muons in their final state. For instance, in $\bar{B}^0 \to \bar{K}^{*0}\mu^+\mu^-$ and the long-distance charm contributions that proceed by $c\bar{c} \to \mu\bar{\mu}$. `L0Muon` searches for muons with the largest p_T, whereas `L0DiMuon` searches for the largest p_T from combining pairs of muons. To

achieve this each muon chamber is evaluated and sampled in four regions. Each region will contain multiple hits. Mapping these hits into a straight line will identify a muon and its total p_T. If a single muon with p_T >1.76 GeV or a dimuon pair with the combined $p_{T1} \times p_{T2} > 1.6$ GeV^2 is detected then the event will be sent to the software trigger for further processing. Likewise, the `L0Calorimeter` and `L0Electron/L0Photon` searched for hadrons, electrons and photons by splitting the calorimeters into segments, but the E_T is calculated. If a hadron has a $E_T > 3.6$ GeV or a photon/electron has a $E_T >$ 3 GeV, then they are triggered on [65]. The L0 trigger provided an efficient reduction of events over the duration of Run 1 and Run 2 of the LHCb experiment.

2.2.6.2 The software trigger

While a hardware trigger is efficient in reducing the amount of data, it has to make a fast decision using coarse information. As a consequence, high energy particle physics experiments often apply a software trigger that can be performed separately on a CPU farm, in order to use information from all components of the detector to trigger on events. The LHCb detector is no exception, it applies a software trigger, also known as the High Level Trigger (HLT) that performs offline reconstruction on $b\bar{b}$ events using $\approx$ 29000 cores (2012 onwards) [65].

The HLT is split into stages; High Level Trigger 1 (HLT1) and High Level Trigger 2 (HLT2). HLT1 is the first stage of the HLT. It is used by the LHCb collaboration, to filter on successful events from the hardware trigger to reduce the rate. To reduce the rate, the software of the HLT1 performs a partial event reconstruction. It is a partial event reconstruction as only information from the VELO, tracking stations and the muon stations is used to filter the events. The process of the partial reconstruction is as follows. Firstly, all events are reconstructed in the VELO, before cuts are placed on the events. The cuts are on the p_T and the IP, where the p_T is required to be > 1.6 GeV/c [64] and the IP is required to be >100μm. As a result only high IP and momentum tracks are selected for further reconstruction. The next part of the partial reconstruction in the HLT1 is to reconstruct hits in the muon stations. Hits in the muon stations ensure the track has a high p_T. Once the hits in the muon stations are identified,

an extrapolation is performed to the VELO. This extrapolation must be consistent with hits in the tracking stations. If not the candidate is rejected. This extrapolated track is then fitted with a Kalman fitter [66]. If the fit is successful, the track itself and the event it is associated to goes on to the next stage of the of the HLT which is HLT2.

The second stage of the HLT is the HLT2. This trigger is a sophisticated system of algorithms that is used to perform a full event reconstruction. In the same way as the HLT1, only events that have passed the previous triggers will be be evaluated. To achieve a full reconstruction the LHCb experiment imports information from all sub-systems of LHCb such as the RICH and calorimeters to the HLT2. This includes kinematic, charge and mass constraints. The main strength of the HLT2 is that it operates with both inclusive and exclusive trigger lines, as well as placing selections on b hadron decays based on their topology. The selections based on the topology of the B decays are a separate class of triggers known as "topological triggers" [66]. The topological triggers apply multivate techniques to make the best selections of events based on the topology of the decay. Explicitly, a classifier based on a Boosted Decision Tree (BDT) modified to include discrete variables is used. This classifer is called the Bonsai BDT (BBDT). The details on the BBDT can be found in Ref [66], as the content goes beyond the scope of this thesis. In addition to the topological triggers, an external set of triggers are required for this analysis and are discussed in Chapter 4.

For completeness it should be mentioned that during Run 2 an additional stream was added to the software trigger designed for certain analyses. This stream known as the "Turbo stream" is available for analyses that do not require additional reconstruction after the software trigger. In this stream, one can use the reconstructed objects from the HLT as inputs for physics analysis. This stream is not used in this analysis and therefore is only acknowledged. A full description can be found in [67].

The LHCb trigger is a complete, extensive system that allows one to select $b\bar{b}$ events, reconstructing their decay products and properties. It has served as a fundamental input to LHCb during Run 1 and Run 2, and will continue to develop in size and capability in the future of the LHCb experiment.

2.2.7 Generating simulated events

All particle physics experiments require simulation to quantify results and replicate conditions experienced in the detector. This thesis uses simulated events that have been produced by the LHCb simulation framework GAUDI [68]. Particles are generated by the GAUSS package [69]. GAUSS applies two sub-generators PYTHIA [70] and EVTGEN [71]. PYTHIA is used to generate pairs of b-quarks through minimum bias, pp collisions at the LHC. EVTGEN generates the decays of B hadrons into secondary particles. Once these particles have been generated, their interactions within the LHCb detector are simulated using the GEANT4 package [72]. This simulates the particle's responses in all subsections of the detector that have been mentioned in this chapter. After these interactions have been simulated their output is digitized by the application BOOLE [73] and then reconstructed by the package BRUNEL [73]. Finally, after reconstruction the analysis is performed by the physics analysis software DAVINCI [74]. This complex system of generation, simulation and analysis produces the simulated events for the LHCb experiment.

2.2.8 Performance and upgrade

The LHCb experiment has proved to be a pioneering experiment in B physics over both Run 1 and Run 2 of the LHC. The experiment has detected the most $b\bar{b}$ pairs of any experiment, with 50 times more $b\bar{b}$ pairs than the B factories [75]. This has enabled the LHCb collaboration to pursue an extensive B physics programme, which includes studying a variety of B-mesons and rare decays. The LHC is undergoing its second long shutdown (LS2) period, where the main experiments at the LHC will be modified in order to deal with the higher luminosity that will be delivered. The LHCb detector will be upgraded by the LHCb collaboration such that it can run with a luminosity of 2×10^{23} cm^{-2}s^{-1} and aim to collect 50 fb^{-1} of data in 5 years [75]. This luminosity will improve the precision on measurement of rare decays like $\bar{B}^0 \to \bar{K}^{*0}\mu^+\mu^-$.

The systems that are to be updated in the LHCb detector include the VELO, where the aim is to move away from silicon strips to hybrid pixel detectors. The geometry of

the VELO will remain the same, with two modules coming together when the beam is running and retracting during injection. Nevertheless, the modules will become *L*-shaped instead of semicircular to ultimately achieve a closer distance to the beam. The next component that is undergoing a significant change is the RICH 1 detector, due to degradation of the detector and to improve the PID. Explicitly, the optical system will be upgraded with new mirrors, readout electronics and an optical stand. The testing of the new RICH 1 mirrors are described in Appendix B, which were the authors service contribution to the experiment. Moreover, the tracking stations will be updated. In particular, the TT will be replaced with a new tracking station called the Upstream Tracker (UT). In addition, the T1-T3 tracking stations will be replaced by a single scintillating fibre tracker know as the SciFi tracker. One important component that needs to be updated to cope with the larger luminosity is the trigger. With an increase in luminosity the hardware trigger would be incapable of dealing with the significant increase in $b\bar{b}$ pairs produced. As a consequence, the collaboration has decided to remove the L0 trigger and implement a trigger that purely runs in software. The aim will be to write 2-5 GB/s to storage [76]. As the L0 trigger will be withdrawn, the M1 station will be removed. Other changes to the muon system will be additional shielded and adaptations to the electronics. Finally, the calorimeter will also be upgraded with new electronics.

Chapter 3

Modelling non-local contributions in $\bar{B}^0 \to \bar{K}^{*0}\mu^+\mu^-$ transitions

In recent years the $b \to s\ell^+\ell^-$ sector has seen many discrepancies in experimental measurements when compared to the SM. Despite global analyses implying that these anomalies could be due to NP effects, in the form of a massive vector particle entering at loop-level, it is argued that alternatively this effect could be the result of the non-local contributions, interfering with the penguin decay. The aim of this analysis to measure the interference of these non-local contributions with the penguin decay in $\bar{B}^0 \to \bar{K}^{*0}\mu^+\mu^-$ transitions. This is achieved through the development of a model that includes all possible non-local contributions in addition to the penguin component, and is used to perform a maximum likelihood fit to the LHCb experimental data. This chapter describes the model. An overview of the structure of the signal model is given and the way in which the non-local contributions are modelled. The model is compared to other existing models, that have tried to model the non-local charm loop in $\bar{B}^0 \to \bar{K}^{*0}\mu^+\mu^-$ transitions. Next, the distributions of the angular observables are produced and an investigation into how the non-local contributions affect lepton universality tests is performed.

3.1 The model

A model containing both non-local and short-distance contributions to $\bar{B}^0 \to \bar{K}^{*0}\mu^+\mu^-$ transitions was constructed by considering the $\bar{B}^0 \to \bar{K}^{*0}\mu^+\mu^-$ differential decay rate (see Eq 1.49 in Chapter 1). The decay rate contains P-wave $\bar{K}^{*0}$ contributions, and for now S-wave contributions are ignored, with their effect investigated later in Chapter 4. As previously noted, the differential decay rate depends on eight observables, J_i. Each J_i is independent and formed from bilinear combinations of the 6 transversity amplitudes of the $\bar{K}^{*0}$. The non-local contributions are inserted directly into the amplitude expressions. Equations 3.1, 3.2 and 3.3 show the transversity amplitudes for $\bar{B}^0 \to \bar{K}^{*0}\mu^+\mu^-$, containing the non-local contributions, $\mathcal{G}_{0,\perp,\parallel}(q^2)$.

$$\mathcal{A}_0^{\mathrm{L,R}}(q^2) = -8N\frac{m_B m_{K^*}}{\sqrt{q^2}}\left\{(C_9 \mp C_{10})A_{12}(q^2) + \frac{m_b}{m_B + m_{K^*}}C_7 T_{23}(q^2) + \mathcal{G}_0(q^2)\right\}, \tag{3.1}$$

$$\mathcal{A}_\parallel^{\mathrm{L,R}}(q^2) = -N\sqrt{2}(m_B^2 - m_{K^*}^2)\left\{(C_9 \mp C_{10})\frac{A_1(q^2)}{m_B - m_{K^*}} + \frac{2m_b}{q^2}C_7 T_2(q^2) + \mathcal{G}_\parallel(q^2)\right\}, \tag{3.2}$$

$$\mathcal{A}_\perp^{\mathrm{L,R}}(q^2) = N\sqrt{2\lambda}\left\{(C_9 \mp C_{10})\frac{V(q^2)}{m_B + m_{K^*}} + \frac{2m_b}{q^2}C_7 T_1(q^2) + \mathcal{G}_\perp(q^2)\right\}, \tag{3.3}$$

In these equations, m_B is the mass of the B^0, and $m_{K^{*0}}$ is the mass of the K^{*0}. The λ, β_ℓ and N terms, are identical to those in the penguin only amplitudes (see Equations 1.41, 1.42 and 1.43). To model the form factors $A_1, A_{12}, V, T_1, T_2, T_{23}$, the combination of Light Cone Sum Rules and Lattice QCD [13] is used. These are the same expressions as given by Equations 1.36 and 1.37 in Chapter 1. The individual form factors are determined by the values of the $a_{0,1,2}$ coefficients from the $z-$expansion. In the model, the uncertainties and correlations between the $a_{0,1,2}$ coefficients of all the different form

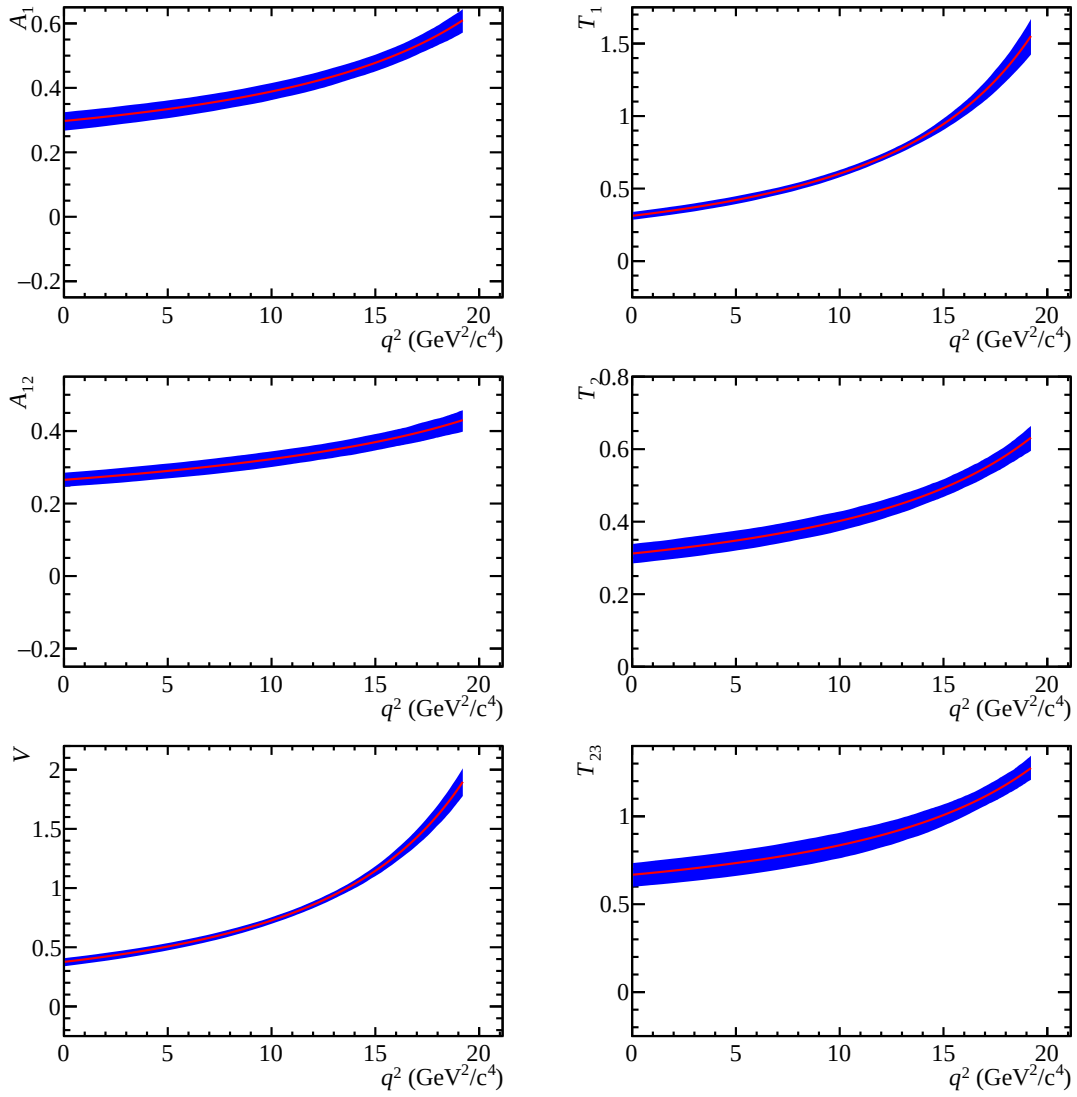

Figure 3.1: $\bar{B}^0 \to \bar{K}^{*0}\mu^+\mu^-$ form factors, $A_1, A_{12}, V, T_1, T_2, T_{23}$. The red line represents the central values of the form factors and the blue band represents the 68% confidence interval obtained by varying coefficients of the z-expansion within their uncertainties.

factors are accounted for. This helps reduce any possible error in the form factors, for instance in T_{23} (see Chapter 1). Figure 3.1 shows the form factors, constructed using the model. In this figure, the red, line corresponds to the central values of the form factors, and the blue band represents the 68% confidence interval produced by varying the $a_{0,1,2}$ coefficients of the $z-$expansion within their uncertainties. Comparing Figure 3.1 to the expected distributions of the form factors shown by Figure 1.4, the model is successful in accurately reproducing the form factors. Furthermore, the terms, $C_{7,9,10}$, are the effective Wilson Coefficients, which denote the strengths of different couplings in the short-distance component. In Equations 3.1, 3.2, 3.2, the notation is $C_i = C_i^{\text{eff}} - C_i^{\text{eff}'}$,

i	C_i	C_i'
7	-0.307	-0.006
9	4.27	0
10	-4.166	0

Table 3.1: SM Wilson Coefficient values obtained at the scale of $m_b = 4.8$GeV. The values are for both, C_i and $C_i^{'}$ and are taken from the literature [11].

where the prime term is the chiral partner. The values used for the terms (C_i^{eff}, $C_i^{\text{eff}'}$) that go into the total effective Wilson Coefficient are provided in Table 3.1.

The terms $\mathcal{G}_{0,\perp,\parallel}(q^2)$ are the functions used to describe the non-local contributions in $\bar{B}^0 \to \bar{K}^{*0}\mu^+\mu^-$ transitions. The non-local expressions remain unchanged under left and right chirality, which means only three non-local expressions are needed, which can be inserted directly into the amplitude expressions. These three expressions are,

$$\mathcal{G}_0 = \frac{m_b}{m_B + m_{K^*}} T_{23}(q^2)\zeta^0 e^{i\omega^0} + A_{12}(q^2)\sum_j \eta_j^0 e^{i\theta_j^0} A_j^{\text{res}}(q^2), \tag{3.4}$$

$$\mathcal{G}_\parallel = \frac{2m_b}{q^2} T_2(q^2)\zeta^\parallel e^{i\omega^\parallel} + \frac{A_1(q^2)}{m_B - m_{K^*}}\sum_j \eta_j^\parallel e^{i\theta_j^\parallel} A_j^{\text{res}}(q^2), \tag{3.5}$$

$$\mathcal{G}_\perp = \frac{2m_b}{q^2} T_1(q^2)\zeta^\perp e^{i\omega^\perp} + \frac{V(q^2)}{m_B + m_{K^*}}\sum_j \eta_j^\perp e^{i\theta_j^\perp} A_j^{\text{res}}(q^2), \tag{3.6}$$

Each of the $\mathcal{G}_{0,\perp,\parallel}$ terms contain a sum over the q^2 dependant terms A_j^{res}. Each A_j^{res} represents a vector, $c\bar{c}$ resonant contribution that is modelled as a simple relativistic Breit-Wigner. This modelling approach is inspired by the analysis presented in Ref [45], which determined the impact of hadronic contributions in the decay $B^+ \to K^+\mu^+\mu^-$. The results in Ref [45] revealed that this simplistic approach was adequate in the determination of the interference. In this analysis, the relativistic Breit-Wigners are modelled via the isobar method, that is described by the following expression,

$$A_j^{\text{res}}(q^2) = \frac{m_{\text{res}\,j}\Gamma_{\text{res}\,j}}{(m_{\text{res}\,j}^2 - q^2) - i m_{\text{res}\,j}\Gamma_j(q^2)}, \tag{3.7}$$

where $\Gamma_{\mathrm{res}\,j}$ and $m_{\mathrm{res}\,j}$ denote the natural width and pole mass for the given resonance. The values for these terms are taken from Ref [77]. $\Gamma_j(q^2)$ is the running width, that is a function of q^2 and expressed by,

$$\Gamma_j(q^2) = \frac{p}{p_{\mathrm{res}\,j}} \frac{m_{\mathrm{res}\,j}}{q} \Gamma_{\mathrm{res}\,j}, \tag{3.8}$$

In the model, the concept that each Breit-Wigner amplitude has a natural width and pole mass, is used to include a variety of different resonances. For instance, through modelling wide resonances such as the $\rho(770)$, in addition to extremely narrow resonances like the J/ψ. The complete list of resonant contributions included in this model and analysis is; ρ^0, ϕ, J/ψ, $\psi(2S)$, $\psi(3770)$, $\psi(4040)$ and $\psi(4160)$. Light quark resonant contributions are expected to be suppressed by the CKM mechanism, or by loops compared to final states involving charmonium resonances. Therefore these resonant contributions are omitted in the model. In the future it is expected that broad light-states will become more apparent with more data. The model has been constructed with this in mind so it can easily accommodate additional states subject to what is required by the data. Each Breit-Wigner amplitude is multiplied by a complex number that has a magnitude, η_j^λ, and phase, θ^λ, measured relative to the Wilson Coefficient C_9. This is demonstrated clearly in Equations 3.1, 3.2 and 3.3. As there are three non-local amplitudes, it means that each resonance has three magnitudes, $\eta_j^{0,\perp,\parallel}$, and phases, $\theta_j^{0,\perp,\parallel}$, to be determined. By convention, the measurements of $\bar{B}^0 \to V\bar{K}^{*0}$ decays, define the phases $\theta_\perp$ and $\theta_\parallel$ to be relative to the phase θ_0. This means that there is a single phase θ_0, that governs the interference between the resonant and penguin amplitudes, which can be determined in a fit to the data. The magnitudes, $\eta_j^{0,\perp,\parallel}$ for every hadronic resonance is given by the following,

$$|\eta_j^0|^2 = \frac{f_j^0 \mathcal{B}(\overline{B}^0 \to V\overline{K}^{*0}) \times \mathcal{B}(V \to \mu^+\mu^-)}{\tau_B \int \left| 8N \frac{m_B m_{K^*}}{\sqrt{q^2}} A_j^{\rm res}(q^2) A_{12}(q^2) \right|^2 dq^2},$$

$$|\eta_j^{\parallel}|^2 = \frac{f_j^{\parallel} \mathcal{B}(\overline{B}^0 \to V\overline{K}^{*0}) \times \mathcal{B}(V \to \mu^+\mu^-)}{\tau_B \int \left| N\sqrt{2}(m_B^2 - m_{K^*}^2) A_j^{\rm res}(q^2) \frac{A_1(q^2)}{m_B - m_{K^*}} \right|^2 dq^2}, \tag{3.9}$$

$$|\eta_j^{\perp}|^2 = \frac{f_j^{\perp} \mathcal{B}(\overline{B}^0 \to V\overline{K}^{*0}) \times \mathcal{B}(V \to \mu^+\mu^-)}{\tau_B \int \left| N\sqrt{2\lambda} A_j^{\rm res}(q^2) \frac{V(q^2)}{m_B + m_{K^*}} \right|^2 dq^2},$$

In these expressions the denominator is the integral over q^2 for the amplitude that contains the resonant contribution j, while the numerator contains information on the branching fraction and measurements of the magnitudes of $\bar{B}^0 \to V\bar{K}^{*0}$ decays, where V is the resonance j. Therefore, with additional measurements of the relative phases, $\theta_j^{0,\perp,\parallel}$ from $\bar{B}^0 \to V\bar{K}^{*0}$ decays, this means that the exact values of the $\eta_j^{0,\perp,\parallel}$ and $\theta_j^{\perp,\parallel}$ parameters, excluding the free phase, can be obtained for the non-local component relative to the penguin component in $\bar{B}^0 \to \bar{K}^{*0}\mu^+\mu^-$ transitions.

However, in the normalisation expressions the measurements of the branching fractions and magnitudes/phases can only be used if they exist. For the decays, $\bar{B}^0 \to J/\psi\bar{K}^{*0}$ and $\bar{B}^0 \to \psi(2S)\bar{K}^{*0}$, there exist measurements of the magnitudes and phases, from analyses performed by the LHCb, BaBar and Belle collaborations [78–80]. The branching franction measurements for these decay has also been performed and can be found in Refs [78, 81]. For the decay $\bar{B}^0 \to \phi\bar{K}^{*0}$, measurements on both the amplitudes and phases, and the branching fraction, also exist and have been measured by the LHCb, Belle and BaBar collaborations [82–84]. It follows that for the $J/\psi, \psi(2S), \phi$ resonances, it is relatively simple to determine the $\eta^{0,\perp,\parallel}$ and $\theta^{\perp,\parallel}$ parameters, leaving a single phase for each resonant contribution. For the remaining resonant contributions the process is not as simple. Branching fraction measurements only exist for the transition $\bar{B}^0 \to \rho^0\bar{K}^{*0}$ [85, 86], and no measurements exist for the magnitudes ($\eta_{\rho^0}^{0,\perp,\parallel}$) and phases

Mode	$(\eta_j^{\parallel}, \theta_j^{\parallel}\,[rad])$	$(\eta_j^{\perp}, \theta_j^{\perp}\,[rad])$	η_j^0
$B^0 \to \rho^0 K^{*0}$	$(1.5 \quad , \quad 2.6)$	$(1.9 \quad , \quad 2.6)$	5.1×10^{-1}
$B^0 \to \phi K^{*0}$	$(2.5 \times 10^1 \quad , \quad 2.6)$	$(3.2 \times 10^1 \quad , \quad 2.6)$	1.0×10^1
$B^0 \to J/\psi K^{*0}$	$(4.9 \times 10^3 \quad , -2.9)$	$(6.5 \times 10^3 \quad , \quad 2.9)$	7.1×10^3
$B^0 \to \psi(2S) K^{*0}$	$(5.3 \times 10^2 \quad , -2.8)$	$(8.1 \times 10^2 \quad , \quad 2.8)$	9.6×10^2
$B^0 \to \psi(3770) K^{*0}$	$(9.3 \times 10^{-1}, -2.9)$	$(1.5 \quad , \quad 2.9)$	1.7
$B^0 \to \psi(4040) K^{*0}$	$(2.9 \times 10^{-1}, -2.9)$	$(5.6 \times 10^{-1}, \quad 2.9)$	6.0×10^{-1}
$B^0 \to \psi(4160) K^{*0}$	$(8.3 \times 10^{-1}, -2.9)$	$(2.0 \quad , \quad 2.9)$	1.8

Table 3.2: Input values for the long-distance charm components to be inserted into the amplitude expressions $\mathcal{G}_\lambda$. The input values are taken from Refs [45, 77–86].

($\theta_{\rho^0}^{0,\perp,\parallel}$). The approach taken is to use the values of the magnitudes and phases for the decay $\bar{B}^0 \to \phi \bar{K}^{*0}$ as an input for the magnitudes and phases of the $\bar{B}^0 \to \rho^0 \bar{K}^{*0}$. Given the branching fraction of $\bar{B}^0 \to \rho^0 \bar{K}^{*0}$ is very small and we will be fitting for the magnitude and phase this assumption is valid. A different approach is also taken for the higher mass resonances beyond the $\psi(2S)$ and $D\bar{D}$ threshold, namely the $\bar{B}^0 \to \psi(3770)\bar{K}^{*0}$, $\bar{B}^0 \to \psi(4040)\bar{K}^{*0}$ and $\bar{B}^0 \to \psi(4160)\bar{K}^{*0}$ decays, where no branching fraction or angular analyses exist. The procedure for these decays is to take an approximation for the branching fraction, by calculating a ratio of branching fractions for $\bar{B}^+ \to \psi(2S)\bar{K}^+$ decays with $\bar{B}^+ \to V^{'}\bar{K}^+$ decays, where $V^{'} \to \mu^+\mu^-$is given by Ref [45]. Once this ratio has been calculated, it is scaled by the branching fraction of $\bar{B}^0 \to \psi(2S)\bar{K}^{*0}$ [81]. This gives an approximation that is valid and in good agreement with predictions. In regards to the magnitudes and phases of these higher states, the measurements for the magntiudes and phases for $\bar{B}^0 \to J/\psi\bar{K}^{*0}$ [78], are used. The final values for the relative magnitudes and phases of the transversity amplitudes, that are used as input values for the amplitudes in the model is give by Table 3.2. The final term in the non-local expressions is a complex number, $\zeta^{0,\perp,\parallel}e^{i\omega 0,\perp,\parallel}$, where the $\zeta^{0,\perp,\parallel}$ terms are the magnitudes and the $\omega^{0,\perp,\parallel}$ terms are the phases. This single complex number per amplitude that multiplies the tensor form factors, denotes all non-local terms that enter relative to C_7. These terms need to be determined from experimental fits to the data, and in the absence of such fits the central values are set to 0, or set to sensible values for comparisons to other models.

3.2 Model comparisons

The empirical model presented in the previous section was compared to alternative parameterisations of the non-local contributions in $\bar{B}^0 \to \bar{K}^{*0}\mu^+\mu^-$ transitions. A comparison was made to the model provided in Ref [2], where the authors try to account for the non-local charm loop by using QCD light-cone sum rule calculations of the $B \to K^*$ matrix elements up to $q^2 < 4m_c^4$, that are then extrapolated using a dispersion relation to higher q^2 values. External inputs such as the rate and amplitude structure of $\bar{B}^0 \to J/\psi\bar{K}^{*0}$ and $\bar{B}^0 \to \psi(2S)\bar{K}^{*0}$ decays are also included. However, these are the only resonant contributions that are considered in Ref [2]. For that reason only these resonances are included in our model when performing the comparison.

Moreover, in Ref [2] the authors do not include factorisable next-to-leading order corrections in their modelling of the charm loop. In light of this, all the phases of the long-distance amplitudes relative to the short-distance amplitudes were set to be zero. Given also that the authors in Ref [2] use a different amplitude basis to the one presented in Chapter 1, the comparison was made in the basis of Ref [2], given the simplicity of translating our amplitudes into their basis. The results of the comparison are provided by Figure 3.2. In Figure 3.2 the prediction from Ref [2] is shown by the solid, magenta band. The black and cyan lines (solid, dotted and dashed) illustrate our model. Each line represents a different phase choice (0 or π) for the free phases $\theta^0_{J/\psi}$ and $\theta^0_{\psi(2S)}$, while the remaining phases $\theta^{\perp,\parallel}_{J/\psi}$, $\theta^{\perp,\parallel}_{\psi(2S)}$ are set to zero. As our amplitudes include terms ζ^λ, ω^λ, where λ=0,$\perp$,$\parallel$, the values of these terms have been set to $\zeta \sim 0.8|C_7|$, $\omega=\pi$ such that they are consistent with those in Ref [13] and predicted by Ref [2]. The results reveal that when we set all the phases of the J/ψ and $\psi(2S)$ to be zero (black dotted line), the model is consistent with that of Ref [2]. However, what is interesting is the effect that occurs when including the measured phases of the resonances. When only the free phases $\theta^0_{J/\psi,\psi(2S)} = 0$ are included (solid cyan line) there is a good agreement, but when $\theta^0_{J/\psi,\psi(2S)} = \pi$ are included (dashed cyan line) the models appear inconsistent with each other. This suggests that the two models will disagree at level that is determined by what one sets for the free phase. When trying to understand the long-distance charm contributions, the authors in Ref [2] suggest that the inclusion of charm pushes

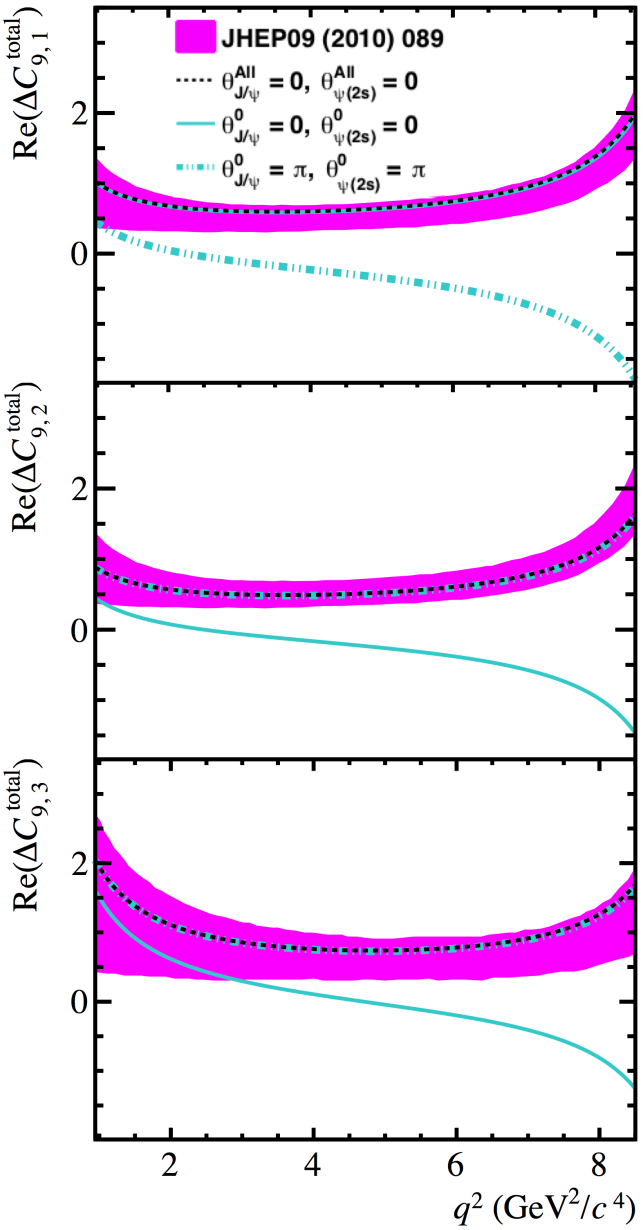

Figure 3.2: The prediction of the effect of the non-local contributions to the $\bar{B}^0 \to \bar{K}^{*0}\mu^+\mu^-$ amplitudes as a function of q^2. The effect of the long-distance contributions using the model described in Sec 3.1, with only the J/ψ and $\psi(2S)$ resonances are considered is shown by the cyan lines. The solid cyan line is obtained by setting the free phases $\theta^0_{J/\psi,\psi(2S)}$ to be 0, and the dashed-dotted cyan line is obtained the free phases to be π. An additional line is included to show the effect of setting all phases of the J/ψ and $\psi(2S)$ to be 0 for Equations 3.4 3.5 3.6. Also provided in the figure are the predictions from Ref [2] (magenta band).

observables such as P_5' away from experimental measurements. However, as this model does not include the measurements of the resonant contributions, and also only includes two resonant contributions, no conclusions can be made. This motivates Section 3.3, which shows how the phases impact the angular observables using the empirical model.

Another comparison was made to the model presented in Ref [3]. In Ref [3], the authors model the charm loop analytically through calculating the charm loop at $q^2 < 0$, through a z−expansion that is truncated after the second order and also calculated to next-to-leading order in α_s. This approach is valid up to $q^2 < m^2_{\psi(2S)}$, meaning that one cannot include all possible resonant contributions across the full q^2 range. In light of this, our model is evaluated up to $q^2 < m^2_{\psi(2S)}$ for a fair comparison. Similarly to the authors in Ref [2], the authors in Ref [3] only consider contributions from the J/ψ and $\psi(2S)$, and use inputs from experimental measurements of $\bar{B}^0 \to J/\psi\bar{K}^{*0}$ and $\bar{B}^0 \to \psi(2S)\bar{K}^{*0}$ decays. Only these resonant contributions are therefore considered in our model when making the comparison.

Moreover, unlike Ref [2], the amplitude basis used in Ref [3] is the same basis as used by our model, meaning a direct comparison of the amplitudes $A_{\perp\parallel,0}$ can be made. The only difference is that the transformation $\eta_j^{\perp}$ = -$\eta_j^{\perp}$ is applied as the phase convention in Ref [3] is the mirror of the one we use in our model. Next, the values for the non-local parameters, ζ and ω in our model were set such that they were consistent with those in Ref [3], where specifically $\zeta \sim 15\%|\ C_7\ |$ and $\omega = \pi$.

Figure 3.3 and Figure 3.4 show the distributions of the non-local contributions for our model and the model presented in Ref [3], for the three different amplitudes containing non-local contributions, in terms of real (Figure 3.3) and imaginary (Figure 3.4) components. The distributions of the amplitudes using our model are shown for the phase choices $\theta^0_{J/\psi,\psi(2S)} = 0,\ \pi\ ,\ \frac{\pi}{8}$ (cyan lines). The dotted, magenta line corresponds to the amplitude distribution from Ref [3].

The results suggest the agreement between the two models is dependent on the choice of the phase, where a good agreement is given by setting $\theta^0_{J/\psi,\psi(2S)} = \pi/8$. There appears to be a slight disagreement with the imaginary part of the amplitudes $A_{\perp}$ and $A_{\parallel}$. However, this was investigated and found to be merely due to the choice of ω=π. Comparisons made with more formal approaches show that the empirical model presented in Section 3.1 is a valid description of the non-local contributions.

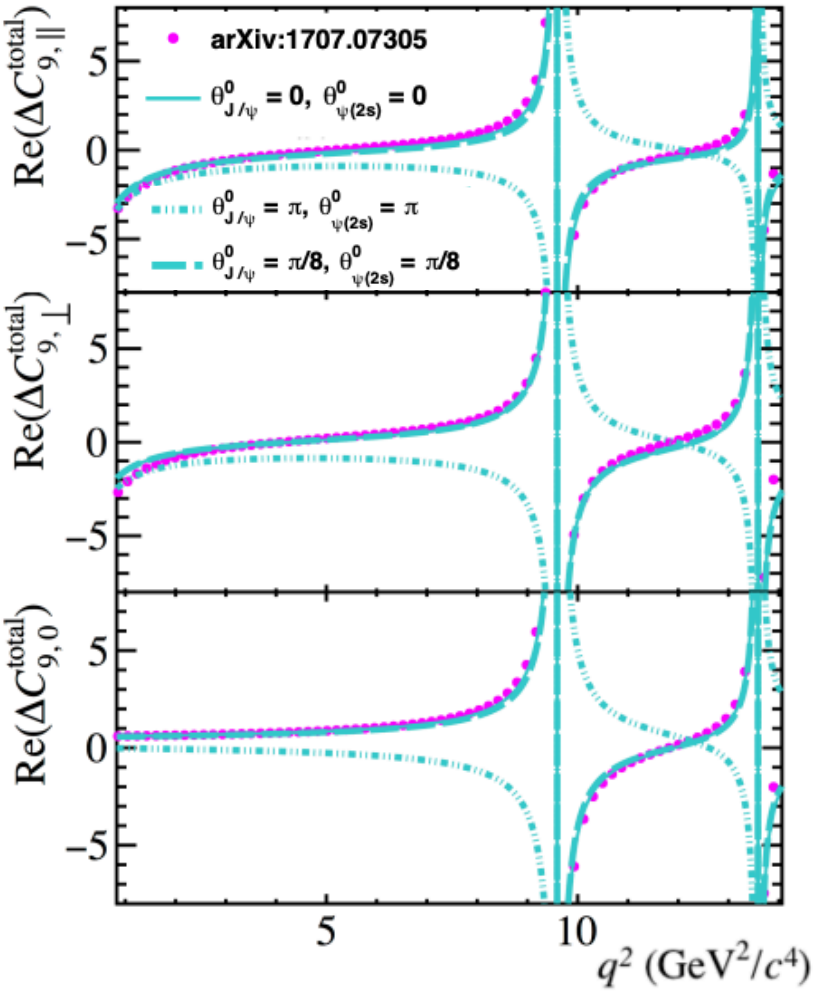

Figure 3.3: The prediction of the effect of the non-local contributions on the real component of the $\bar{B}^0 \to \bar{K}^{*0}\mu^+\mu^-$ amplitudes, as a function of q^2. The effect of the long-distance contributions using the model described in Sec 3.1, where only the J/ψ and $\psi(2S)$ resonances are considered. The predictions are madee for choices of the free phase $\theta^0_{J/\psi,\psi(2S)}$=0, π and $\frac{\pi}{8}$ and are shown by the cyan lines. The prediction using the model from Ref [3] is shown by the dotted, magenta line.

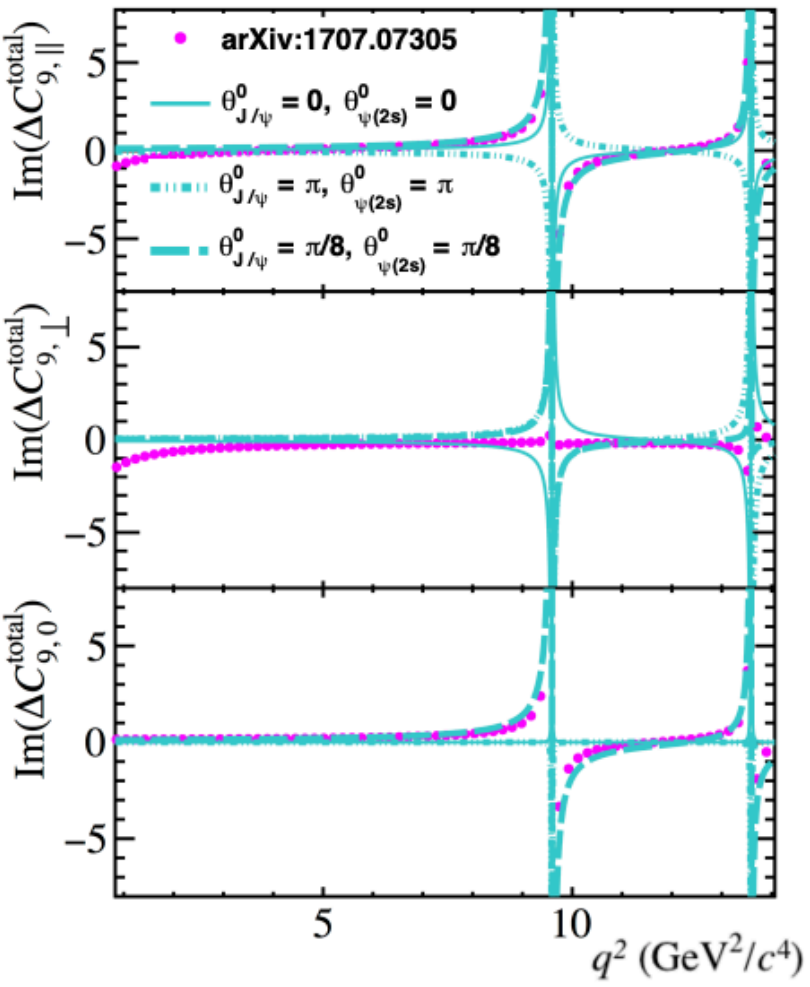

Figure 3.4: The prediction of the effect of the non-local contributions on the imaginary component of the $\bar{B}^0 \to \bar{K}^{*0}\mu^+\mu^-$ amplitudes, as a function of q^2. The effect of the long-distance contributions using the model described in Sec 3.1, where only the J/ψ and $\psi(2S)$ resonances are considered. The predictions are made for choices of the free phase $\theta^0_{J/\psi,\psi(2S)}$=0, π and $\frac{\pi}{8}$ and are shown by the cyan lines. The prediction using the model from Ref [3] is shown by the dotted, magenta line.

3.3 The effect of the non-local contributions on the $\bar{B}^0 \to \bar{K}^{*0}\mu^+\mu^-$ angular observables

The model presented in Section 3.1 can be used to study the effect of hadronic contributions on the $\bar{B}^0 \to \bar{K}^{*0}\mu^+\mu^-$ angular observables. As mentioned previously the $\bar{B}^0 \to \bar{K}^{*0}\mu^+\mu^-$ angular distribution can be written in terms of 8 CP-averaged observables S_i, $F_{\rm L}$, $A_{\rm FB}$, where i = 3,4,5,7,8,9, along with *optimised observables* that are observables constructed from combinations of the CP-averaged observables. The effect of the non-local charm loop on the CP-averaged observables and the optimised observables that include $P_5^{'}$, is studied. Figure 3.5 and Figure 3.6 show the distributions for the observables $P_5^{'}$, $A_{\rm FB}$, S_7 and $F_{\rm L}$, in the SM, in the q^2 regions of [0,15.0] GeV$^2/c^4$ (Figure 3.5) and [15.0,19.0] GeV$^2/c^4$ (Figure 3.6). While, Figure 3.7 and Figure 3.8 shows the distributions for the observables S_3, S_7, S_5, S_8 and S_9, in the q^2 regions of [0,15.0] GeV$^2/c^4$ (Figure 3.7) and [15.0,19.0] GeV$^2/c^4$ (Figure 3.8). The lack of knowledge of the free phase θ_j^0, means that all possible phase combinations are considered. The cyan bands in these figures are produced by scanning over all possible values of the free phase. Two phase combinations have been directly specified on the Figures 3.5, 3.6 3.7 and 3.8; $\theta_j^0 = 0$ (dashed band) and $\theta_j^0 = \pi$ (solid dark band). In all these bands the uncertanties on the form factors taken from Ref [13] are varied according to the covariance matrix. The data from LHCb Run 1 is shown by the data points and the theoretical predictions computed by the `flavio` package [87] are displayed by the magenta band. The freedom of the phase allows a large region of the observable space to be populated. In particular, this is demonstrated for the observables S_7 and S_9, which at both low and high q^2 vary widely in values for a given choice of the phase. These observables are perfect examples of how dependent observables can be on the strong phases. Using this knowledge one can use the angular distribution to determine the exact phase for a given resonance, precisely determining the hadronic contribution. $P_5^{'}$ is one such observable that has been given widespread consideration because of the large tension seen between data and theoretical predictions [4]. In Figure 3.5 and Figure 3.6, $P_5^{'}$ shows a large dependence on the free phase, which appears more prominent, closer to the resonances. The results are in good agreement with the theoretical predictions.

However, by scanning over all possible phases it appears no combination of the phases describe the data. This implies that the deviation in this observable cannot just be explained purely by the resonant contributions. This concept can also be applied to the other observables in these figures.

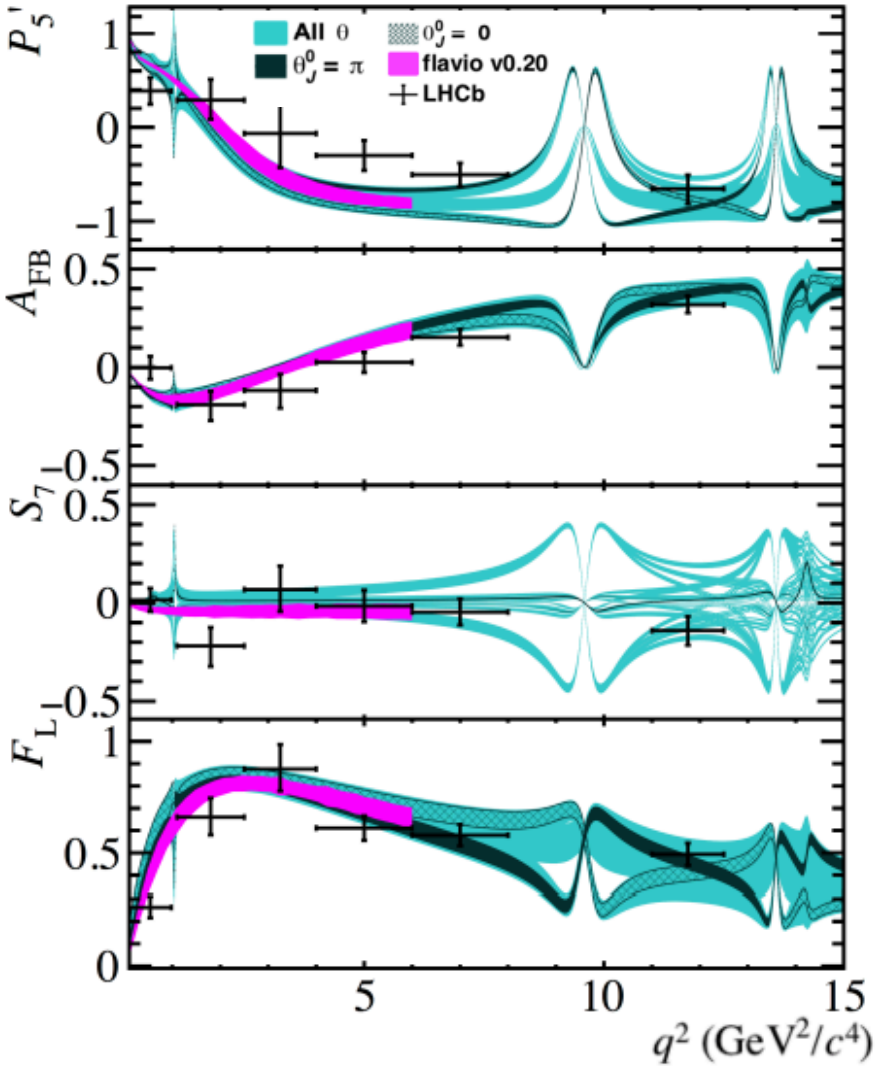

Figure 3.5: The distributions of the angular observables $P_5^{'}$, $A_{\rm FB}$, S_7, $F_{\rm L}$ as a function of q^2, in the region of $q^2 \in$[0,15.0]GeV$^2/c^4$, and produced using the model described in Section 3.1. The distributions are shown for the regions below (left) and above (right) the open charm threshold. Scanning over all possible combinations of the free phase θ_j^0 for all resonant contributions produces the cyan bands. Specific choices of the free phase are highlighted; the hatched band where θ_j^0=0 and the dark band where θ_j^0=π. The theoretical predictions for the observables (magenta band) have been reproduced by the `flavio` package [87]. The experimental data from the LHCb experiment is shown by the data points.

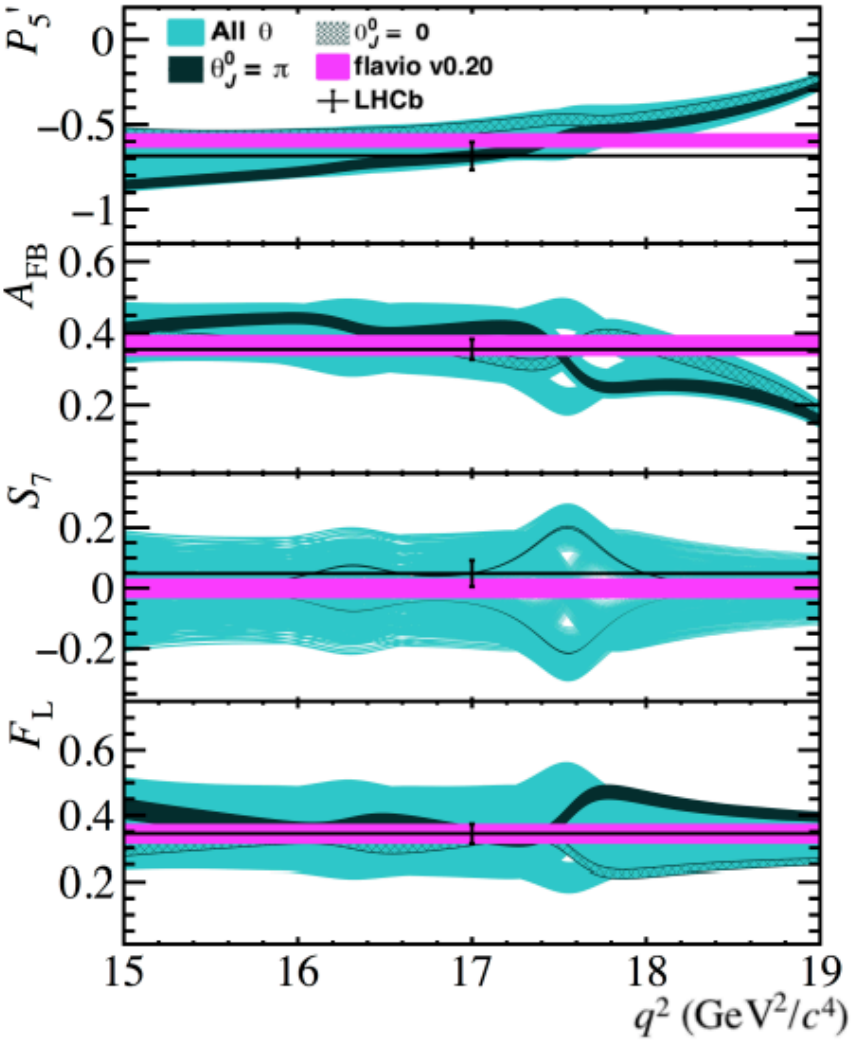

Figure 3.6: The distributions of the angular observables $P_5^{'}$, $A_{\rm FB}$, S_7, $F_{\rm L}$ as a function of q^2, in the high q^2 region of [15.0,19.0]GeV$^2/c^4$, and produced using the model described in Section 3.1. The distributions are shown for the regions below (left) and above (right) the open charm threshold. Scanning over all possible combinations of the free phase θ_j^0 for all resonant contributions produces the cyan bands. Specific choices of the free phase are highlighted; the hatched band where θ_j^0=0 and the dark band where θ_j^0=π. The theoretical predictions for the observables (magenta band) have been reproduced by the `flavio` package [87]. The experimental data from the LHCb experiment is shown by the data points.

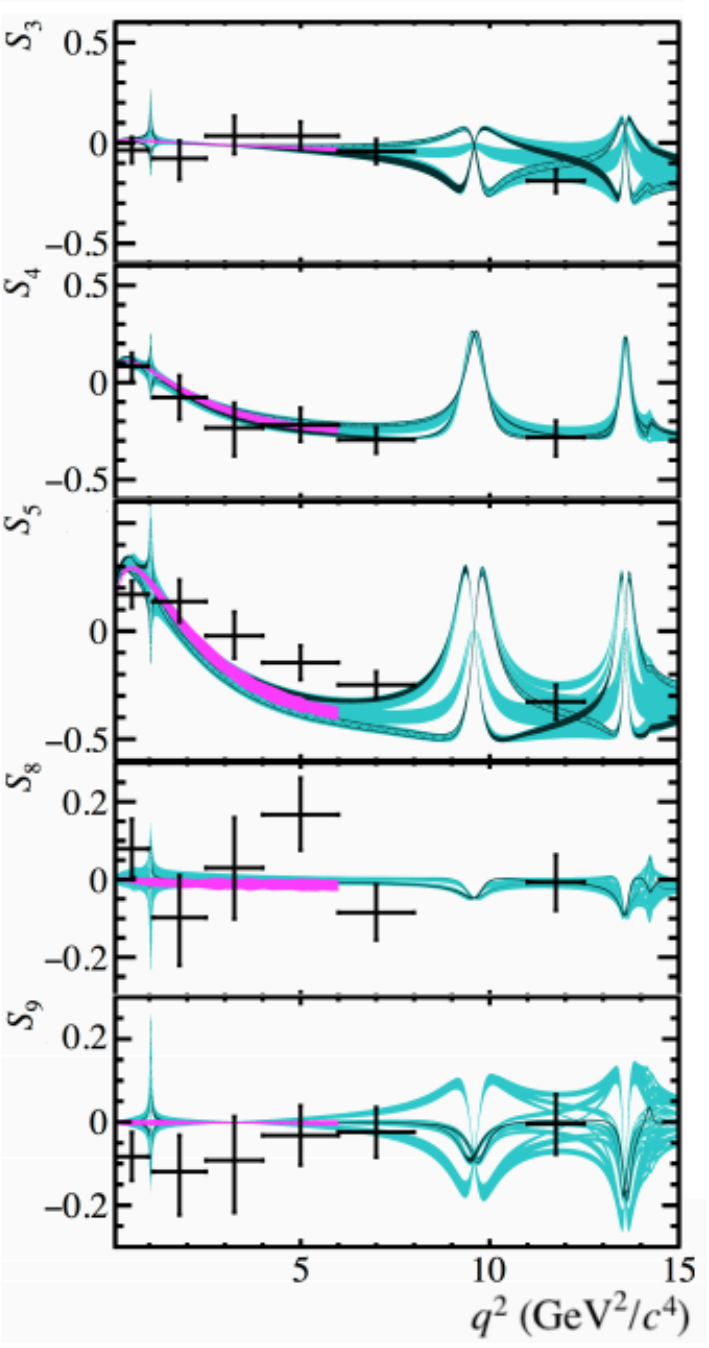

Figure 3.7: The distributions of the angular observables $S_{3,4,5,8,9}$ as a function of q^2, in the region of $0 < q^2 < 15.0$ GeV$^2/c^4$, produced using the model described in Section 3.1. The distributions are shown for the regions below (left) and above (right) the open charm threshold. Scanning over all possible combinations of the free phase θ_j^0 for all resonant contributions produces the cyan bands. Specific choices of the free phase are highlighted; the hatched band where θ_j^0=0 and the dark band where θ_j^0=π. The theoretical predictions for the observables (magenta band) have been reproduced by the `flavio` package [87]. The experimental data from the LHCb experiment is shown by the data points.

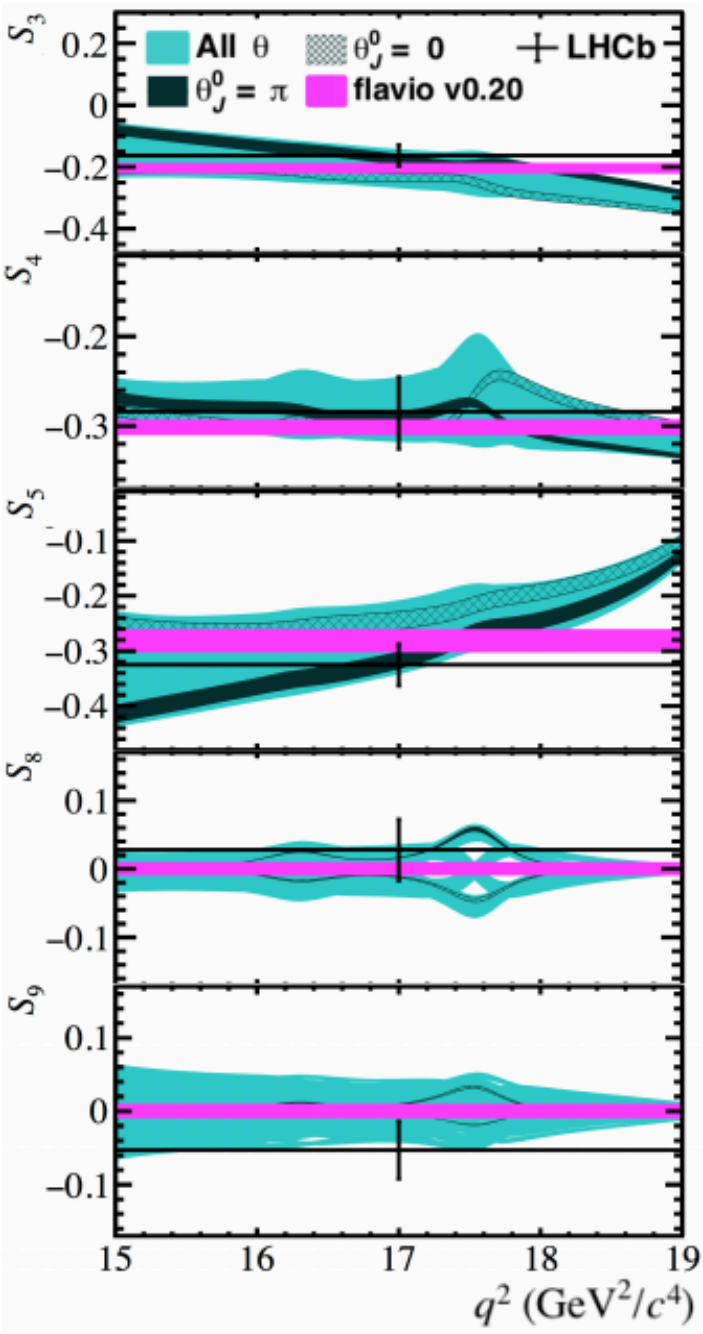

Figure 3.8: The distributions of the angular observables $S_{3,4,5,8,9}$ as a function of q^2, in the region of $15.0 < q^2 < 19.0$ GeV$^2/c^4$, and produced using the model described in Section 3.1. The distributions are shown for the regions below (left) and above (right) the open charm threshold. Scanning over all possible combinations of the free phase θ_j^0 for all resonant contributions produces the cyan bands. Specific choices of the free phase are highlighted; the hatched band where θ_j^0=0 and the dark band where θ_j^0=π. The theoretical predictions for the observables (magenta band) have been reproduced by the `flavio` package [87]. The experimental data from the LHCb experiment is shown by the data points.

In addition to the CP-averaged observables, which are calculated based on the model in Section 3.1, for the strong phases, one can also study the effect of weak phases. By introducing weak phases into the model, interference between strong and weak phases can cause CP violation giving rise to CP-odd observables. The CP-odd observables that arise in the presence of weak phases are provided earlier in Chapter 1 by Eq 1.52 and the direct CP asymmetry is explicitly shown by Eq 3.10.

$$A_{\rm CP} = \frac{d(\Gamma - \bar{\Gamma})}{dq^2} \Big/ \frac{d(\Gamma + \bar{\Gamma})}{dq^2} \tag{3.10}$$

The impact of the non-local charm loop on the CP-odd observables and the direct CP asymmetry is illustrated by Figure 3.9 and Figure 3.10. In both Figure 3.9 and Figure 3.10, the phase choices for the free phase θ_j^0 is all resonance contributions set to -$\frac{\pi}{2}$, 0, $\frac{\pi}{2}$. The observables are shown for two NP scenarios. The first being $C_9^{\rm NP}$= -1 -1.0i shown by Figure 3.9 and the second being $C_7^{\rm NP}$= -0.03i, $C_9^{\rm NP}$= -1 shown by Figure 3.10, where $C_{7,9}^{\rm NP}$ is the shift to the SM Wilson Coefficients. In both cases, the sensitivity to the weak phases becomes prominent near the resonances, in the same way as the CP-averaged observables. Nevertheless, in the NP case shown by Fig 3.9 the CP violating effects are dramatically enhanced in comparison to the NP case shown by Fig 3.10. This suggests that hadronic contributions can probe CP violating effects at a level that is dependant on the structure of NP. Moreover, it can provide a sensitivity to the imaginary parts of the Wilson Coefficient C_9. However, it should be mentioned that the sensitivity to the imaginary part of the Wilson Coefficients is best understood by alternative analyses. For instance, for C_9 a time dependant analyses such as $B_s \to J/\psi\phi$ or $B^0 \to K^{*0}\mu^+\mu^-$ with $K^{*0} \to K_s^0\pi^0$, and for C_7, $B \to K^*\gamma$ decays are essential. Nonetheless, it is interesting to understand the profound ability the hadronic contributions have to modify the CP-odd observables.

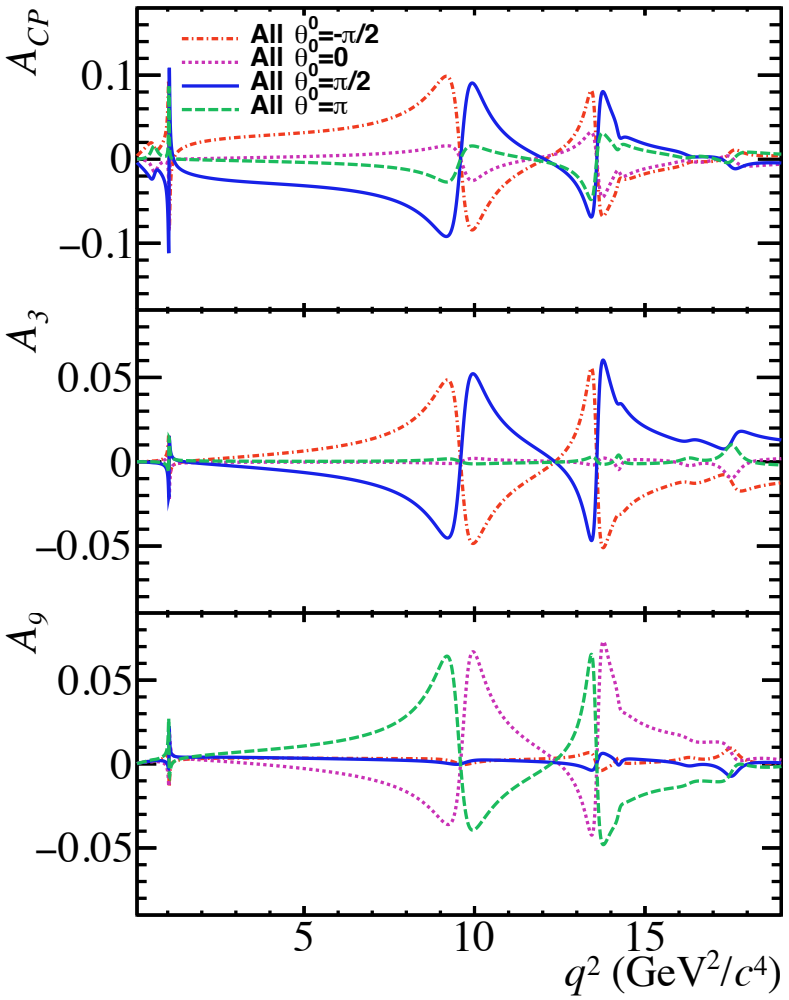

Figure 3.9: The distributions of the observables A_{CP}, $A_{3,9}$ as a function of q^2 produced using the model described in Section 3.1. The observables are constructed under the new physics model with $C_9^{\rm NP}$= -1 -1.0i. The distributions have been produced for specific choices of the free phase θ_j^0 where the free phase for all resonances has been set to $-\pi/2$ (red, dashed-dotted line), 0 (magenta, dotted line), $\pi/2$ (solid, blue line) and π (green, dashed line).

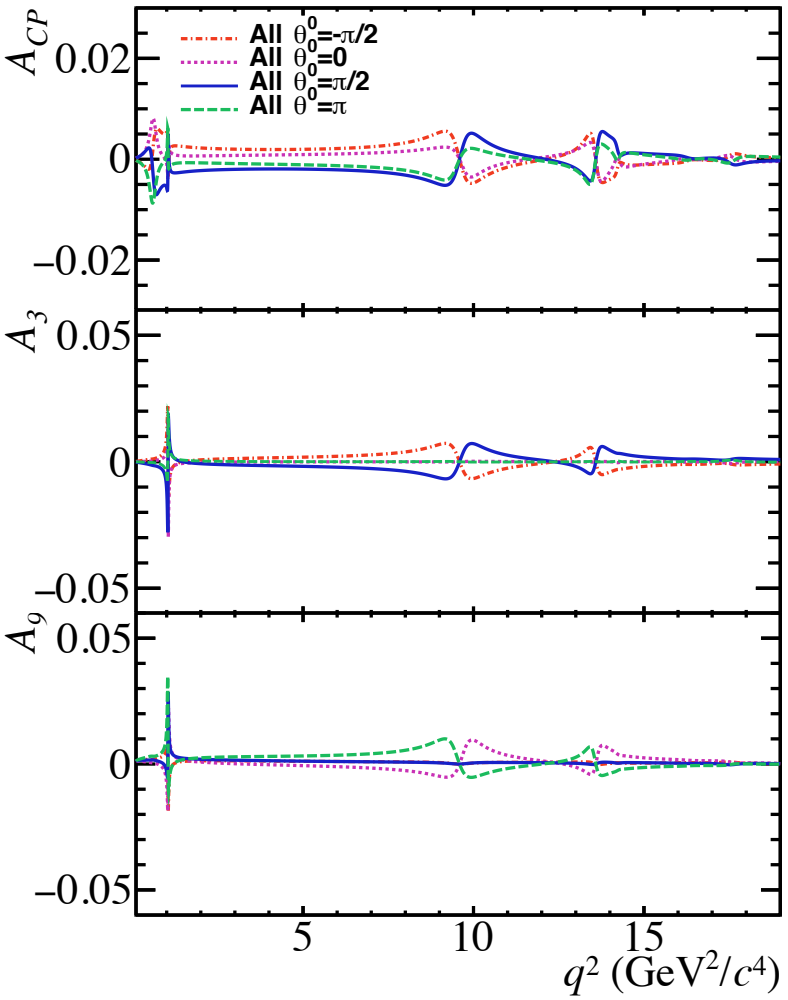

Figure 3.10: The distributions of the observables A_{CP}, $A_{3,9}$ as a function of q^2 produced using the model described in Section 3.1. The observables are constructed under the new physics models that has $C_7^{\rm NP}$= -0.03i ,$C_9^{\rm NP}$ =-1.0. The distributions have been produced for specific choices of the free phase θ_j^0 where the free phase for all resonances has been set to $-\pi/2$ (red, dashed-dotted line), 0 (magenta, dotted line), $\pi/2$ (solid, blue line) and π (green, dashed line).

3.4 Hadronic effects in tests of lepton universality

While this analysis focuses on one anomalous $b \to s\ell^+\ell^-$ result, this section briefly discusses the way in which our model can be used to help understanding the anomalous results seen in lepton universality tests. Lepton flavour universality assumes the coupling of leptons (e, μ, τ) to gauge bosons is independent of the lepton flavour. To test this assumption ratios, R, of branching fractions are constructed, where the only difference is the leptons in the final state. The exact form of the ratios R_K and R_{K^*} is given by Equation 3.11.

$$R_{K^{(*)}} = \frac{\int_{q^2_{min}}^{q^2_{max}} \frac{d\Gamma(B \to K^{(*)}\mu^+\mu^-)}{dq^2} dq^2}{\int_{q^2_{min}}^{q^2_{max}} \frac{d\Gamma(B \to K^{(*)}e^+e^-)}{dq^2} dq^2} \tag{3.11}$$

Given that these tests reveal possible NP contributions entering the Wilson Coefficient C_9 [33, 34, 88, 89], it is important to understand exactly the contribution from non-local charm loops in the presence of NP. This is because the cancellations of hadronic uncertainties that one obtains from the ratios R, are no longer exact. The model in Section 3.1 can provide an accurate determination of the non-local charm loop, where the only missing component is the free phase that will be determined by a fit to the experimental data. This model is used to provide a prediction of the ratios, taking into account any dependence on the free phase θ^0_j. This study was performed by taking different scenarios of $C_9^{\rm NP}$ between -2 and -0.5. All resonant contributions were included in this study. Moreover, all possible values of the free phase were considered to produce a 68% confidence interval for R_{K^*}. In regards to R_K, the values in Ref [45] were used and the confidence interval was determined by assuming that the hadronic parameters were uncorrelated. It was found that the form factor variation was much less than the variation of the phase. Figure 3.11 illustrates the results for R_{K^*} in different NP scenarios. The results are given in Table 3.3. Both Table 3.3 and Figure 3.11 show how as $C_9^{\rm NP}$ gets smaller, the deviations of R_{K^*} from unity increase. Figure 3.11 shows how at lower values of $C_9^{\rm NP}$ there is more variation in the free phase. However, it is clear

Observable	$C_{9\,\mu}^{\rm NP} = -0.5$	$C_{9\,\mu}^{\rm NP} = -1.0$	$C_{9\,\mu}^{\rm NP} = -1.5$	$C_{9\,\mu}^{\rm NP} = -2.0$
	$1.1 < q^2 < 6.0$ GeV$^2/c^4$			
R_{K^*}	$[0.902, 0.912]$	$[0.827, 0.850]$	$[0.769, 0.808]$	$[0.727, 0.784]$
R_K	$[0.888, 0.889]$	$[0.792, 0.794]$	$[0.712, 0.718]$	$[0.651, 0.658]$
	$15 < q^2 < 19$ GeV$^2/c^4$			
R_{K^*}	$[0.889, 0.894]$	$[0.796, 0.806]$	$[0.719, 0.735]$	$[0.658, 0.680]$
R_K	$[0.888, 0.889]$	$[0.792, 0.794]$	$[0.712, 0.718]$	$[0.651, 0.658]$

Table 3.3: Predictions for the lepton flavour universality observables $R_{K^{(*)}}$ as a function of $C_9^{\rm NP}$. The values for $R_{K^{(*)}}$ are shown for both large and small recoil. The prediction for R_{K^*} is obtained using the model described in Sec 3.1 where all possible values for the free phase θ_j^0 is considered. For R_K the prediction is obtained from using the results of measurement of short- and long-distance contributions in $B^+ \to K^+\mu^+\mu^-$ decays [45].

in Figure 3.11 that R_{K^*} is showing a larger variation in the phase compared to R_K. Nevertheless, in Ref [34] the variation for R_{K^*} is 6 times larger than the variation seen in Figure 3.11. This study shows the power of this model and how it can be utilised as an input to the work on other important anomalies that have been seen. To conclude, the model and the studies presented in this Chapter that have been performed using the model, have been published in a peer-reviewed journal (Ref [1]). Therefore validating the model, as an approach to determine the impact of the long distance contributions in $\bar{B}^0 \to \bar{K}^{*0}\mu^+\mu^-$ transitions.

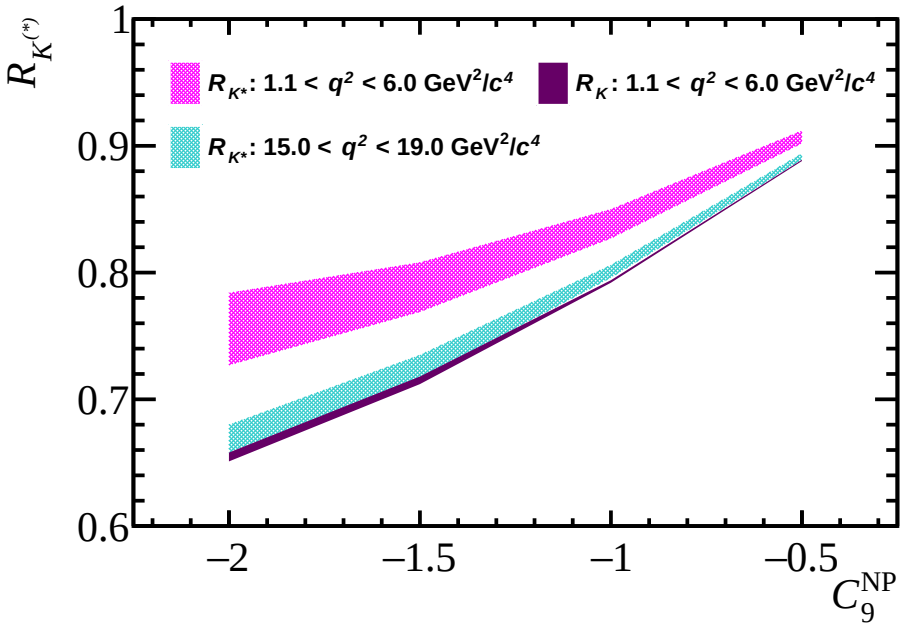

Figure 3.11: Predictions for the lepton flavour universality observables R_{K^*} as a function of $C_9^{\rm NP}$. The R_{K^*} is shown for both large recoil (hatched magenta) and small recoil (hatched cyan) while R_K is shown at only large recoil (solid burgundy) because at small recoil the R_K values are identical to those at large recoil. The predictions for R_{K^*} are obtained using the model described in Sec 3.1 where all possible values for the free phase θ_j^0 are considered. For R_K the prediction is obtained from using the results of the measurement of short- and long-distance contributions in $B^+ \to K^+\mu^+\mu^-$ decays [45].

Chapter 4

Analysis Strategy

The aim of this analysis is to determine the impact of the non-local contributions in $\bar{B}^0 \to \bar{K}^{*0}\mu^+\mu^-$, through performing a maximum likelihood fit to data collected by the LHCb experiment. The model presented in Chapter 3 will be used to perform such a fit in the 5 dimensions of cos θ_K, cos θ_ℓ, ϕ, $m_{K\pi\mu\mu}$ and q^2. This chapter is dedicated to presenting the strategy employed to prepare for such a fit. Section 4.2 describes the selection procedure used in this analysis to obtain samples rich in $\bar{B}^0 \to \bar{K}^{*0}\mu^+\mu^-$ events and low in background events. A strategy to model the background is presented in Section 4.4. Section 4.5 describes how experimental effects, such as the detector resolution and reconstruction efficiencies, are accounted for. The chapter concludes by discussing the S-wave component in the $K\pi$ system that can enter $\bar{B}^0 \to \bar{K}^{*0}\mu^+\mu^-$ transitions and how it is accounted for in this analysis.

4.1 Data samples

The analysis presented in this thesis makes use of the $p\bar{p}$ data collected by the LHCb experiment in two different data taking periods. The total dataset contains Run 1 data that was collected in 2011 and 2012, and Run 2 data that was collected in 2016. The sample size of the Run 1 dataset includes 1fb $^{-1}$ of integrated luminosity that was acquired in 2011 at a centre of mass ($\sqrt{s}$) of 7 TeV, and 2 fb $^{-1}$ of integrated luminosity

acquired in 2012 at $\sqrt{s} = 8$ TeV. The Run 2 dataset comprises only 1.67 fb $^{-1}$ integrated luminosity collected in 2016 at $\sqrt{s} = 13$ TeV. As a result, any mention of Run 2 in this thesis refers to only 2016 data. Given the datasets were taken in two different running periods, the selection criteria and experimental effect are treated separately for Run 1 and Run 2, which is demonstrated later in this chapter.

4.2 Selection of $\bar{B}^0 \to \bar{K}^{*0}\mu^+\mu^-$ decays

This section describes the selection procedure used in this analysis to identify $\bar{B}^0 \to \bar{K}^{*0}\mu^+\mu^-$ candidates. The complete selection procedure can be divided into four sections; trigger and stripping, preselection, treatment of specific background processes, and a multivariate selection. Each section forms a fundamental component of the processing of the data. The procedure begins with the trigger. A description of the full trigger system for the LHCb detector is given in Chapter 2. Therefore, in Section 4.2.1 only the specific trigger requirements for the $\bar{B}^0 \to \bar{K}^{*0}\mu^+\mu^-$ angular analysis are described. After the trigger, the data is "stripped" through various criteria that aim at reducing the overall size of the dataset while maintaining a significant fraction of the signal processes. Following on from the stripping the data is then passed through a preselection stage. The aim of the preselection stage is to further reduce the size of the dataset by removing combinatorial background events, where combinatorial background events are events that have one or more of the particles in the decay, "combined" with random particles from other b- and c-decays to form a candidate that mimics the true signal candidate. These decays are referred to as combinatorial background events which are either combinatorial $\mu\mu$ events or combinatorial $K\pi$ events. The preselection, despite its effectiveness in reducing combinatorial backgrounds, cannot reduce specific background processes. A special treatment must be then applied to these backgrounds, alternatively known as "peaking backgrounds" and is described in Section 4.2.3. The last stage of the selection of $\bar{B}^0 \to \bar{K}^{*0}\mu^+\mu^-$ events is to apply a multivariate analysis (MVA) selection. The MVA uses a classifier which is trained on data until it can distinguish between signal and background events, and therefore further reduces contributions from combinatorial backgrounds that might be remaining after the preselection stage.

4.2.1 Trigger and Stripping requirements

The triggers and the trigger requirements in the Run 1 and Run 2 data taking periods were slightly different. These differences were in both the hardware (L0 trigger) and software triggers (HLT1, HLT2). A complete list of the triggers for the data taking periods is given in Table 4.1 and the criteria for these trigger is given in Appendix C. For the hardware trigger in Run 1 only `L0Muon` was used, whereas for Run 2, either `L0Muon` or `L0DiMuon` could be used. `L0DiMuon` as briefly mentioned in Chapter 2, selects pairs of muons with a given transverse momentum. Other changes were to the software triggers. `Hlt1TrackAllL0` is a trigger line that triggers on all tracks that pass `L0`. This trigger line was used only in Run 1. In Run 2 the trigger line `Hlt1TrackMVA` and `Hlt1TwoTrackMVA` were used. These trigger lines use a MVA approach to select either a single track (`Hlt1TrackMVA`) or two tracks (`Hlt1TwoTrackMVA`) that have passed all prior hardware triggers. Moreover, the `Hlt2DiMuonDetached` line was used to select low mass dimuon events through applying different criteria. This trigger line was only applied for Run 1, and was decommissioned for Run 2, due to an interval bug. For all the triggers mentioned, the intrinsic information goes beyond the scope of this thesis and is therefore omitted. Moreover, in both data taking periods various topological triggers are used. These are the triggers, `Hlt2Topo[2,3,4]BodyBBDT`, `Hlt2TopoMu[2,3,4]BodyBBDT`, `Hlt2Topo[2,3,4]Bo` and `Hlt2TopoMu[2,3,4]Body`. More information on the topological triggers can be found in Chapter 2.

The trigger efficiencies for both Run 1 and 2016 data are given by Table 4.2. In this table there are two efficiencies for 2016 data, that are dependant on whether the `L0Muon` or `L0DiMuonn` trigger lines have been applied given that either one of these is used (see Table 4.1). The trigger efficiencies for both Run 1 and 2016 data that both use `L0Muon` are consistent. There is a slight difference when the `L0DiMuon` trigger is used, where the efficiency increases, this is because the number of muons is matched and so fewer background events with only a single muon enter into the data samples. As mentioned previously, after the trigger, the data is stripped where various selection criteria are applied. The stripping is applied using a dedicated stripping version and line. The lines are generally constant over the data taking periods. Instead, it is normally the version

Dataset	Stage	Triggers
Run 1	L0	L0Muon
	HLT 1	Hlt1TrackAllL0 or Hlt1TrackMuon
	HLT 2	Hlt2Topo[2,3,4]BodyBBDT, Hlt2TopoMu[2,3,4]BodyBBDT, Hlt2SingleMuon or, Hlt2DiMuonDetached
2016	L0	L0Muon or L0DiMuon
	HLT 1	Hlt1TrackMVA, Hlt1TwoTrackMVA or
	HLT 2	Hlt2Topo[2,3,4]Body, Hlt2TopoMu[2,3,4]Body or Hlt2SingleMuon

Table 4.1: List of the triggers applied at different stages for both Run 1 (2011, 2012) and Run 2 (2016) data. The criteria for these trigger is given in Appendix C.

Run	Trigger efficiency	
1		78.2%
2 (2016)	`L0Muon`	76.64%
	`L0DiMuon`	80.00%

Table 4.2: The trigger efficiencies for both Run 1 and 2016 data

of the stripping that changes per data taking period. Table 4.3 shows the stripping requirements for Run 1 and Table 4.4 shows the stripping requirements for Run 2. In both these tables, all the reconstructed particles in the decay $\bar{B}^0 \to \bar{K}^{*0}\mu^+\mu^-$ have specific stripping selections. Moreover, requirements on the tracks and the number of hits in the SPD are given. For both Run 1 and Run 2, many of the selection criteria remain identical, such as the requirements for the B meson and the dimuon pair ($\mu^+\mu^-$). The cuts on the DIRA angle (the direction angle of the B) and the IPχ^2 (the difference in χ^2 by including a track to a vertex) were the same over both data taking periods. Another parameter that remained constant was the DLL$_{\mu\pi}$. This parameter defined in Chapter 2 was required to be > -3. Moreover, the SPD multiplicity, defined as number of hits in the SPD had the same cut (<600) for both data taking periods. Several other selections were changed in the stripping for Run 2 data (see Table 4.4). For the K^{*0} the

Candidate	Selection
B	vertex χ^2/ndf <8
B	flight distance χ^2 >121
B	DIRA angle <14mrad
B	4800 MeV/c^2 < M < 7200 MeV/c^2
B	IP χ^2 < 16
$\mu^+\mu^-$	vertex χ^2/ndf <9
$\mu^+\mu^-$	$m(\mu^+\mu^-)$ < 7100MeV/c^2
K^{*0}	vertex χ^2/ndf <9
K^{*0}	$m(K^+\pi^-)$ <6200MeV/c^2
K^{*0}	flight distance χ^2 >9
tracks	min IP χ^2 >9
tracks	ghost probability <0.4
muon	IsMuon
muon	DLL$_{\mu\pi}$ > -3
GEC	SPD Multipicity < 600

Table 4.3: Stripping requirements for Run 1 data.

cut on the flight distance χ^2 was increased from 9 to 16. The flight distance was defined in Chapter 2, and the flight distance χ^2 is defined as the change in χ^2 from changing two vertices to a single vertex. The cut on the K^{*0} vertex χ^2 was also changed for Run 2, where it was increased to >9. Moreover, the ghost probability is the probability of having a track that is formed from hits that are not associated to a given particle. The cut on the ghost probability was changed from 0.4 (Stripping v20, v20r1) to 0.5 (Stripping v8r1). These changes are solely influenced by the conditions the data was taken with and have been taken into account throughout the processing of the data, such that the end result is not affected.

To conclude, the stripping retention rates for both Run 1 and 2016 data are given in Table 4.5. The retention rate is defined as the efficiency of the stripping line at selecting signal events. In Table 4.5, it shows that the stripping retention rates are the same for both running periods, which means the stripping efficiency was the same for both Run 1 and 2016 data.

Candidate	Selection
B	vertex χ^2/ndf <8
B	flight distance χ^2 >121
B	DIRA angle <14mrad
B	4800 MeV/c^2 < M < 7200 MeV/c^2
B	IP χ^2 < 16
$\mu^+\mu^-$	vertex χ^2/ndf <9
$\mu^+\mu^-$	$m(\mu^+\mu^-)$ < 7100MeV/c^2
K^{*0}	vertex χ^2/ndf <8
K^{*0}	$m(K^+\pi^-)$ <6200MeV/c^2
K^{*0}	flight distance χ^2 >16
K^{*0}	min IP χ^2 >0
tracks	ghost probability <0.5
muon	IsMuon
muon	DLL$_{\mu\pi}$ > -3
muon	min IP χ^2 >9
hadron	min IP χ^2 >6
GEC	SPD Multipicity < 600

Table 4.4: Stripping requirements for the 2016 data.

Run	Retention rate
1	0.167
2 (2016)	0.167

Table 4.5: The stripping retention rate for both Run 1 and 2016 data

4.2.2 Preselection criteria

Following on from the trigger and the stripping is the second step of the selection procedure; the preselection. The preselection as mentioned previously, is a procedure that applies various cuts and criteria to dramatically reduce the combinatorial background. In the analysis, the combinatorial background can enter by replacing any of the tracks for the four bodies in the decay $\bar{B}^0 \to \bar{K}^{*0}\mu^+\mu^-$ decay, with a random track from the rest of the event. Table 4.6 illustrates the preselection criteria applied to the data in this analysis. The preselection is the same for both Run 1 and Run 2 data. Moreover, it is the same preselection as used by the previous $\bar{B}^0 \to \bar{K}^{*0}\mu^+\mu^-$ analysis [4]. For the coordinate of the primary vertex in both the x (PV_x) and y (PV_y) direction, the mean value is less than 5 mm. Whereas, the coordinate in the z direction, (PV_y) is increased as a consequence of the beam having length in z. Moreover, a requirement is imposed on the angle measured relative to the beampipe for a given particle's track, such that the track is within the angular acceptance of the LHCb detector. Other requirements on the tracks, are that pairs of tracks must have opening angles, $\theta_{open} < 1$ mrad, so more of the particles in the decay move in the forward direction and do not leave the detector. The remaining preselection requirements are on the individual daughter particles in the $\bar{B}^0 \to \bar{K}^{*0}\mu^+\mu^-$ decay. For the hadrons, K and π both must have passed through the RICH system. Loose PID criteria are placed on the π and the K, requiring that $\mathrm{DLL}_{K\pi}$ >-5 for the K, and $\mathrm{DLL}_{K\pi} < 25$ for the π. The last requirement is on the dimuons, and is that each muon must be identified as a muon. All these preselection requirements are applied to each dataset used in this analysis in order to greatly reduce

Candidate	Selection
PV_x	$\mid x - \langle x \rangle \mid$ <5 mm
PV_y	$\mid y - \langle y \rangle \mid$ <5 mm
PV_z	$\mid z - \langle z \rangle \mid$ <200 mm
Track	0< θ < 400 mrad
Pairs of tracks (θ_{open})	$\theta_{open} > 1$ mrad
K	$\mathrm{DLL}_{K\pi}$ > -5
π	$\mathrm{DLL}_{K\pi} < 25$

Table 4.6: Preselection criteria for both Run 1 and Run 2 data used in this analysis.

Run	Efficiencies
1	14.02%
2 (2016)	11.51%

Table 4.7: The preselection efficiencies for both Run 1 and 2016 data

the combinatorial background. The efficiencies for the preselection for both Run 1 and 2016 data are given by Table 4.7.

4.2.3 Treatment of specific background processes

Despite best efforts in both the trigger and preselection, there are a subset of background processes that pass the criteria and still remain in the data samples after these two stages. These specific background processes are also known as peaking backgrounds, as they appear to "peak" in the $K^+\pi^-\mu^+\mu^-$ invariant mass ($m_{K\pi\mu\mu}$) distribution. A peaking background can be formed by: misidentifying one or more particles of a particular decay; swapping the particle hypotheses of two particles in the signal decay; or associating a particle from the rest of the event, with a particular decay such that the combined state mimics the signal process. These all give rise to different $m_{K\pi\mu\mu}$ distributions that can overlap with the signal region. The decay $\bar{B}^0 \to \bar{K}^{*0}(K^-\pi^+)\mu^+\mu^-$ as mentioned previously is a 4-body decay that contains a combination of leptons and hadrons in the final state. With a variety of decay products, there are a wide range of peaking backgrounds that can affect $\bar{B}^0 \to \bar{K}^{*0}\mu^+\mu^-$ candidates.

The first peaking background addressed comes from the decay $B_s^0 \to \phi\mu^+\mu^-$, with $\phi \to K^+K^-$. The way this decay can mimic a $\bar{B}^0 \to \bar{K}^{*0}\mu^+\mu^-$ event is by the K^- in $B_s^0 \to \phi(\to K^+K^-)\mu^+\mu^-$ being misidentified as a π^-. The π^- is lighter than the K^-, where the pion mass is 140 MeV/c^2, compared to the kaon mass of 494 MeV/c^2. Since the B_s^0, with a mass of 5366.88 MeV [77] is greater than the B^0, with mass 5279.64 MeV [77], the peak will appear in the upper mass sideband of the B^0 mass spectrum. The $K\pi$ invariant mass is computed by recalculating the 4-vectors of the π under the assumption that it has a kaon mass. To reject these events a cut is applied that removes events if,

$$m_B \in [5321, 5411]\text{MeV}/c^2 \tag{4.1}$$

and a cut is applied that removes events if,

$$\begin{aligned} &m_{K(\pi\to K)} \in [1010, 1030]\text{MeV}/c^2 \text{ and } -10 < \text{DLL}_{K\pi}(\pi) < 10, \text{or} \\ &m_{K(\pi\to K)} \in [1030, 1075]\text{MeV}/c^2 \text{ and } \text{DLL}_{K\pi}(\pi) > 10 \end{aligned}$$

This rejection of $B_s^0 \to \phi\mu^+\mu^-$ candidates results in only 0.75% entering relative to the signal yield.

Another, peaking background associated with a B_s^0 decay is $\bar{B}_s^0 \to K^{*0}\mu^+\mu^-$. Similarly, this background will peak will appear in the upper mass sideband of the B^0 mass spectrum because of the larger B_s^0 mass. However, unlike $B_s^0 \to \phi\mu^+\mu^-$, $\bar{B}_s^0 \to K^{*0}\mu^+\mu^-$ is a $b \to d$ transition, which means it is heavily suppressed in comparison to $b \to s$ transitions, such as $\bar{B}^0 \to \bar{K}^{*0}\mu^+\mu^-$. The ratio of $b \to d$ transitions to $b \to s$ is directly proportional to the ratio of CKM matrix elements,

$$\left|\frac{V_{td}}{V_{ts}}\right|^2 \sim \frac{1}{22} \tag{4.2}$$

The ratio of CKM elements is a component in the calculating of the ratio of the branching fraction of $\bar{B}_s^0 \to K^{*0}\mu^+\mu^-$ compared to the branching fraction of $\bar{B}^0 \to \bar{K}^{*0}\mu^+\mu^-$. The branching fraction for $\bar{B}^0 \to \bar{K}^{*0}\mu^+\mu^-$ is 9.4×10^{-7} [77], and the branching fraction of $\bar{B}_s^0 \to K^{*0}\mu^+\mu^-$ is 2.9×10^{-8} [77]. Thus, the ratio of the branching fractions is,

$$\frac{\text{BF}(\bar{B}_s^0 \to K^{*0}\mu^+\mu^-)}{\text{BF}(\bar{B}^0 \to \bar{K}^{*0}\mu^+\mu^-)} = 0.031 \tag{4.3}$$

Given that the ratio of the rate of production of B_s^0 to B^0 is,

$$\frac{f_{B_s}}{f_{B^0}} = \frac{1}{4} \tag{4.4}$$

the suppression factor of $\bar{B}_s^0 \to K^{*0}\mu^+\mu^-$ to $\bar{B}^0 \to \bar{K}^{*0}\mu^+\mu^-$ is,

$$\frac{f_{B_s}}{f_{B^0}} \times \frac{\mathrm{BF}(\bar{B}_s^0 \to K^{*0}\mu^+\mu^-)}{\mathrm{BF}(\bar{B}^0 \to \bar{K}^{*0}\mu^+\mu^-)} = 0.0077 \tag{4.5}$$

The application of these cuts results in the $\bar{B}_s^0 \to K^{*0}\mu^+\mu^-$ contributing only 0.77% of the selected events. The decay $\bar{B}_s^0 \to K^{*0}\mu^+\mu^-$ cannot be vetoed from this analysis as its final state is identical to $\bar{B}^0 \to \bar{K}^{*0}\mu^+\mu^-$. However, to deal with this issue, the 0.77% of $\bar{B}_s^0 \to K^{*0}\mu^+\mu^-$ events are later given weights through a multivariate technique, that is described in Section 4.2.4.

Potential background events, that peak in $m_{K\pi\mu\mu}$ can originate from $\Lambda_b \to pK^-\mu^+\mu^-$ decays. This background can occur through two scenarios. One is the misidentification of the of the proton as a pion ($p \to \pi$) and the other is the double misidentification of the proton as a kaon ($p \to K$), and the kaon as a pion ($K \to \pi$). In both cases the misidentification of particles cause the pK^- combination to appear as a K^{*0} state.To reject this peaking background a similar methodology that was used to reject $B_s^0 \to \phi\mu^+\mu^-$ candidates is used, where the invariant mass is calculated using the 4-momentum vectors. In the case where the p is mistaken for a π, the 4 momentum is calculated with m_π instead of m_p such that the invariant mass $m_{(p\to\pi)K\mu\mu}$ is calculated. For the other situation, where the p is mistaken for a K, and K is mistaken for a π, the 4 momentum the invariant mass, $m_{(p\to K)(K\to\pi)\mu\mu}$ is calculated assuming the proton is a kaon, and the kaon is a pion. Events are then rejected if the following criteria are satisfied,

$$m_{(p\to\pi)K\mu\mu} \in [5565, 5665]\mathrm{MeV}/c^2 \text{ and } \mathrm{DLL}_{p\pi} > 0, \text{ or}$$
$$m_{(p\to K)(K\to\pi)\mu\mu} \in [5565, 5665]\mathrm{MeV}/c^2 \text{ and } \mathrm{DLL}_{K\pi}(\pi) > 0$$

where, the invariant mass is within a given window in the upper mass sideband, and the DLL for both the π/p and K/π hypotheses are required to be greater than zero. The decays $B^0 \to J/\psi K^{*0}$, where $J/\psi \to \mu^+\mu^-$ and $B^0 \to \psi(2S)K^{*0}$, where $\psi(2S) \to \mu^+\mu^-$ form part of the signal contribution in this analysis, swaps of the particles in these decays can result in background events that peak in the invariant mass $m_{K\pi\mu\mu}$. This is achieved by either the $\pi-$ in the $K^+\pi^-$ state being misidentified as a μ^-, or the K^+ in the $K^+\pi^-$ state, being misidentified as a μ^+. To veto this background, various selection criteria is applied. The criteria are selected in a particular way to minimise the amount of signal loss in this analysis. The dimuon invariant mass is recomputed under both hypotheses; the invariant mass ($m_{(\pi\to\mu)\mu}$) assuming that the π^- is misidentified as a μ^-; and the invariant mass ($m_{(K\to\mu)\mu}$) assuming the K^+ has been mistaken for a μ^+. Once the invariant mass has been recomputed, the event is rejected if the mass lies within windows around the J/ψ or $\psi(2S)$ pole masses. Other requirements are also imposed on whether the muon has been identified as a muon, and the $\mathrm{DLL}_{\mu\pi}$, to reject background events from $B^0 \to J/\psi K^{*0}$ decays. Events are rejected if,

$$\begin{aligned} m_{(\pi\to\mu)\mu} \in [3036, 3156]\mathrm{MeV}/c^2 \text{ and} \\ \mathrm{DLL}_{\mu\pi}(\pi) > 5 \text{ or } \texttt{isMuon}(\pi) \end{aligned} \tag{4.6}$$

and,

$$\begin{aligned} m_{(K\to\mu)\mu} \in [3036, 3156]\mathrm{MeV}/c^2 \text{ and} \\ \mathrm{DLL}_{\mu\pi}(K) > 5 \text{ or } \texttt{isMuon}(K) \end{aligned} \tag{4.7}$$

Similarly, to reject background from $B^0 \to \psi(2S)K^{*0}$ decays, events are rejected if,

$$\begin{aligned} m_{(\pi\to\mu)\mu} \in [3626, 3746]\text{MeV}/c^2 \text{ and} \\ \text{DLL}_{\mu\pi}(\pi) > 5 \text{ or } \texttt{isMuon}(\pi) \end{aligned} \tag{4.8}$$

and,

$$\begin{aligned} m_{(K\to\mu)\mu} \in [3626, 3746]\text{MeV}/c^2 \text{ and} \\ \text{DLL}_{\mu\pi}(K) > 5 \text{ or } \texttt{isMuon}(K) \end{aligned} \tag{4.9}$$

Equally important are the background events caused by the double misidentification of the K as a π, and the π as a K in the signal decay $B^0 \to K^{*0} \to (K^+\pi^-)\mu^+\mu^-$. Events formed from this double misid can be easily vetoed by placing requirements on the behaviour of the K and π through the $\text{DLL}_{K\pi}$ parameter, where

$$\text{DLL}_{K\pi}(K) > \text{DLL}_{K\pi}(\pi) \tag{4.10}$$

In addition, a background from $B^+ \to K^+\mu^+\mu^-$ decays is present when a random π^- in the detector combines with the K^+ in the $B^+ \to K^+\mu^+\mu^-$ decay, such that the final state appears as $K^+\pi^-\mu^+\mu^-$, thus mimicking the final state of the $B^0 \to K^{*0}\mu^+\mu^-$ decay. As a pion is added to this decay, the effect will be a peak in the upper mass sideband of the $B^0 \to K^{*0}\mu^+\mu^-$ decay. A hard veto is applied to directly remove all possible candidates. The veto is defined as follows,

$$m_{K\pi\mu\mu} > 5380\text{MeV}/c^2 \text{ and } m_{K\mu\mu} \in [5220, 5340]\text{MeV}/c^2 \tag{4.11}$$

Despite the $B^+ \to K^+\mu^+\mu^-$ veto having a positive effect on reducing the $B^+ \to K^+\mu^+\mu^-$ candidates in this analysis, it has effect of sculpting the angular distribution of the background in a non-trivial manner. Studies of this veto and its effect are presented in Section 4.4.2.

The final background discussed is from $B^0 \to \rho(\to \pi\pi)\mu^+\mu^+$ decays. These events enter the background if one of the pions is mistaken for a kaon. Nonetheless, $B^0 \to \rho(\to$

$\pi\pi)\mu^+\mu^+$ is a $b \to d$ transition, instead of a $b \to s$ transition, and therefore is suppressed by the ratio of CKM matrix elements,

$$\left|\frac{V_{td}}{V_{ts}}\right|^2 \sim 0.21 \tag{4.12}$$

This decay is further suppressed by the ratio of the number of $B^0 \to \rho(\to \pi\pi)\mu^+\mu^+$ decays to the number of $\bar{B}^0 \to \bar{K}^{*0}\mu^+\mu^-$ that decay at LHCb. As a result, this decay is simply ignored, instead of implementing a specific veto. In the future, with more data from the LHCb detector with Run 3, this assumption might need to be assessed for its validity.

4.2.4 Multivariate analysis

The final step in the selection of $\bar{B}^0 \to \bar{K}^{*0}\mu^+\mu^-$ candidates is to perform a multivariate analysis. Multivariate analysis techniques are widely used in particle physics to classify events into signal or background, based on a selection of given variables. These techniques are successful as their foundation lies in training a classifier that discriminates between signal and background, learning the behaviour and characteristics of the events in the dataset along the way. In this analysis, a multivariate classifier in the form of a Boosted Decision Tree (BDT) [90, 91] is implemented to maximise the amount of signal and suppress any remaining background events that might enter from combinatorial and peaking backgrounds. The BDT is applied to an initial dataset, and used to classify events as either signal or background events, given criteria on a variables. $B^0 \to K^{*0}\mu^+\mu^-$ decays in the upper mass sideband region ($m_{K\pi\mu\mu} \in$[5350,7000] MeV/c^2), from data are used for the background, for the signal, $B^0 \to J/\psi K^{*0}$ decays in data, that have been weighted using the technique (*sPlot*) given in Ref [92] are used. In summary, the *sPlot* technique removes background events by deriving weights ($sWeights$) that are applied to the data, to obtain a pure sample of $B^0 \to J/\psi K^{*0}$ decays. The BDT is trained on both Run 1 and Run 2 data using a given set of variables. These variables are presented in Table 4.8. The variables shown in Table 4.8 were carefully selected, such that the BDT does not change the angular distributions of the signal significantly. The variables include the B^0 momentum, B^0 transverse momentum p_T, B^0 lifetime,

BDT variable
B^0 momentum
B^0 transverse momentum, p_T
B^0 lifetime
$K^+\pi^-\mu^+\mu^-$vertex χ^2
B^0 direction angle, (DIRA)
$\mathrm{DLL}_{K\pi}(K)$
$\mathrm{DLL}_{K\pi}(\pi)$
$\mathrm{DLL}_{\mu\pi}(\mu)$
muon isolation variables (Run 2 only)

Table 4.8: The BDT variables used in this analysis, for both Run 1 and Run 2 data.

direction of the B^0 direction angle, and the χ^2 of the final state particle ($K^+\pi^-\mu^+\mu^-$). The particle identification variables, $\mathrm{DLL}_{K\pi}(K)$, $\mathrm{DLL}_{K\pi}(\pi)$ and $\mathrm{DLL}_{\mu\pi}(\mu)$, also enter the BDT. The remaining variables that enter the BDT are the muon isolation variables for the two muons, that are used only for Run 2 data. The muon isolation variable is defined as the number of extra tracks that can form a vertex with a muon track [93]. These extra tracks are not tracks corresponding to the signal decay and therefore are background tracks. In the training of the BDT, the $k-folding$ technique is applied to maximise the performance of the classifier. The $k-folding$ technique involves taking the data samples, and dividing them into 10 separate subsets, each with the same number of entries. The BDT is trained on 9 of these subsets using the variables given in Table 4.8. The resulting BDT classifier is then evaluated on the remaining untrained sample. Once this is achieved, the process is repeated but with a different combination of the 9 subsets. i.e one of the previous trained subsets is removed and the subset used to train the BDT is put into the training. This means that the training dataset is different as the events are different and so a new BDT can be trained. One can play this game, 10 times corresponding to the total number of subsets, and resulting in 10 different BDT classifiers, where each classifier are allocated to its corresponding 10% sample of the data that has not been trained and is used for the performance checks. This technique is an essential and successful tool in the multivariate analysis used in this analysis.

4.2.4.1 Optimisation of the BDT

Candidate decays are selected by placing a cut that maximises the signal significance, defined as,

$$\xi = \frac{n_{\rm sig}}{\sqrt{n_{\rm sig} + n_{\rm nbkg}}} \tag{4.13}$$

In Equation 4.13, $n_{\rm sig}$ is the $\bar{B}^0 \to \bar{K}^{*0}\mu^+\mu^-$ signal yield, which is calculated as follows,

$$n_{\rm sig} = \sigma_{b\bar{b}} \times A \times \Gamma \times {\rm L} \times \frac{n_{\rm bdt}}{n_{\rm tot}} \tag{4.14}$$

where, $\sigma_{b\bar{b}}$ is the cross section for production of $b\bar{b}$ pairs at the LHC, Γ is the branching fraction for $\bar{B}^0 \to \bar{K}^{*0}\mu^+\mu^-$, L is the integrated luminosity, A is a constant which accounts for the fraction of final state particles in the $\bar{B}^0 \to \bar{K}^{*0}\mu^+\mu^-$ decay that are produced within the LHCb acceptance. The term, $n_{\rm bdt}$ is the number of weighted signal candidates, accounting for the corrections to the simulation, that pass the given BDT cut. These events correspond to $\bar{B}^0 \to \bar{K}^{*0}\mu^+\mu^-$ simulated decays in the region, $m_B \in$[5230, 5330] MeV/c^2 and in the $m_{K\pi}$ window of, 796$<$ $m_{K\pi}$ $<$996 MeV/c^2. Moreover, $n_{\rm tot}$ is the total number of decays simulated. The number of background events, $n_{\rm bkg}$, used in the calculation of the significance is estimated using $\bar{B}^0 \to \bar{K}^{*0}\mu^+\mu^-$ background decays passing the preselection, lying in the upper mass region, $m_B \in$[5700, 7000] MeV/c^2. The upper mass sideband is a good representation of the background as it is mostly background events with a very small amount of signal. This means by studying this region, we can determine an accurate parametrisation of the background. This region is fitted with an exponential function that is defined by a single parameter λ. This functional form then allows one to extrapolate the background yield down to the signal region. Figure 4.1 shows the fits to the upper mass sideband at a BDT cut value of 0.1 for both Run 1 (a) and Run 2 (b) for illustration.

Finally, the results for the BDT optimisation are given by Figure 4.2 for Run 1 and Run 2 data. Both subfigures of Figure 4.2 show the significance, ξ, as a function of

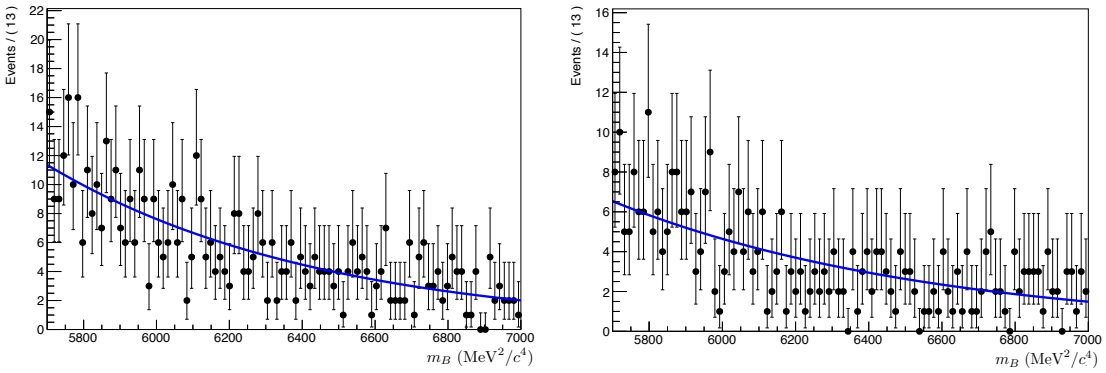

(a) Run 1 (b) Run 2

Figure 4.1: $B^0 \to K^{*0}\mu^+\mu^-$ data for both Run 1 and Run 2, in the upper mass sideband region of $m_B \in$[5700, 7000] MeV/c^2, with a BDT cut value of 0.1, each fitted with an exponential function.

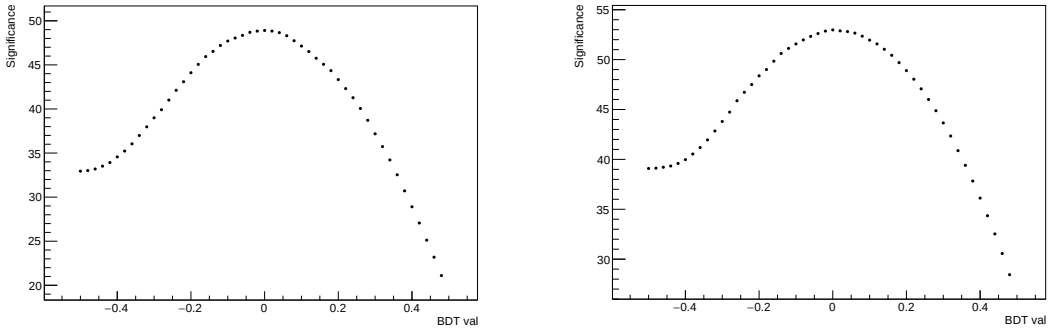

(a) Run 1 (b) Run 2

Figure 4.2: The significance ξ as a function of BDT cut value for Run 1 (a) and Run 2 (b) data.

BDT cut value. For the Run 1 distribution there is a clear peak at a BDT value of 0. The optimal BDT cut value is selected such that it is slightly to the right of this peak. The reason why the BDT is taken to be slightly to the right is so that we cut slightly higher to avoid any possible fluctuations that might have biased the peak. The resulting BDT cut value is chosen to be 0.1 and the significance at this value is 47.14. At this BDT cut value, the signal efficiency was found to be 77% and the background rejection efficiency was found to be 95%. Moving on to the Run 2 results, Figure 4.2 shows that the distribution of BDT values still peaks at 0. This means that the same optimal point of 0.1 seems appropriate for Run 2. At this cut value the significance is 51.95. At this BDT cut value the signal efficiency was found to be 87% and the background rejection

efficiency was found to be 97%. The results reveal that the optimal working points for both Run 1 and Run 2 are stable against uncertainties in the expected signal and background yields, by comparison of this BDT to that of the one used by the current nominal analysis and the results seen in the previous analysis in Ref [4].

4.2.5 Summary of the selection criteria

The selection procedure detailed in this section involved several steps to reduce the rate from background events arising from both combinatorial events and peaking background events, and to maximise the number of signal candidates for $\bar{B}^0 \to \bar{K}^{*0}\mu^+\mu^-$ decays. The final number of data events included in this analysis is given by Table 4.9. In Table 4.9, the number of events have been specified for the individual years of both Run 1 and Run 2. Moreover, the number of events are specified for the full m_{B^0} mass region used in this analysis (5100 MeV/c^2 < m_{B^0} < 5700 MeV/c^2) and the signal region (5239.58 MeV/c^2 < m_{B^0} < 5319.58 MeV/c^2). More information regarding the regions used in this analysis will be presented in detail in Section 4.15. The numbers in this table include a cut on $m_{K\pi}$ using a 100 MeV window around the nominal K^{*0} mass ($m_{K^{*0}}$ ∈[796,996] MeV/c^2). The motivation for this cut is explained in detail in Section 4.6. The total number of signal candidates used in this analysis, when combining Run 1 and 2016 data is 817,196. The total number of events used in this analysis across the whole m_{B^0} region (required for modelling backgrounds) is 1,141,783. With more data from 2017 and 2018 available in the future, and with Run 3 of the LHC, will increase the number of $\bar{B}^0 \to \bar{K}^{*0}\mu^+\mu^-$ candidates will increase. Nevertheless, the number of events is adequate for this analysis and the selection procedure has maximised the the efficiency.

		Number of events	
Run	Year	Signal region ($m_{B^0} \in [5239.58, 5318.58]$MeV/$c^2$)	Full region ($m_{B^0} \in [5100, 5700]$MeV/c^2)
1	2011	129,365	184,080
	2012	297,707	428,680
2	2016	390,124	529,023
Total		817,196	1,141,783

Table 4.9: The number of events used in the analysis for both Run 1 and 2016 data.

4.3 Accounting for differences between data and simulation

In this analysis, simulated events are used to determine the resolution function (see Section 4.5.1), deduce the angular acceptance and the corrections to this acceptance (see Section 4.5.2) and background contributions. With this in mind it is essential that the simulation reflects the data accurately. This section discusses how the differences between data and simulation are accounted for in this analysis. Section 4.3.1 presents the resampling of the particle identification variables, which is the first step of the procedure to correct the simulation. Once the PID variables have been resampled, a reweighting procedure is implemented. Distributions of the various kinematic variables from data are used to derive weights that are then applied to reweight the simulation samples. The reweighting procedure is described in Section 4.3.2.

4.3.1 PID resampling

The resampling procedure is a method that is applied to correct the particle identification (PID) variables using corrections derived from data. All simulated samples used in this analysis have the PID variables accounted for. The reason for this is that in the simulation, the PID variables are not reconstructed correctly, which poses an issue as the PID variables are used in both the BDT (See Section 4.2.4) and the rejection of specific peaking backgrounds (See Section 4.2.3). The resampling procedure begins by selecting large calibration samples rich in the particles we want to derive PID corrections for. In this analysis, the particles we want to correct the PID variables for are the K, π and μ. The calibration samples selected for these particles are $D^{*+} \to D^0(\to K^+\pi^-)\pi^+$ and $J/\psi \to \mu^+\mu^-$. The $D^{*+} \to D^0(\to K^+\pi^-)\pi^+$ is used to identify the π and the K. $J/\psi \to \mu^+\mu^-$ allows one to extract PID information about the muons. Once the calibration samples have been selected, each calibration sample is used to produce a 3D histogram binned in the number of long tracks (`nTracks`), pseudorapidity of the event, and transverse momentum of the track. For each track in the simulated sample, which has a given `nTracks`, η, and p_T, one looks at the 3D histogram from the calibration sample, and matches the `nTracks`, η, and p_T from the simulated sample

to the corresponding bin in the histogram. Once this bin has been selected, the PID variables are located in the calibration sample and a correction is derived from them. Figures 4.3 and 4.4 shows the PID variables for $B^0 \to J/\psi K^{*0}$ simulation that have both been resampled and reweighted following the procedures described in Sections 4.3.1 and 4.3.2. Explicitly, Figure 4.3 shows the resampled and reweighted PID variables for the Run 1 simulation and Figure 4.4 shows the resampled and reweighted PID variables for the Run 2 simulation. In these figures, the blue data points are $B^0 \to J/\psi K^{*0}$ simulated events that have been both resampled and reweighted. The black data points are *sWeighted* $B^0 \to J/\psi K^{*0}$ data events. To illustrate the effect of the PID resampling, $B^0 \to J/\psi K^{*0}$ simulated events that have only been reweighted and not PID resampled are included. These events are shown by the red data points. In these figures, the PID variables; $\mathrm{DLL}_{K\pi}(K)$ and $\mathrm{DLL}_{K\pi}(\pi)$ show a good agreement between the reweighted and resampled simulation and the sWeighted data. They also show that the simulation which is only reweighted, does not match the sWeighted data. This demonstrates the importance of resampling the PID variables. For the muon PID variables; $\mathrm{DLL}_{\mu\pi}(\mu^+)$ and $\mathrm{DLL}_{\mu\pi}(\mu^-)$, there appear to be some differences, which are also different for Run 1 and Run 2. The differences are believed to be caused by muons going outside the acceptance of the detector, and could be treated as a systematic uncertainty.

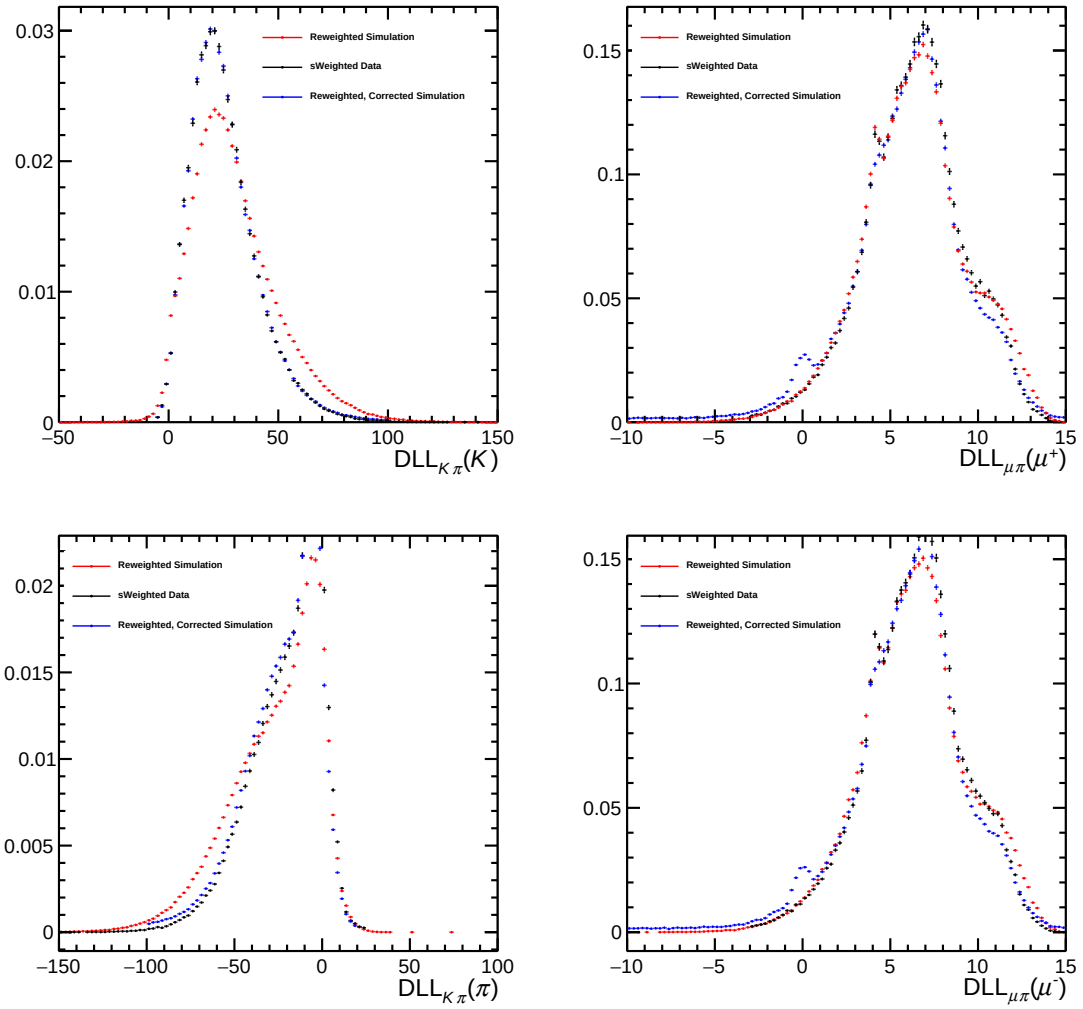

Figure 4.3: Distributions of the reweighted and resampled PID variables that enter the BDT for Run 1. The black points correspond to *sWeighted* $B^0 \to J/\psi K^{*0}$ data. The red points correspond to $B^0 \to J/\psi K^{*0}$ simulation that has been reweighted but not resampled. The blue data points refers to $B^0 \to J/\psi K^{*0}$ simulation that has been both reweighted and resampled, where the reweighting has been applied through the procedure given in Section 4.3.2.

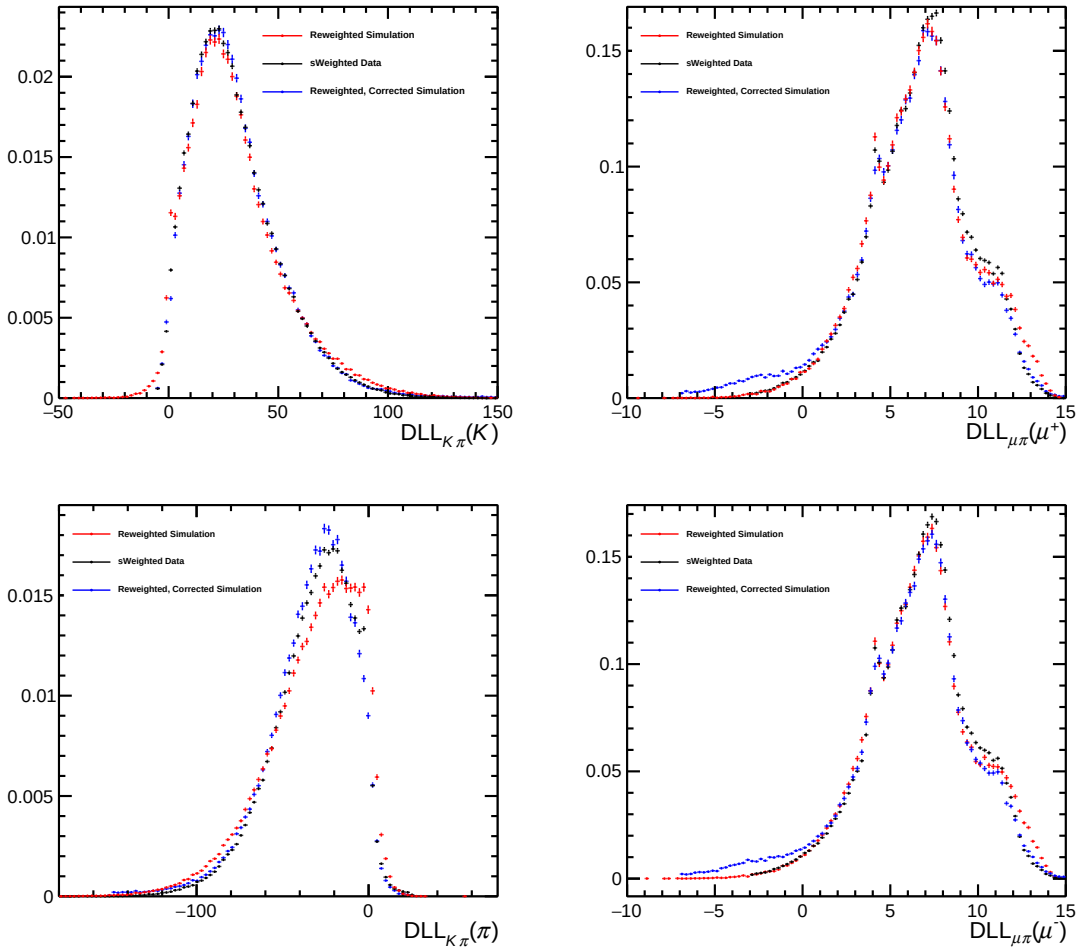

Figure 4.4: Distributions of the reweighted and resampled PID variables for Run 2. These variables also enter the BDT. The black points correspond to *sWeighted* $B^0 \to J/\psi K^{*0}$ data. The red points correspond to $B^0 \to J/\psi K^{*0}$ simulation that has been reweighted but not resampled. The blue data points refers to $B^0 \to J/\psi K^{*0}$ simulation that has been both reweighted and resampled, where the reweighting has been applied through the procedure given in Section 4.3.2.

4.3.2 Reweighting the simulation

A reweighting procedure is implemented that derives weights from $B^0 \to J/\psi K^{*0}$ decays in data to correct the simulation. This is to ensure that the BDT distribution and the variables that enter the BDT are correctly modelled in the simulation. The *sPlot* technique, which was mentioned earlier in Section 4.2.4 was applied to weight $B^0 \to J/\psi K^{*0}$ data, removing background contributions that come from combinatorial events and $\bar{B}^0_s \to J/\psi K^{*0}$ decays. Figure 4.5 shows the fits to the invariant mass ($m_{K\pi\mu\mu}$) in $B^0 \to J/\psi K^{*0}$ data for both Run 1 and Run 2. The solid blue line represents the total pdf, the magenta dashed line corresponds to $\bar{B}_s \to J/\psi K^{*0}$ events and the red dashed line represents the exponential used to model the background contributions. Once the data has had the *sPlot* technique applied, the data is used to derive weights based on correcting the B^0 transverse momentum, $p_T^{B^0}$, the χ^2_{Vtx} of the B^0, and the number of tracks. The weights are derived for the number of tracks first, then the $p_T^{B^0}$ and finally the χ^2_{Vtx} of the B^0. Once all weights have been derived they are applied to reweight the simulated samples. The result of the reweighting procedure is shown by the distributions of the BDT and the BDT variables, presented in both Figure 4.6 for Run 1 and Figures 4.7 and 4.8 for Run 2. It is clear that the agreement between data and simulation are good, from the figures. Especially for the BDF and the muon isolation variables, where for the latter a zoomed in plot has to be given to show the small differences (Figure 4.8).

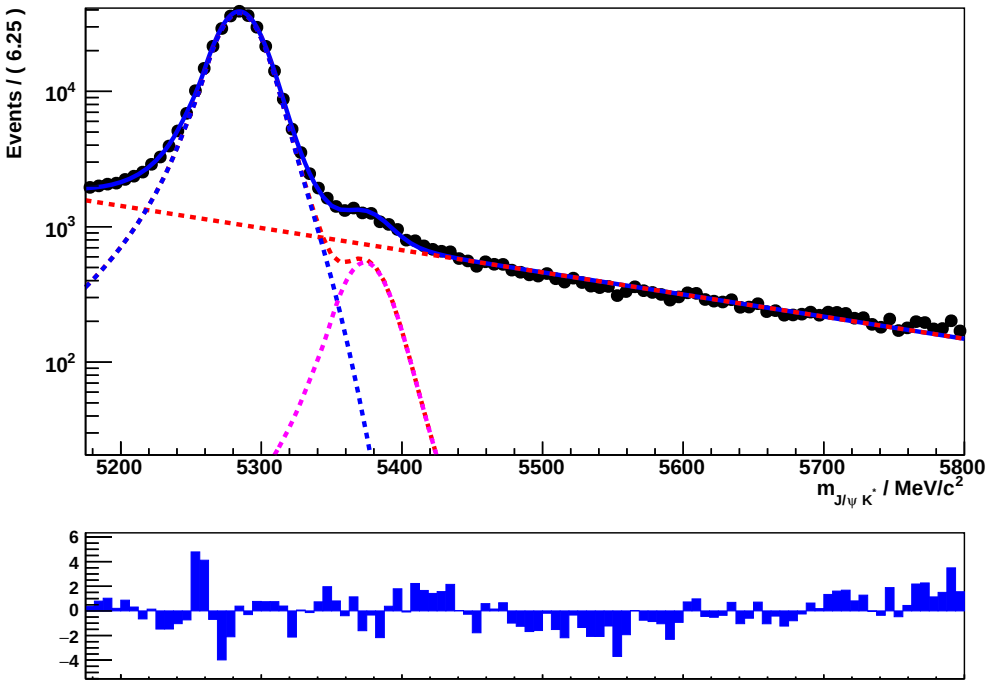

(a) Run 1

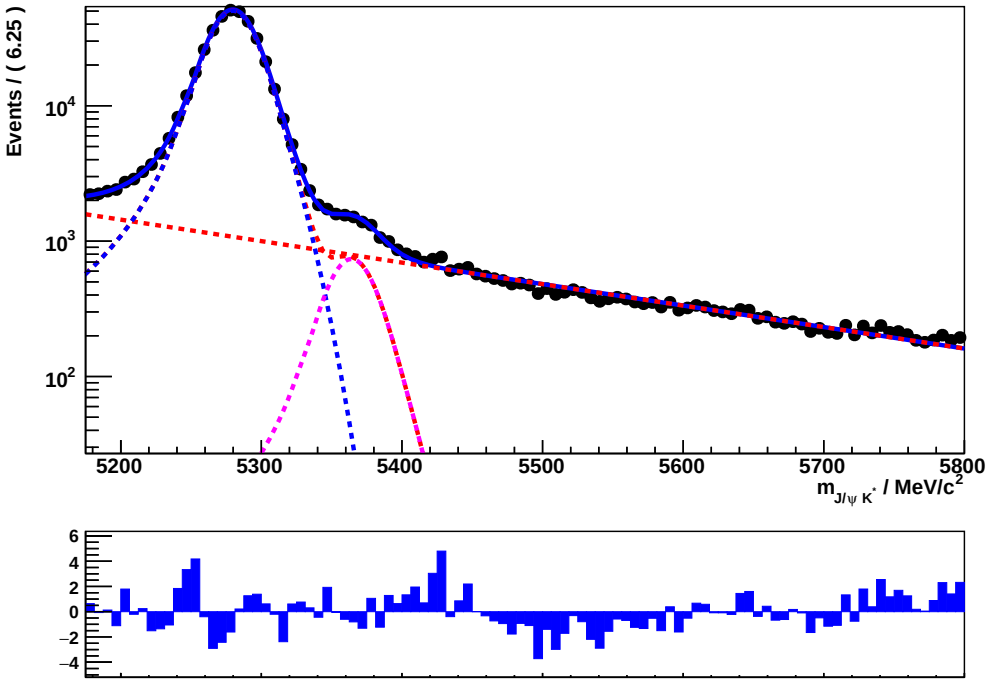

(b) Run 2

Figure 4.5: The fits to the invariant mass $m_{K\pi\mu\mu}$ in $B^0 \to J/\psi K^{*0}$ data for both Run 1 and Run 2. The solid blue line represents the total probability density function (pdf). The blue dashed line is the Crystal Ball function used to fit $\bar{B}^0 \to J/\psi K^{*0}$ events and the magenta dashed line corresponds to the Crystal Ball function used to fit $\bar{B}_s \to J/\psi K^{*0}$ events. The red dashed line represents the exponential used to model the background contributions.

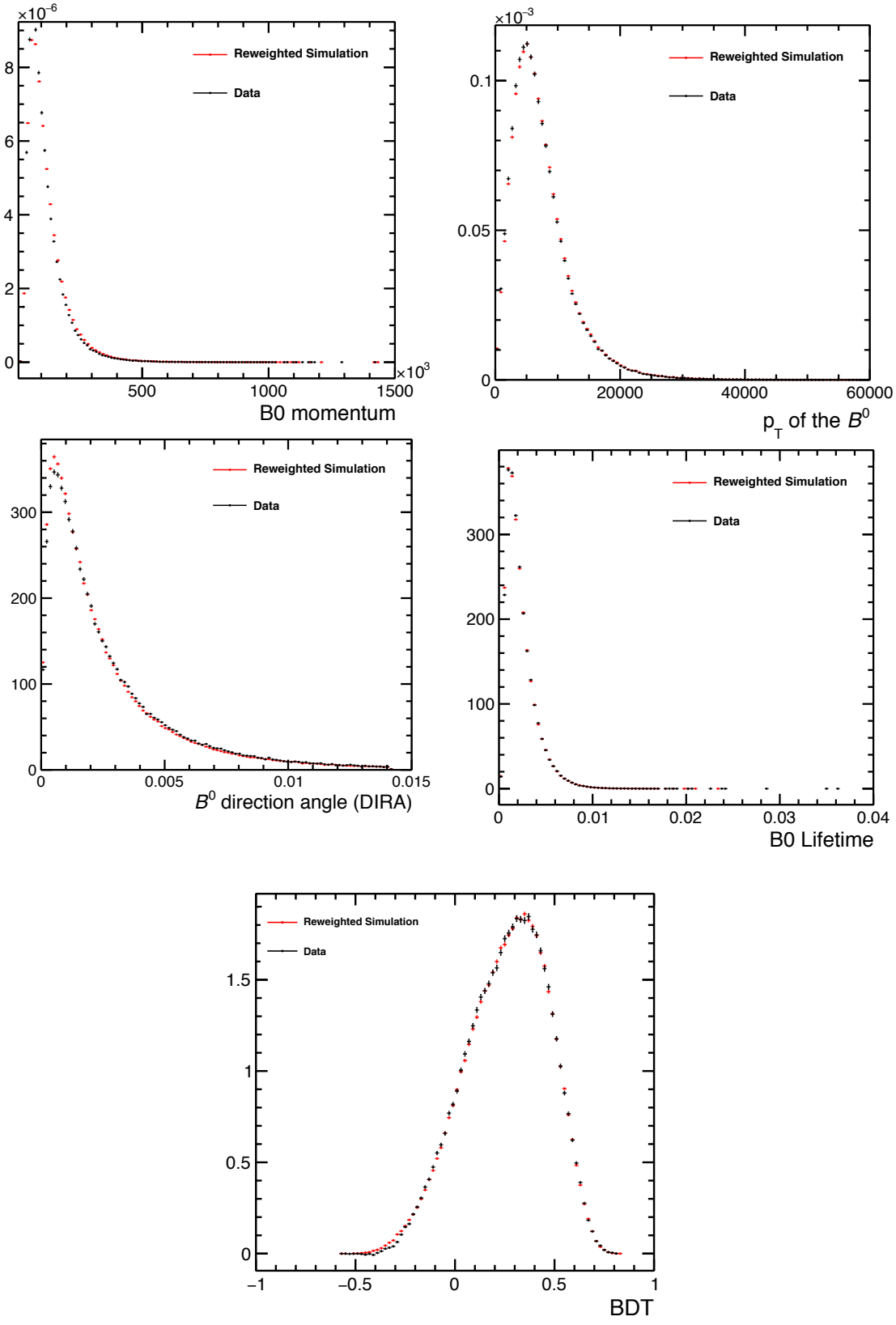

Figure 4.6: Distributions of the reweighted variables that enter the BDT for Run 1. The black points corresponds to *sWeighted* $B^0 \to J/\psi K^{*0}$ data and the red points correspond to reweighted $B^0 \to J/\psi K^{*0}$ simulation.

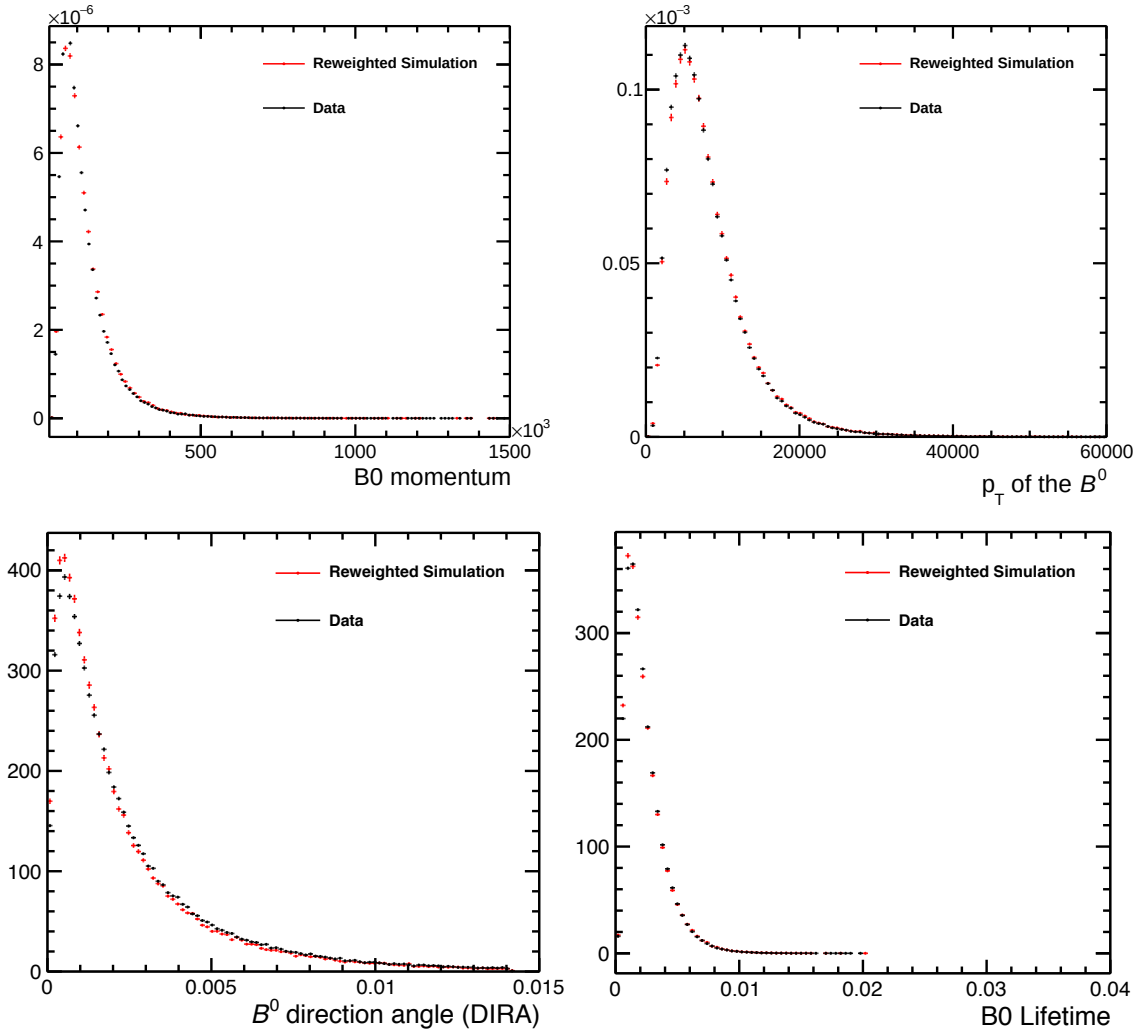

Figure 4.7: Distributions of the reweighted variables that enter the Boosted Decision Tree for Run 2. The black points corresponds to weighted $B^0 \to J/\psi K^{*0}$ data and the red points correspond to reweighted $B^0 \to J/\psi K^{*0}$ simulation.

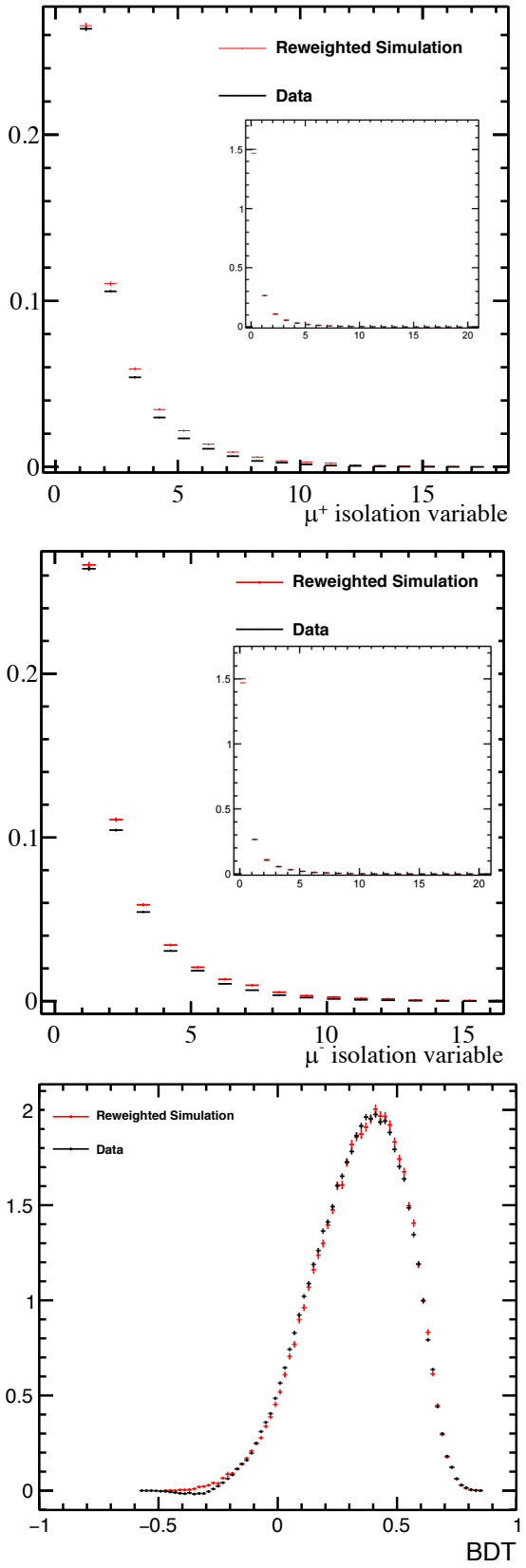

Figure 4.8: Distributions of the reweighted variables that enter the Boosted Decision Tree for Run 2. The black points corresponds to weighted $B^0 \to J/\psi K^{*0}$ data and the red points correspond to reweighted $B^0 \to J/\psi K^{*0}$ simulation. For the muon isolation variable distributions the plot is zoomed in, and the full distribution is shown as a subplot of the figure.

4.4 Modelling background contributions

In order, to measure the phase difference between short- and long-distance contributions in $B^0 \to K^{*0}\mu^+\mu^-$, a significant amount of effort has been put into reducing contributions from background processes. Nevertheless, despite the extensive efforts, there can be contributions from background processes that pass the selection and enter into the datasets used in this analysis. For these events a background model is implemented to describe the remaining background events in the signal region. This section is dedicated to presenting the background model that is implemented in this analysis.

4.4.1 The background model

This analysis uses a B^0 mass constraint. The consequence of this for the signal is that it improves the measurement of the q^2 resolution (see Section 4.5.1) precisely across the whole q^2 range and in the presence of multiple hadronic resonances that have varying resolutions in the regions they are located in. This constraint is implemented by taking every event and recalculating the momentum of all tracks in the event by fluctuating the measured momentum within the reported uncertainties until the total invariant mass of the $K\pi\mu\mu$ system ($m_{K\pi\mu\mu}$) is equal to the true B^0 mass (5279.58 MeV/c^2 [77]). The consequence of this is that for the signal it improved the measurement of the momentum and is useful for determining the resolution as any spread in the values is solely due to resolution effects. Nevertheless, this poses an issue for determining the backgrounds. Backgrounds events are often determined by using the upper mass sideband in the B^0 mass, where the upper mass sideband is rich in background events. However, by constraining the events to the true B^0 mass, we artificially remove the upper mass sideband. Therefore, to understand the backgrounds a different approach is taken. The approach taken is to define a narrow region around the true B^0 mass, which will be denoted the signal region. The signal region is chosen to be 80 MeV around the true B^0 mass ($m_B \in$[5239.58, 5319.58]) to maximise the number of signal candidates with relatively small amount of background events. The next step is then to understand the angular distribution of the background events in the signal region. This is achieved by

Definition of Region	m_B region (MeV/c^2)	Centre of region (MeV/c^2)
Background	[5130, 5210]	5170
Signal	[5239.58, 5319.58]	5279.58
Background	[5440, 5520]	5480
Background	[5520, 5600]	5560
Background	[5600, 5680]	5640
Background	[5680, 5760]	5720
Background	[5760, 5840]	5800

Table 4.10: Regions in m_B used in this analysis, that are defined as either signal or background regions.

opening up regions in the upper mass sideband of the unconstrained B^0 mass, where the widths of each region is set to be the same as the width of the signal region. Table 4.10 shows the regions in the upper mass sideband used. For each upper mass sideband region given in Table 4.10, we constrain $m_{K\pi\mu\mu}$ to the centre of that region. The background parameters at the centre of each upper mass sideband region are then used to determine a linear relation ($\mathcal{P}_{bkg}(\Omega, q^2, m)$) that is used to extrapolate back down to the signal region to determine a description of the background in the signal region. To describe the background is the signal region we use the following parametrization,

$$\begin{aligned}
\mathcal{P}_{bkg}(\Omega, q^2, m) &= f_{res}\mathcal{P}_{res,bkg}(\Omega, q^2, m) + f_{non-res}\mathcal{P}_{non-res,bkg}(\Omega, q^2, m) \\
&= f_{res}\mathcal{P}_{res,bkg}(\Omega, q^2, m) + (1 - f_{res})\mathcal{P}_{non-res,bkg}(\Omega, q^2, m) \\
&= f_{res}[f_{J/\psi} \cdot \mathcal{P}_{J/\psi}(\Omega, q^2, m) + (1 - f_{J/\psi}) \cdot \mathcal{P}_{\psi(2S)}(\Omega, q^2, m)] \\
&\quad + (1 - f_{res})\mathcal{P}_{non-res,bkg}(\Omega, q^2, m)
\end{aligned} \tag{4.15}$$

The background pdf $\mathcal{P}_{bkg}$ is shown in Eq 4.15 to be formed from two sub-pdfs, $\mathcal{P}_{res,bkg}$ and $\mathcal{P}_{non-res,bkg}$, where the relative amount of each pdf is controlled by a given fraction, f_{res} and $f_{non-res}$, where $f_{non-res} = (1 - f_{res})$. Explicitly, $\mathcal{P}_{res,bkg}$ is the background pdf that describes the resonant, combinatorial background. This pdf can be split into two resonant, background components, $\mathcal{P}_{J/\psi}$ and $\mathcal{P}_{\psi(2S)}$. $\mathcal{P}_{J/\psi}$ denotes the resonant J/ψ, background component and $\mathcal{P}_{\psi(2S)}$ denotes the resonant $\psi(2S)$, background component. Moreover, $\mathcal{P}_{non-res,bkg}$ describes the non-resonant, combinatorial background. All the pdfs are functions of the angles Ω, (where $\Omega(\cos\,\theta_\ell,\ \cos\,\theta_\ell,\ \phi)$), the invariant mass of the dimuon system, q^2 and mass, m. For this analysis, the pdfs are assumed to

be factorisable in all of the dimensions. This means for each dimension, 3 different pdfs are combined to make the full pdf for the background. For example, $\mathcal{P}_{J/\psi}$ is a pdf formed from three different pdfs in dimensions (Ω, q^2, m). The angular pdf is a 2^{nd} order Chebychev polynominal and is associated to all three pdfs, $\mathcal{P}_{J/\psi}$, $\mathcal{P}_{\psi(2S)}$ and $\mathcal{P}_{non-res,bkg}$. For each Chebychev polynominal there are 6 parameters, which means in total there are 18 parameters for the angular part of the background. The q^2 dependence, for the non-resonant pdf, $\mathcal{P}_{non-res,bkg}$ is modelled by a Weibull function. This function is defined by 2 parameters. For the resonant pdfs, $\mathcal{P}_{J/\psi}$ and $\mathcal{P}_{\psi(2S)}$, Crystal Ball functions are used. The Crystal Ball functions are assumed to be symmetric which means that there are 4 parameters per Crystal Ball function. Hence, for the q^2 component of the background, it follows that there are 10 parameters defined. Lastly, for the mass, m dependence, an exponential function is used. This exponential function is shared amongst all three pdfs ($\mathcal{P}_{J/\psi}$, $\mathcal{P}_{\psi(2S)}$ and $\mathcal{P}_{non-res,bkg}$) and is described by 1 parameter. Consequently, in total with the addition of the two fractions that are shared between all three pdfs (f_{res}, $f_{J/\psi}$), there are 31 parameters that fully describe the background. One cannot assume the background parameters are identical for Run 1 and Run 2 data, due to different detector configurations during operation. Therefore, this means there are 31 background parameters for Run 1 and 31 background parameters for Run 2 in total, across all mass bins. As an example, the resulting distributions from a background only fit to toy Run 1 data is given later by Figures 4.10 and 4.11, which also include modelling of the $B^+ \to K^+\mu^+\mu^-$ veto which is described in the next section.

4.4.2 The effect of the $B^+ \to K^+\mu^+\mu^-$ veto

Previously, in Section 4.2.3, a veto was presented, that is used in this analysis to reject peaking background events from the decay $B^+ \to K^+\mu^+\mu^-$ combining with a random pion. The veto removes all events with $m_{K\mu\mu} \in$ [5220,5340] MeV/c^2, and $m_{K\pi\mu\mu} >$ 5380 MeV/c^2. However, this veto has the effect of sculpting the angular distribution of the background, introducing a non-smooth dependence of the angular and q^2 distribution of the background on $m_{K\pi\mu\mu}$. Figure 4.9 presents three plots from three different angles to show the effect of the veto in the cos θ_K, q^2 and $m_{K\pi\mu\mu}$ phase space. The plots

were produced using the the function TGenPhaseSpace [94] in ROOT [95]. As shown in Figure 4.9 the effect of the veto spans the whole q^2 spectrum and upper mass sideband. However, it is localised in $\cos\theta_K$, where it occurs only at high $\cos\theta_K$ values. It is important to account for the effect of the veto as it can modify the values of the background parameters. The veto and its effect is modelled in the background model by simply removing the region of phase space affected. The background model as presented in Section 4.4.1 is used to fit a background only toy to determine the correct background parameters. Figures 4.10 and 4.11 show the projections of a fit to a background only toy, that has had the phase space region affected by the $B^+ \to K^+\mu^+\mu^-$ veto removed. In Figures 4.10 and 4.11, the events in red are the events after the cut, and the black line shows the projection of a fit to the toy dataset with the cut in. For completeness, the events before the cut are also shown, as well as a projection of a fit to a dataset without the cut applied. The projection of the fit to the events both with and without the cut, shows in both cases that the pdf captures the events and shape of the background well. As a result, the parameters obtained from the fit to the toy, can then be used for the final background parameters used in this analysis.

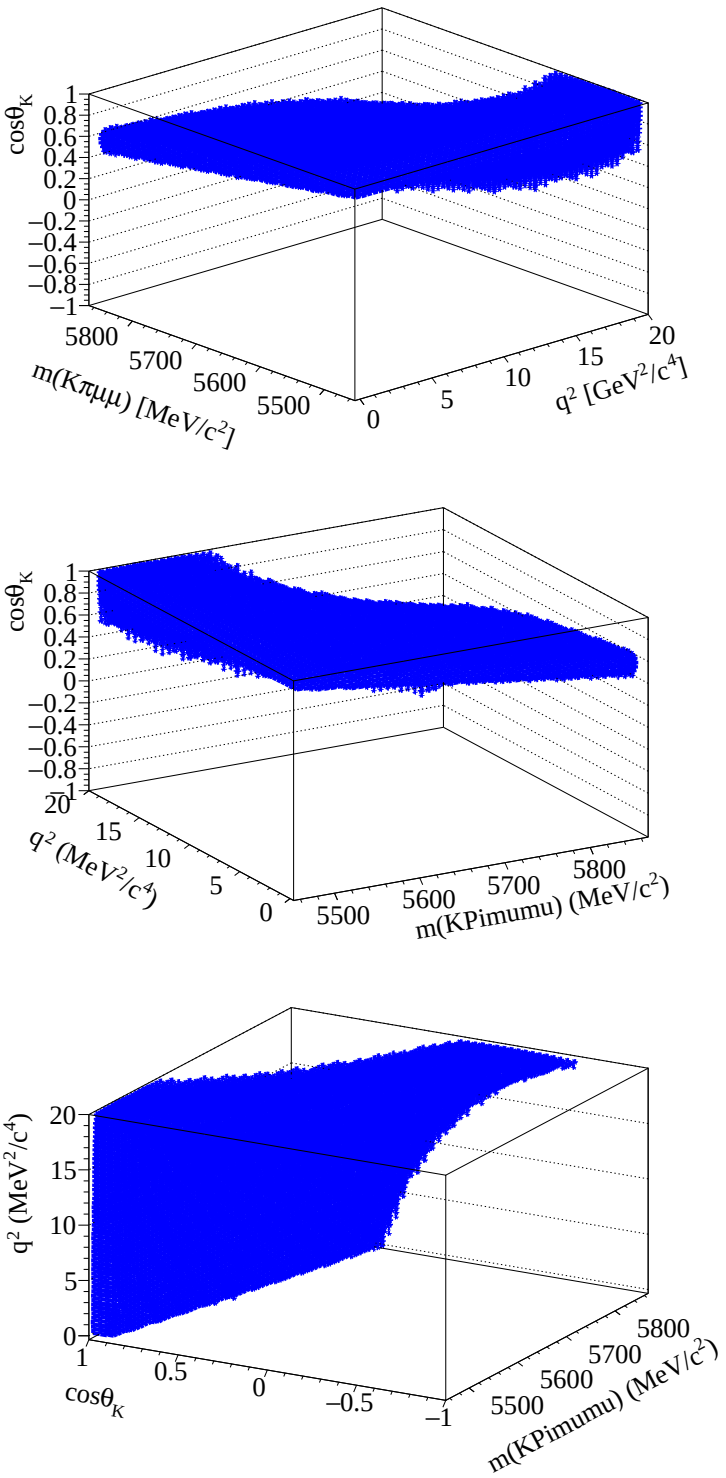

Figure 4.9: Distributions of the veto affected cos θ_K, q^2 and $m_{K\pi\mu\mu}$ phase space. The three plots show the affected phase space from different orientations and before any cuts have been applied.

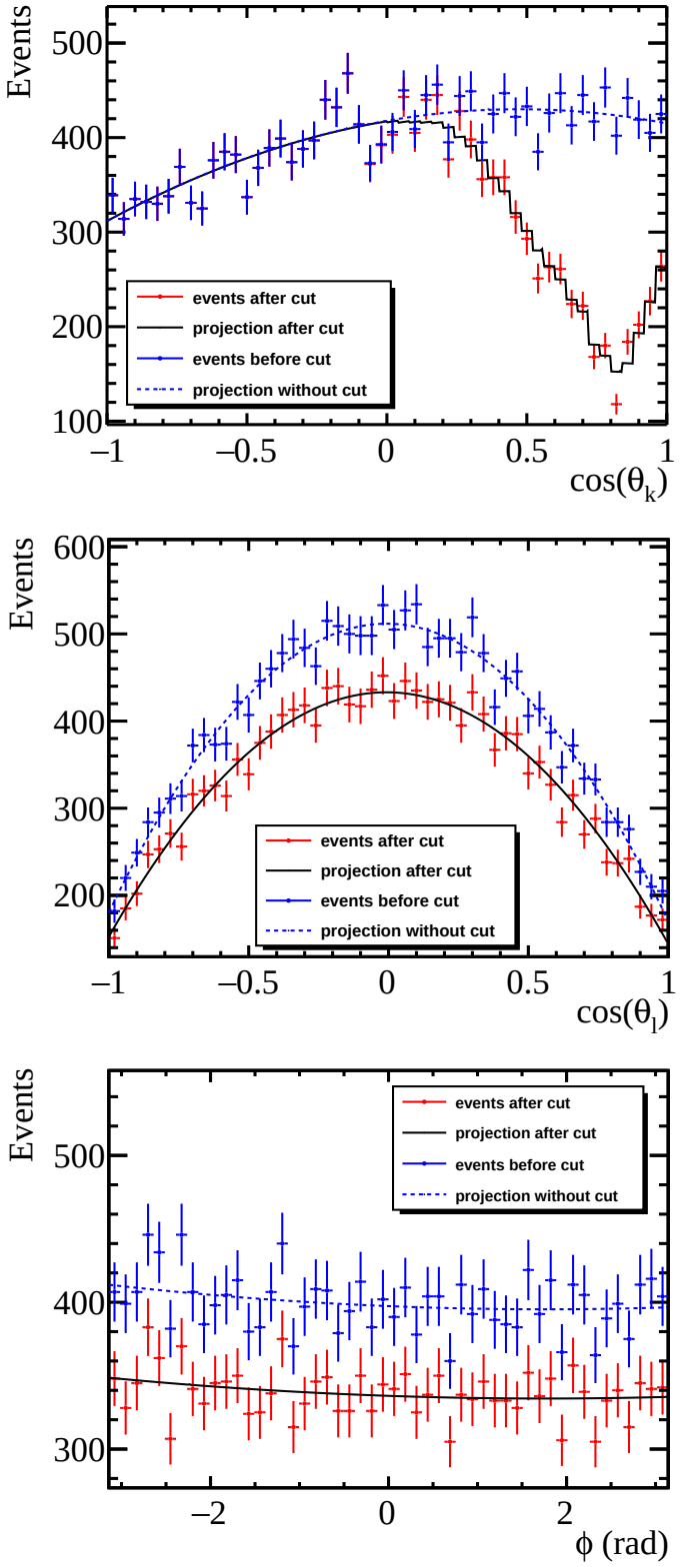

Figure 4.10: Projections of fits to the angles in toy data with and without the effect of the veto included. The blue data points correspond to events that have not had the veto applied and the projection of a fit to this data set is shown by the dashed, blue line. The red data points, refer to events that have the cut applied and the black line is the projection of the fit to the data with veto applied.

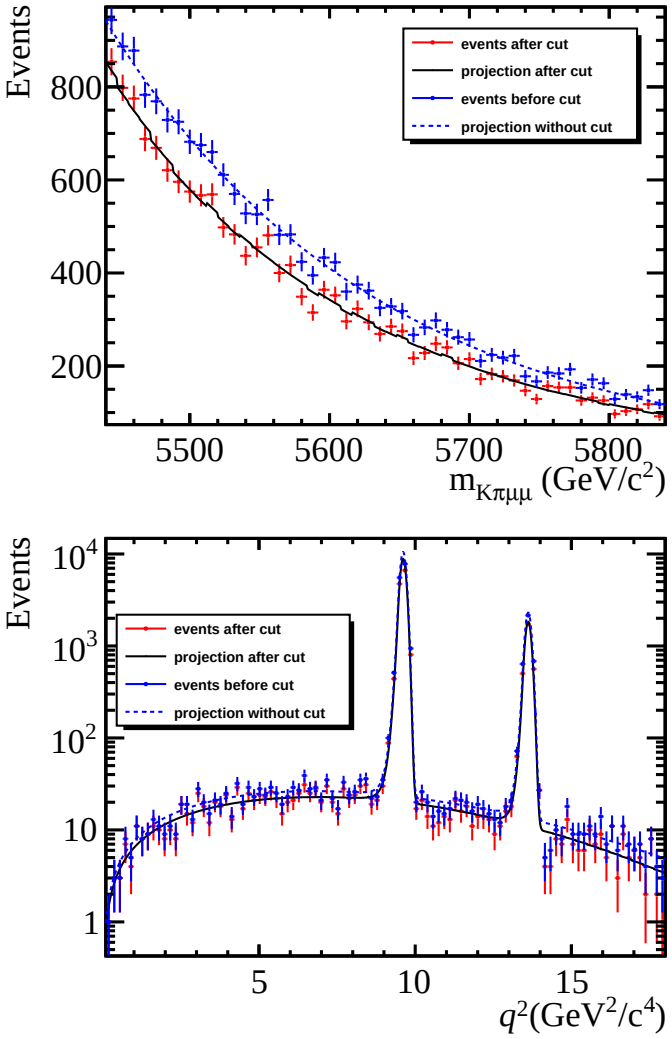

Figure 4.11: Projections of fits to $m_{K\pi\mu\mu}$ and q^2 in toy data with and without the effect of the veto included. The blue data points correspond to events that have not had the veto applied and the projection of a fit to this data set is shown by the dashed, blue line. The red data points, refer to events that have the cut applied and the black line is the projection of the fit to the data with veto applied.

4.5 Modelling detector effects

Detector effects are factors that modify the physics results or introduce certain behaviour, as a consequence of the detector itself. It is important to model these effects as they provide misleading information and characteristics that can influence the physics measurement. In precision experiments such as LHCb this is extremely important as one wants to compare the measurement to existing theoretical predictions. For this analysis that aims to measure the interference between short- and long-distance contributions in $\bar{B}^0 \to \bar{K}^{*0}\mu^+\mu^-$ transitions various detector effects have been considered and are

described in this section.

4.5.1 Resolution model in q^2

The model described in Chapter 3 includes many charmonium resonances across the full dimuon invariant mass spectrum. These resonances not only occur at a significantly larger rate than the penguin component, but vary in natural width. Resonances such as the J/ψ, $\psi(2S)$ and $\phi(1020)$ have a natural width that is significantly narrower than the resolution in the dimuon mass. Whereas, other resonances such as the $\psi(4040)$ and $\psi(4160)$ are broader and so the effect of the resolution is much smaller. As this analysis aims to measure precisely the contribution from the non-local charm loop, the detector resolution needs to be accurately modelled and accounted for.

4.5.1.1 Procedure for the resolution model

The procedure for determining the detector resolution in q^2 across the full q^2 spectrum in this analysis is discussed. The method follows the same approach as that given in Ref [45] that measured the interference between short- and long-distance contributions in the $B^+ \to K^+\mu^+\mu^-$ decay. In Ref [45], the resolution was split into three separate regions. Each region had the same resolution function but different values for the parameters. The motivation for this was that the resolution in each of the regions varied dramatically. In this analysis the same resolution function and regions are implemented. The regions are defined as the ϕ region (Region 1) with $q^2 \in [0.0445, 3.24]\text{GeV}^2/c^4$, J/ψ region (Region 2) with $q^2 \in [3.4, 11.56]$ GeV$^2/c^4$ and the $\psi(2S)$ region (Region 3) with $q^2 \in [11.56, 19.22]$ GeV$^2/c^4$. These three regions when combined cover the fitting range of $q^2 \in [0.1, 18.0]$ GeV$^2/c^4$ which is used in this analysis. For the resolution function, the shape implemented is a double-sided Crystal Ball function combined with a Gaussian distribution. The exact form of the resolution function is given by Equation 4.16.

$$R(q^2, \mu) = fG(q^2, \mu, \sigma_G) + (1 - f)C(q^2, \mu, \sigma_C, \alpha_l, \alpha_u, \eta_l, \eta_u) \tag{4.16}$$

The double-sided Crystal Ball function is defined as

$$C(q^2, \mu, \sigma_C, \alpha_l, \alpha_u, \eta_l, \eta_u) \propto \begin{cases} A_l(B_l - \delta)^{-\eta_l} & if \;\; \delta < \alpha_l \\ exp(-\delta^2/2) & if \;\; \alpha_l < \delta < \alpha_u \\ A_u(B_u + \delta)^{-\eta_u} & if \;\; \delta > \alpha_u \end{cases} \tag{4.17}$$

where,

$$\delta = (q2 - \mu)/\sigma_C$$

$$A_{l,u} = \left(\frac{n_{l,u}}{|\alpha_{l,u}|}\right)^{\eta_{l,u}} e^{-|\alpha_{l,u}|^2/2} \tag{4.18}$$

$$B_{l,u} = \left(\frac{n_{l,u}}{|\alpha_{l,u}|}\right) - \mid \alpha_{l,u} \mid$$

It can be seen in Eq 4.16 that the resolution function is a function of q^2 and depends on 8 parameters. The parameter μ defines the mean, which is common between both the Gaussian and the double-sided Crystal Ball function. The parameters $\sigma_{G,C}$ denotes the widths of the Gaussian and Crystal Ball function respectively. f is the relative fraction of the Gaussian with respect to the Crystal Ball function. The double-sided Crystal Ball function is asymmetric which means the upper and lower tail parameters are different. Therefore, the tail parameters are $\alpha_{l,u}$ and $\eta_{l,u}$, where l symbolises the lower tail and u the upper tail. To determine these parameters for each of the three regions that form the full resolution model, a combination of simulation and data taken from the LHCb experiment and corresponding to Runs 1 and 2 of the LHC, is used. The complete list of samples used is given in Section 4.1. For the MC samples, the tracks have been momentum smeared based on the work described in Ref [96]. The requirement to have the track momentum smeared is to ensure the reconstructed B^0 mass distribution is similar in data and simulation. In this analysis, the resolution function in each region is described in the following sections.

4.5.1.2 Resolution in the J/ψ and $\psi(2S)$ regions

The resolution in the J/ψ and $\psi(2S)$ regions is determined by the same method, which begins by validating the choice of the model by fitting the $B^0 \to J/\psi K^{*0}$ and $B^0 \to \psi(2S)K^{*0}$ simulation with a relativistic Breit-Wigner that has been convolved with the resolution function defined in Equation 4.16. Figure 4.12 shows the fits to the q^2 distribution from the $B^0 \to J/\psi K^{*0}$ simulation, for Run 1 and Run 2. Figure 4.13 shows the fits for the $\psi(2S)$ for both Run 1 and Run 2. For Run 2 the LHCb collaboration, did not produced a pure $B^0 \to \psi(2S)K^{*0}$ simulation sample, so instead, $B^0 \to K^{*0}\mu^+\mu^-$ simulation is used and the distribution of the difference between true and reconstructed q^2 is calculated using only events from the $\psi(2S)$ region. This distribution is then fitted with a relativistic Breit-Wigner that has been convolved with the resolution function. To ensure that the resolution at the core of the J/ψ and $\psi(2S)$ is modelled precisely, the core parameters μ, σ_G and σ_C are taken from a fit to $B^0 \to J/\psi K^{*0}$ and $B^0 \to \psi(2S)K^{*0}$ data evaluated very close to the resonances, where the interference with the rare mode is negligible. Figure 4.14 shows the fits to the core of the J/ψ in $B^0 \to J/\psi K^{*0}$ data for both Run 1 and Run 2. Similarly, Figure 4.15 shows the fits to the core of the $\psi(2S)$ in $B^0 \to \psi(2S)K^{*0}$ data for Run 1 and Run 2.

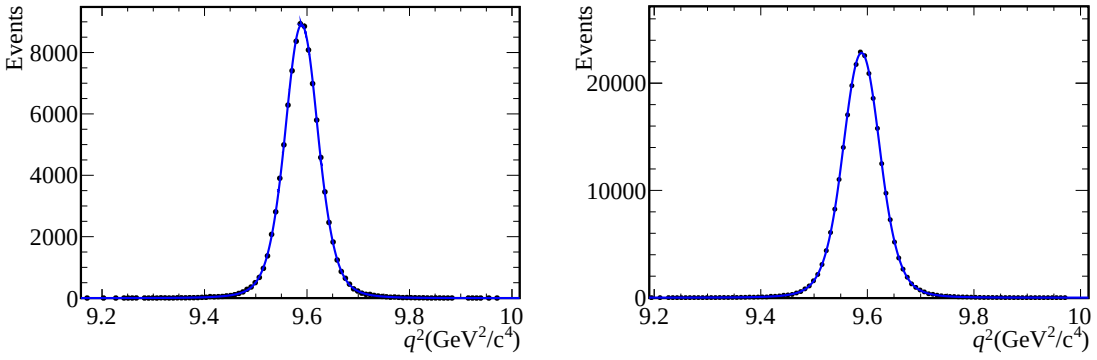

(a) Run 1 (b) Run 2

Figure 4.12: Fits to the dimuon mass distribution for the $B^0 \to J/\psi K^{*0}$ simulation for Run 1 (a) and Run 2 (b).

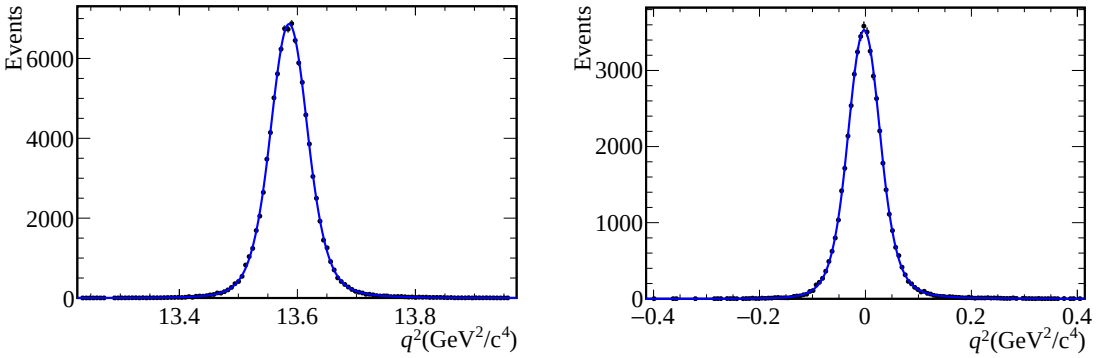

(a) Run 1 (b) Run 2

Figure 4.13: Fits to the dimuon mass distribution for (a) Run 1 using the $B^0 \to \psi(2S)K^{*0}$ simulation sample and (b) Run 2 simulation, where the sample is $B^0 \to K^{*0}\mu^+\mu^-$, and the difference between true and reconstructed q^2 is constructed in the $\psi(2S)$ region.

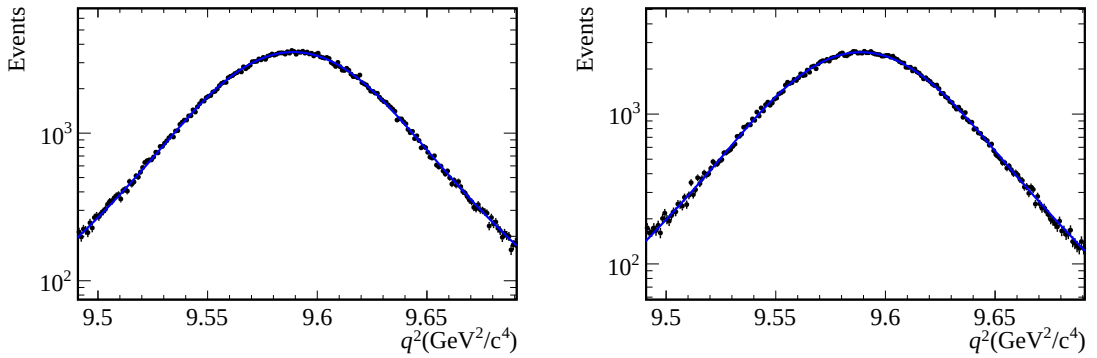

(a) Run 1 (b) Run 2

Figure 4.14: Fits to the core of the J/ψ which have been obtained from $B^0 \to K^{*0}\mu^+\mu^-$ data. (a) illustrates the core fit for Run 1 and (b) illustrates the core fit for Run 2.

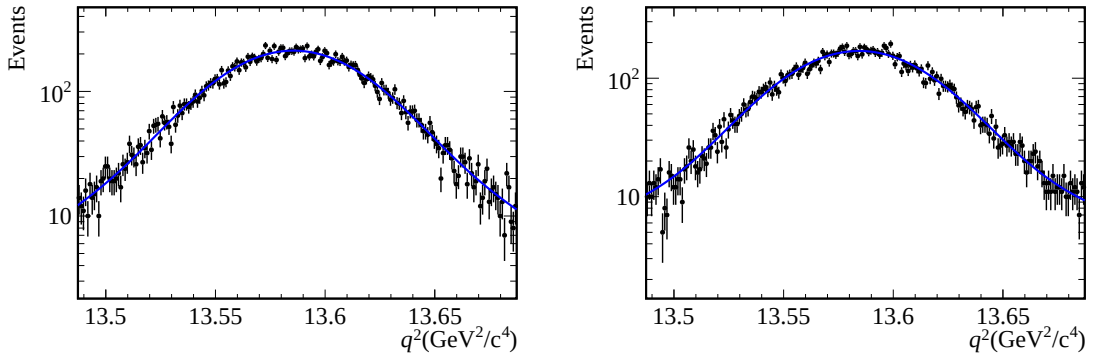

(a) Run 1 (b) Run 2

Figure 4.15: Fits to the core of the dimuon mass distribution for $B^0 \to K^{*0}\mu^+\mu^-$ data events that have been selected to only include $\psi(2S)$ events. (a) shows the fit for Run 1 and (b) shows the fit for Run 2.

The resolution parameters for the J/ψ region are given by Table 4.11 for Run 1 and Table 4.12 for Run 2. Likewise, the resolution parameters for the $\psi(2S)$ are given by Table 4.13 for Run 1 and Table 4.14 for Run 2. For the J/ψ region, the parameters are generally consistent between Run 1 and Run 2 with small differences in the values of the parameters, however the errors show large differences. This is because of the statistics available in the simulation and data after all the selection criteria have been applied was quite different for both Run 1 and Run 2. For the $\psi(2S)$ region, both the values and errors show differences between Run 1 and Run 2. This again is due to the statistics available and how the $\psi(2S)$ occurs at a lower magnitude. Nevertheless, for both the J/ψ and $\psi(2S)$ regions, the parameters are within agreement for this analysis, and are expected to be different due to different running conditions of the detector over the two data taking periods. Moving on, the results show that $\delta\mu \neq 0$, for both the J/ψ and $\psi(2S)$ region. This is because the Crystal Ball function is non-symmetric, therefore one tail is bigger than the other and pulls the mean away from the peak. Furthermore, the results displayed in these tables reveal that the tail parameters $a_{l,u}$ are consistent in absolute value with each other. As a result, the choice is made then to symmetrize these parameters for both the J/ψ and $\psi(2S)$ resolution functions, such that a_l = -a_u, and float the single alpha parameter in the fit, to obtain a better understanding of the resolution in the tails.

Parameter	Value
$\delta\mu$	$-3.66\times10^{-4} \pm 1.19\times10^{-5}$
σ_C	$4.40\times10^{-2} \pm 1.84\times10^{-3}$
σ_G	$2.77\times10^{-2} \pm 4.98\times10^{-4}$
f	$4.47\times10^{-1} \pm 4.70\times10^{-2}$
α_l	$-9.98\times10^{-1} \pm 1.75\times10^{-1}$
α_u	$1.04 \pm 1.76\times10^{-1}$
η_l	17.10 ± 7.74
η_u	11.07 ± 3.03

Table 4.11: The resolution parameters for the J/ψ region for Run 1. The tail parameters are obtained from fits to $B^0 \to J/\psi K^{*0}$ simulation and the core parameters are obtained from fitting the core of J/ψ in $B^0 \to K^{*0}\mu^+\mu^-$ data. The parameter $\delta\mu$ denotes the shift to the mean which is centered at the J/ψ peak value that is the PDG value.

Parameter	Value
$\delta\mu$	$-3.56\times10^{-4} \pm 1.42\times10^{-5}$
σ_C	$4.47\times10^{-2} \pm 5.52\times10^{-3}$
σ_G	$2.72\times10^{-2} \pm 2.066\times10^{-3}$
f	$4.22\times10^{-1} \pm 1.59\times10^{-1}$
α_l	$-1.16 \pm 3.64\times10^{-2}$
α_u	$1.21 \pm 3.88\times10^{-2}$
η_l	14.95 ± 1.96
η_u	$10.19 \pm 9.38\times10^{-1}$

Table 4.12: The resolution parameters for the J/ψ region for Run 2. The tail parameters are obtained from fits to $B^0 \to J/\psi K^{*0}$ simulation and the core parameters are obtained from fitting the core of J/ψ in $B^0 \to K^{*0}\mu^+\mu^-$ data. The parameter $\delta\mu$ denotes the shift to the mean which is centered at the J/ψ peak value that is the PDG value.

Parameter	Value
$\delta\mu$	$-3.57\times10^{-4} \pm 4.55\times10^{-5}$
σ_C	$5.73\times10^{-2} \pm 1.54\times10^{-2}$
σ_G	$3.03\times10^{-2} \pm 1.67\times10^{-3}$
f	$6.50\times10^{-1} \pm 1.29\times10^{-1}$
α_l	$-1.10 \pm 6.66\times10^{-2}$
α_u	$1.10 \pm 6.73\times10^{-2}$
η_l	$6.24 \pm 5.75\times10^{-1}$
η_u	11.94 ± 2.12

Table 4.13: The resolution parameters for the $\psi(2S)$ region for Run 1. The tail parameters are obtained from fits to $B^0 \to \psi(2S)K^{*0}$ simulation and the core parameters are obtained from fitting the core of $\psi(2S)$ in $B^0 \to K^{*0}\mu^+\mu^-$ data. The parameter $\delta\mu$ denotes the shift to the mean which is centered at the $\psi(2S)$ peak value that is the PDG value.

Parameter	Value
$\delta\mu$	$-5.47\times10^{-4} \pm 5.67\times10^{-5}$
σ_C	$7.64\times10^{-2} \pm 2.72\times10^{-2}$
σ_G	$3.07\times10^{-2} \pm 1.33\times10^{-3}$
f	$7.23\times10^{-1} \pm 6.49\times10^{-2}$
α_l	$-9.40\times10^{-1} \pm 1.42\times10^{-1}$
α_u	$1.07 \pm 1.52\times10^{-1}$
η_l	$5.62 \pm 8.51\times10^{-1}$
η_u	8.59 ± 1.88

Table 4.14: The resolution parameters for the $\psi(2S)$ region for Run 2. The tail parameters are obtained from fits to $\psi(2S)$ events from $B^0 \to K^{*0}\mu\mu$ simulation. The core parameters are obtained from fitting the core of $\psi(2S)$ in $B^0 \to K^{*0}\mu^+\mu^-$ data. The parameter $\delta\mu$ denotes the shift to the mean which is centered at the $\psi(2S)$ peak value that is the PDG value.

4.5.1.3 Resolution in the ϕ region

A different approach is taken to obtain the resolution in the ϕ region. This is because the branching fraction of $B^0 \to K^{*0}\phi(\to \mu^+\mu^-)$ is much smaller and the width of the ϕ is much larger. The method is to simply take events in the ϕ region in $B^0 \to K^{*0}\mu^+\mu^-$ simulation and compute the distribution of the difference between true and reconstructed q^2. This distribution is then fitted with the resolution function as defined by Equation 4.16. The resulting fits are shown in Figure 4.16 for both Run 1 and Run 2. The resolution parameters obtained from these fits are given by Table 4.15 for Run 1 and Table 4.16 for Run 2. Similarly to the resolution in the other two regions, the results show that $\delta\mu \neq 0$ because the Crystal Ball function is asymmetric and causes a pull of the mean from 0. The alpha parameters for the ϕ region are not fitted for in the model fits, and therefore are kept asymmetrical. This holds due to the parameters from the fit being almost identical, with then only differences coming from the η parameters, which is not significant as the α parameters control the tails and therefore this methodology holds.

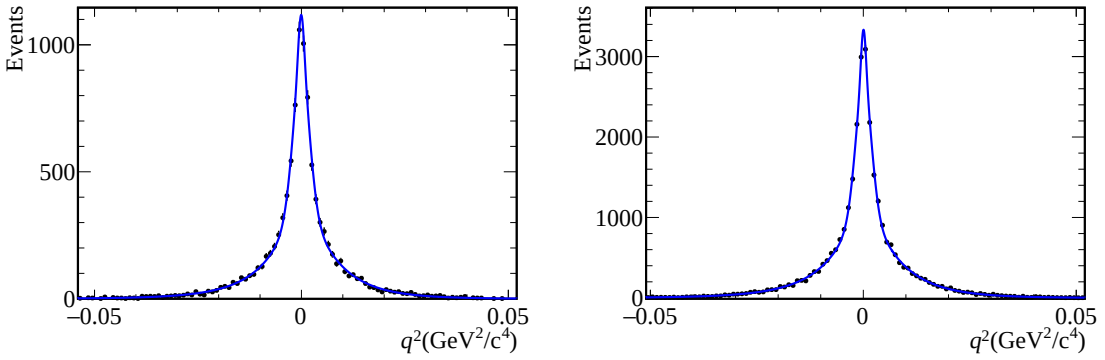

(a) Run 1 (b) Run 2

Figure 4.16: Fits to the dimuon mass distribution using $B^0 \to K^{*0}\mu^+\mu^-$ simulation events to construct the difference between true and reconstructed q^2, in the $\psi(2S)$ region. The fits are shown for Run 1 (a) and Run 2 (b).

Parameter	Value
$\delta\mu$	-4.76×10^{-5} ± 4.68×10^{-5}
σ_C	2.02×10^{-3} ± 2.76×10^{-4}
σ_G	7.21×10^{-2} ±2.76×10^{-4}
f	3.33×10^{-2} ± 2.47×10^{-2}
α_l	-2.80×10^{-1} ± 2.21×10^{-2}
α_u	2.93×10^{-1} ± 2.33×10^{-2}
η_l	18.84 ± 7.95
η_u	9.31 ± 1.71

Table 4.15: Results from the fit to $B^0 \to K^{*0}\mu^+\mu^-$ Run 1 Monto Carlo using a resolution function that consists of a double-sided Crystal Ball and a Gaussian. $\delta\mu$ denotes the shift to the mean.

Parameter	Value
$\delta\mu$	4.96×10^{-5} ± 2.63×10^{-5}
σ_C	1.86×10^{-3} ± 1.07×10^{-4}
σ_G	5.88×10^{-4} ± 8.66×10^{-5}
f	2.87×10^{-2} ± 8.36×10^{-3}
α_l	-2.53×10^{-1} ± 9.63×10^{-3}
α_u	2.63×10^{-1} ± 9.80×10^{-3}
η_l	19.00 ± 3.76
η_u	9.18 ± 8.10×10^{-1}

Table 4.16: Results from the fit to $B^0 \to K^{*0}\mu^+\mu^-$ Run 2 simulation using a resolution function that consists of a double-sided Crystal Ball and a Gaussian. $\delta\mu$ denotes the shift to the mean which is centred at the J/ψ peak value that is the PDG value.

4.5.2 Angular acceptance effects

The geometry of the detector, trigger reconstruction and selection can shape the angular distribution of $\bar{B}^0 \to \bar{K}^{*0}\mu^+\mu^-$ decays. These *angular acceptance effects*, distort the distributions of the three of the angles, cos θ_K, cos θ_ℓ, ϕ and q^2, that describe the final state of the $\bar{B}^0 \to \bar{K}^{*0}\mu^+\mu^-$ decay. It is important to account for the angular acceptance effects, as any shaping of the angular distribution influences the angular analysis. The angular acceptance, ε is obtained in all four dimensions (cos θ_K, cos θ_ℓ, ϕ, q^2), as a sum of Legendre polynomials. The exact form of the acceptance is a follows,

$$\varepsilon(\cos\theta_K, \cos\theta_\ell, \phi, q^2) = \sum_{ijqr} c_{ijqr} P_i(\cos\theta_\ell) P_j(\cos\theta_K) P_q(\phi) P_r(q^2) \tag{4.19}$$

where, $P_m(x)$ are Legendre polynomials that have an order of m and are functions of x. The terms c_{ijqr} are the angular acceptance coefficients. The coefficients c_{ijqr} are determined through a moment analysis of simulated $\bar{B}^0 \to \bar{K}^{*0}\mu^+\mu^-$ decays, generated according to a phase space decay and reweighted to obtain a flat distribution in q^2 [4]. The orders of the polynominals are chosen to be those of Ref [4], that give a good description of the angular acceptance. Specifically, in q^2 the Legendre polynomials ($P_r(q^2)$) have an order of 5, the cos θ_ℓ Legendre polynomials ($P_i(\cos\theta_\ell)$ have an order of 4, the cos θ_K Legendre polynomials ($P_j(\cos\theta_K)$) have an order of 5 and the ϕ Legendre polynomials ($P_q(\phi)$) have an order of 6. The result for the final acceptances for the toy studies and the data fits is shown by Figure 4.17. In Figure 4.17 the "nominal" acceptance parameterisation (solid red line), which refers to the acceptance defined in Ref [4], is compared to the recalculated acceptance (solid black line) for the "unbinned" fits, which are the fits that are to be performed to the data with the model defined in Section 3.1. The simulated $\bar{B}^0 \to \bar{K}^{*0}\mu^+\mu^-$ decays are shown by the black data points for this analysis, and the red data points for the simulated $\bar{B}^0 \to \bar{K}^{*0}\mu^+\mu^-$ decays in Ref [4].

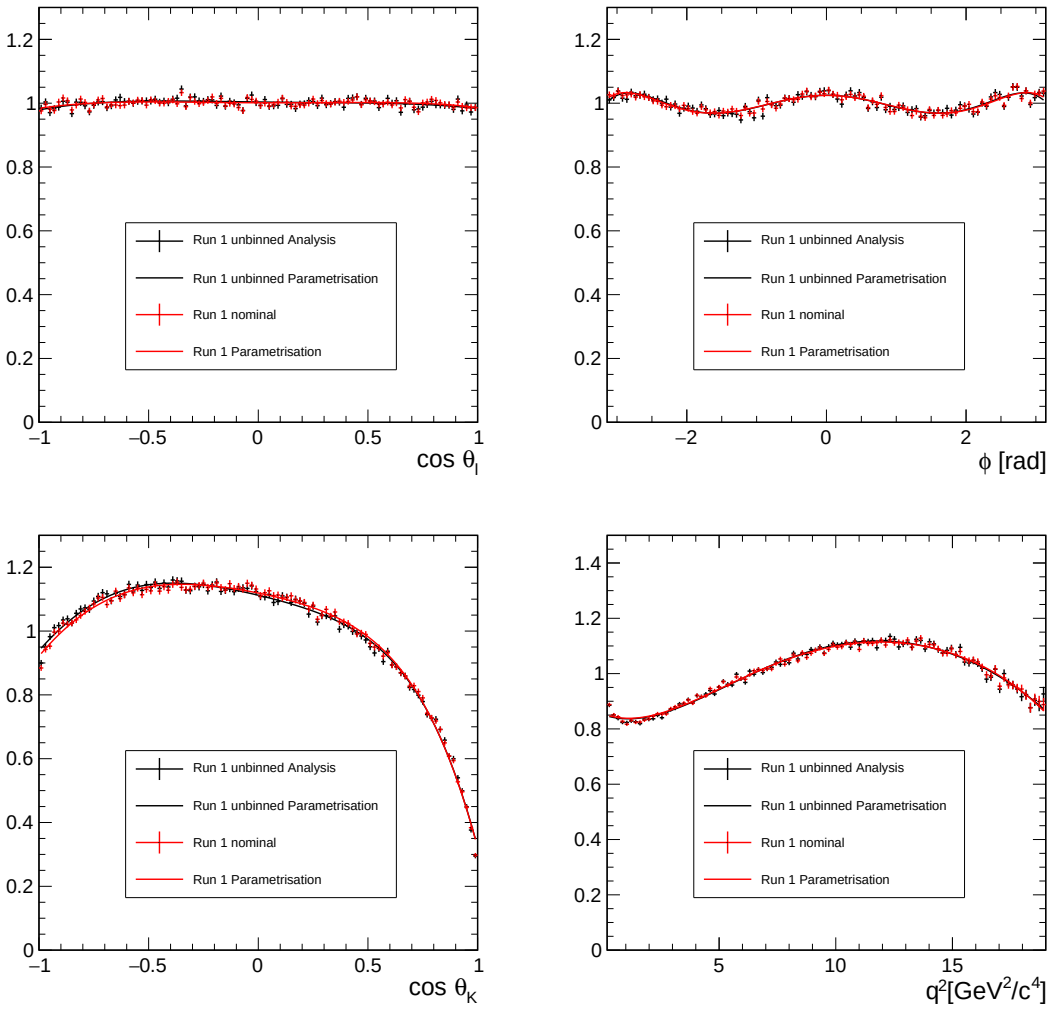

Figure 4.17: The acceptance parameterisation used in the analysis compared to the acceptance in the previous analysis [4]. The solid black line is the acceptance used in this analysis, the data used in this analysis is shown by the black data points.The parameterisation used in Ref [4] is shown by the solid red line and the corresponding data by the red data points.

4.6 Including an S-wave contribution in the $K\pi$ system

The differential decay rate for $\bar{B}^0 \to \bar{K}^{*0}\mu^+\mu^-$ transitions is shown in Chapter 1 to be formed only of a P-wave component of the $K\pi$ system. Nevertheless, there is a significant S-wave component that needs to be accounted for (see Ref [97]). The S-wave component for $\bar{B}^0 \to \bar{K}^{*0}\mu^+\mu^-$ transitions is described through two chiral amplitudes, $A_{00}^{L/R}$. Equation 4.20 shows the total S-wave amplitude for $\bar{B}^0 \to \bar{K}^{*0}\mu^+\mu^-$ used in this analysis [98].

$$\mathcal{A}_{00} = N\sqrt{\frac{\lambda_{K_0^{*0}}}{q2}}\left[(C_9 \mp C_{10})F_1 + \frac{2m_b}{(m_B + m_K^*)}C_7 F_T + \mathcal{G}_{00}(q^2)\right] \tag{4.20}$$

where,

$$N = G_F \alpha V_{tb} V_{ts}^* \sqrt{\frac{q^2\sqrt{\lambda_{K_0^{*0}}}\beta_\ell}{3.1024\pi^5 m_B^3}} \tag{4.21}$$

and,

$$\lambda_{K_0^{*0}} = m_B^4 + m_{K_0^{*0}}^4 + q^4 - 2(m_B^2 m_{K_0^{*0}}^2 + m_{K_0^{*0}}^2 q^2 + m_B^2 q^2) \tag{4.22}$$

The Wilson Coefficients that enter the S-wave amplitude are set to the standard Wilson Coefficients values as given by Ref [11]. These Wilson Coefficients are decoupled from the Wilson Coefficients that enter the P-wave amplitudes by introducing two scale factors, where one multiplies the vector component of Equation 4.20 and the other multiplies the tensor component of Equation 4.20. These scale factors are simply coefficients which are set to 1 in the model, and when the both toy fits and the fit to the data is performed these coefficients are fitted for.

The terms $F_{1,T}$ that enter into the S-wave amplitudes expression in Equation 4.20 are the S-wave form factors. The expression for the S-wave form factors is taken from Ref [99] and is given by the following,

$$F_{1,T}(q^2) = \frac{F(0)}{1 + \alpha_F q^2/m_B^2 + b_F(q^2/m_B^2)^2} \tag{4.23}$$

	$F(0)$	α_F	b_F
$F_1^{\bar{B}^0\bar{K}^{*0}(800)}$	0.27	-2.1	1.2
$F_T^{\bar{B}^0\bar{K}^{*0}(800)}$	0.30	-2.2	1.2

Table 4.17: The $B \to K^{*0}$ S-wave form factor parameter values taken from Ref [99].

where, $F(0)$, a_F and b_F, are the individual form factor coefficients given by Table 4.17. Only contributions from the $\bar{K}_0^{*0}(800)$ are considered. This is because the S-wave form factors are not well understood. For example, the uncertainty on the individual coefficients is unknown and the correlations between the individual coefficients is not provided in Ref [99]. This lack of knowledge of the S-wave form factors poses an issue in attempting a fit to the data. A naive approach is taken where all the coefficients of the S-wave form factors are give a 20% uncertainty. Later on in Chapter 6, a systematic uncertainty is determined for the lack of knowledge of the S-wave form factors.

The S-wave amplitudes also receive contributions from non-local contributions. These resonant S-wave contributions are inserted in the same way as the resonant P-wave contributions, where the resonant contributions are added directly into the amplitude expressions. $\mathcal{G}_{00}(q^2)$ in Eq 4.20 denotes the resonant S-wave contributions. The form of $\mathcal{G}_{00}(q^2)$ is given as,

$$\mathcal{G}_{00}(q^2) = \sum_{j=J/\psi,\psi(2S)} \eta_j^0 e^{i\theta_j^0} A_j^{\rm res}(q^2) \tag{4.24}$$

Similarly, in Eq 4.24, each resonance is modelled as a relativistic Breit-Wigner and is assigned a complex number defined with a given magnitude η_j^{00} and phase, θ_j^{00}, where $j = J/\psi, \psi(2S)$. Only S-wave contributions from the J/ψ and $\psi(2S)$ are considered, as the S-wave contributions from other hadronic resonances can be safely assumed to be negligible, as the S-wave amplitude will only be a small fraction of the already small total amplitude.

The expression for the S-wave amplitude given in Equation 4.20 does not contain an $m_{K\pi}$ dependence. Therefore before the S-wave amplitude can be inserted into the model, an $m_{K\pi}$ dependence needs to be introduced. This has to enter into both the P-wave and S-wave amplitudes. For the P-wave this is done by multiplying each amplitude

by the following integral, $\mathcal{L}_P$.

$$\mathcal{L}_P = \int_{796\text{MeV/c}^2}^{996\text{MeV/c}^2} |g(m_{K\pi})|^2 dm_{K\pi} \tag{4.25}$$

where, $g(m_{K\pi})$ represents a relativistic Breit-Wigner with the mass and width of the $K^{*0}(892)$. The integral is performed in the 100 MeV/c^2 window around the K^{*0} pole mass. For the S-wave amplitudes, the $m_{K\pi}$ dependence enters by multiplying the amplitudes by the integral $\mathcal{L}_S$, where $\mathcal{L}$ is defined as,

$$\mathcal{L}_S = \int_{796\text{MeV/c}^2}^{996\text{MeV/c}^2} |f(m_{K\pi})|^2 dm_{K\pi} \tag{4.26}$$

where, $f(m_{K\pi})$ is a S-wave lineshape in $m_{K\pi}$ modelled through the LASS approach [100]. As in Equation 4.25, the integral presented in Equation 4.26 is integrated over a 100 MeV/c^2 window around the K^{*0} pole mass. All the J observables that enter the total differential decay rate, defined by Equation 4.29, will contain these integrals, $\mathcal{L}$. The J observables that are made from bilinear combinations of purely P-wave amplitudes will only have $\mathcal{L}_P$. The S-wave observables $J_i^{'}$ are defined by Eq 4.28. These observables are made from bilinear combinations of P-wave and S-wave amplitudes. These J observables they will contain the integrals $\mathcal{L}_{S-P}$, where $\mathcal{L}_{S-P}$ is defined as,

$$\mathcal{L}_{S-P} = \int_{796\text{MeV/c}^2}^{996\text{MeV/c}^2} f(m_{K\pi}) g(m_{K\pi})^* dm_{K\pi} \tag{4.27}$$

The differential decay rate for $\bar{B}^0 \to \bar{K}^{*0}\mu^+\mu^-$ transitions containing both P- and S-wave amplitudes is given by Equation 4.29.

$$
\begin{aligned}
J_{1c}^{'} &= \frac{1}{3}|A_{00}^{L}|^2 + \frac{1}{3}|A_{00}^{R}|^2 \\
J_{2c}^{'} &= \frac{2}{\sqrt{3}}\Big[\mathrm{Re}(A_{00}^{L}A_{0}^{L*}) + (L \to R)\Big] \\
J_{4}^{'} &= \sqrt{\frac{2}{3}}\Big[\mathrm{Re}(A_{00}^{L}A_{\parallel}^{L*}) + (L \to R)\Big] \\
J_{5}^{'} &= 2\sqrt{\frac{2}{3}}\Big[\mathrm{Re}(A_{00}^{L}A_{\perp}^{L*}) - (L \to R)\Big] \\
J_{7}^{'} &= 2\sqrt{\frac{2}{3}}\Big[\mathrm{Im}(A_{00}^{L}A_{\parallel}^{L*}) - (L \to R)\Big] \\
J_{9}^{'} &= \sqrt{\frac{2}{3}}\Big[\mathrm{Im}(A_{00}^{L}A_{\perp}^{L*}) + (L \to R)\Big]
\end{aligned}
\tag{4.28}
$$

$$
\begin{aligned}
\frac{\mathrm{d}^4\Gamma[\bar{B}^0 \to \bar{K}^{*0}\mu^+\mu^-]}{\mathrm{dcos}\,\theta_\ell\,\mathrm{dcos}\,\theta_K\,\mathrm{d}\phi\,\mathrm{d}q^2} = \frac{9}{32\pi}[&J_{1s}\sin^2\theta_K + J_{1c}\cos^2\theta_K + J_{1c}^{'}(1-\cos^2\theta_\ell) \\
&+J_{2s}\sin^2\theta_K\cos2\theta_\ell + J_{2c}\cos^2\theta_K\cos2\theta_\ell \\
&+J_{2c}^{'}\cos^2\theta_K(1-\cos2\theta_\ell) + J_3\sin^2\theta_K\sin^2\theta_\ell\cos2\phi \\
&+J_4\sin2\theta_K\sin2\theta_\ell\cos\phi + J_4^{'}\sin2\theta_\ell\sin\theta_K\cos\phi \\
&+J_5\sin2\theta_K\sin\theta_\ell\cos\phi + J_5^{'}\sin\theta_\ell\sin\theta_K\cos\phi \\
&+J_{6s}\sin^2\theta_K\cos\theta_\ell + J_7\sin2\theta_K\sin\theta_\ell\sin\phi \\
&+J_7^{'}\sin\theta_\ell\sin\theta_K\sin\phi + J_8\sin2\theta_K\sin2\theta_\ell\sin\phi \\
&+J_8^{'}\sin2\theta_\ell K\sin\theta_K\sin\phi + J_9\sin^2\theta_K\sin^2\theta_\ell\sin2\phi]
\end{aligned}
\tag{4.29}
$$

The model containing both P-wave and S-wave amplitudes was used to reproduce the S-wave amplitudes given by Eq 4.28. The results are shown by Figure 4.18. In this figure, the red line denotes the central values of the observable. The band of all possible values has been omitted from Figure 4.18 because the uncertainties in the S-wave form factors are unknown. In Figure 4.18 all observables agree with predictions and clearly show the effect of the resonances. In light of this, the angular distribution as presented by Equation 4.29 can be used to fit to the data.

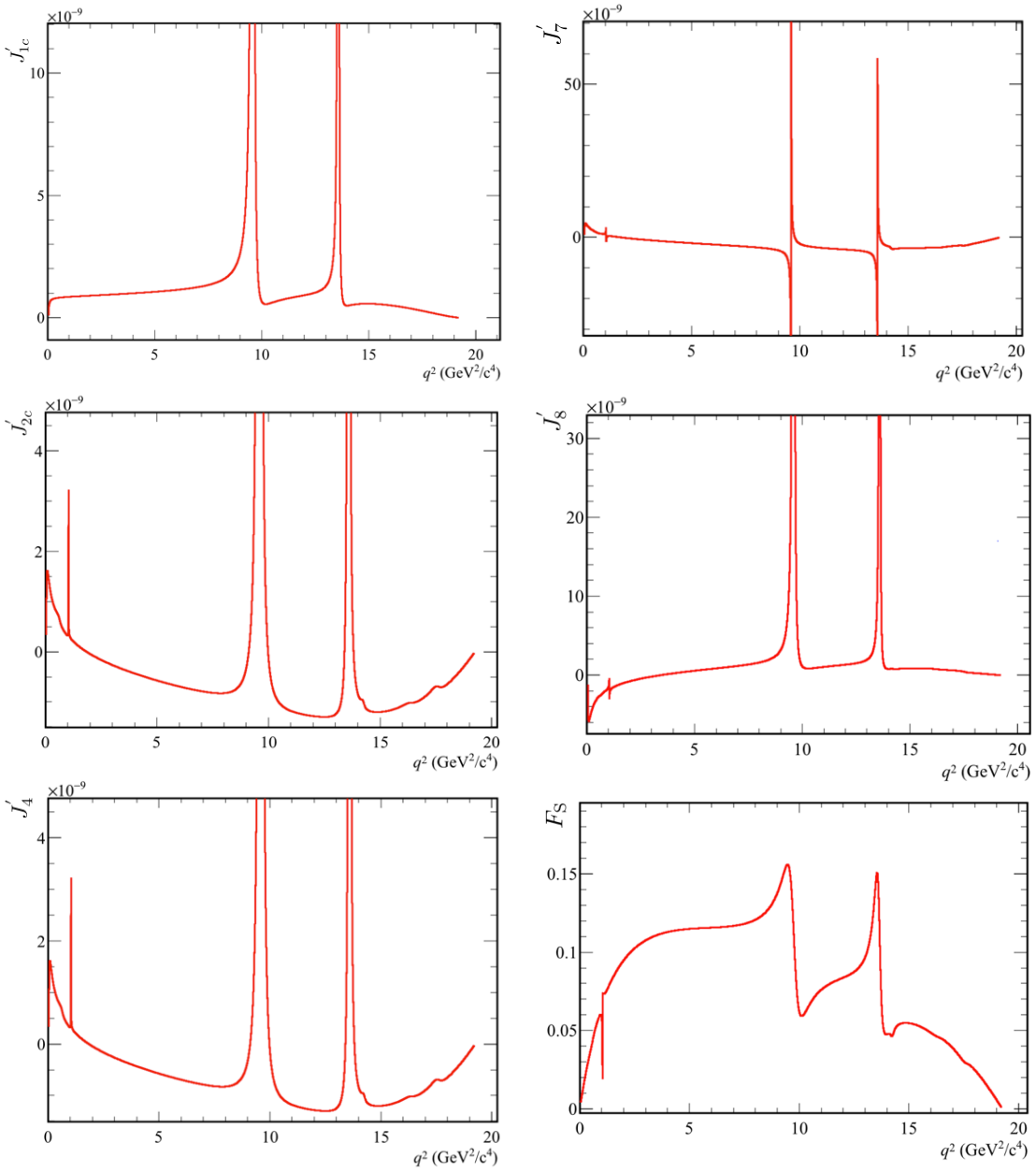

Figure 4.18: Distributions for the S-wave angular observables J'_{1c}, J'_{2c}, J'_4, J'_7, J'_8 and F_S as a function of q^2. The red line corresponds to the central values of the observables. Possible fluctuations in the form factors have been omitted due to the lack of knowledge of the S-wave form factors. The expressions for the S-wave angular observables have been taken from Ref [101].

Chapter 5

Toy Studies

The statistical precision and stability of the fit was investigated through generating and fitting toy data samples using the signal and background models, described in Section 3.1 and Section 4.4. Each toy was generated according to the expected number of signal and background events in Run 1 and Run 2 data. Detector effects are accounted for using the approach taken in Section 4.5. With regards to the non-local contributions, the free phase θ_i^0 are set to one of the four solutions that describe the data in the mirrored decay, $B^+ \to K^+\mu^+\mu^-$ [45]. The exact solution used corresponds to where both $\theta^0_{J/\psi}$ and $\theta^0_{\psi(2S)}$ are both negative. The sign of all other resonances remains the same across all four solutions, where the higher resonances and θ^0_ρ are all negative, while θ^0_ϕ is positive. The non-local contributions entering C_7, i.e ζ_λ and ω_λ, is set to values based on Ref [3]. Preliminary studies of the toys revealed that for the resonant contributions that occur with a much lower magnitude, i.e the low q^2 resonances (ρ^0), high q^2 resonances ($\psi(3770)$, $\psi(4040)$, $\psi(4160)$) and the $\zeta^{\parallel,\perp,0}$, $\omega^{\parallel,\perp,0}$ parameters, fitting for magnitude and phase was problematic. This was because the value for the magnitude was very low and would reach a limit of 0, which meant that there would be no sensitivity to the phase. The outcome of this was that for these non-local contributions a change to fitting for the real and imaginary parts of the complex number was made.

A five dimensional maximum likelihood fit in the dimensions of q^2, cos θ_K, cos θ_ℓ, ϕ and $m_{K\pi\mu\mu}$ was performed to the toy data samples. The background parameters were obtained from fits to the upper mass sidebands in the data and fixed to these values.

This meant that only the signal parameters were floating in the simultaneous (signal and background) fit. For each signal parameters in a given fit the starting values for the parameters were fluctuated according to a Gaussian distribution centred at the true value and with a width set to 10% of the true value. In the fits, all non-local contributions are fitted for. This includes resonant contributions and the $\bar{B}^0 \to \bar{K}^{*0}\mu^+\mu^-$ form factors. With regards to the dominant J/ψ and $\psi(2S)$ resonances, for which there are experimental measurements, preliminary studies also revealed that the fit was capable of determining the free phase θ_j^0 to a very good precision. This meant that there was no extra sensitivity gained from fitting the phases $\theta_j^\perp$ and $\theta_j^\parallel$, given that these are measured relative to the free phase. In light of this result, these phases are fixed to their previously measured values. Additionally, the parameter $\eta^0_{J/\psi}$ is fixed in order to set the scale of the fit, and therefore all other parameters are measured relative to $\eta^0_{J/\psi}$. In addition, it is noted that only the vector form factors are fitted for and the tensor form factors are fixed to their true values. The tensor form factors are fixed as there is a degeneracy with the constant coefficient of the tensor form factors with the $\zeta_{\perp,\parallel,0}$ and $\zeta_{\perp,\parallel,0}$ parameters. This is demonstrated by the combination of Equation 5.1, which shows the tensor component ($\mathcal{G}_0^T$) of the non-local terms $\mathcal{G}_0$ that enter the longitudinal amplitude, and Equation 1.36 in Chapter 1 that shows the structure of a form factor.

$$\mathcal{G}_0^T = \frac{m_b}{m_B + m_{K^*}} T_{23}(q^2)\zeta^0 e^{i\omega^0} \tag{5.1}$$

In each fit, the vector form factors were Gaussian constrained to their true values, using input from the covariance matrix of all form factor parameters given by Ref [13]. The magnitude of the Wilson Coefficients, C_9 and C_{10} are fitted for and the phases remain fixed to the true values. For the terms $C_9^\prime$, $C_{10}^\prime$ the model dependent assumption is made that we can fix these parameters to their SM values. The other Wilson Coefficients, C_7 and $C_7^\prime$ are fixed as these parameters are better understood from $b \to s\gamma$ measurements [102].

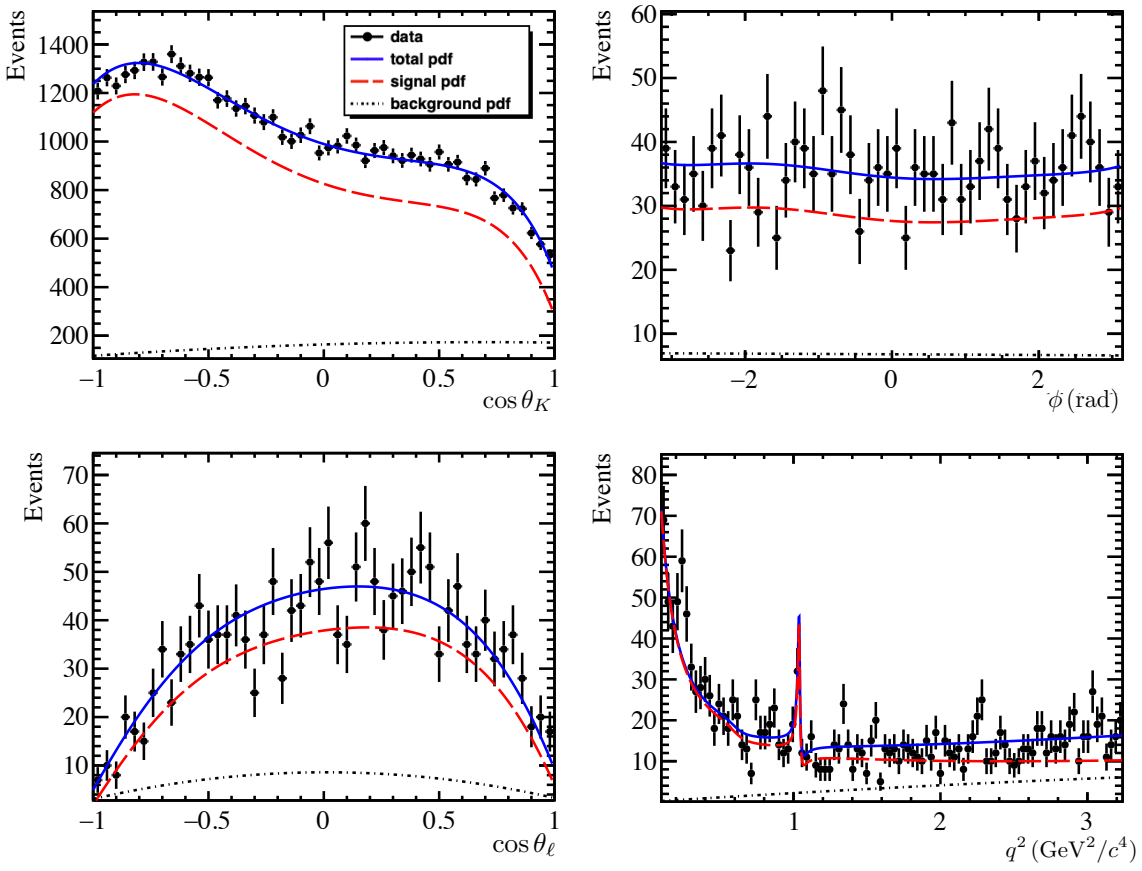

Figure 5.1: The projections of a fit to a toy dataset in the dimensions of cos θ_K, cos θ_ℓ, ϕ and q^2 and shown for the low q^2 region of [0.1, 3.34] GeV$^2/c^4$. The data is shown by the black data points and the pdf used to fit this data is the combined signal and background pdf displayed by the solid, blue line. The individual pdfs that form the total pdf are also presented, where the signal pdf is shown by the dashed, red line and the background pdf is shown by the dotted-dashed, black line.

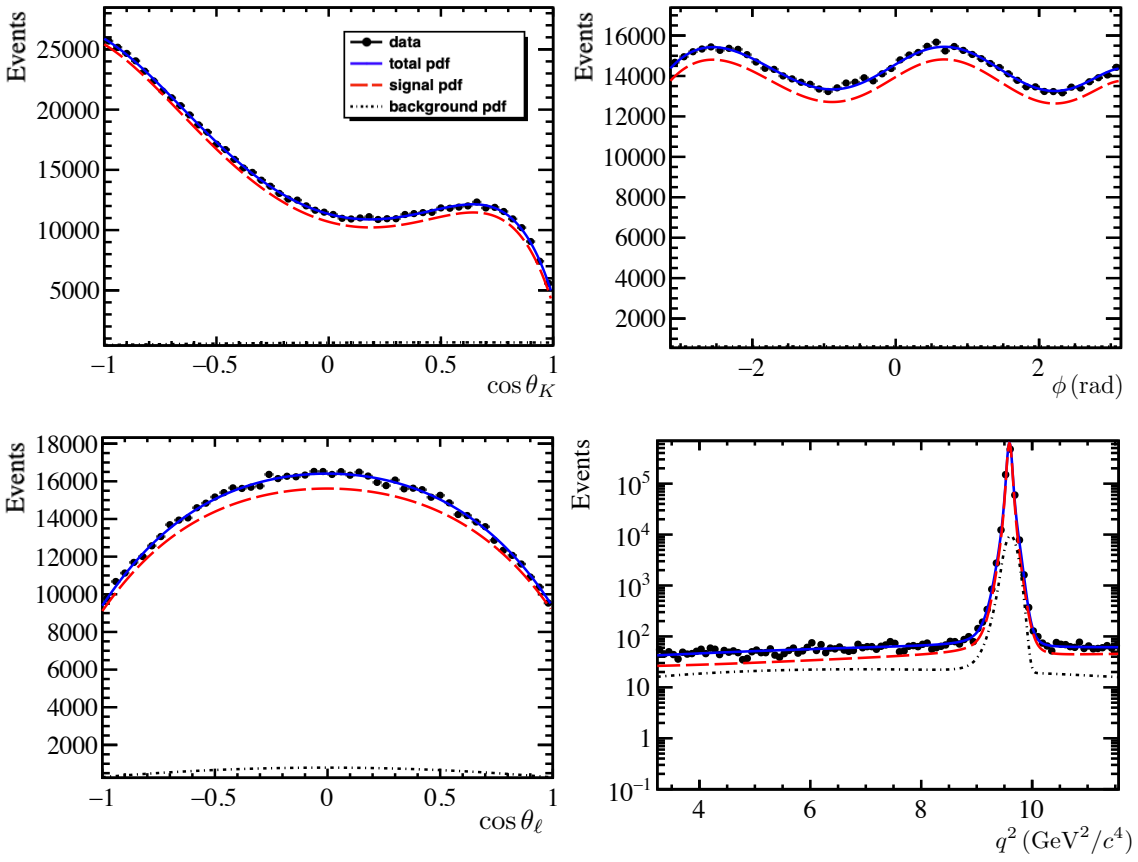

Figure 5.2: The projections of a fit to a toy dataset in the dimensions of cos θ_K, cos θ_ℓ, ϕ and q^2 and shown for the central q^2 region of [3.34, 11.56] GeV$^2/c^4$. The data is shown by the black data points and the pdf used to fit this data is the combined signal and background pdf displayed by the solid, blue line. The individual pdfs that form the total pdf are also presented, where the signal pdf is shown by the dashed, red line and the background pdf is shown by the dotted-dashed, black line.

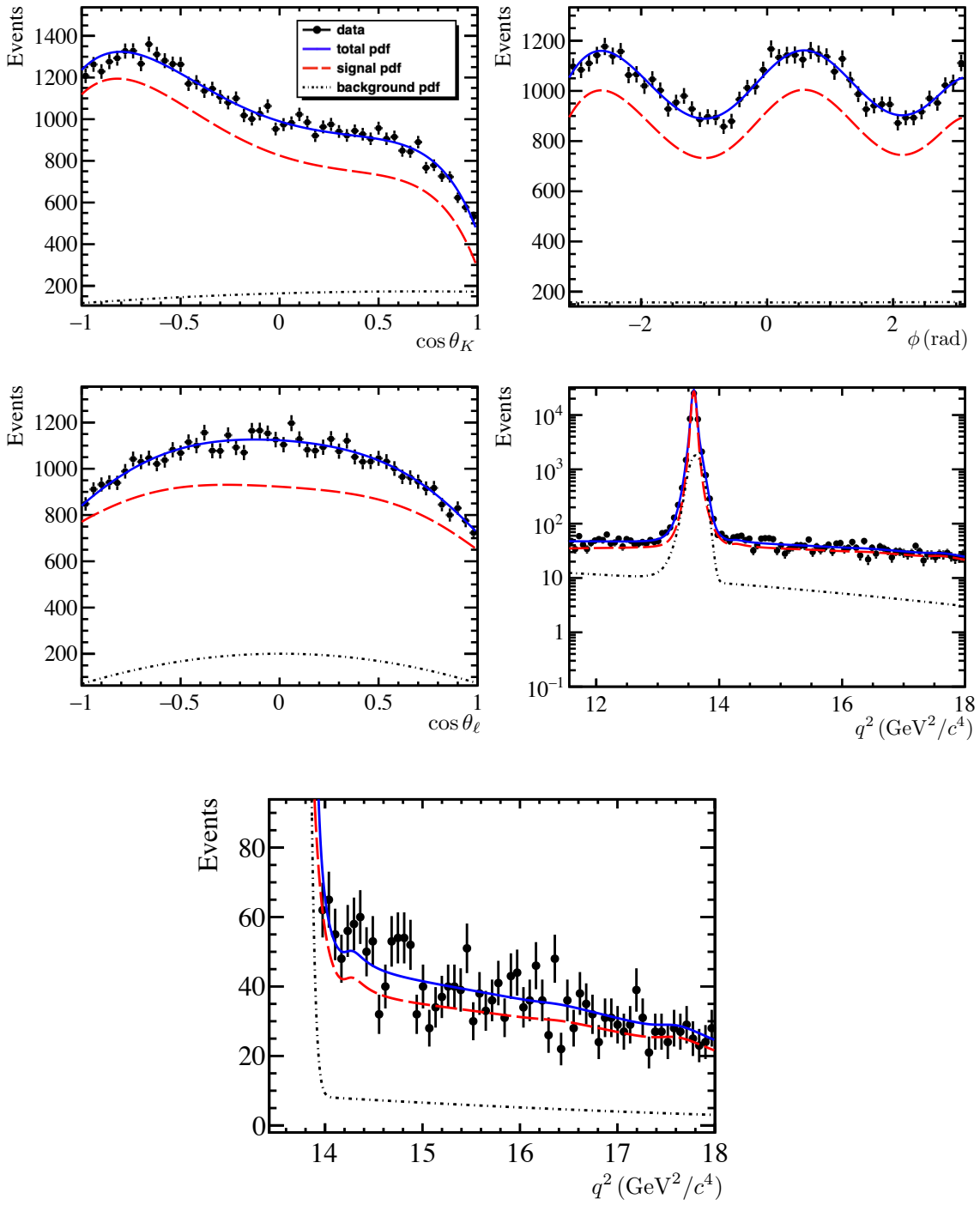

Figure 5.3: The projections of a fit to a toy dataset in the dimensions of cos θ_K, cos θ_ℓ, ϕ and q^2 and shown for the high q^2 region of [11.56, 18.0] GeV$^2/c^4$. The data is shown by the black data points and the pdf used to fit this data is the combined signal and background pdf displayed by the solid, blue line. The individual pdfs that form the total pdf are also presented, where the signal pdf is shown by the dashed, red line and the background pdf is shown by the dotted-dashed, black line.

Figures 5.1, 5.2, 5.3, show the projections of a fit to a single toy in the dimensions (q^2, cos θ_K, cos θ_ℓ, ϕ). In each of these figures, the blue line shows the total pdf (signal + background), the red dashed line shows the signal pdf, the black dot-dash represents the background pdf and the data points show the toy data. It is evident in these figures that there is some discrepancy where the total pdf does not fully fit to the data. This was investigated and found to because contributions from the background had not been implemented yet, as additional features for the background model needed to be investigated and implemented into the model. This work goes beyond the scope of this thesis. Nevertheless, for the studies in this Chapter, this effect was taken into account in the determination of the parameters and the conclusions are still valid. In Figure 5.1, the q^2 projection plot (bottom right) clearly shows the ϕ resonance shown through a rising and falling structure and the slight hump to the left of the ϕ is the ρ^0 resonance. In Figure 5.2 (bottom right) the dominant J/ψ resonance (at 9.59 GeV$^2/c^4$) is visible and likewise in Figure 5.3 (centre right) the dominant $\psi(2S)$ (at 13.59 GeV$^2/c^4$) is also clearly visible. For the higher resonances ($\psi(3770)$, $\psi(4040)$, $\psi(4160)$) a zoomed in plot of the projection in q^2 has been added to Figure 5.3 (bottom) to illustrate these resonant contributions that contribute with a much smaller magnitude and are broad. The fit results from 500 fits to toy datasets were analysed. For each toy, the pull was calculated for every parameter of interest, floating in the fit. The pull, p is defined as,

$$p = \frac{x^i_{fit} - x^i_{true}}{\Delta x^i} \tag{5.2}$$

where, x^i_{fit} is the fit value of a given parameter i, Δx^i is the error on the value reported from the Hessian error matrix of the fit, and x^i_{true} is the parameter's true value. While this was the case for the majority of parameters, the pulls for $|C_9|$ and $|C_{10}|$ were calculated with asymmetric errors. This was because studies revealing that the distribution of the reported fit values for $|C_9|$ and $|C_{10}|$ were non Gaussian and asymmetric. The asymmetric errors were calculated through a profile likelihood at ΔNLL = 0.5 as calculated by MINOS [103]. The previous expression for the pull cannot be applied in the case of asymmetric errors. The pull for a parameter with asymmetric errors is calculated by either using Equation 5.3 or Equation 5.4, where Equation 5.3 is used if the reported fit value is less than or equal to the true value of the parameter, and

if not then one uses Equation 5.4 [104]. In Equation 5.3, Δx^i_+ is the positive MINOS error and in Equation 5.4, Δx^i_- is the negative minos error.

$$p = \frac{x^i_{true} - x^i_{fit}}{\Delta x^i_+} \tag{5.3}$$

$$p = \frac{x^i_{fit} - x^i_{true}}{\Delta x^i_-} \tag{5.4}$$

The distributions of the pulls from toys that converged successfully and with a positive definite error matrix are given in Figures 5.4, 5.5, 5.6. The fraction of fits that converged successfully was 96%. In these figures, the pull distributions are shown for the non-local contributions and the Wilson Coefficients. In each pull distribution, the black data points show the pull values for the toys. The pulls should be Gaussianly distributed, so one can fit a Gaussian pdf to this distribution to obtain values for the μ and σ. Each Gaussian is expected to have a μ of 0 and a σ of 1, demonstrating that the results of the fit are unbiased and the coverage of the fit is good. In Figures 5.4, 5.5, 5.6 the result of the fit can be seen by the solid, red line and Table 5 summarises the values for the μ and σ reported by the Gaussian fit to the pull distributions. Table 5 and Figure 5.4, show the pull of $|C_9|$ follows a Gaussian distribution, and the reported μ and σ from the Gaussian fit are consistent with a standard Gaussian distribution, demonstrating the coverage is good for this parameter. The distribution of the value of $|C_9|$, shown in Figure 5.7 by the data points, is consistent with the true value of $|C_9|$ (solid, red line). Nevertheless, there appears to be a slight bias in the values of the μ and σ reported for $|C_{10}|$. However, the most likely value of $|C_{10}|$ is consistent with the true value as shown in Figure 5.7. Furthermore, the 1σ asymmetric interval band for $|C_{10}|$ was determined by taking each fit that passed with a positive definite error matrix and calculating the difference between the fit value and the true value. If the difference was less than or equal to the error on $|C_{10}|$ then it was recorded as an event that was within 1σ. Applying this to all the fits, the 1σ asymmetric interval band for $|C_{10}|$ was calculated to be 0.66 $\pm$ 0.02. This suggests the coverage was adequate for $|C_{10}|$. That aside, fitting the model with larger toy data samples removes this bias, as demonstrated by the pull distribution for $|C_{10}|$ from toys with $10\times$ the number of statistics. This indicates that there are no issues in the fit, and instead we are dominated by the statistics available.

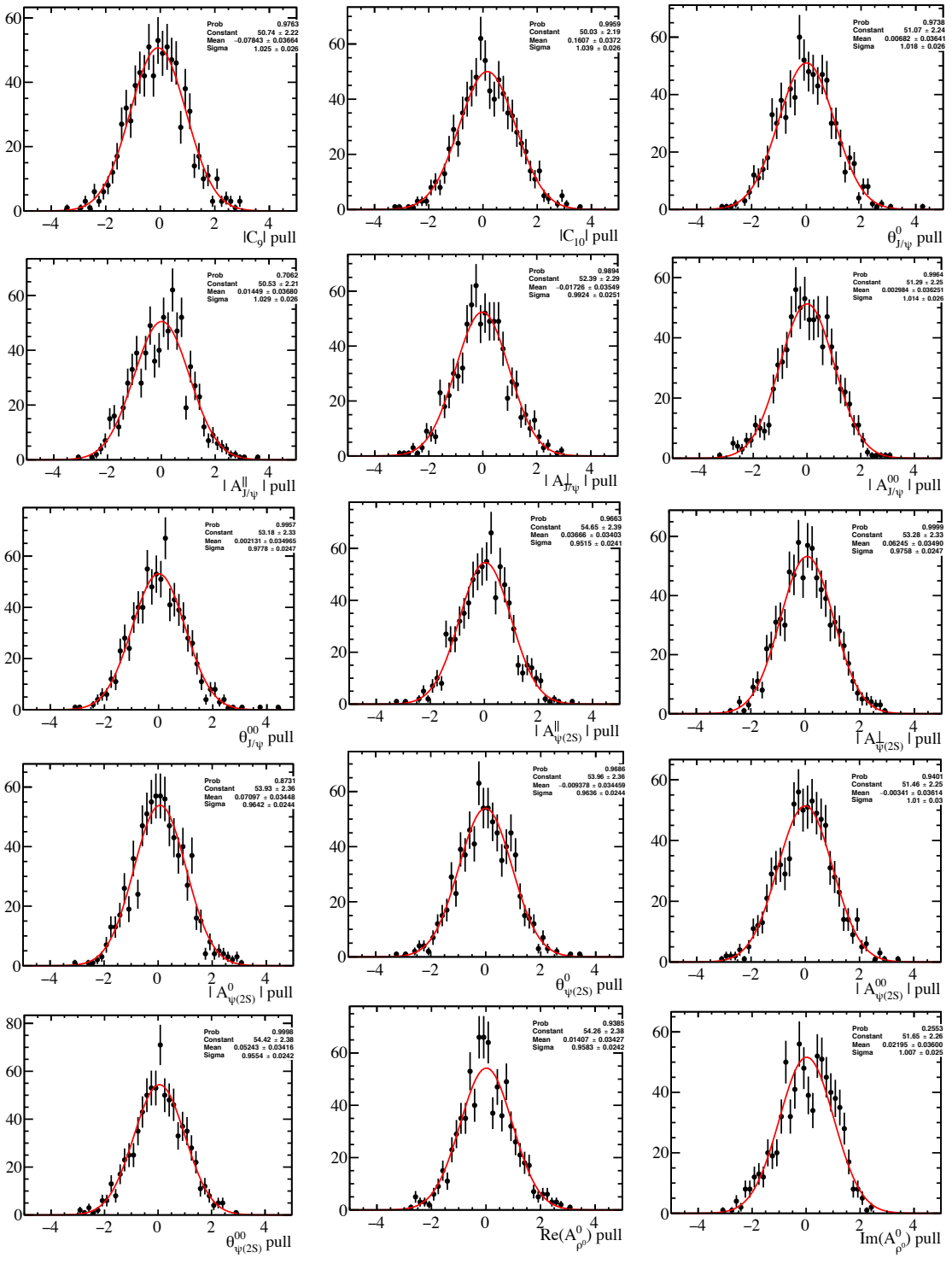

Figure 5.4: The pull distributions for the Wilson Coefficients and the non-local contributions from toy studies. The black data points represent the pull values and the solid, red line is the Gaussian fit to the pull distribution.

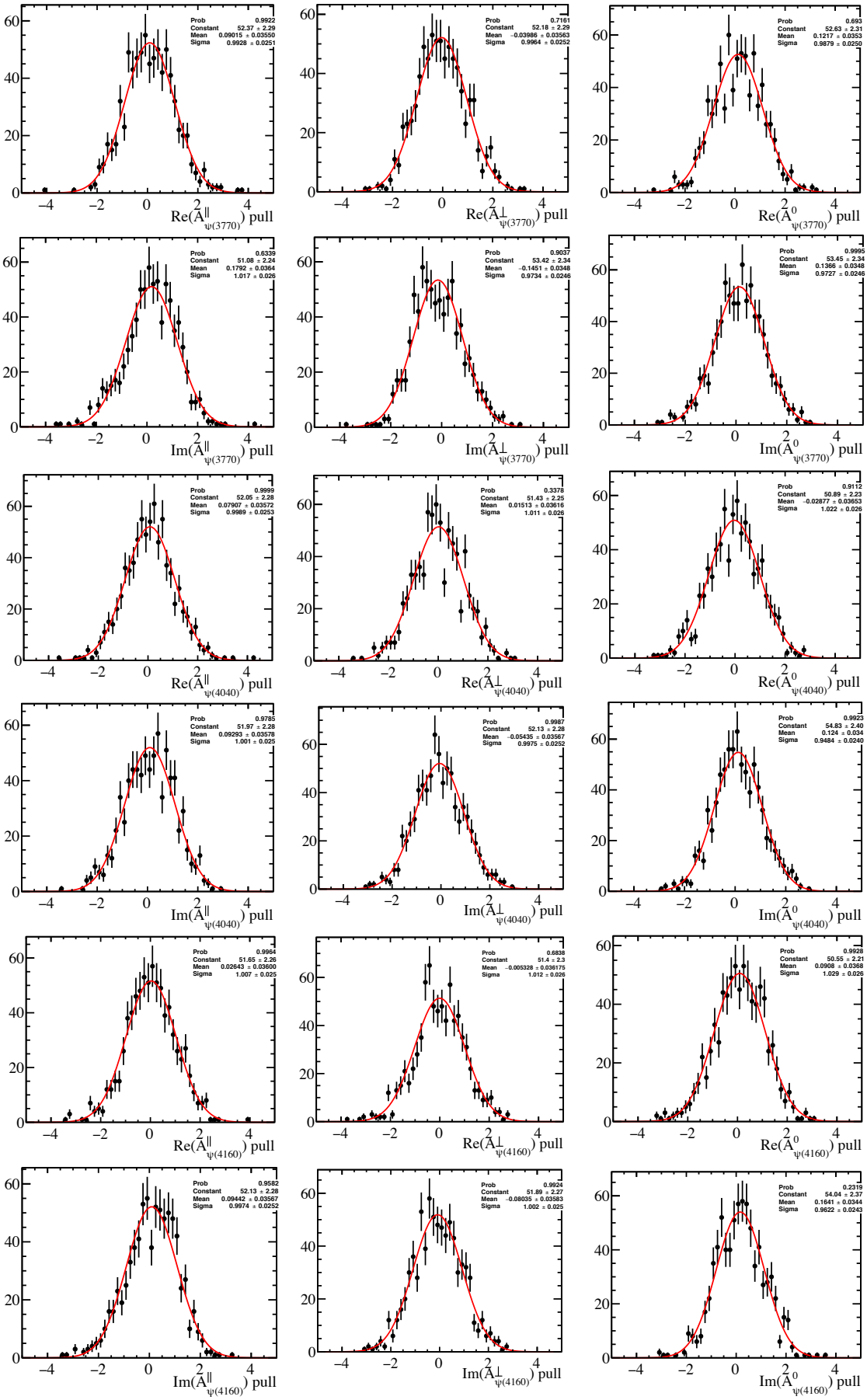

Figure 5.5: The pull distributions for the higher resonances from the toy studies. The black data points represent the pull values and the solid, red line is the Gaussian fit to the pull distribution.

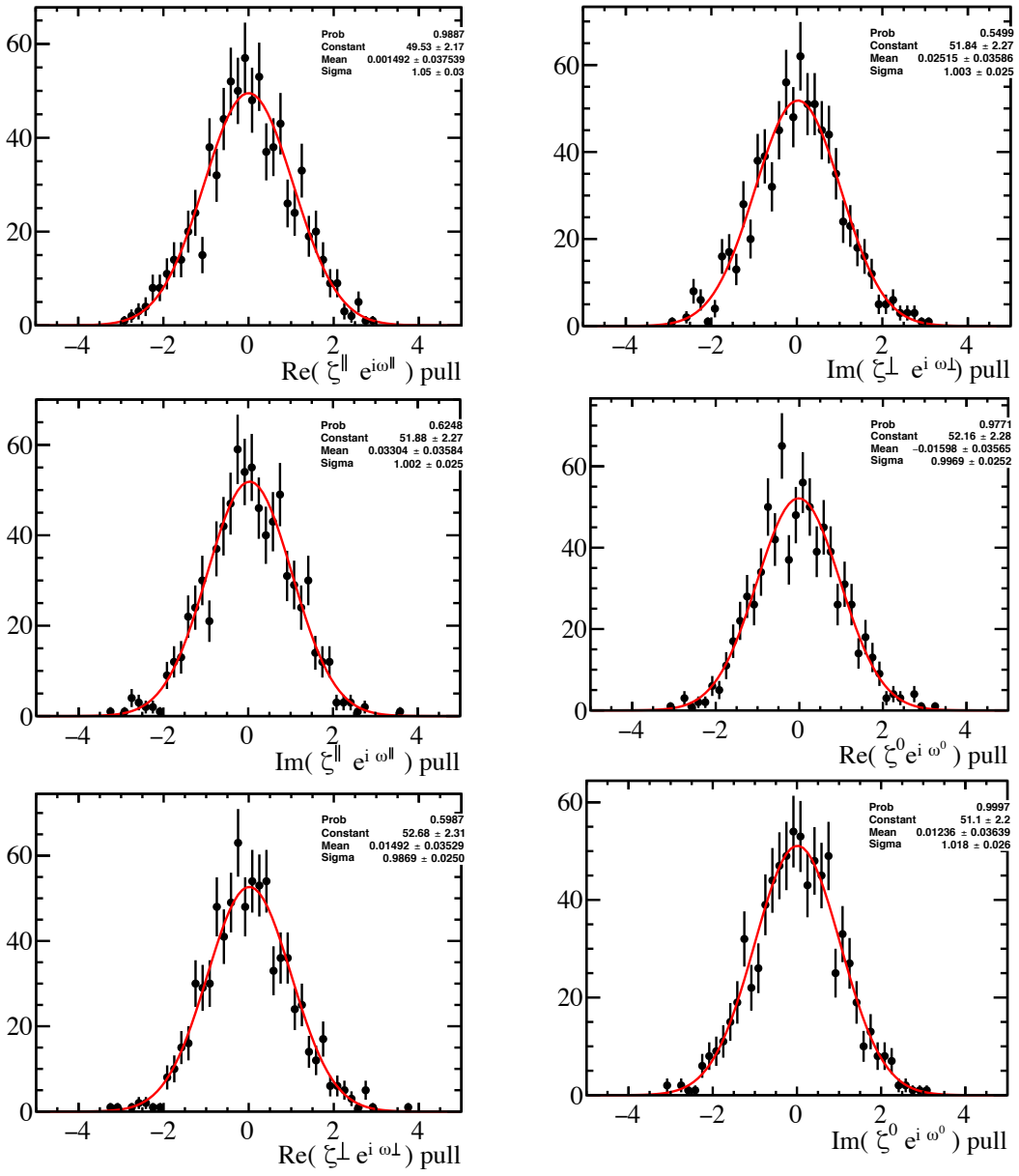

Figure 5.6: The pull distributions for the real and imaginary components of the non-local contributions $\zeta^{\parallel,\perp,0}e^{i\omega^{\parallel,\perp,0}}$. The black data points represent the pull values and the solid, red line is the Gaussian fit to the pull distribution.

Parameter	μ	σ
$\lvert C_9\rvert$	-7.84 $\times 10^{-2}$ $\pm$ 3.66 $\times 10^{-2}$	1.03 $\pm$ 2.59 $\times 10^{-2}$
$\lvert C_{10}\rvert$	1.61 $\times 10^{-1}$ $\pm$ 3.72 $\times 10^{-2}$	1.04 $\pm$ 2.63 $\times 10^{-2}$
$\theta^0_{J/\psi}$	6.82 $\times 10^{-3}$ $\pm$ 3.64 $\times 10^{-2}$	1.02 $\pm$ 2.58 $\times 10^{-2}$
$\eta^{\parallel}_{J/\psi}$	1.45 $\times 10^{-2}$ $\pm$ 3.68 $\times 10^{-2}$	1.03 $\pm$ 2.60 $\times 10^{-2}$
$\eta^{\perp}_{J/\psi}$	-1.73 $\times 10^{-2}$ $\pm$ 3.55 $\times 10^{-2}$	0.99 $\pm$ 2.51 $\times 10^{-2}$
$\eta^{00}_{J/\psi}$	2.98 $\times 10^{-3}$ $\pm$ 3.63 $\times 10^{-2}$	1.01 $\pm$ 2.56 $\times 10^{-2}$
$\theta^{00}_{J/\psi}$	2.13 $\times 10^{-3}$ $\pm$ 3.50 $\times 10^{-2}$	0.98 $\pm$ 2.47 $\times 10^{-2}$
$\eta^{\parallel}_{\psi(2S)}$	3.67 $\times 10^{-2}$ $\pm$ 3.40 $\times 10^{-2}$	0.95 $\pm$ 2.41 $\times 10^{-2}$
$\eta^{\perp}_{\psi(2S)}$	6.25 $\times 10^{-2}$ $\pm$ 3.49 $\times 10^{-2}$	0.98 $\pm$ 2.47 $\times 10^{-2}$
$\eta^{0}_{\psi(2S)}$	7.10 $\times 10^{-2}$ $\pm$ 3.45 $\times 10^{-2}$	0.96 $\pm$ 2.44 $\times 10^{-2}$
$\theta^{0}_{\psi(2S)}$	9.38 $\times 10^{-3}$ $\pm$ 3.45 $\times 10^{-2}$	0.96 $\pm$ 2.44 $\times 10^{-2}$
$\eta^{00}_{\psi(2S)}$	-3.41 $\times 10^{-3}$ $\pm$ 3.61 $\times 10^{-2}$	1.01 $\pm$ 2.56 $\times 10^{-2}$
$\theta^{00}_{\psi(2S)}$	5.24 $\times 10^{-2}$ $\pm$ 3.42 $\times 10^{-2}$	0.96 $\pm$ 2.42 $\times 10^{-2}$
$\mathrm{Re}(\mathrm{A}^0_{\rho^0})$	1.41 $\times 10^{-2}$ $\pm$ 3.43 $\times 10^{-2}$	0.96 $\pm$ 2.42 $\times 10^{-2}$
$\mathrm{Im}(\mathrm{A}^0_{\rho_0})$	2.20 $\times 10^{-2}$ $\pm$ 3.70 $\times 10^{-2}$	1.01 $\pm$ 2.55 $\times 10^{-2}$
$\mathrm{Re}(\mathrm{A}^{\parallel}_{\psi(3770)})$	9.02 $\times 10^{-2}$ $\pm$ 3.55 $\times 10^{-2}$	0.99 $\pm$ 2.51 $\times 10^{-2}$
$\mathrm{Im}(\mathrm{A}^{\parallel}_{\psi(3770)})$	1.79 $\times 10^{-1}$ $\pm$ 3.64 $\times 10^{-2}$	1.02 $\pm$ 2.57 $\times 10^{-2}$
$\mathrm{Re}(\mathrm{A}^{\perp}_{\psi(3770)})$	-3.99 $\times 10^{-2}$ $\pm$ 3.56 $\times 10^{-2}$	1.00 $\pm$ 2.52 $\times 10^{-2}$
$\mathrm{Im}(\mathrm{A}^{\perp}_{\psi(3770)})$	-1.45 $\times 10^{-1}$ $\pm$ 3.48 $\times 10^{-2}$	0.97 $\pm$ 2.46 $\times 10^{-2}$
$\mathrm{Re}(\mathrm{A}^0_{\psi(3770)})$	1.22 $\times 10^{-1}$ $\pm$ 3.53 $\times 10^{-2}$	0.99 $\pm$ 2.50 $\times 10^{-2}$
$\mathrm{Im}(\mathrm{A}^0_{\psi(3770)})$	1.37 $\times 10^{-1}$ $\pm$ 3.48 $\times 10^{-2}$	0.97 $\pm$ 2.46 $\times 10^{-2}$
$\mathrm{Re}(\mathrm{A}^{\parallel}_{\psi(4040)})$	7.91 $\times 10^{-2}$ $\pm$ 3.57 $\times 10^{-2}$	1.00 $\pm$ 2.53 $\times 10^{-2}$
$\mathrm{Im}(\mathrm{A}^{\parallel}_{\psi(4040)})$	9.29 $\times 10^{-2}$ $\pm$ 3.58 $\times 10^{-2}$	1.00 $\pm$ 2.53 $\times 10^{-2}$
$\mathrm{Re}(\mathrm{A}^{\perp}_{\psi(4040)})$	1.51 $\times 10^{-2}$ $\pm$ 3.62 $\times 10^{-2}$	1.01 $\pm$ 2.56 $\times 10^{-2}$
$\mathrm{Im}(\mathrm{A}^{\perp}_{\psi(4040)})$	-5.43 $\times 10^{-2}$ $\pm$ 3.57 $\times 10^{-2}$	1.00 $\pm$ 2.52 $\times 10^{-2}$
$\mathrm{Re}(\mathrm{A}^0_{\psi(4040)})$	-2.88 $\times 10^{-2}$ $\pm$ 3.65 $\times 10^{-2}$	1.02 $\pm$ 2.58 $\times 10^{-2}$
$\mathrm{Im}(\mathrm{A}^0_{\psi(4040)})$	1.24 $\times 10^{-1}$ $\pm$ 3.39 $\times 10^{-2}$	0.95 $\pm$ 2.40 $\times 10^{-2}$
$\mathrm{Re}(\mathrm{A}^{\parallel}_{\psi(4160)})$	2.64 $\times 10^{-2}$ $\pm$ 3.60 $\times 10^{-2}$	1.01 $\pm$ 2.55 $\times 10^{-2}$
$\mathrm{Im}(\mathrm{A}^{\parallel}_{\psi(4160)})$	9.44 $\times 10^{-2}$ $\pm$ 3.57 $\times 10^{-2}$	1.00 $\pm$ 2.52 $\times 10^{-2}$
$\mathrm{Re}(\mathrm{A}^{\perp}_{\psi(4160)})$	5.33 $\times 10^{-3}$ $\pm$ 3.62 $\times 10^{-2}$	1.01 $\pm$ 2.56$\times 10^{-2}$
$\mathrm{Im}(\mathrm{A}^{\perp}_{\psi(4160)})$	-8.04 $\times 10^{-2}$ $\pm$ 3.58 $\times 10^{-2}$	1.00 $\pm$ 2.53 $\times 10^{-2}$
$\mathrm{Re}(\mathrm{A}^0_{\psi(4160)})$	9.08 $\times 10^{-2}$ $\pm$ 3.68 $\times 10^{-2}$	1.03 $\pm$ 2.60 $\times 10^{-2}$
$\mathrm{Im}(\mathrm{A}^0_{\psi(4160)})$	1.64 $\times 10^{-1}$ $\pm$ 3.44 $\times 10^{-2}$	0.96 $\pm$ 2.43 $\times 10^{-2}$
$\mathrm{Re}(\zeta^{\parallel}e^{i\omega\parallel})$	1.49 $\times 10^{-3}$ $\pm$ 3.75 $\times 10^{-2}$	1.05 $\pm$ 2.66 $\times 10^{-2}$
$\mathrm{Im}(\zeta^{\parallel}e^{i\omega\parallel})$	3.30 $\times 10^{-2}$ $\pm$ 3.58 $\times 10^{-2}$	1.00 $\pm$ 2.53 $\times 10^{-2}$
$\mathrm{Re}(\zeta^{\perp}e^{i\omega\perp})$	1.49 $\times 10^{-2}$ $\pm$ 3.53 $\times 10^{-2}$	0.99 $\pm$ 2.50 $\times 10^{-2}$
$\mathrm{Im}(\zeta^{\perp}e^{i\omega\perp})$	2.52 $\times 10^{-2}$ $\pm$ 3.59 $\times 10^{-2}$	1.00 $\pm$ 2.54 $\times 10^{-2}$
$\mathrm{Re}(\zeta^{0}e^{i\omega 0})$	-1.60 $\times 10^{-2}$ $\pm$ 3.56 $\times 10^{-2}$	1.00 $\pm$ 2.52 $\times 10^{-2}$
$\mathrm{Im}(\zeta^{0}e^{i\omega 0})$	1.24 $\times 10^{-2}$ $\pm$ 3.64 $\times 10^{-2}$	1.02 $\pm$ 2.57 $\times 10^{-2}$

Table 5.1: The reported values for the μ and σ for the non-local contributions and the Wilson Coefficient, from fitting a Gaussian to the pull distributions presented in Figures 5.4, 5.5, 5.6.

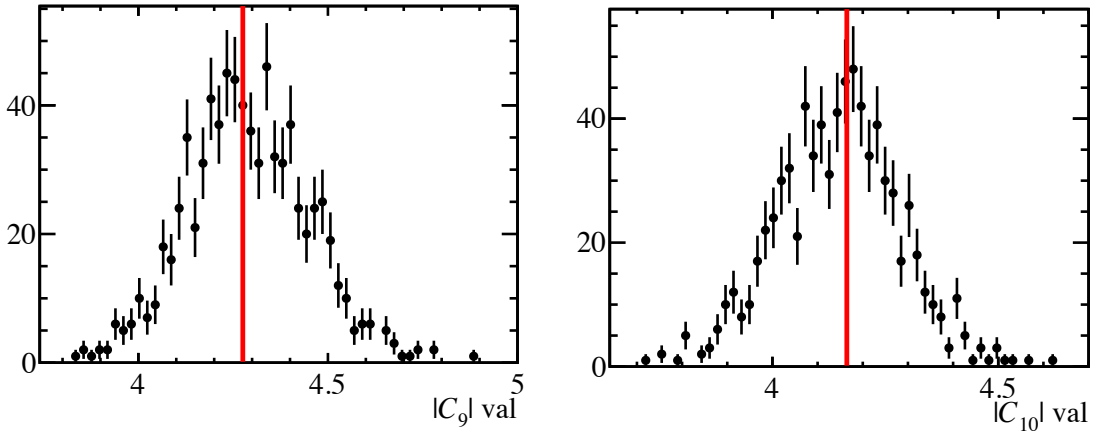

Figure 5.7: The distribution of the fit values for $|C_9|$ and $|C_{10}|$ from toys that have converged successfully with a positive definite error matrix. The black data points show the fit values and the solid red line denotes the true value of the given Wilson Coefficient.

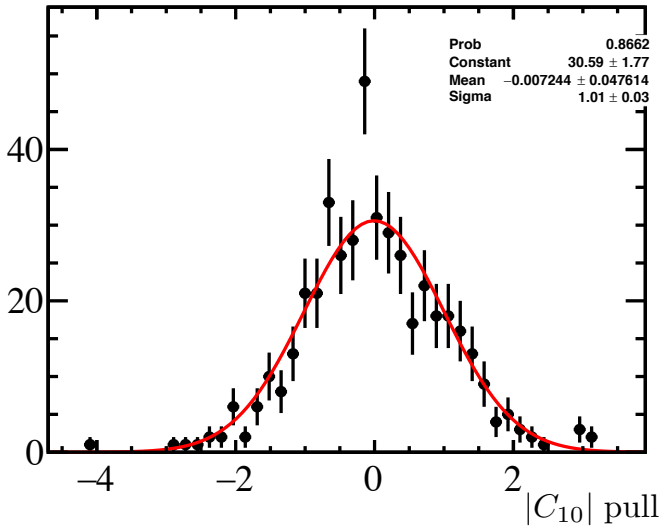

Figure 5.8: The pull distribution of $|C_{10}|$ from toys with 10× more candidates and have converged successfully with a positive definite correlation matrix. The pull values are shown by the black data points, and the Gaussian fit performed to this distribution is shown by the solid, red line.

For the non-local contributions there are variations in the pull distributions and Gaussian fit results. The pull distributions for the magnitudes and phases of both the P-wave and S-wave amplitudes for the J/ψ resonance, all follow a Gaussian distribution, as shown in Figure 5.4. The reported μ and σ from these plots is given in Table 5 and are consistent with a standard Gaussian distribution. Similar behaviour is seen for the $\psi(2S)$, where the P-wave and S-wave amplitudes all demonstrate good pull distributions and have a good coverage. Regarding the higher resonances above the $\psi(2S)$ and $D\bar{D}$ threshold,

the general pattern is that the reported σ are all consistent with unity, however there is a bias in the mean across the various real and imaginary components of the amplitudes. Therefore, for these parameters the bias will be taken as a systematic uncertainty in the final fit. Moving onto the non-local contributions $\zeta^{\parallel,\perp,0}$ and $\omega^{\parallel,\perp,0}$, it is apparent that all these terms exhibit a Gaussian distribution (see Figure 5.6) and the values for the μ and σ are all compatible with a standard Gaussian.

The coefficients of the form factors are not considered as parameters of interest because the data does not significantly improve their precision. Therefore, the form factors from the fit are compared to their values in the literature [13]. Figure 5.9 shows the 68% confidence interval (magenta band) of possible values for the vector form factors, A_1, A_{12} and V, by taking the values and covariance matrix of the coefficients reported from the fit and constructing the form factors using the parametrisation used in the model. This band of values, is compared to the 68% confidence interval (blue band) obtained from varying the predicted values of the form factors taken from Ref [13]. For completeness the central values given by Ref [13] are shown by the dashed black line. The results reveal that for each form factor, the 68% confidence interval produced by the fit lies within the 68% confidence interval taken from Ref [13]. This shows that the fit only marginally improves the precision on the form factors.

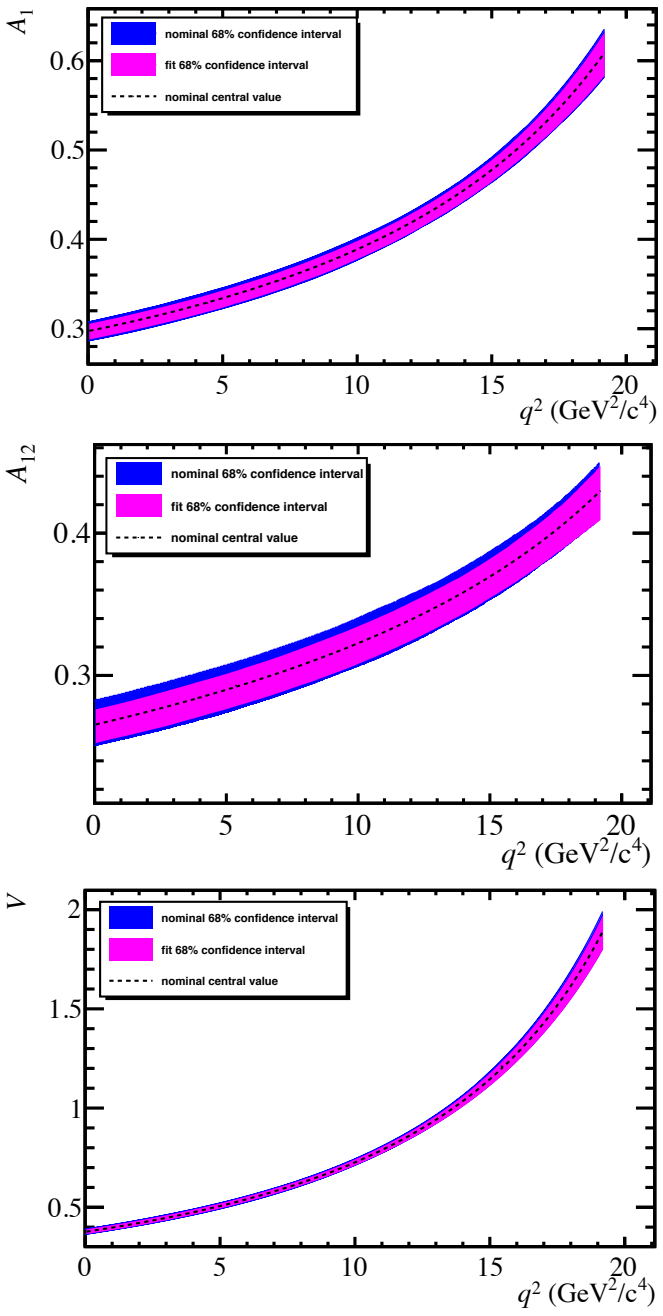

Figure 5.9: The distributions of the vector, form factors resulting from the fits, compared to the predicted theory calculation. The magenta band refers to the 68% confidence interval reported from constructing the form factors in the model using the fit values for the coefficients as input. The blue band, refers to the 68% confidence interval constructed from the nominal parametrisation of the form factors taken from Ref [13]. The dashed black line is the nominal, central values for the form factors taken also from Ref [13].

The results of the fit were used to reconstruct the distributions of the angular observables. For each toy fit that converged successfully, with a positive definite covariance matrix, the fit results were then fed into the model. Each observable was then constructed using all of these parameters, and with resolution effects applied, where the only difference to the resolution function presented in Section 4.5.1 was that the α parameters that were fitted for in the fit, were inserted into the resolution function. The observables are shown by both Figure 5.10 and Figure 5.11.

Figure 5.10 presents the distributions of the observables $P_5^{'}$ and $A_{\rm FB}$, while Figure 5.11 shows the distributions of the observables F_L, $S_{3,4,5,7,8,9}$. In both these figures the blue band of values represents the 68% confidence interval produced using the uncertainties of the fit parameters. Moreover, in Figure 5.10 the comparison of the complete model with the resonances is compared to the 68% band of values produced from the model using the fit results, with only the penguin contributions. Only fit values for the Wilson Coefficients, resolution effects and form factors are considered for this band of possible values, as all other resonant parameters are obsolete. In Figure 5.10, it is clear how the impact of the resonant contributions can drastically change the distribution of the angular observables, and in particular for $P_5^{'}$, changes the region between 1.0 $< q^2 <$ 6.0 GeV$^2c^4$, where the tension with the SM is present. To conclude, all the distributions of the angular observables present unique features, which are enhanced by the presence of the non-local contributions, verifying the conclusions given in Section 3.1.

In summary, the toy studies have revealed that the statistical precision and stability of the fit is adequate. The hadronic resonant contributions can be determined to a good precision. The precision in the Wilson Coefficients is satisfactory and the slight deviations are explained by the statistics available. A greater understanding of the form factors is achieved from the toy fits, where the results reveal that the fit only marginally improves the precision of these terms. These toy fits have validated the model and its approach, therefore allowing the analysis to progress to fit to the Run 1 and Run 2 data collected by the LHCb experiment. The final fit goes beyond the scope of this dissertation, due to the fact that the analysis is blinded and additional features needed to be implemented into the background model, before a fit to the data could be performed.

Nevertheless, the timeline for this analysis is to be completed by the end of 2020, where all the results regarding the studies presented in this Chapter will be used as input.

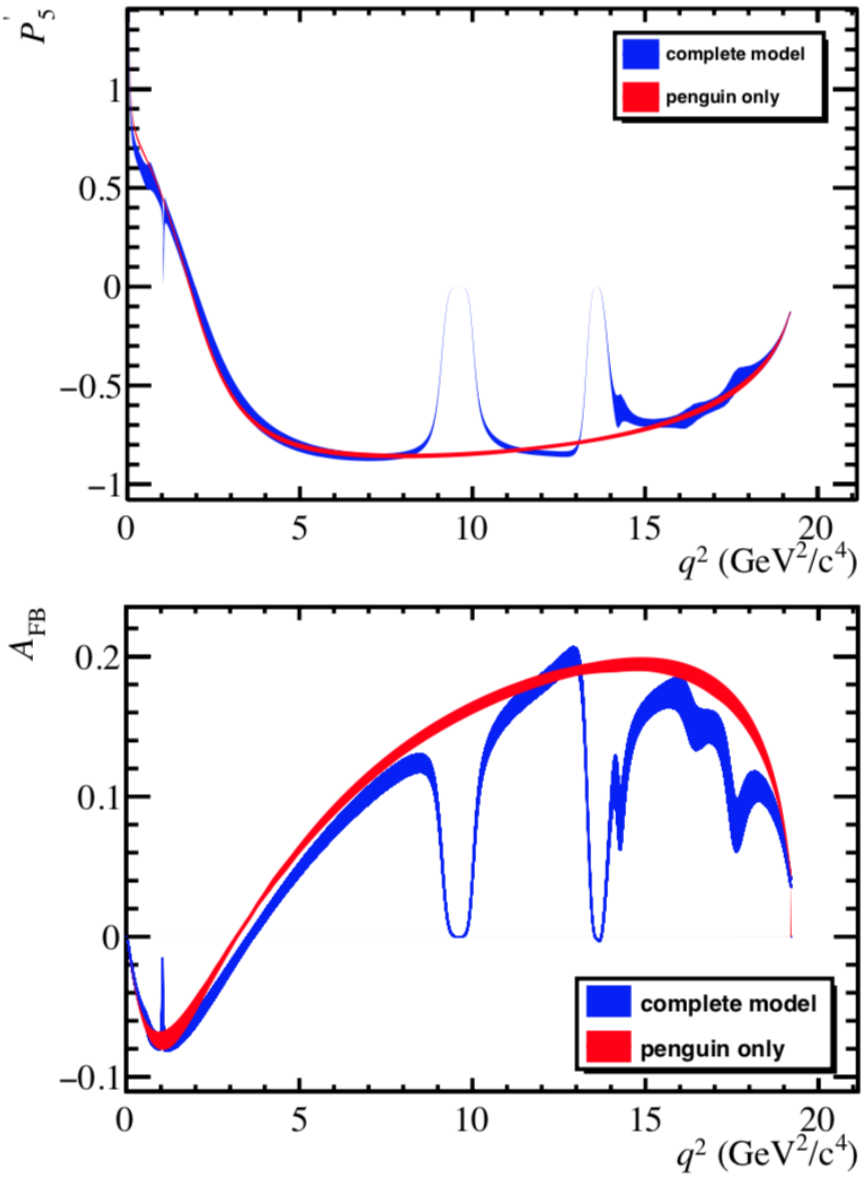

Figure 5.10: The distributions of the angular observables P_5', $A_{\rm FB}$, F_L. The blue band is the 68% interval constructed using the reported fit values from the toys.

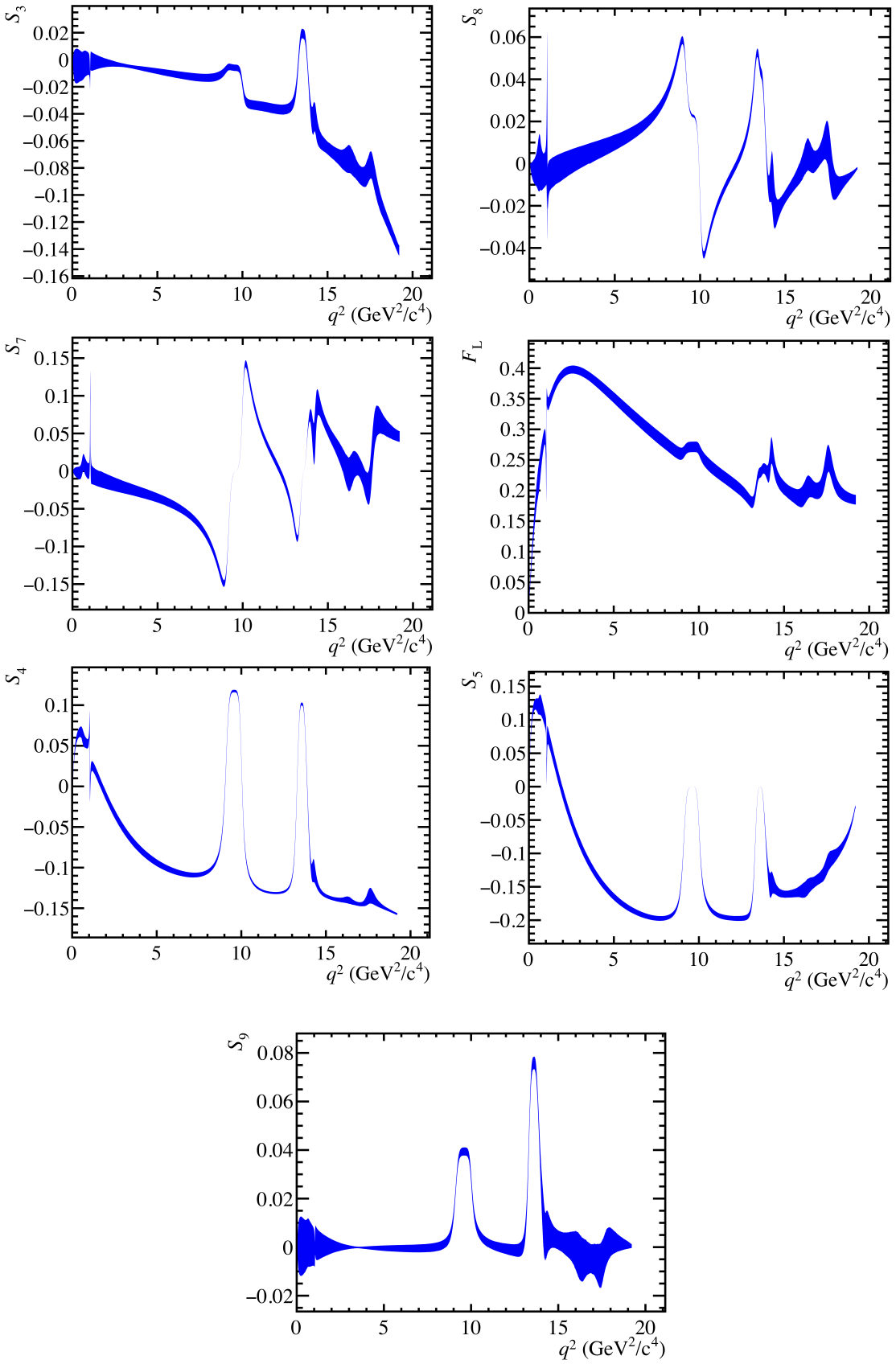

Figure 5.11: The distributions of the angular observables F_L, $S_{3,4,5,7,8,9}$. The blue band is the 68% interval constructed using the reported fit values from the toys.

Chapter 6

Systematic uncertainties

A precise measurement of the impact of the non-local contributions to $\bar{B}^0 \to \bar{K}^{*0}\mu^+\mu^-$ transitions is reliant not only on determining the interference between the amplitudes, but also by considering experimental effects that can introduce a bias to the results, and should be treated as systematic uncertainties. This chapter is dedicated to discussing the systematic uncertainties associated with assumptions assumed in the modelling of the signal and the experimental systematics. The systematic uncertainties associated with the background model go beyond the scope of this dissertation. Specifically, this chapter discusses the origin of the systematic uncertainties, how different approaches are utilised for different systematic effects, and finally how the results influence the final measurement.

6.1 Model dependant systematics

Model dependant systematics are a subset of systematic uncertainties that influence the final result based on choices and assumptions made in the model. For instance, they could arise from any limitations in the model, or from simple cuts and selection procedures. The model dependant systematics that affect this analysis are: the systematic uncertainty from ignoring the effect of exotic charmonium states in the model and the

systematic uncertainty introduced from the lack of knowledge of the parametrisation of the S-wave form factors.

6.1.1 Impact of exotic charmonium-like states

Charmonium-like states with a quark content of $|c\bar{c}ud\rangle$ have been studied by the b-factories and the LHCb experiment. The first observation of such states was performed by the Belle experiment, where the exotic $\mathrm{Z}(4430)^-$ was observed in the $\psi(2S)\pi^+$ invariant mass spectrum of $\bar{B}^0 \to \psi(2S)K^-\pi^+$ decays [105, 106]. A full angular analysis of $\mathrm{Z}(4430)^- \to \psi(2S)\pi^+$ was later performed by the Belle [80] experiment. LHCb also performed a measurement of the $\mathrm{Z}(4430)^-$ state using 3fb $^{-1}$ of data corresponding to Run 1 of the LHC [107]. Since the first observation of the exotic $\mathrm{Z}(4430)^-$ state, a further two states have been observed, the $\mathrm{Z}(4330)^+$ and the $\mathrm{Z}(4200)^+$ that were seen in the $J/\psi\pi^\pm$ invariant mass spectrum by the Belle collaboration [81]. In the analysis presented in Ref [97], the authors studied the impact of the $\mathrm{Z}(4430)^-$ on the angular distribution of $B^0 \to J/\psi K^+\pi^-$ where $\mathrm{Z}(4430)^- \to J/\psi\pi^-$. As the $\mathrm{Z}(4430)^-$ is a resonance in $m_{K\pi}$ it affects the cos θ_K distribution, manifesting itself as a peak at -0.5 . In this analysis, a systematic is assigned for the exotic charmonium-like states that can be introduced into the angular distribution through the $c\bar{c}$ states of the J/ψ and $\psi(2S)$, and are not included in the model. The size of the systematic uncertainty is estimated by generating multiple toys with $10\times$ the number of candidates expected. Each toy is generated with a unique seed and contains the exotic contributions that have been measured by Belle and BarBar collaborations, namely the $\mathrm{Z}(4430)^\pm$ and $\mathrm{Z}(4200)^+$ exotic states. These exotic components are described in the helicity amplitude basis, $H^{0,+,-}$. The penguin contributions and the non-local contributions as modelled in Section 3.1 are recast into this helicity formalism using Ref [19], before they are inserted into the toys. Furthermore, every toy generated includes acceptance and resolution effects, where the acceptance is described in Section 4.5.2 and the resolution is based on the resolution function described in Section 4.5.1. Moreover, the values for the magnitudes and phases of the transversity amplitudes in the $H_{0,+,-}$ helicity basis for the exotic contributions are set to the values taken from measured values from Belle [80, 81]. Table 6.1 shows the

Resonance	$\mid H_0 \mid$	$\arg(H_0)$	$\mid H_+ \mid$	$\arg(H_+)$	$\mid H_- \mid$	$\arg(H_-)$
$Z(4430)^+$	1.12 ± 0.32	-0.31 ± 0.26	1.17 ± 0.46	0.77 ± 0.25	1.17 ± 0.46	0.77 ± 0.25
$Z(4200)^+$	0.71 ± 0.37	2.14 ± 0.40	3.23 ± 0.79	3.00 ± 0.15	3.23 ± 0.79	3.00 ± 0.15
$Z(4430)^-$	8.85± 2.57	-2.97 ± 0.77	8.83 ± 2.75	-2.80 ± 0.27	8.83 ± 2.75	-2.80 ± 0.27

Table 6.1: The exotic resonances considered in the model along with the values of the magnitudes and phases for their transversity amplitudes measured relative to the resonance they decay to the J/ψ and $\psi(2S)$ respectively. All exotic resonances have a spin parity of $J = 1^+$. The first two resonances, $Z(4430)^+$ and $Z(4200)^+$ are resonances in $J/\psi\pi^+$ invariant mass spectrum, and the last resonance, $Z(4430)^-$ is a resonance in the $\psi(2S)\pi^+$ invariant mass spectrum.

input values in the $H_{0,+,-}$ helicity basis. The values are measured relative to the J/ψ for the channels $Z(4430)^- \to J/\psi\pi^-$ and $Z(4200)^- \to J/\psi\pi^-$, and measured relative to the $\psi(2S)$ for the channel $Z(4430)^- \to \psi(2S)\pi^+$. As a consequence of the fact that these values are measured relative to the J/ψ and $\psi(2S)$, when the exotic components are inserted with these values the $Z(4430)^- \to J/\psi\pi^-$ and $Z(4200)^- \to J/\psi\pi^-$ amplitudes have to be normalised to the value of $|A^0_{J/\psi}|$ at the J/ψ pole mass. For the case of the $Z(4430)^- \to \psi(2S)\pi^+$ amplitudes, they are normalised by $|A^0_{\psi(2S)}|/|A^0_{J/\psi}|$, where both $A^0_{\psi(2S)}$ and $A^0_{J/\psi}$ are evaluated at the pole masses of the J/ψ and $\psi(2S)$ respectively. Moreover, the input values for the non-local contributions entering in $\bar{B}^0 \to \bar{K}^{*0}\mu^+\mu^-$, the free phases, θ^0_j are set to 0. These toys are denoted the "exotic" toys. Next, additional toys are generated which are almost identical to the exotic toys, in terms of the same phases, generation seed, detector effects, helicity basis and statistics, however the only difference is that they do not contain any Z states in them. These toys are denoted "non-exotic" toys. Next, each exotic and non-exotic toy with the same seed is fitted using the model provided in Section 3 and the difference between the results of the fit average is used to determine a systematic. Table 6.2 summarizes the systematic uncertainty from ignoring the contribution of the $Z(4430)^\pm$ and $Z(4200)^+$ in the fit on parameters that are significantly affected in the fit. The results reveal that the effect of the $Z(4430)^\pm$ and $Z(4200)^+$ on the Wilson Coefficients and $\theta^0_{\psi(2S)}$ is less than 20% of the statistical uncertainty. The largest systematic uncertainty is associated with $\theta^0_{J/\psi}$ which has a systematic uncertainty that is 20% greater than the statistical uncertainty. The values of the magnitudes for the amplitudes of the $Z(4430)^\pm$ and

$Z(4200)^+$ states reported by Belle have large errors. In light of this an overestimate for the contribution is performed where each amplitude is doubled. This assumption of doubling the amplitudes is compatible with the error reported in the Belle analyses [80, 81]. The systematic uncertainties for the parameters that are mostly effected in this scenario where all the magnitudes of the $Z(4430)^{\pm}$ and $Z(4200)^+$ amplitudes have been multiplied by a factor of two is shown by Table 6.3. The systematic uncertainty associated with $\theta^0_{J/\psi}$ approximately doubles going up by a factor of 2.14. Likewise, the systematic uncertainty for $|C_9|$ approximately doubles going up by a factor of 2.38. The effect on $\theta^0_{\psi(2S)}$ has a smaller increase at a factor of 1.76, while the biggest effect is in $|C_{10}|$ where the change in the systematic uncertainty is at the level of 3.25. As an illustration of the impact of the exotic contributions, Figure 6.1 and Figure 6.2 show the effect on the cos θ_K and $m_{(c\bar{c})\pi}$ distributions when exotic states are included. In both these figures, the red points show the distribution of cos θ_K with the normal magnitude of the exotic amplitudes included, the green points show the distribution where the amplitudes of the exotic contributions have been doubled, and the blue points shows the distribution with no exotic states. In particular, the effect of the exotic states on cos θ_K is evident below -0.5. To summarise, the results reveal that even by doubling the size of the amplitudes for the exotic states, the systematic uncertainty on the Wilson Coefficients is not the most dominant. The phases are affected significantly. Nevertheless, the precision on the phases reported from the fit are extremely good and a small bias will not hinder the final result, given the statistics we have for both Run 1 and Run 2 data. Looking to the future, Belle II running it offers the chance to remeasure the exotic states, making improvements on the large uncertainty. This information, could reduce the systematic uncertainties even further.

Parameter	Systematic uncertainty	Systematic uncertainty/statistical uncertainty
$\theta^0_{J/\psi}$	5.92×10^{-3}	1.20
$\theta^0_{\psi(2S)}$	3.24×10^{-3}	0.17
$\|C_9\|$	2.07×10^{-2}	0.13
$\|C_{10}\|$	1.61×10^{-2}	0.12

Table 6.2: The systematic uncertainties and the systematic uncertainties as a fraction of the statistical uncertainties in various parameters, when ignoring the contribution of exotic $Z(4430)^{\pm}$ and $Z(4200)^+$ states in the empirical model. The values given are for the Wilson Coefficients C_9, C_{10} and the phases, $\theta^0_{J/\psi}$ $\theta^0_{\psi(2S)}$. The effect on the other parameters in the fit is found to be negligible.

Parameter	Systematic uncertainty	Systematic uncertainty/statistical uncertainty
$\theta^0_{J/\psi}$	1.27×10^{-2}	2.57
$\theta^0_{\psi(2S)}$	5.84×10^{-3}	0.30
$\lvert C_9 \rvert$	4.88×10^{-2}	0.31
$\lvert C_{10} \rvert$	5.21×10^{-2}	0.39

Table 6.3: The systematic uncertainties and the systematic uncertainties as a fraction of the statistical uncertainties in various parameters, when ignoring the contribution of exotic $\mathrm{Z}(4430)^{\pm}$ and $\mathrm{Z}(4200)^{+}$ states in the empirical model when all the $\mathrm{Z}(4430)^{\pm}$ and $\mathrm{Z}(4200)^{+}$ amplitudes have their magnitudes doubled. The values given are for the Wilson Coefficients C_9, C_{10} and the phases, $\theta^0_{J/\psi}$ $\theta^0_{\psi(2S)}$. The effect on the other parameters in the fit is found to be negligible.

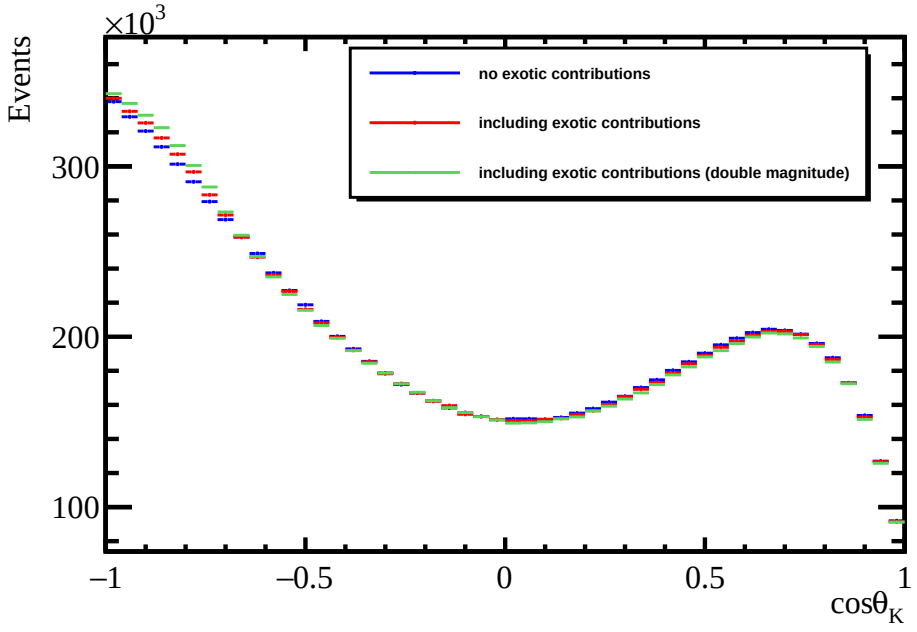

Figure 6.1: $\cos\theta_K$ distribution illustrating the effect of introducing the exotic states into the model. The blue data points correspond to the model without any exotic contributions. The red data points refer to the model with the exotic contributions and the green data points correspond to the model with the exotic contributions where the magnitudes of the exotic contributions are doubled.

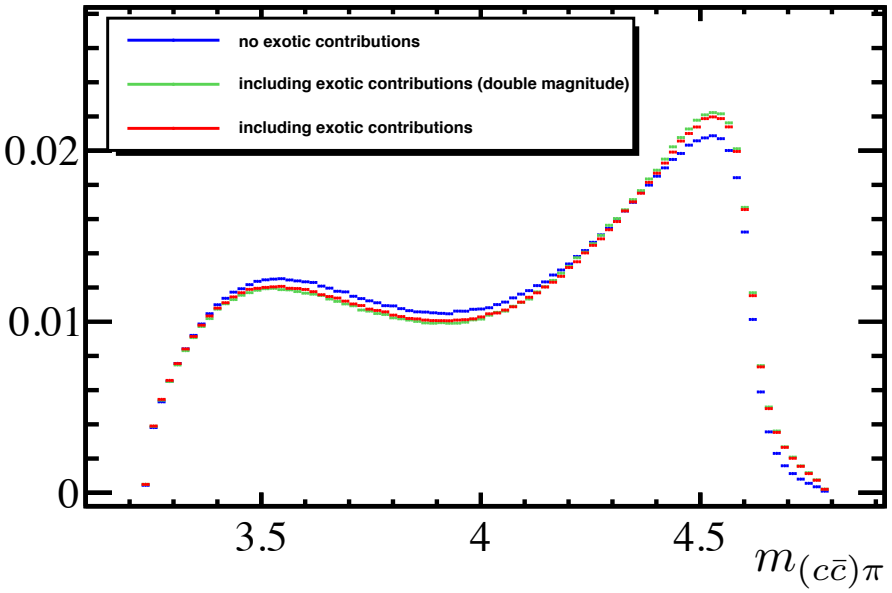

Figure 6.2: $m_{(c\bar{c})\pi}$ distribution showing the effect of the exotic states. The blue data points correspond to the model without any exotic contributions. The red data points refer to the model with the exotic contributions and the green data points correspond to the model with the exotic contributions where the magnitudes of the exotic contributions are doubled.

6.1.2 Uncertainty in the S-wave form factors

The S-wave amplitude for the $\bar{B}^0 \to \bar{K}^{*0}\mu^+\mu^-$ decay has two form factors, $F_{1,T}$, associated with it. In Chapter 3 it was discussed that these two form factors have a large uncertainty associated to them as a result of the difficultly in calculating the form factors. A systematic uncertainty for the lack of knowledge of the S-wave form factor is determined by generating a toy data set with 10× more events than the expected statistics from Run 1 and Run 2 combined. The toy was generated with the same initial phases and magnitudes for the resonant contributions as the ones used in the toy studies in Section 5. Again, resolution and acceptance effects were accounted for in the toy. Once the toy was generated, two fits were performed using the model defined in Chapter 3. In one of the fits, the model was the nominal model where the S-wave form factors, $F_{1,T}$ are those defined in Ref [99]. For the other fit, the only difference to the previous toy was that the model is adjusted such that the S-wave form factors $F_{1,T}$ are replaced with the form factors that enter into the longitudinal, P-wave amplitude, A_0 as defined in Ref [13]. Explicitly, F_1 was replaced by A_{12} and F_T was replaced by

T_{23}. Both fits converged successfully and with a positive definite correlation matrix. By taking the difference between the fit results from the two fits for each parameter, one would obtain a shift in this given parameter. This shift is then a measure of the systematic uncertainty on the choice of the S-wave form factor.

Table 6.4 shows the systematic uncertainties and the systematic uncertainties as a fraction of the statistical uncertainty for various parameters in the fit. Only parameters that have a systematic uncertainty that is greater than 5% of the statistical uncertainty are included in the table. The results indicated the uncertainties are large, implying that the S-wave form factor can have a significant impact, particularly on $|C_9|$, where the systematic uncertainty is 72% of the statistical uncertainty. Other parameters that show a large effect are the magnitudes of the $\psi(2S)$ amplitudes ($\eta_{\psi(2S)}^{\parallel,\perp,0}$) which have a systematic uncertainty that is at the level of 100% of the statistical uncertainty. In light of this, the shape of the S-wave form factor was investigated when it was replaced with the form factors corresponding to the A_0 amplitude. Figure 6.3 shows the comparison between the nominal implementation of the S-wave form factors (solid, blue line), and the S-wave form factors, where the coefficients have been replaced with those from the form factors corresponding to the A_0 amplitude, as demonstrated by the hatched, red line. In both plots, there is a significant difference between the two different parametrisations. For F_1, both the nominal and swapped parametrisations start at the same point because the α_0 coefficient is similar in both parametrisations. Nevertheless, as one moves to higher q^2 values the difference becomes more apparent and at the largest q^2 values there is a significant difference. For F_1, the difference is apparent from the start with no similarities between the two parametrisations. That aside, the nominal S-wave form factors are consistent with the $B^+ \to K^+$ form factors (see Figure 6.4 [108]). This implies that these form factors could be used as an approximation for the $B^0 \to K^*$ form factors, and could be investigated in the future. This suggests the current systematic is a gross overestimate and alternative solutions should be investigated.

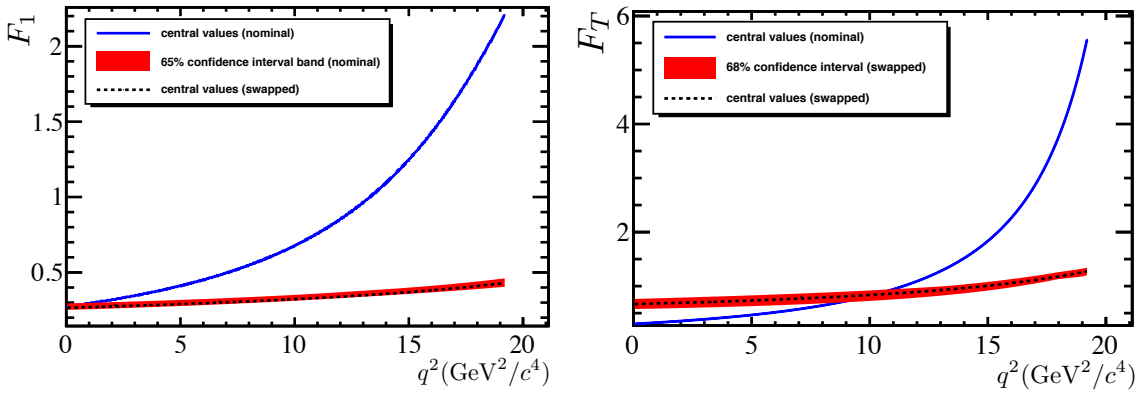

Figure 6.3: Distributions for the S-wave form factors, F_1 and F_T. The solid, blue line denoted the S-wave form factors modelled using the nominal approach in Section 4.6. The hatched red line corresponds to the S-wave form factors when the coefficients have been replaced by the coefficients of the form factors corresponding to the A_0 amplitude.

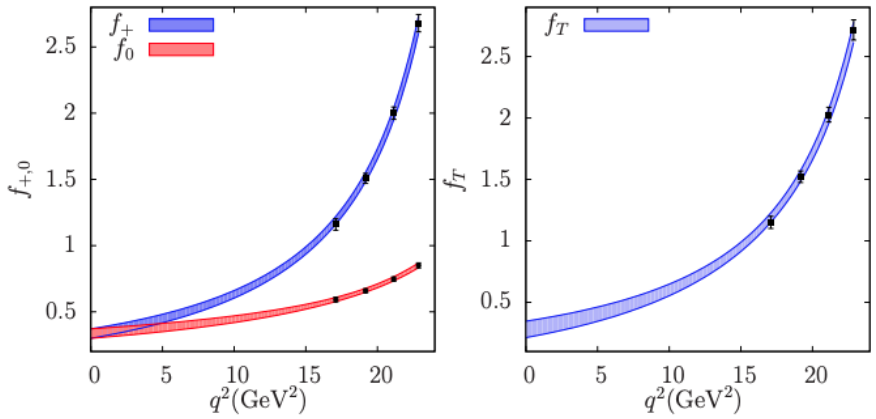

Figure 6.4: Distributions for the $B^+ \to K^+$ form factors, f_0, f_+, f_T taken from Ref [108]. The notation is that $f_+ = F_1$ and $f_T = F_T$. f_0 denotes the scalar form factor that is not needed in our model. The data points are synthetic data points generated from the form factor fit, and the band of values is constructed from the uncertainties.

Parameter	Systematic uncertainty	Systematic uncertainty/Statistical uncertainty
$\|C_9\|$	1.15×10^{-1}	7.23×10^{-1}
$\|C_{10}\|$	2.12×10^{-2}	1.57×10^{-1}
$\theta^0_{J/\psi}$	2.86×10^{-4}	5.80×10^{-2}
$\eta^{00}_{J/\psi}$	1.19×10^{-6}	7.25×10^{-2}
$\theta^{00}_{J/\psi}$	2.82×10^{-3}	7.10×10^{-2}
$\eta^{\parallel}_{\psi(2S)}$	2.02×10^{-5}	9.58×10^{-1}
$\eta^{\perp}_{\psi(2S)}$	2.41×10^{-5}	1.01
$\eta^{0}_{\psi(2S)}$	3.01×10^{-5}	1.07
$\eta^{00}_{\psi(2S)}$	9.97×10^{-6}	5.66×10^{-1}
$\theta^{00}_{\psi(2S)}$	6.75×10^{-4}	1.25×10^{-1}
$\mathrm{Re}(\mathrm{A}^0_{\rho^0})$	6.35×10^{-6}	4.68×10^{-1}
$\mathrm{Im}\ (\mathrm{A}^0_{\rho^0})$	2.90×10^{-6}	2.46×10^{-1}
$\mathrm{Re}(\mathrm{A}^{\parallel}_{\psi(3770)})$	1.61×10^{-6}	1.09×10^{-1}
$\mathrm{Re}(\mathrm{A}^{\perp}_{\psi(3770)})$	7.35×10^{-7}	5.38×10^{-2}
$\mathrm{Im}(\mathrm{A}^{\perp}_{\psi(3770)})$	4.87×10^{-6}	3.60×10^{-1}
$\mathrm{Re}(\mathrm{A}^0_{\psi(3770)})$	1.23×10^{-6}	9.07×10^{-2}
$\mathrm{Re}(\mathrm{A}^{\parallel}_{\psi(4040)})$	2.82×10^{-6}	1.99×10^{-1}
$\mathrm{Im}(\mathrm{A}^{\parallel}_{\psi(4040)})$	6.07×10^{-6}	3.65×10^{-1}
$\mathrm{Re}(\mathrm{A}^{\perp}_{\psi(4040)})$	9.89×10^{-6}	8.03×10^{-1}
$\mathrm{Im}(\mathrm{A}^{\perp}_{\psi(4040)})$	5.56×10^{-6}	4.46×10^{-1}
$\mathrm{Re}(\mathrm{A}^0_{\psi(4040)})$	1.71×10^{-6}	1.19×10^{-1}
$\mathrm{Im}(\mathrm{A}^0_{\psi(4040)})$	4.05×10^{-6}	2.76×10^{-1}
$\mathrm{Re}(\mathrm{A}^{\parallel}_{\psi(4160)})$	3.55×10^{-6}	2.24×10^{-1}
$\mathrm{Im}(\mathrm{A}^{\parallel}_{\psi(4160)})$	6.69×10^{-6}	4.04×10^{-1}
$\mathrm{Re}(\mathrm{A}^{\perp}_{\psi(4160)})$	1.04×10^{-5}	8.10×10^{-1}
$\mathrm{Im}(\mathrm{A}^{\perp}_{\psi(4160)})$	7.38×10^{-6}	6.30×10^{-1}
$\mathrm{Im}(\mathrm{A}^0_{\psi(4160)})$	5.55×10^{-6}	4.12×10^{-1}
$\mathrm{Re}(\zeta^{\parallel} e^{i\omega\parallel})$	7.76×10^{-3}	3.89×10^{-1}
$\mathrm{Re}(\zeta^{\perp} e^{i\omega\perp})$	1.27×10^{-2}	6.68×10^{-1}
$\mathrm{Im}(\zeta^{\perp} e^{i\omega\perp})$	6.16×10^{-3}	7.25×10^{-2}
$\mathrm{Re}(\zeta^{0} e^{i\omega 0})$	1.03×10^{-1}	6.12×10^{-1}

Table 6.4: The systematic uncertainties and the systematic uncertainties as a fraction of the statistical uncertainties arising from the lack of knowledge on the S-wave form factors. Only parameters that have a systematic uncertainty that is greater than 5% of the statistical uncertainty are given.

6.2 Experimental systematics

Experimental systematics are systematic uncertainties that arise from effects caused by the detector and the way the experiment has been conducted. They can manifest themselves as limitations in the experimental equipment, environmental effects or even in the structure of the detector itself. In our measurement of the interference between the non-local contributions and the penguin component in $\bar{B}^0 \to \bar{K}^{*0}\mu^+\mu^-$ transitions there exist experimental effects that need to be accounted for in the final result. These include the effects of residual peaking backgrounds, the systematic uncertainty associated with the acceptance correction, the affect of ignoring the resolution of the measurement of the angles and the systematic uncertainty arising from the background model. All of these systematics are discussed in this section, apart from the systematic uncertainty associated with the background modelling. This is because additional modelling is still being done for the background which means a total systematic associated with the background could not be completed at this stage.

6.2.1 Angular resolution

In this analysis, only the detector resolution in the q^2 spectrum (see Section 4.5.1) is accounted for. The resolution in the angles was ignored, as it was deemed that any resolution effects in the angles is small. As a result, any minute resolution effects in the angles are taken as a systematic uncertainty. In order to determine a systematic uncertainty from ignoring the resolution in the angles, the following procedure was adopted. To begin, the $\bar{B}^0 \to \bar{K}^{*0}\mu^+\mu^-$ simulation was taken and the following cuts were applied: $m_B \in$ [5243,5323] MeV/c^2, and $m_{K\pi} \in$ [796,996] MeV/c^2. The events that passed the selection criteria were then used to determine the Lorentz 4-vectors, which were then used to compute the reconstructed, x^{rec} and true angles, x^{tru}. Here, x denotes θ_ℓ, θ_K and ϕ. By determining these angles one could then compute the difference between them Δx, defined as $\Delta x = x^{rec} - x^{tru}$. Distributions were then produced for $\Delta\theta_\ell$, $\Delta\theta_K$ and $\Delta\phi$, that were then each fitted with a triple Gaussian pdf. Each triple Gaussian pdf was defined by three means $\mu_{1,2,3}$, three widths $\sigma_{1,2,3}$ and two fractions

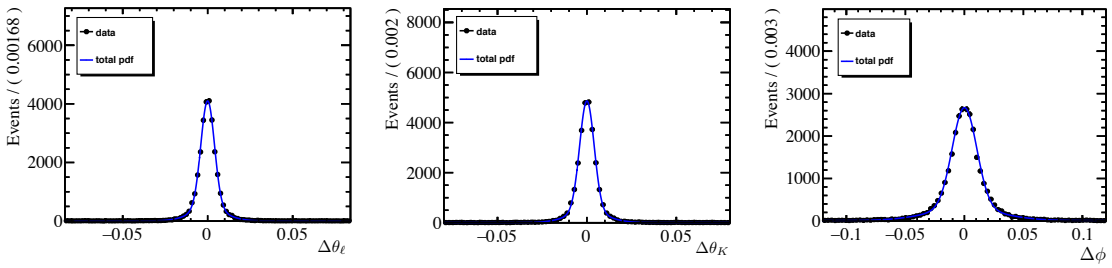

Figure 6.5: The fits performed using a triple Gaussian pdf to the distributions $\Delta\theta_\ell$, $\Delta\theta_K$ and $\Delta\phi$. The data is shown by the black data points and the total Gaussian pdf is shown by the solid, blue line.

Parameter	Value
σ_1	$3.99 \times 10^{-3} \pm 4.69 \times 10^{-5}$
σ_2	$1.02 \times 10^{-2} \pm 2.57 \times 10^{-4}$
σ_3	$1.28 \times 10^{+0} \pm 8.21 \times 10^{-3}$
μ_1	$-1.56 \times 10^{-2} \pm 3.43 \times 10^{-5}$
μ_2	$3.08 \times 10^{-5} \pm 1.64 \times 10^{-4}$
μ_3	$-2.34 \times 10^{-2} \pm 1.12 \times 10^{-2}$
f_1	$7.84 \times 10^{-1} \pm 1.18 \times 10^{-2}$
f_2	$6.81 \times 10^{-1} \pm 2.34 \times 10^{-3}$

Table 6.5: The fit parameters obtained from fitting a triple Gaussian pdf to the $\Delta\theta_\ell$ distribution in the $\bar{B}^0 \to \bar{K}^{*0}\mu^+\mu^-$ simulation.

$f_{1,2}$, where the f_1 is the relative amount of the second Gaussian, G_2 to the first Gaussian, G_1 and f_2 is the relative amount of the third Gaussian, G_3 to the other two Gaussians. Figure 6.5 illustrates the resulting fits of the triple Gaussian pdf to $\Delta\theta_\ell$, $\Delta\theta_K$ and $\Delta\phi$ distributions from the $\bar{B}^0 \to \bar{K}^{*0}\mu^+\mu^-$ simulation that has been preselected. The resulting fit parameters are also given by Table 6.5 for the $\Delta\theta_\ell$ fit, Table 6.6 for the $\Delta\theta_K$ fit and Table 6.7 for the $\Delta\phi$ fit.

High statistics toys with 10× the number of candidates expected from both Run 1 and Run 2, were generated with q^2 resolution effects, acceptance effects and the magnitudes and phases of the non-local contributions were set to the same initial values as those used in the toy studies in Chapter 5. All toys were also generated with the angles smeared according to the results from the triple Gaussian fits to $\Delta\theta_\ell$, $\Delta\theta_K$ and $\Delta\phi$, as given by Tables 6.5, 6.6 and 6.7. Each toy sample generated was fitted twice using the same model, however in one of the fits the angles were smeared by the triple Gaussian pdfs, and in the other fit the angles remained unsmeared. Next, the difference was calculated between the two fit results for all parameters, for all toys, and used to

Parameter	Value
σ_1	$4.05 \times 10^{-3} \pm 4.51 \times 10^{-5}$
σ_2	$1.07 \times 10^{-2} \pm 2.75 \times 10^{-4}$
σ_3	$3.69 \times 10^{+2} \pm 1.84 \times 10^{2}$
μ_1	$-1.62 \times 10^{-2} \pm 3.36 \times 10^{-5}$
μ_2	$4.01 \times 10^{-5} \pm 1.77 \times 10^{-4}$
μ_3	$2.35 \times 10^{-1} \pm 1.57 \times 10^{-1}$
f_1	$7.98 \times 10^{-1} \pm 1.07 \times 10^{-2}$
f_2	$6.83 \times 10^{-1} \pm 2.33 \times 10^{-3}$

Table 6.6: The fit parameters obtained from fitting a triple Gaussian pdf to the $\Delta\theta_K$ distribution in the $\bar{B}^0 \to \bar{K}^{*0}\mu^+\mu^-$ simulation.

Parameter	Value
σ_1	$1.04 \times 10^{-2} \pm 1.29 \times 10^{-4}$
σ_2	$3.08 \times 10^{-2} \pm 6.85 \times 10^{-4}$
σ_3	$5.00 \times 10^{+2} \pm 3.77 \times 10^{2}$
μ_1	$6.99 \times 10^{-5} \pm 9.26 \times 10^{-5}$
μ_2	$-1.12 \times 10^{-4} \pm 4.43 \times 10^{-4}$
μ_3	$6.58 \times 10^{-2} \pm 1.29 \times 10^{-1}$
f_1	$7.43 \times 10^{-1} \pm 1.02 \times 10^{-2}$
f_2	$6.75 \times 10^{-1} \pm 2.38 \times 10^{-3}$

Table 6.7: The fit parameters obtained from fitting a triple Gaussian pdf to the $\Delta\phi$ distribution in the $\bar{B}^0 \to \bar{K}^{*0}\mu^+\mu^-$ simulation.

determine the average difference for a given parameter. Table 6.8 shows the systematic uncertainty for the parameters that have a systematic uncertainty that is greater than 5% of the statistical uncertainty. In this table, the systematic uncertainty is shown, in addition to the systematic uncertainty as a fraction of the statistical uncertainty. The largest effect can be seen in $\theta^0_{J/\psi}$ where this parameter has a systematic uncertainty that is 18% of the statistical uncertainty. The next largest effect is seen in $\eta^{00}_{J/\psi}$ which has a systematic uncertainty that is 16.6% of the statistical uncertainty. The impact on the other magnitudes for the J/ψ and also the $\psi(2S)$ are at a similar level of 10% of the statistical uncertainty. For the Wilson Coefficients, the systematic uncertainty on $|C_9|$ is only just greater than 5% of the statistical uncertainty, with a value of 5.57% of the statistical uncertainty, and hence the effect is small. On the other hand, the effect is greater for $|C_{10}|$ with a systematic that is 11.8% of the statistical uncertainty. With the addition of Run 3 data, this systematic should reduce. Nevertheless, in the fit to Run 1 and Run 2 combined, if this becomes one of the most dominant systematics to the

Parameter	Systematic uncertainty	Systematic uncertainty/Statistical uncertainty
$\|C_9\|$	8.84×10^{-3}	5.57×10^{-2}
$\|C_{10}\|$	1.59×10^{-2}	1.18×10^{-1}
$\theta^0_{J/\psi}$	8.92×10^{-4}	1.81×10^{-1}
$\eta^{\parallel}_{J/\psi}$	1.45×10^{-6}	1.21×10^{-1}
$\eta^{\perp}_{J/\psi}$	1.36×10^{-6}	1.07×10^{-1}
$\eta^{00}_{J/\psi}$	1.25×10^{-6}	7.63×10^{-2}
$\theta^{00}_{J/\psi}$	8.79×10^{-4}	1.62×10^{-1}
$\eta^{\parallel}_{\psi(2S)}$	1.39×10^{-6}	6.59×10^{-2}
$\eta^{\perp}_{\psi(2S)}$	3.69×10^{-6}	1.55×10^{-1}
$\eta^{0}_{\psi(2S)}$	3.31×10^{-6}	1.18×10^{-1}
$\mathrm{Re}(\mathrm{A}^0_{\psi(4040)})$	7.83×10^{-7}	5.47×10^{-2}
$\mathrm{Im}(\mathrm{A}^{\parallel}_{\psi(4160)})$	9.54×10^{-7}	5.76×10^{-2}
$\mathrm{Im}(\mathrm{A}^0_{\psi(4160)})$	6.97×10^{-7}	5.18×10^{-2}
$\mathrm{Re}(\zeta^{\parallel}e^{i\omega\parallel})$	1.01×10^{-3}	5.04×10^{-2}
$\mathrm{Re}(\zeta^{\perp}e^{i\omega\perp})$	2.74×10^{-3}	1.44×10^{-1}
$\mathrm{Re}(\zeta^{0}e^{i\omega 0})$	1.24×10^{-2}	7.41×10^{-2}

Table 6.8: The systematic uncertainties and the systematic uncertainties as a fraction of the statistical uncertainties in various parameters, when ignoring the effect of the angular resolution. Only parameters that have a systematic uncertainty that is greater than 5% of the statistical uncertainty are given.

Wilson Coefficients, then it might be beneficial to include the angular resolution in the model, and float only a subset of the parameters.

6.2.2 Angular acceptance correction

The angular acceptance given in Section 4.5.2 is determined from simulation and takes the form of a sum of Legendre polynomials, of orders four for $\cos\theta_\ell$, five for q^2 and $\cos\theta_K$, and six for ϕ. Two systematic uncertainties are associated to the angular acceptance: the systematic uncertainty in using a finite simulation size to determine the acceptance, and the uncertainty in the orders of the Legendre polynomials to model the acceptance. Both these systematics were investigated. Finite or limited simulation samples can influence the reported values and precision of the angular coefficients. The size of the systematic

uncertainty was estimated by performing pseudo experiments using the nominal and systematically varied acceptance correction. All toys contain resolution effects, and have identical starting values for the non-local contributions as the toy studies given in Chapter 5. The angular acceptance given in Ref [4] is taken and its coefficients are varied according to the covariances, as reported by the moment analysis of the simulation. This altered version of the angular acceptance is then added to the model and used to fit the toy datasets. No significant deviations in the fit parameters were reported, revealing the systematic uncertainty arising from the finite size of the simulation used to determine the acceptance correction is negligible. The orders of the Legendre polynomials can affect the modelling of the angular acceptance. Lower order Legendre polynomials are less computationally expensive to calculate and do not suffer from some of the issues higher order polynomials do. Nevertheless, higher order polynomials can allow one to capture the shape of the acceptance better. The decision that is made in this analysis is to use a lowest order sum of Legendre polynomials to describe the acceptance correction. The systematic uncertainty associated with this choice can be determined by modifying the acceptance to include higher orders. Previous analyses that have used this method do determine the effect of using low order polynomials and showed that the impact is small [4]. This conclusion is valid for this analysis and so the systematic uncertainty associated with the choice of the order of the Legendre polynomials for the angular acceptance is assumed to be negligible.

6.2.3 Peaking backgrounds

A systematic uncertainty was determined for the effect of residual peaking backgrounds. For each peaking background given in Section 4.2.3, its distribution is determined and modelled by a kernel density function. Pseudo-data was injected with the expected residual peaking background level and fitted back with our nominal model that ignored this contribution. Due to the small fraction of residual peaking backgrounds, the effect of ignoring their contribution was found to be negligible.

Chapter 7

Conclusions

The effect of the non-local contributions to $\bar{B}^0 \to \bar{K}^{*0}\mu^+\mu^-$ transitions has been studied in this thesis. The analysis is the first to study the effect of hadronic contributions with quantum numbers $\mathrm{J^{PC}} = 1^{--}$, across the full q^2 region, $0.1 < q^2 < 18.0$ GeV$^2/c^4$, in this channel. This has been achieved through the development of a model that contains both the penguin decay and the non-local contributions. The non-local contributions are modelled as relativistic Breit-Wigner amplitudes and non-local contributions that enter C_7. The simplistic modelling has been verified as a suitable approach by comparing the model to alternative models for the charm loop, in a reduced q^2 region, and finding a good agreement. The model considers both the P-wave and S-wave $\bar{K}^{*0}$ amplitudes, where in each the non-local contributions have also been accounted for.

The LHCb detector has produced data samples rich in $\bar{B}^0 \to \bar{K}^{*0}\mu^+\mu^-$ candidates over both Run 1 and Run 2 of the LHC. A framework has been developed that uses the empirical model to perform a five dimensional, unbinned, maximum likelihood fit to the LHCb data, in the dimensions of $\cos\theta_K$, $\cos\theta_\ell$, ϕ, q^2 and $m_{K\pi\mu\mu}$. The total model contains both signal and background components. A data driven approach is taken in the modelling of the background events, by including effects from the $B \to K^+\mu^+\mu^-$ veto and considering the impact of recalculating the momenta of the final state particles using the B^0 mass constraint. Detector effects such as angular acceptance effects and detector resolution have been studied in detail, and implemented into the model. The q^2 resolution is given as a Gaussian convoluted with a double sided Crystal Ball function,

implemented in three q^2 region, and a fast fourier transform is used to convolve the model with the resolution function.

The samples collected from the LHCb experiment contain not only $\bar{B}^0 \to \bar{K}^{*0}\mu^+\mu^-$ candidates, but unwanted events from background processes and stray particles in the detector from other particle decays. In order to maximise the number of $\bar{B}^0 \to \bar{K}^{*0}\mu^+\mu^-$ candidates, to perform such a complex fit, a strategy has been applied to process and select the candidates using various criteria. A BDT has been trained on both Run 1 and Run 2, to help remove the combinatorial background and maximise the signal yield.

Toy fits have been performed with the same statistics as the combined Run 1 and Run 2 datasets to test the stability and statistical precision of the fit. The results from the toy fits reveal that the coverage for the Wilson Coefficients is good and that the precision on these parameters is dominated by the statistics available. With more statistics available with Run 3 of the LHC, these values will be obtained to an even greater precision. Moreover, the results from the toy fits reveal that the model can pin down the non-local contributions. The free phase for the dominant J/ψ and $\psi(2S)$ resonances has a pull distribution that is consistent with a standard Gaussian distribution, that has a μ of 0 and a σ of 1, showing the coverage of the fit is good. Moreover, the magnitudes of the J/ψ and $\psi(2S)$ amplitudes are in agreement with the experimental inputs from $B \to VK^{*0}$ decays. These results demonstrate that the fit can determine these resonance contributions extremely well. The larger mass resonant contributions above the $D\bar{D}$ threshold, exhibit a small bias, which is to be accounted for as a systematic uncertainty in the final values reported in a measurement of the data. Other resonant contributions such as the ρ^0, $\zeta^{\parallel,\perp,0}$, $\omega^{\parallel,\perp,0}$ demonstrate a pull distribution that also is consistent with a standard unit Gaussian distribution. Although in the fit, the vector form factors are allowed to vary, the result reveal that there is no additional gain from fitting these parameters and the measurements are only slightly better than the result published by theorists. The largest systematic in the analysis is found to be in in the free phase of the J/ψ resonance ($\theta^0_{J/\psi}$) when considering the impact of exotic charmonium-like states, with quark content $|c\bar{c}ud\rangle$. The systematic uncertainty as a fraction of the statistical uncertainty in this parameter is at 1.2. The results for the other non-local parameters and Wilson Coefficients was found to be negligible. Moreover,

systematic uncertainties arising from ignoring the resolution in the angles was found to be minimal. An investigation into the systematic uncertainty associated with the S-wave form factor was performed. However, the uncertainties in the coefficients meant that the systematic uncertainty was an overestimate of the effect. Additional methods to determine a more precise systematic uncertainty for this effect should be investigated in the future.

The results from the toy fits have concluded that the statistical precision on the Wilson Coefficients C_9 and C_{10} are at the level of 3.76% and 3.23%. These values that have been obtained using the empirical model can be compared to statistical precision obtained from alternative models that can be used to determine the Wilson Coefficients in $\bar{B}^0 \to \bar{K}^{*0}\mu^+\mu^-$ transitions. The statistical precision of the binned q^2 fit as presented in Ref [109], is at the level of 4.37% for C_9 and 6.38% for C_{10}. Moreover, the statistical precision of the direct fit approach to the Wilson Coefficients, as described in Ref [109], reports a precision of 4.01% for C_9 and 4.92% for C_{10}. The results clearly reveal that the simplistic model used in this analysis can achieve an improved precision on the Wilson Coefficients.

With validation of the model obtained from toy fits the next stage is to perform the final fits to the data, with a deeper level of background modelling. This however goes beyond the time duration of this thesis. A simultaneous fit of the combined data from both Run 1 and Run 2 of the LHC is due to be published by the end of the summer of 2020, which uses the authors model to perform the fit and will use all the studies performed in this dissertation, for the publication. The final result will allow us to obtain a deeper understanding of the impact of the non-local contributions to $\bar{B}^0 \to \bar{K}^{*0}\mu^+\mu^-$ transitions, and answer the question as to whether these non-local contributions are the cause of the anomalous results seen by the LHCb experiment.

Appendix A

Theory convention for the $\bar{B}^0 \to \bar{K}^{*0}\mu^+\mu^-$ decay angles.

A.1 $\cos\theta_\ell$ definition in the theory basis

$$\cos\theta_\ell = \frac{\vec{p}^{\,\mu\mu}_{\mu^-} \cdot \vec{p}^{\,\mu\mu}_{B}}{|\vec{p}^{\,\mu\mu}_{\mu^-}||\vec{p}^{\,\mu\mu}_{B}|} \tag{A.1}$$

A.2 $\cos\theta_K$ definition in the theory basis

$$\cos\theta_K = \frac{\vec{p}^{\,K\pi}_{K} \cdot \vec{p}^{\,K\pi}_{B}}{|\vec{p}^{\,K\pi}_{K}||\vec{p}^{\,K\pi}_{B}|} \tag{A.2}$$

A.3 ϕ definition in the theory basis

$$\begin{aligned} \cos\phi &= \vec{n}^{\,B}_{K\pi} \cdot \vec{n}^{\,B}_{\mu^-\mu^+} \\ \sin\phi &= (\vec{n}^{\,B}_{K\pi} \times \vec{n}^{\,B}_{\mu^-\mu^+}) \cdot \frac{\vec{p}^{\,B}_{K\pi}}{|\vec{p}^{\,B}_{K\pi}|} \end{aligned} \tag{A.3}$$

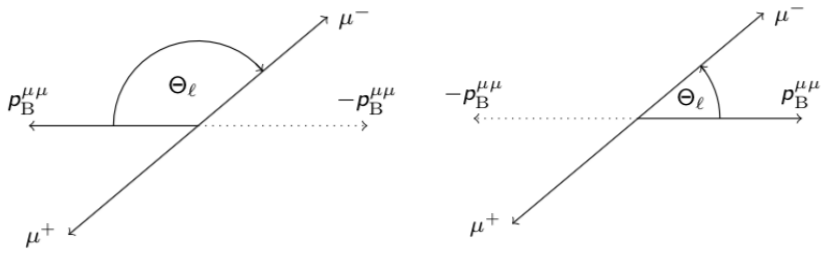

Figure A.1: θ_ℓ defined for (a) the $\bar{B}^0$ decay and (b) the B^0 decay in the theory basis [17]

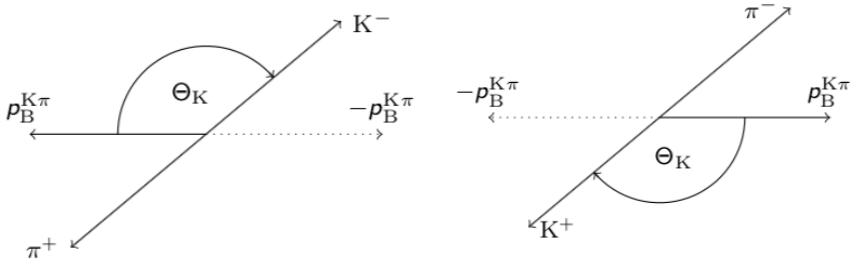

Figure A.2: θ_K defined for (a) the $\bar{B}^0$ decay and (b) the B^0 decay in the theory basis [17]

Appendix B

Optical Mirror testing for the LHCb RICH 1 upgrade

B.1 Motivation

As mentioned in Chapter 2, the LHC is undergoing a long shut down period during 2019 and 2020, to prepare for Run 3 which starts in 2021. The LHCb detector, like many of the high energy physics experiments at CERN, is using this long shut-down (LS2) to improve the detector and software, in order to cope with the higher luminosity that will be delivered in Run 3. One subsystem of the LHCb detector that is being upgraded is the RICH 1 subsystem. The mechanical arrangement and the optical system are both being upgraded. In particular, the spherical and flat mirrors are being replaced. The mirrors are an important component of RICH 1 as they are used to reflect light emitted from the particles to the HPDs. This chapter presents and describes studies performed on a subset of prototype mirrors to identify possible suppliers based on the quality of the mirrors and if the optical requirements were met. The requirements on the mirrors are that they consistent with the current LHCb RICH 1 mirrors. This means they need to have as a minimum requirement the same quality and durability. Specifically, the requirements tested in this chapter were the optical properties of the mirrors, in terms of their reflectivity, coating, and imaged spot size. These optical requirements are

essential because if the mirrors do not have adequate optical properties it will affect the particle identification of the RICH detectors, and therefore the results outputted from Run 3 of the LHCb detector.

B.2 Methodology

B.2.1 Existing RICH mirrors

The spherical and flat mirrors currently in the RICH 1 system have been used for both Run 1 and Run 2 of the LHC. In Chapter 2, a diagram (see Figure 2.9) of the RICH 1 system was provided. In this figure the optical system and in particular the mirrors are visible. RICH 1 uses a combination of both spherical and flat mirrors, to direct light to the HPDs. Firstly, there are two planes of flat mirrors, situated on the left of the RICH 1 system both above and below the beampipe (as shown on Figure 2.9). On each plane there are 8 mirrors, making in total 16 flat, mirrors. These 16 identical, flat rectangular mirrors have the dimensions 380 mm $\times$ 347.5 mm and are 6.5mm thick. The mirrors are made out of Simax glass (borosilicate glass type 3.3) and coated with Al + SiO_2 + HfO_2. The coating is applied to ensure maximum reflection of the light. Next, there are two spherical mirrors in the RICH 1 optical system. These spherical mirrors are positioned on the right hand side of the RICH, above and below the beampipe (as shown by Figure 2.9). The two spherical mirrors are made out of carbon fibre composites (CFRP [49]) and have dimensions 830mm $\times$ 630mm, making them both extremely light and much larger than the flat, glass mirror. The spherical mirrors like the flat, glass mirrors are coated, however for the spherical mirrors the coating material is Al+MgF_2. The RICH 1 mirrors have been reliable and sufficiently served the LHCb detector during both Run 1 and Run 2. In light of this, the prototype mirrors that have been tested for the RICH 1 mirror upgrade have many specifications and properties identical to the old mirrors.

B.2.2 Experimental setup

Prototype spherical and flat mirrors were tested in an underground laboratory at CERN, using the same apparatus that was used to test the existing Run 1/2 mirrors. Figure B.1 illustrated the experimental setup. A flat or spherical mirror was placed parallel to the laser on a metal support. Next, a diode laser, which acted as a point source was aimed at the prototype mirror. The laser was at a distance d from the mirror. The laser could be moved closer or further away from the prototype mirror. The change in distance then of the laser was denoted dx. To begin the measurement, the light from the laser was focussed onto the prototype mirror. This generated a spot on the prototype mirror, which was then reflected off the prototype mirror and onto a spherical mirror of radius of 7800 mm. Then, the light was reflected off the spherical mirror back onto the prototype mirror, before it was reflected back towards the laser and detected by a 16 bit CCD camera. The resulting CCD image was a 767×511 grid, where each pixel had an area of $9\mu\text{m}^2$. During the experiment the laser was kept at a constant temperature over the duration of the measurement by a cooling system. The apparatus was surrounded by black, opaque curtains to stop any external light entering whilst the prototype flat mirror was being tested. To perform a background subtraction a CCD image was taken with the laser turned off and subtracted from the image which was taken with the laser on. All these factors helped ensure that the results were not biased.

B.2.3 Calculation of the D_0

In the RICH optical system, the mirrors produce a spot when the Cherenkov photons are reflected from them. This spot has a shape and size that is determined by the mirror itself and how the light is distributed on the given mirror. To characterise the spot, the quantity D_0 is used. D_0 corresponds to the diameter of the smallest circle that encases 95% of the light. For the testing of the prototype mirrors for the RICH 1 optical system upgrade, D_0 was calculated. As mentioned in the previous section, to test the prototype spherical and flat mirrors, a laser was used as the source of light and to produce the desired spot. Once this spot was produced it was recorded by a CCD camera. D_0 was

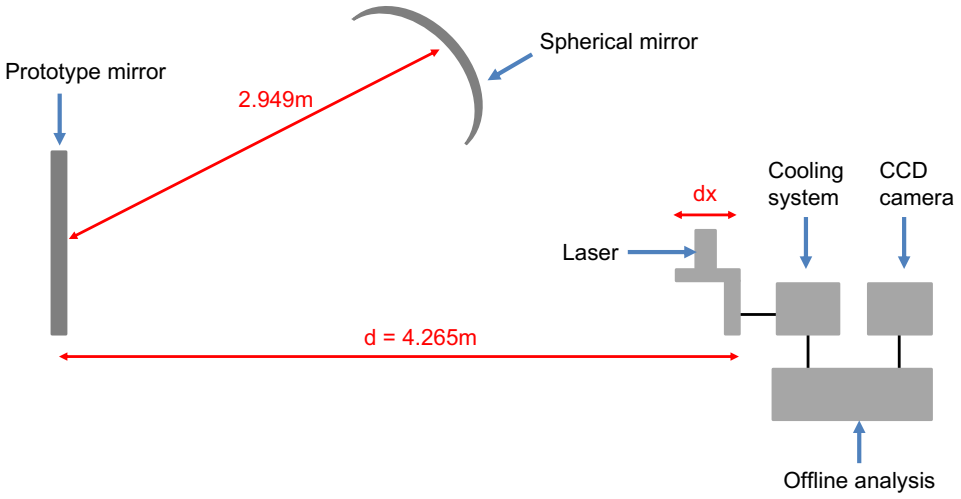

Figure B.1: Experimental setup in the lab for testing the prototype RICH 1 mirrors.

calculated using the resulting CCD image of the spot. Initially, the total amount of light in the entire CCD image was obtained. Each pixel in the CCD image contained a given amount of charge. Therefore, summing over all pixels (767 × 511) gave the total integral. The next step was to find the integral of the spot. By definition, the smallest spot will be centred at the centre of mass (CoM). The CoM (x_{CoM}, y_{CoM}) was calculated by summing over the integral in the x pixels and y pixels, before dividing each sum by the total CCD image integral. Equation B.1 shows the definition of the CoM used for the mirror testing.

$$x_{CoM} = \frac{\int_0^{767} x \cdot \mathcal{I}(x,y)}{\int_0^{767} \mathcal{I}(x,y)}, \qquad y_{CoM} = \frac{\int_0^{511} y \cdot \mathcal{I}(x,y)}{\int_0^{511} \mathcal{I}(x,y)} \tag{B.1}$$

Once the spot was obtained the D_0 could be calculated. Given the D_0 is the distance of the circle containing 95% of the light, it was calculated by taking the centre of the spot and moving away radially from the centre, until the integral of the light was 95% of the total light. The distance was then the radius and to obtain D_0, we applied the following equation,

$$D_0 = 2 \cdot p \cdot \Delta z. \tag{B.2}$$

where p was the pixel width and Δz was the radius from the centre.

B.2.4 Requirements and Specifications

Flat and spherical mirrors for the RICH 1 upgrade were testing using the method described in Section B.2.2. Explicitly, three mirrors were tested. Two of these mirrors were flat, glass composite mirrors. These glass mirrors were produced by the Czech Republic company, Olomouc. The glass used for the prototype flat mirrors was the same substrate as the current RICH 1 flat mirrors and was Simax. Of these two flat, glass mirrors tested one was coated with Al + SiO_2 + HfO_2 and the other was left uncoated. It should be noted the coating was the same coating that is on the existing flat, mirrors in the RICH 1 system. Excluding the coating, both glass mirrors had the same specifications. Moreover, a single spherical, prototype mirror was tested. This spherical mirror was produced in Arizona by the company, CMA. The prototype spherical mirror was an uncoated, carbon fibre composite mirror. This mirror was uncoated, as CMA noted that they did not have the capability to produce these mirrors coated. As a result, in the future, a coating supplier will need to be found and have to be able to deal with the issue that the mirrors are spherical and large, which can make achieving an even coating difficult. For all mirrors tested the requirement was that D_0 <2.5 mm and, if the mirror was coated, then the reflectivity was required to be greater than 85% in the region, $\lambda \in$[250 - 400 nm]. These two specifications were investigated when testing the prototype mirrors.

B.3 Results

B.3.1 Flat mirrors

This section presents the results obtained for the two prototype, flat mirrors presented in Section B.2.4. The results from different tests are presented for the uncoated, flat mirror first, and then followed then by the different test results for the coated, flat mirror.

B.3.1.1 Uncoated flat mirror

The first test to be performed on the uncoated flat glass mirror was measuring D_0 as a function of distance. The distance, dx, as shown on Figure B.1, was incremented in steps of 3 mm starting from 42 cm and finishing at 57 cm. At each dx value tested, two images were taken, one with the laser on and one without. The reason for this was to ensure that if the background light changed during the data taking period, it would not affect the result as the two images would have been taken within a short time interval and so the background subtraction it would be accurate. This procedure was applied to all subsequent mirror tests described in this thesis. The current of the laser was set to 33 mA. Later in Section B.3.1.2, one will see that this value of the current is much larger than the current used to image the spot from the coated mirror. This is because the coating results in the spot being more visible due to the reflectivity of the coating. Therefore, to image the spot more clearly on the uncoated mirror, one needs to increase the current. Figure B.2 illustrates several images that have been background subtracted and show the resulting image from the uncoated, flat mirror at different positions, dx, in the range of 42-57 cm.

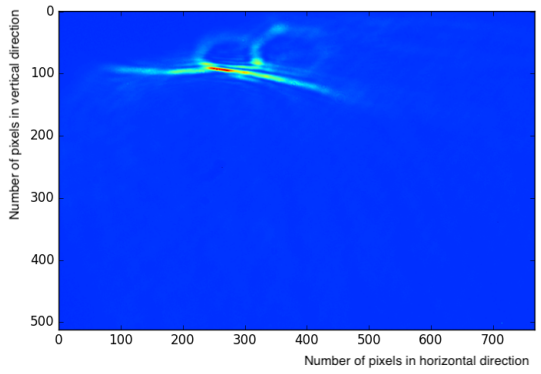

(a) 42.0 cm

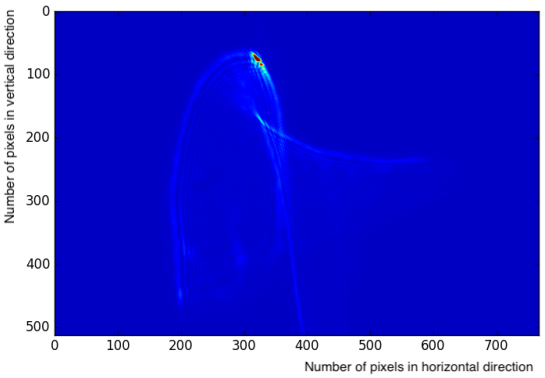

(d) 51.6 cm

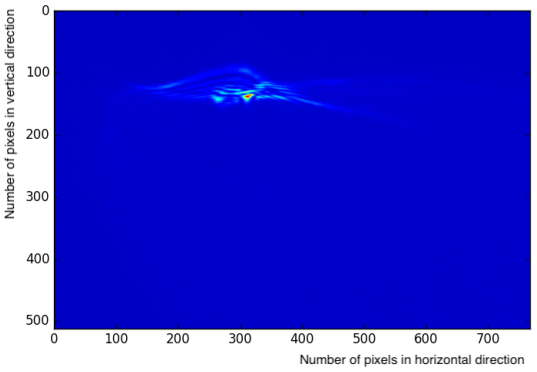

(b) 44.2 cm

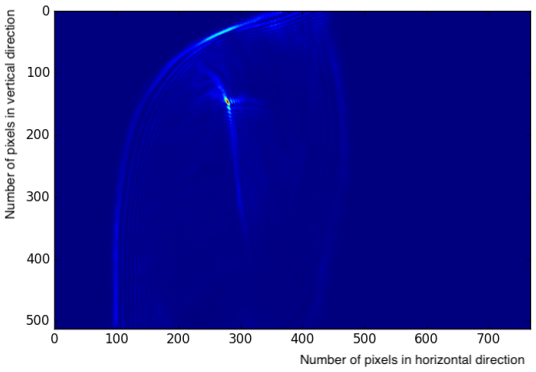

(e) 55.0 cm

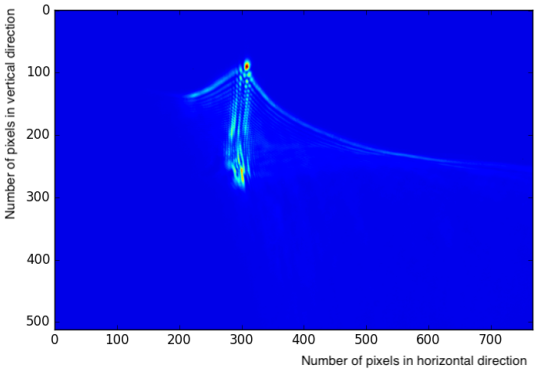

(c) 47.8 cm

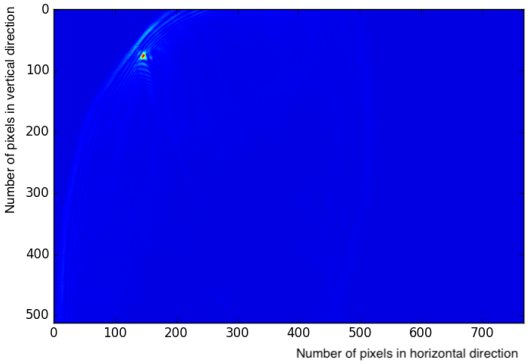

(f) 57.0 cm

Figure B.2: CCD images at different laser positions which show the spot that has been reflected off the uncoated, flat, glass mirror.

From the images presented by Figure B.2, the imaged spots do not appear spot-like, and instead have a different structure. Moreover, in Figure B.2 it is evident that the image of the spot changes drastically over the different dx values. The effect is that at the lowest distance (42cm) the "spot" appears as a blurred almost horizontal line. However, as one increases in distance (dx), the imaged spot becomes larger, more spot-like structure, as well as more better defined. Furthermore, as the distance increases, the image increases in size such that the full spot is no longer captured by the CCD camera. At the largest distance (57cm), it is clear that the spot has increased severely in size and is less visible. For each distance, dx, the image was analysed and different variables were obtained. The value of D_0 was calculated at each point, as well as the position of D_0 in terms of x,y pixel coordinates. The results for these variables are given by Fig B.3. Given that D_0 is defined as the diameter of the smallest circle that encloses 95% of the light, this means D_0 of the mirror corresponds to the minimum in Figure B.3(a). The results reveal that the D_0 of the uncoated flat mirror is 1.924 mm and occurs at a dx of 51.2 cm. Figure B.4 shows the image that corresponds to the minimum D_0 at the distance of 51.2 cm. The requirement is that $D_0 < 2.5$ mm, meaning that the value of the D_0 for the uncoated, flat, prototype mirror is well within the requirements.

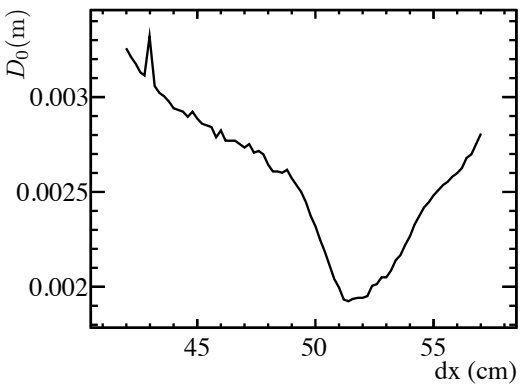

(a) The D_0 as a function of distance

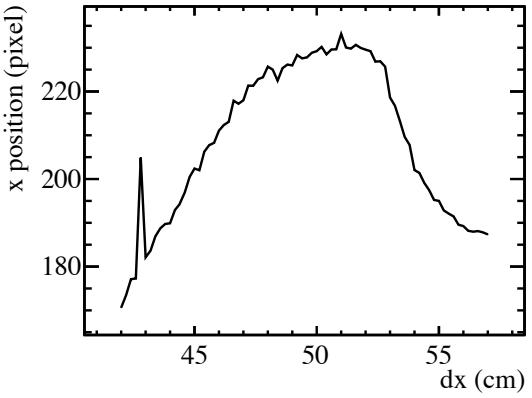

(b) The x position of the D_0 as a function of distance

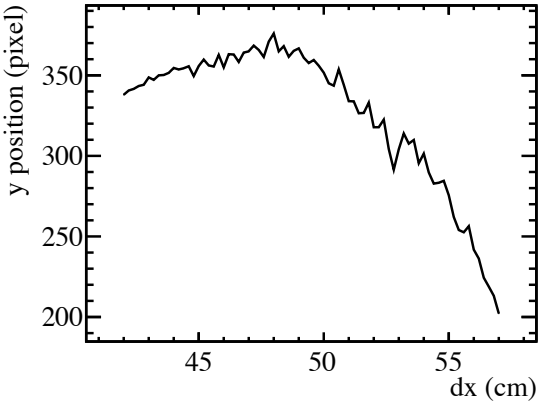

(b) The y position of the D_0 as a function of distance

Figure B.3: The results for the uncoated, flat, glass mirror when varying the laser distance.

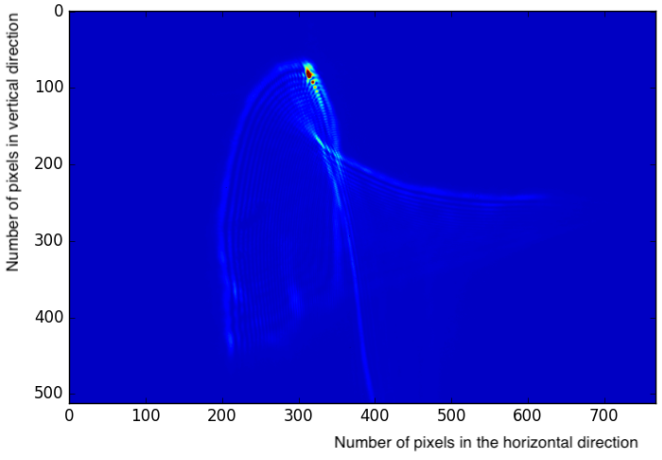

Figure B.4: The CCD image of the spot at the position 51.2 cm that corresponds to the image which has the minimum D_0 for the uncoated, flat, glass mirror.

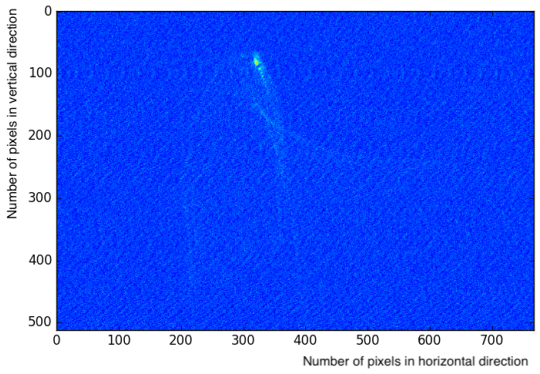

(a) 20 mA

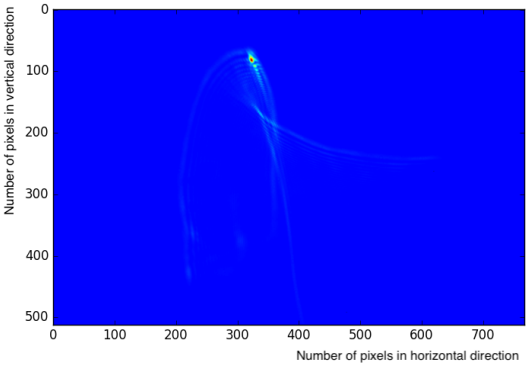

(d) 29 mA

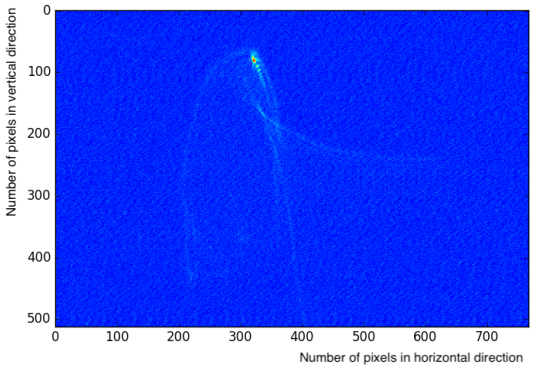

(b) 23 mA

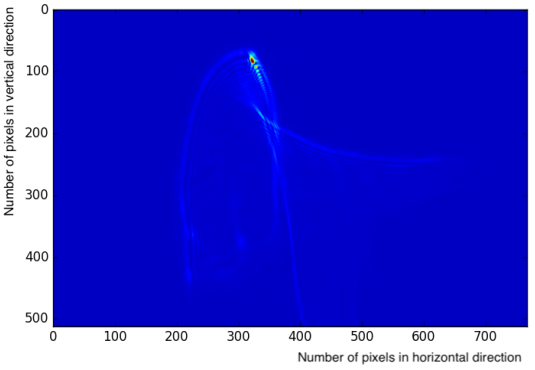

(e) 32 mA

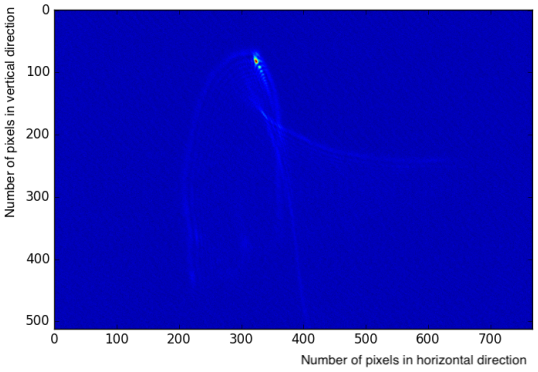

(c) 26 mA

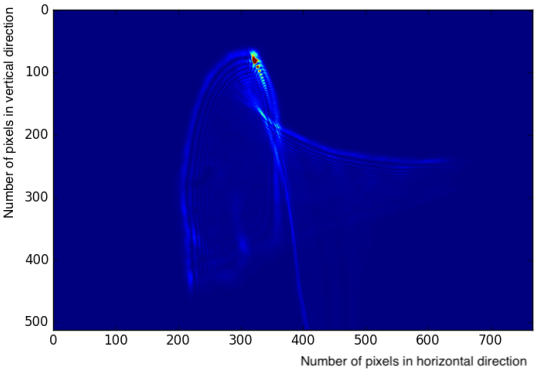

(f) 35 mA

Figure B.5: CCD images at different currents showing the spot that has been reflected off the uncoated, flat, glass mirror.

To follow, the next test performed on the uncoated, flat prototype mirror was the measurement of the D_0 as a function of current (I). The current was varied from 20 mA to 35 mA, in steps of 1 mA. The aim was to observe if the D_0 fluctuated with current, and if so was the effect large. Figure B.5 presents several images of the spot reflected off the testing mirror at different currents. The images in Figure B.5 demonstrate how as the current increases, the spot becomes more visible and sharper. In particular, it is evident that at the lowest current, 20 mA, the current is insufficient to image the spot and therefore appears blurred. It is only at current values that are greater than 28 mA, that the spot appears clear and well defined. For each image and therefore specific current value the D_0 was calculated, along with the x and y pixel position of the D_0. Figure B.6 illustrates the results.

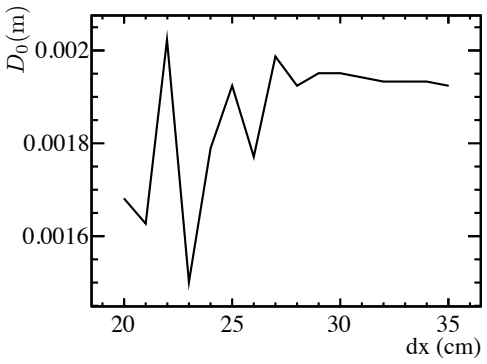

(a) The D_0 as a function of current

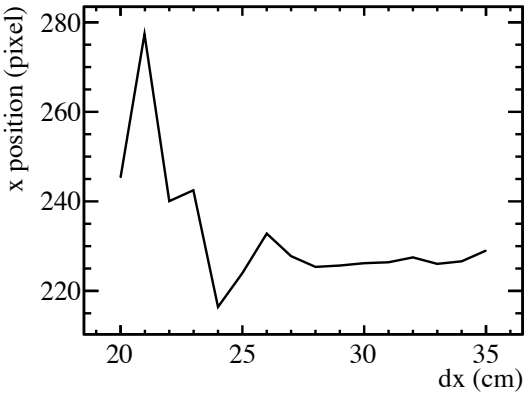

(b) The x position of the D_0 as a function of current

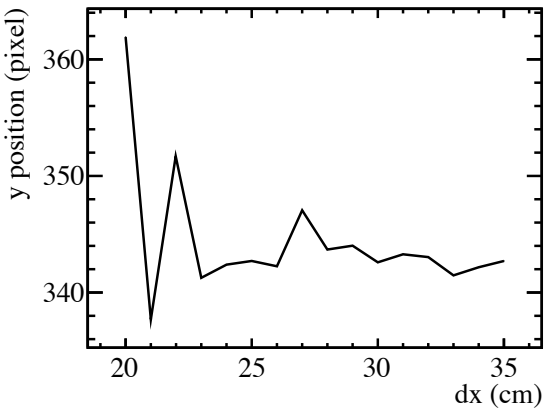

(b) The y position of the D_0 as a function of current

Figure B.6: The results for the uncoated, flat, glass mirror when varying the laser current.

In Figure B.6 (a) the value of D_0 shows larger fluctuations greatly at low current values. The most probable reason for this is that at low current values it is harder to image the spot clearly, and therefore the calculation of the D_0, which takes into account the integral of a given pixel, is more subject to fluctuations. Further, the D_0 appears to remain relatively constant with little changes for currents greater than 28 mA. This implies that the current is sufficient to calculate the D_0 relatively precisely. This is supported by Figure B.5 which as mentioned earlier shows the spot being distinct for currents greater than 28mA. It should be noted that the relatively small fluctuations at the higher current values are believed to originate from environmental fluctuations such as minute changes in background light or temperature. Figure B.6 (b) and (c) illustrate how the position of the D_0 remains somewhat consistent after 28 mA. This supports the suggestion that the current is now sufficient enough to produce an image with a clear D_0.

B.3.1.2 Coated, flat, glass mirror

The coated, flat, glass mirror as described in Section B.2.4 was formed out of Simax glass and coated with Al+SiO_2+HfO_2. The same tests were performed on the mirror where the D_0 was determined as a function of both distance (dx) and current (I). An additional test was performed where the reflectivity of the coating was investigated and is described later in this section. To begin, the measurement of the D_0 as a function of distance (dx) is described. The calculation of the D_0 as a function of position was performed in the same way as the equivalent measurement for the uncoated mirror (see Section B.3.1.1). The distance of the laser on the apparatus was adjusted, and the values tested were incremented in steps of 2 mm, in the range of 35 cm to 46.4 cm. The range of positions tested was different to the uncoated mirror due to the fact that the mirror was coated. Figure B.7 illustrates a subset of images of the spot at different positions (dx) for the coated mirror.

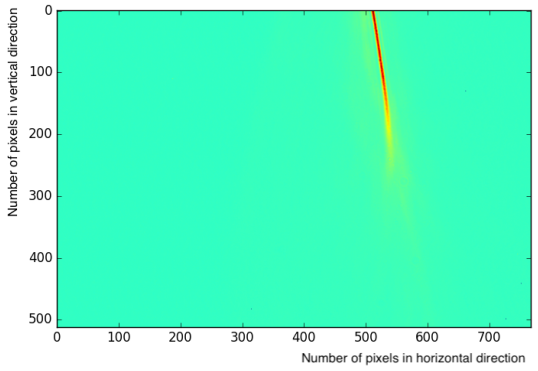

(a) 35.0 cm

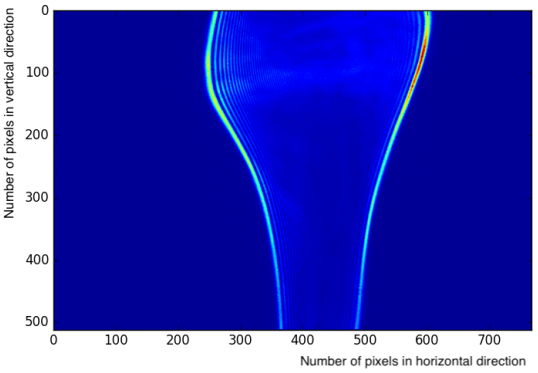

(d) 41.0 cm

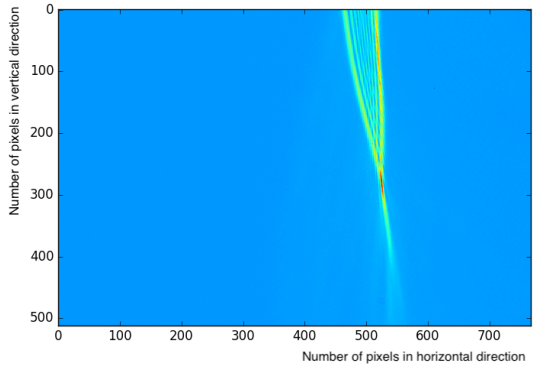

(b) 37.0 cm

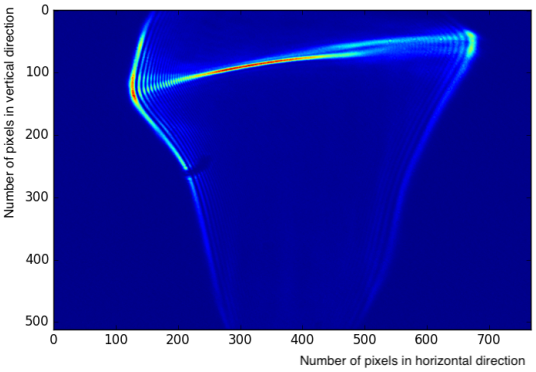

(e) 44.2 cm

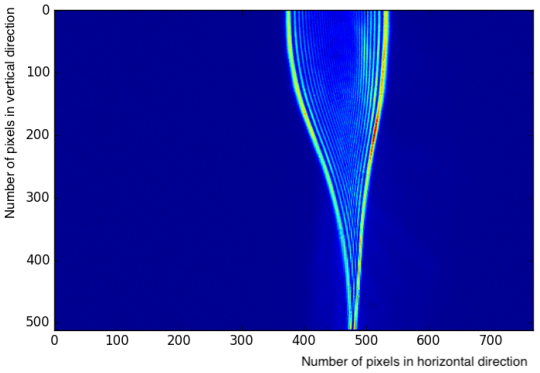

(c) 39.0 cm

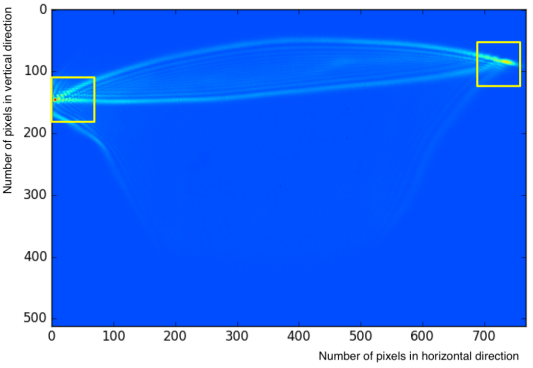

(f) 46.4 cm

Figure B.7: CCD images at different laser positions which image the spot that has been reflected off the coated, flat, glass mirror.

The images shown in Figure B.7 show how at the lowest position (35 cm) the spot appears as a vertical line. As one increases the distance, dx, the vertical line gets wider and a more spot-like structure appears. Nevertheless, there appears to be a turning point where beyond this point, the spot continues to widen, looking less like a spot. It can be seen that at large dx values, the spot spans the whole of the CCD image and has two maximum positions at the edges. These have been highlighted on Figure B.7 (f). The fact that there are two local maximum and that the image changes from vertical to horizontal, supports the suggestion that the mirror is astigmatic. An astigmatic mirror would have more than one radius of curvature. The images shown in Figure B.7 suggest there are two radii of curvature in the horizontal and vertical direction. Moreover, the coated, flat, glass mirror is an identical copy of the uncoated, flat, glass mirror with the only difference being the Al + SiO_2 + HfO_2 coating. This implies that because this astigmatic behaviour is only seen on the coated, flat, glass mirror, then it must be a consequence of the coating. One way the coating could cause this behaviour is through it not being applied correctly, such that the surface at the microscopic level is not smooth. Despite this, a working point for the D_0 was obtained. Figure B.8 shows the D_0 as a function of distance (a), and the location of the D_0 in terms of x and y pixels ((b) and (c)). In Figure B.8 (a) the D_0 minimum is located at 39.0 cm and has a value of 2.185 mm. The image that corresponds to this D_0 value is given by Figure B.9. This minimum D_0 value is greater than the value for the uncoated flat, glass mirror (See Section B.3.1.1), but nevertheless is within the requirements. Figure B.8 (b) and (c) show there is no clear position that defines the D_0. Instead, in both Figure B.8 (b) and (c) the D_0 position varies across various pixels, which could be due to the astigmatic behaviour. This also could explain the large differences between the distances seen between the coated and uncoated mirror. Nevertheless, even though the D_0 was within the requirements the quality of the mirror was not optimal as it was astigmatic. This is something that must be improved as in the current state the mirror will generate a significant amount of correlated noise.

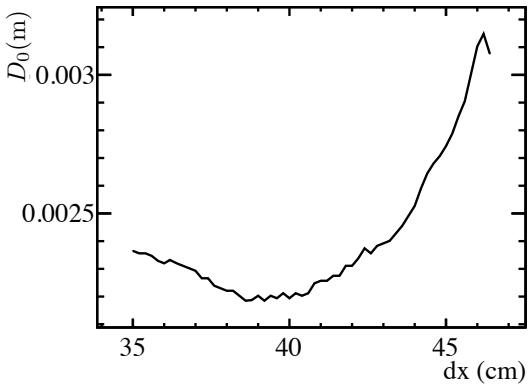

(a) The D_0 as a function of distance.

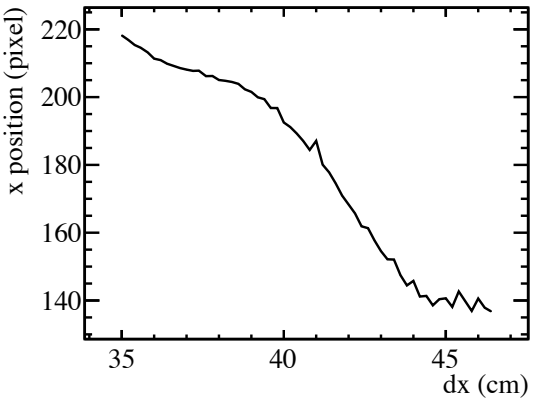

(b) The x position of the D_0 as a function of distance.

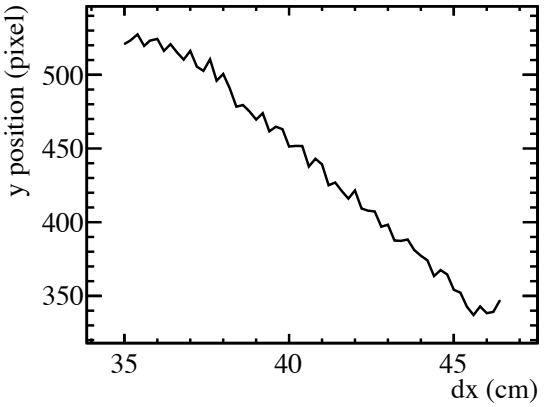

(c) The y position of the D_0 as a function of distance.

Figure B.8: The results for the coated, flat, glass mirror when varying the laser positiom.

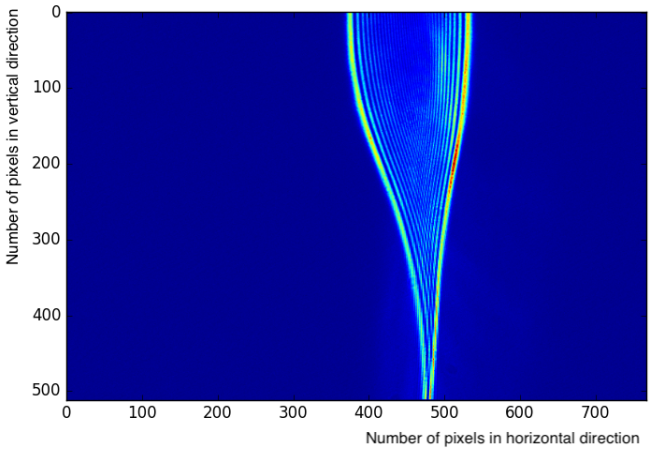

Figure B.9: The CCD image of the spot at the position 39.0 cm and corresponds to the image which has the minimum D_0 for the coated, flat, glass mirror.

For consistency, the D_0 as a function of current was investigated for the coated, flat, glass mirror. It was presumed that the coated, flat, glass mirror would exhibit the same behaviour as the uncoated, flat, glass mirror where D_0 fluctuates at low distances and then levels off at a constant value. However, it was unclear as to whether the problems with the coating would have affected this and so the measurement was repeated. The current was set initially to 1 mA and increased in steps of 1 mA until the final value of 25 mA. The currents tested were lower than those for the uncoated, flat mirror as the coating means that one can reduce the current. Figure B.10 shows several images produced at different currents for the coated mirror. In these images the difference between different currents is less clear, with only significant difference being at the lowest current values. This is believed to be a result of having a layer of coating. Next, Figure B.11 shows the D_0 as a function of current. In this figure, the D_0 as a function of current follows the same behaviour as the uncoated, flat mirror where it fluctuates at low current values, before levelling of at a constant D_0 when it reaches a sufficient current. This suggests that problems in the coating did not affect the D_0 as a function of current.

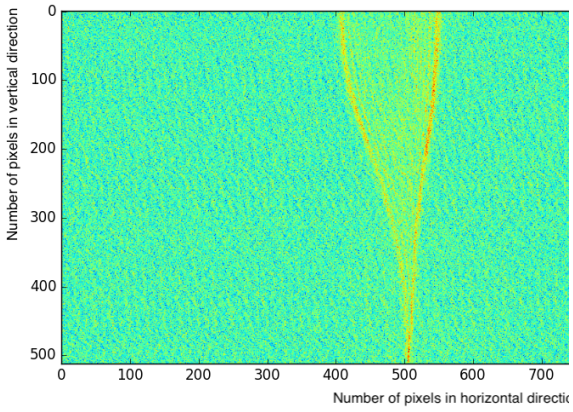

(a) 1 mA

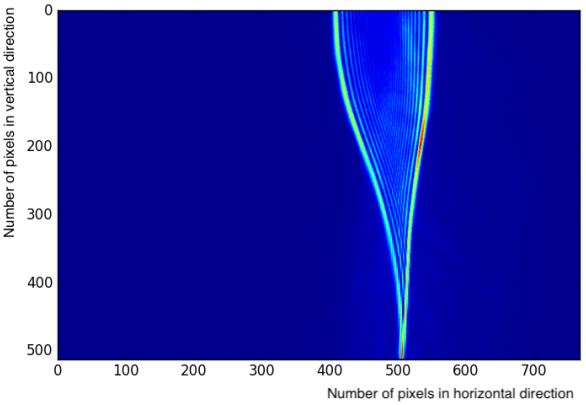

(d) 15 mA

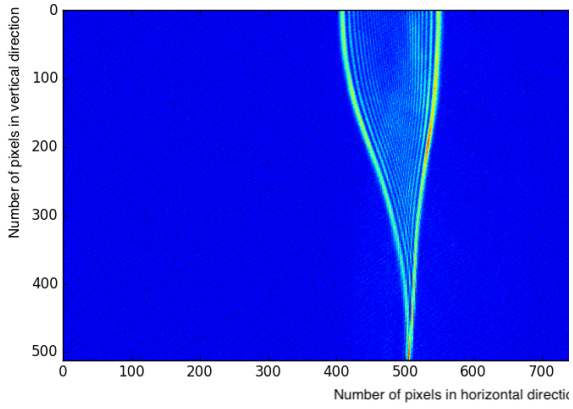

(b) 4 mA

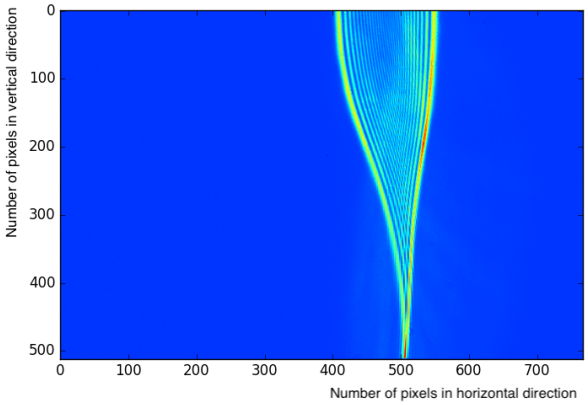

(e) 21 mA

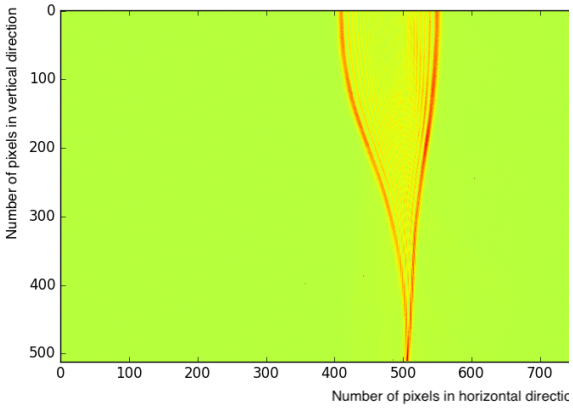

(c) 9 mA

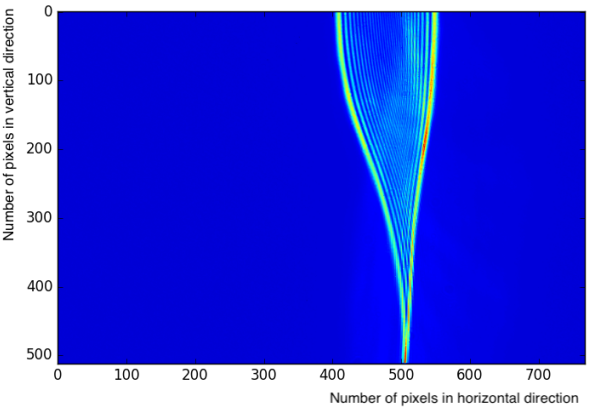

(f) 25 mA

Figure B.10: CCD images at different currents which show the spot that has been reflected off the coated, flat, glass mirror.

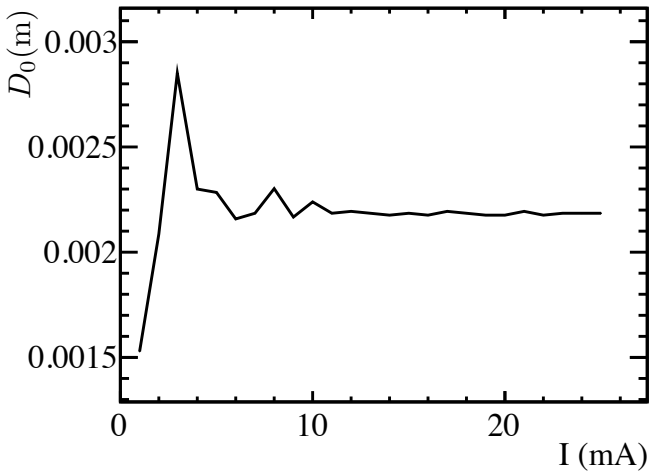

Figure B.11: The D_0 as a function of current, for the coated, flat, glass prototype mirror.

RICH 1 is reliant on the principle that the photons will be reflected of a given mirror. Therefore, the reflectivity of a given mirror is an important property of the mirrors. Each mirror that is in the RICH 1 system has a coating that allows it to reflect photons. As mentioned earlier the coating that is applied to the coated, flat, glass prototype mirror is the same as the coating used on the flat mirrors for both Run 1 and Run 2, which is Al +SiO_2 + HfO_2. The coating on the flat, glass mirror was tested at CERN using a spectrophotometer. The aim was to investigate if the coating provided by the flat, mirror suppliers (Olomouc) met the requirements needed for the RICH 1 optical system. To conduct the measurement, the coated, flat, glass mirror was placed in the spectrometer at an angle of incidence of 30°. The angle of incidence was chosen such that was generally consistent with the angle that the photons hit the mirrors at in the RICH 1 system (25° for spherical and 45° for flat mirrors [49]). Moreover, the measurement was performed across the wavelength range of 200 nm $< \lambda <$ 600 nm, before focussing on the range of interest which was 250-400 nm. The photons that are reflected off the RICH 1 mirrors are expected to have a wavelength in this particular range. As the mirror was seen to exhibit problems with the coating in the D_0 results, different positions on the mirror were tested. Figure B.12 illustrates a diagram of the mirror and the four positions that were selected for testing. These positions were chosen at random and across the whole mirror, to see if the coated was the same across the mirror.

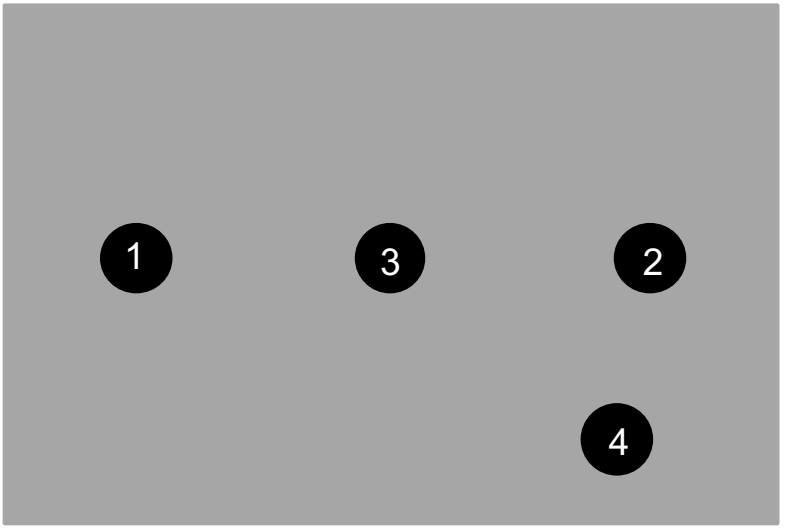

Figure B.12: Schematic of the positions on the coated, flat glass mirror which were tested for the reflectivity.

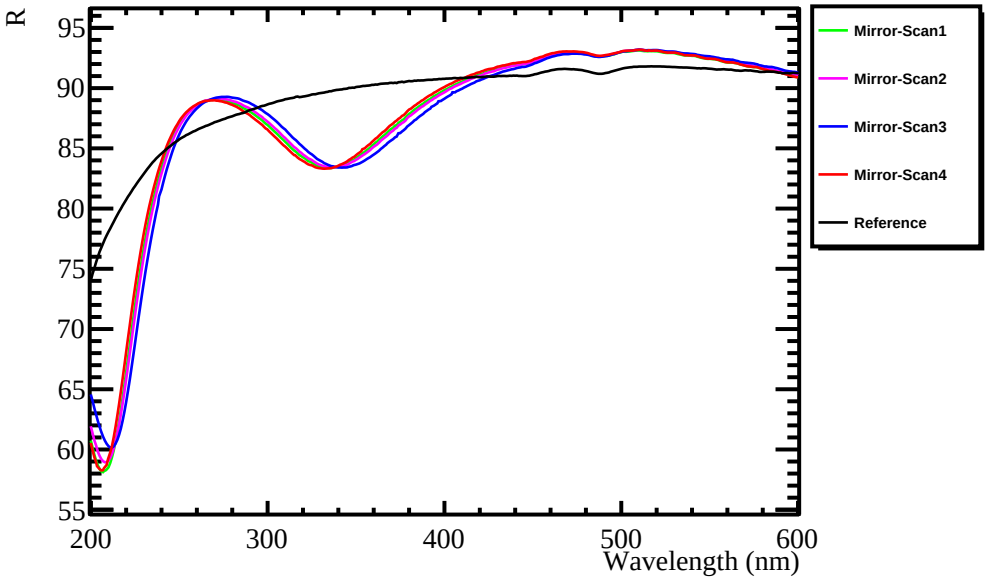

Figure B.13: The reflectivity as a function of wavelength, for the prototype, coated, glass mirror. The coloured lines correspond to different reflectivity measurements taken at the positions illustrated by Figure B.12.

At each of these positions a measurement was taken. Figure B.13 shows the results of the reflectivity for the coated, flat mirror. The results at each different position (see Figure B.12) are shown by the solid coloured lines. The solid, black line illustrates the reference line which is the reflectivity curve for a current RICH 1, coated, flat mirror. The mirrors need to have a high reflectivity in the required range. The requirement is that the reflectivity is greater than 85%, in the wavelength region of $\lambda \in$[250,400]nm. Figure B.13

shows that in this region the reflectivity measured did not meet the requirements. This concluded that the coating was not adequate for the LHCb RICH 1 upgrade mirrors. Nevertheless, the quality of the actual mirror (uncoated glass) was adequate. Therefore, one possibility suggested was that if glass mirrors were to be used in the RICH 1 upgrade then it might be possible to do the coating at CERN or by an alternative coating supplier. These suggestions go beyond the scope of this thesis and therefore the tests into these two options is not discussed.

B.3.2 Spherical mirrors

This section describes the results obtained from the single, spherical mirror as described in Section B.2.4. The single, uncoated, spherical mirror, that was made out of a carbon fibre underwent the same testing as the flat mirror prototypes as described in Sec B.3.1 where the D_0 was measured as a function of position, dx. The distance was incremented in steps of 2 mm, from 54cm to 56cm. Figure B.14 illustrates several images showing the resulting spot imaged from reflections off the spherical mirror at different distances, dx. In the images shown by Figure B.14 the resulting spot is clearer and more localised than the flat, glass prototype mirrors. There also appears to be fewer changes between images in comparison to the results from the flat, glass prototype mirrors. This could be due to a number of possibilities, that could include; the quality of the mirror, the difference in material being carbon fibre compared to glass, or even environmental factors. Moreover,during the testing, for each image produced the D_0 was calculated. Figure B.15 shows the D_0 as a function of position, as well the x and y pixel positions for the D_0.

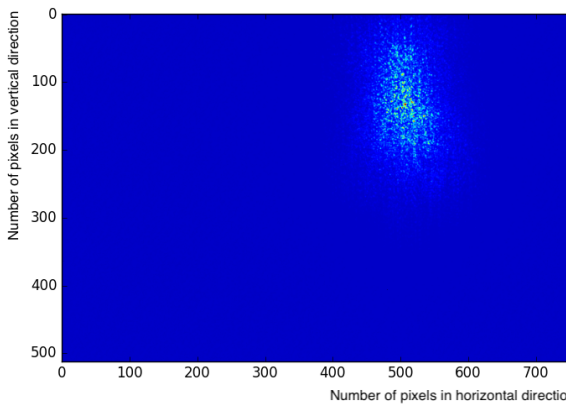

(a) 54.0 cm

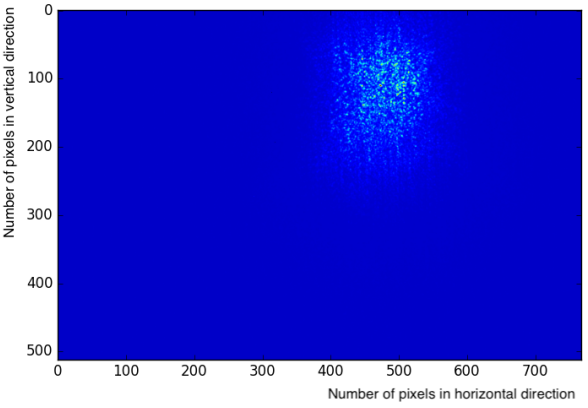

(d) 55.4 cm

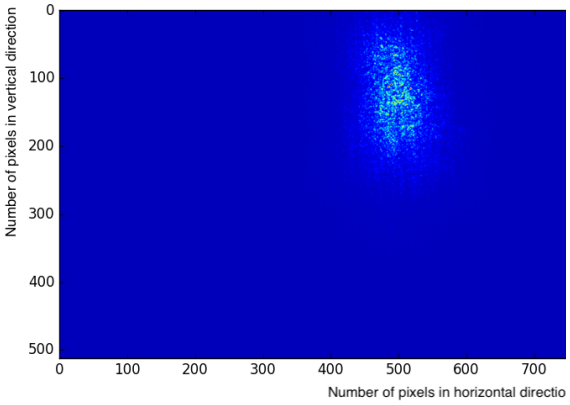

(b) 54.4 cm

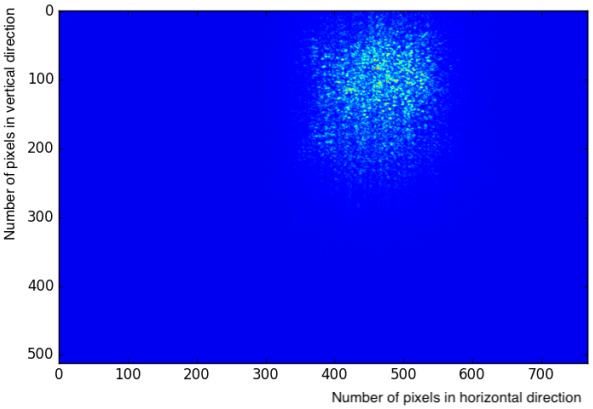

(e) 55.8 cm

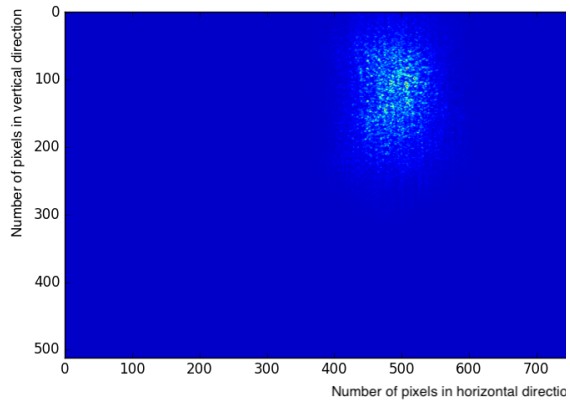

(c) 55.0 cm

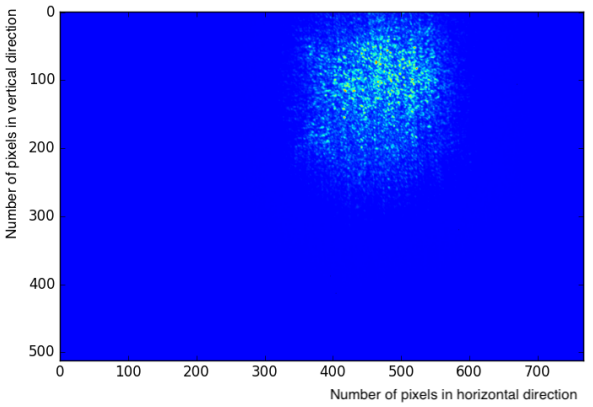

(f) 56.0 cm

Figure B.14: CCD images obtained at various distances, dx showing the spot which has been reflected off the spherical, carbon fibre mirror.

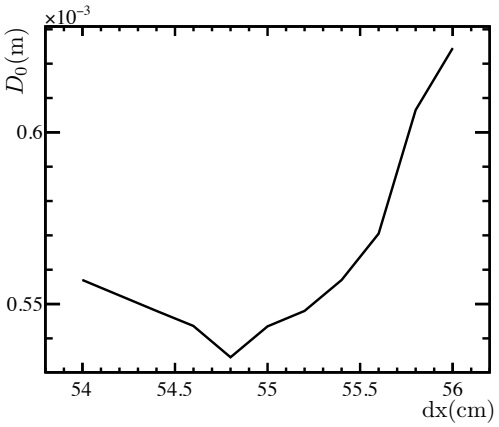

(a) The D_0 as a function of position.

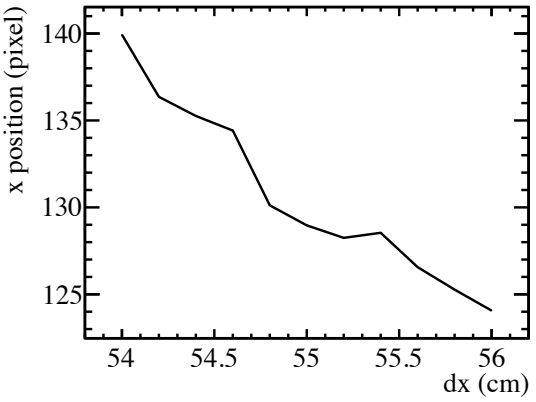

(b) The x position of the D_0 as a function of distance.

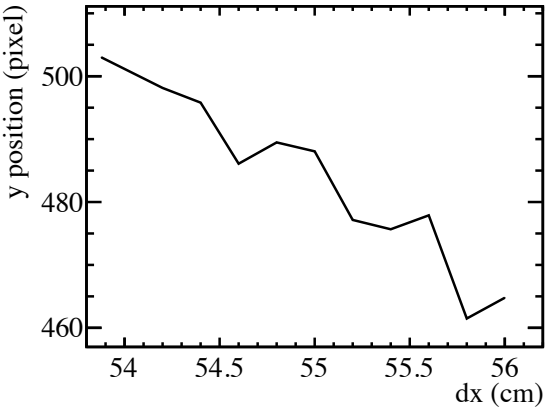

(c) The y position of the D_0 as a function of distance.

Figure B.15: The D_0 as a function of position dx for the spot imaged by reflection off the spherical, carbon, fibre mirror.

Figure B.15 (b) and (c) which shows the x and y position for the D_0 in terms of pixels, indicate that there is no clear minimum for either position and instead the location of the D_0 can vary greatly. This could be due to the fact the mirror is not coated, or even where the light hits on the spherical mirror. Explicitly for the latter, the curvature will affect the distance and where the light hits on the mirror. Nevertheless, in Figure B.15 (a) which shows the D_0 as a function of position, a clear minimum can be found. The minimum D_0 value is 1.069 mm and is located at the distance 54.8 cm. The corresponding image for this position and for the minimum D_0 value is shown by Figure B.16. This value is well within the experimental specifications, showing this prototype mirror is a suitable spherical mirror candidate for the RICH mirror upgrade.

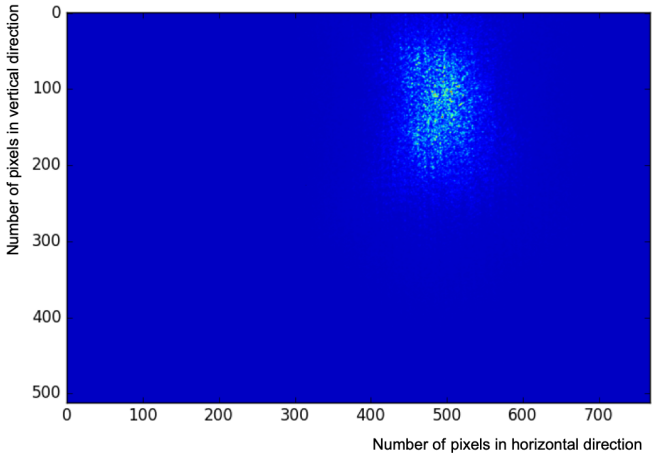

Figure B.16: CCD image of the spot reflected off the spherical mirror, at a laser position of 54.8 cm and corresponding to the minimum D_0.

B.4 Summary

In summary a selection of prototype mirrors that include both spherical and flat mirrors, have been optically tested at CERN to investigate if the mirrors meet the requirements and identify suppliers. The results for the two prototype flat, mirrors tested, the results reveal that while the quality of the flat mirror is adequate, the coating is not. The proposed solution for the upgrade is to obtain the flat mirrors uncoated from the supplier (Olomouc) and undertake the coating at CERN. This is deemed sufficient given the D_0 for the uncoated mirror is 1.924 mm and well within the specifications (<2.5 mm). This will be applied to all 16 flat mirrors needed for the LHCb RICH 1 flat mirror upgrade. The final specifications for the chosen flat mirrors are given by Table B.1. The results from the single uncoated, spherical, carbon fibre mirror indicate that this mirror is a suitable option for the spherical mirrors that will be in the LHCb RICH 1 spherical mirror upgrade. The results show the D_0 (1.069 mm) is well within the requirements (<2.5 mm) and no issues in the quality of this mirror were apparent. It follows that 4 spherical mirrors for the upgrade will be obtained from the company CMA. As noted earlier this company is unable to undertake the coating of these mirrors. One possibility was that this could be a problem for many coating suppliers due to the larger size of these mirrors. Nevertheless, it was believed that CERN might be capable of performing the coating on the spherical mirrors as well. Though discussions with the coating team at CERN, it was deciced that CERN would also coat the spherical mirrors in addition

	Flat mirror
Shape	Rectangle
Size	370 mm × 440 mm
Material	Simax glass
Thickness	7 mm ± 1 mm
Coating	Al +SiO_2 + HfO_2
Supplier	Olomouc

Table B.1: Specifications for the flat mirrors that will be used in the LHCb RICH 1 mirror upgrade.

	Spherical mirror
Shape	Spherical
Size	740 mm × 650 mm
Material	Carbon Fibre Reinforced Polymer (CFRP)
Thickness	$<$ 1.5 mm
Coating	Al +SiO_2 + HfO_2
Supplier	CMA

Table B.2: Specifications for the spherical mirrors that will be used in the LHCb RICH 1 mirror upgrade.

to the flat mirrors. For the 4 spherical mirrors that will be in the LHCb RICH 1 mirror upgrade the final specifications for these mirrors are given by Table B.2.

Appendix C

Criteria on the Trigger Lines

Trigger	p_T	Dimuon p_T	Number of tracks	SPD multiplicity
`L0Muon`	p_T >1.48 GeV/c	–	1	<600
`L0DiMuon`	–	p_T^2 >(1.3 GeV/c)^2	2	<900

Table C.1: Criteria on the L0Muon and L0DiMuon trigger lines [110]

HLT Trigger Line	`Hlt1TrackAllL0`	`Hlt1TrackMuon`
Track IP (mm)	>0.1	>0.1
Number of VELO hits/track	>9	>6
Number of Missed VELO hits/track	<3	–
Number of OT+IT×2 hits/track	>16	–
Track IPχ^2	>16	>16
Track p_T (GeV/c)	>1.7	>1.0
Track p (GeV/c)	>10	>8
Track χ^2/ndf	<2.5	<2.5

Table C.2: Criteria on the `Hlt1TrackAllL0` and `Hlt1TrackMuon` trigger lines [111, 112]

HLT Trigger Line	`Hlt1TrackMVA`	`Hlt1TwoTracksMVA`
Track χ^2/ndf	<2.5	<2.5
Track χ^2	>7.4	>7.0
Ghost probability	<0.2	–
Track p (GeV/c)	–	>5
Track p_T (GeV/c)	1.0< p_T¡25	>0.5
Corrected mass(MeV/c^2)	–	$1000 < m < 10^9$
DIRA	–	>0
Vertex χ^2	–	<10
Intermediate meson p_T (MeV/c)	–	>2000

Table C.3: Criteria on the `Hlt1TrackMVA` and`Hlt1TwoTracksMVA` trigger lines [113]

HLT Trigger Line	`Hlt2SingleMuon`	`Hlt2DimuonDetached`
Track p_T	>1.3 GeV/c	–
Track vertex χ^2/ndf	<2	< 5
Track IPχ^2 with the PV	>200	>9
Dimuon p_T	–	>1.5 GeV/c
Dimuon FD	–	>49
Dimuon vertex χ^2/ndf	–	<25
$m_{\mu\mu}$	–	>1.0 GeV/c^2

Table C.4: Criteria on the `Hlt2SingleMuon` and `Hlt2DimuonDetached` [112]

Variable	Selection Criteria
p_T	>500 MeV
p	>5 GeV
Track χ^2	< 5
IP χ^2	>16
B candidate corrected mass	4 GeV $< m_{corr} <$ 7 GeV
hardest daughter momentum	p_T >1.5 GeV
best daughter track χ^2	track χ^2 <3
sum of daughter track momenta	$\sum p_T >$ 4,4.25, 4.5 GeV (2,3,4-body)
sum of daughter IPχ^2	$\sum IP\chi^2 >$ 100,150, 200 (2,3,4-body)
particle/particle and particle/n-body DOCA	DOCA< 0.15 mm
B candidate flight distance χ^2	FDχ^2 >64
B candidate signed flight distance	FD> 0
prompt D veto	m >2.5 GeV OR 2,3-body IPχ^2 > 16

Table C.5: Criteria for the HLT Topological Lines [114], where in the criteria DOCA is the distance of closest approach for the tracks constructed out of the 2,3,4-body vertices.

Bibliography

[1] T. Blake, U. Egede, P. Owen, K. A. Petridis, and G. Pomery, "An empirical model to determine the hadronic resonance contributions to $\overline{B}^0 \to \overline{K}^{*0}\mu^+\mu^-$ transitions," *Eur. Phys. J.* **C78** (2018) no. 6, 453, arXiv:1709.03921 [hep-ph].

[2] A. Khodjamirian, T. Mannel, A. A. Pivovarov, and Y. M. Wang, "Charm-loop effect in $B \to K^{(*)}\ell^+\ell^-$ and $B \to K^*\gamma$," *JHEP* **09** (2010) 089, arXiv:1006.4945 [hep-ph].

[3] C. Bobeth, M. Chrzaszcz, D. van Dyk, and J. Virto, "Long-distance effects in $B \to K^*\ell\ell$ from analyticity," *Eur. Phys. J.* **C78** (2018) no. 6, 451, arXiv:1707.07305 [hep-ph].

[4] **LHCb** Collaboration, R. Aaij *et al.*, "Angular analysis of the $B^0 \to K^{*0}\mu^+\mu^-$ decay using 3 fb^{-1} of integrated luminosity," *JHEP* **02** (2016) 104, arXiv:1512.04442 [hep-ex].

[5] A. Pich, "The Standard model of electroweak interactions," in *The Standard model of electroweak interactions*, pp. 1–49. 2008. arXiv:0705.4264 [hep-ph]. http://doc.cern.ch/yellowrep/2007/2007-005/cern-2007-005.pdf. [,1(2007)].

[6] D. Griffiths, *Introduction to elementary particles*. John Wiley & Sons, 2008.

[7] F. Halzen and A. D. Martin, *Quarks and Leptons: An Introductory course in modern particle physics*. Wiley (6 Jan. 1984), 1984.

[8] P. A. Cartelle, "Study of the penguin-dominated decay $B_s^0 \to K^{*0}\bar{K}^{*0}$ at LHCb." PhD Thesis, September, 2014. http://cds.cern.ch/record/2004775/files/CERN-THESIS-2014-293.pdf.

[9] T. C. collaboration, "Summer results." http://ckmfitter.in2p3.fr/www/results/plots_summer18/num/ckmEval_results_summer18.html, July, 2018.

[10] K. G. Wilson, "Nonlagrangian models of current algebra," *Phys. Rev.* **179** (1969) 1499–1512.

[11] W. Altmannshofer, P. Ball, A. Bharucha, A. J. Buras, D. M. Straub, and M. Wick, "Symmetries and Asymmetries of $B \to K^* \mu^+ \mu^-$ Decays in the Standard Model and Beyond," *JHEP* **01** (2009) 019, arXiv:0811.1214 [hep-ph].

[12] T. Blake, "Rare $b-$hadron decays." IoP HEPP and AP joint meeting, University of Sussex, 2016.

[13] A. Bharucha, D. M. Straub, and R. Zwicky, "$B \to V \ell^+ \ell^-$ in the Standard Model from light-cone sum rules," *JHEP* **08** (2016) 098, arXiv:1503.05534 [hep-ph].

[14] A. Khodjamirian, T. Mannel, and N. Offen, "Form-factors from light-cone sum rules with B-meson distribution amplitudes," *Phys. Rev.* **D75** (2007) 054013, arXiv:hep-ph/0611193 [hep-ph].

[15] **LHCb** Collaboration, R. Aaij *et al.*, "Measurement of Form-Factor-Independent Observables in the Decay $B^0 \to K^{*0} \mu^+ \mu^-$," *Phys. Rev. Lett.* **111** (2013) 191801, arXiv:1308.1707 [hep-ex].

[16] U. Egede, M. Patel, and K. A. Petridis, "Method for an unbinned measurement of the q^2 dependent decay amplitudes of $\overline{B}^0 \to \overline{K}^{*0} \mu^+ \mu^-$ decays," *JHEP* **06** (2015) 084, arXiv:1504.00574 [hep-ph].

[17] T. Blake and C. Langenbruch, "Angular conventions for the decays $B^0 \to K^{*0} \mu^+ \mu^-$ and $B_s^0 \to \phi \mu^+ \mu^-$." LHCb-INT-2012-021, 2012.

[18] C. Bobeth, G. Hiller, and G. Piranishvili, "CP Asymmetries in bar $B \to \bar{K}^*(\to \bar{K}\pi)\bar{\ell}\ell$ and Untagged $\bar{B}_s$, $B_s \to \phi(\to K^+K^-)\bar{\ell}\ell$ Decays at NLO," *JHEP* **07** (2008) 106, arXiv:0805.2525 [hep-ph].

[19] J. Gratrex, M. Hopfer, and R. Zwicky, "Generalised helicity formalism, higher moments and the $B \to K_{J_K}(\to K\pi)\bar{\ell}_1 \ell_2$ angular distributions," *Phys. Rev.* **D93** (2016) no. 5, 054008, arXiv:1506.03970 [hep-ph].

[20] S. Descotes-Genon, J. Matias, M. Ramon, and J. Virto, "Implications from clean observables for the binned analysis of $B \to K^* \mu^+ \mu^-$ at large recoil," *JHEP* **01** (2013) 048, arXiv:1207.2753 [hep-ph].

[21] S. Descotes-Genon, J. Matias, and J. Virto, "Understanding the $B \to K^* \mu^+ \mu^-$ Anomaly," *Phys. Rev.* **D88** (2013) 074002, arXiv:1307.5683 [hep-ph].

[22] J. Matias, F. Mescia, M. Ramon, and J. Virto, "Complete Anatomy of $\bar{B}_d \to \bar{K}^{*0}(\to K\pi) l^+ l^-$ and its angular distribution," *JHEP* **04** (2012) 104, arXiv:1202.4266 [hep-ph].

[23] **LHCb** Collaboration, R. Aaij *et al.*, "Differential branching fraction and angular analysis of $\Lambda_b^0 \to \Lambda \mu^+ \mu^-$ decays," *JHEP* **06** (2015) 115, arXiv:1503.07138 [hep-ex]. [Erratum: JHEP09,145(2018)].

[24] **LHCb** Collaboration, R. Aaij *et al.*, "Differential branching fractions and isospin asymmetries of $B \to K^{(*)}\mu^+\mu^-$ decays," *JHEP* **06** (2014) 133, arXiv:1403.8044 [hep-ex].

[25] **LHCb** Collaboration, R. Aaij *et al.*, "Angular analysis and differential branching fraction of the decay $B_s^0 \to \phi\mu^+\mu^-$," *JHEP* **09** (2015) 179, arXiv:1506.08777 [hep-ex].

[26] **LHCb** Collaboration, R. Aaij *et al.*, "Angular moments of the decay $\Lambda_b^0 \to \Lambda\mu^+\mu^-$ at low hadronic recoil," *JHEP* **09** (2018) 146, arXiv:1808.00264 [hep-ex].

[27] **LHCb** Collaboration, R. Aaij *et al.*, "Angular analysis of the $B^0 \to K^{*0}e^+e$ decay in the low-q^2 region," *JHEP* **04** (2015) 064, arXiv:1501.03038 [hep-ex].

[28] **LHCb** Collaboration, R. Aaij *et al.*, "Test of lepton universality using $B^+ \to K^+\ell^+\ell^-$ decays," *Phys. Rev. Lett.* **113** (2014) 151601, arXiv:1406.6482 [hep-ex].

[29] **LHCb** Collaboration, R. Aaij *et al.*, "Test of lepton universality with $B^0 \to K^{*0}\ell^+\ell^-$ decays," *JHEP* **08** (2017) 055, arXiv:1705.05802 [hep-ex].

[30] S. Descotes-Genon, L. Hofer, J. Matias, and J. Virto, "On the impact of power corrections in the prediction of $B \to K^*\mu^+\mu^-$ observables," *JHEP* **12** (2014) 125, arXiv:1407.8526 [hep-ph].

[31] W. Altmannshofer and D. M. Straub, "New physics in $b \to s$ transitions after LHC run 1," *Eur. Phys. J.* **C75** (2015) no. 8, 382, arXiv:1411.3161 [hep-ph].

[32] S. Descotes-Genon, L. Hofer, J. Matias, and J. Virto, "Global analysis of $b \to s\ell\ell$ anomalies," *JHEP* **06** (2016) 092, arXiv:1510.04239 [hep-ph].

[33] W. Altmannshofer, C. Niehoff, P. Stangl, and D. M. Straub, "Status of the $B \to K^*\mu^+\mu^-$ anomaly after Moriond 2017," *Eur. Phys. J.* **C77** (2017) no. 6, 377, arXiv:1703.09189 [hep-ph].

[34] B. Capdevila, A. Crivellin, S. Descotes-Genon, J. Matias, and J. Virto, "Patterns of New Physics in $b \to s\ell^+\ell^-$ transitions in the light of recent data," *JHEP* **01** (2018) 093, arXiv:1704.05340 [hep-ph].

[35] W. Altmannshofer, P. Stangl, and D. M. Straub, "Interpreting Hints for Lepton Flavor Universality Violation," *Phys. Rev.* **D96** (2017) no. 5, 055008, arXiv:1704.05435 [hep-ph].

[36] A. Greljo, G. Isidori, and D. Marzocca, "On the breaking of Lepton Flavor Universality in B decays," *JHEP* **07** (2015) 142, arXiv:1506.01705 [hep-ph].

[37] W. Altmannshofer and D. M. Straub, "New Physics in $B \to K^* \mu\mu$?," *Eur. Phys. J.* **C73** (2013) 2646, arXiv:1308.1501 [hep-ph].

[38] L. Di Luzio, M. Kirk, and A. Lenz, "Updated B_s-mixing constraints on new physics models for $b \to s\ell^+\ell^-$ anomalies," *Phys. Rev.* **D97** (2018) no. 9, 095035, arXiv:1712.06572 [hep-ph].

[39] G. Hiller, D. Loose, and I. Niandi, "Flavorful leptoquarks at hadron colliders," *Phys. Rev.* **D97** (2018) no. 7, 075004, arXiv:1801.09399 [hep-ph].

[40] M. Bordone, C. Cornella, J. Fuentes-Martin, and G. Isidori, "A three-site gauge model for flavor hierarchies and flavor anomalies," *Phys. Lett.* **B779** (2018) 317–323, arXiv:1712.01368 [hep-ph].

[41] D. Buttazzo, A. Greljo, G. Isidori, and D. Marzocca, "Toward a coherent solution of diphoton and flavor anomalies," *JHEP* **08** (2016) 035, arXiv:1604.03940 [hep-ph].

[42] J. Lyon and R. Zwicky, "Resonances gone topsy turvy - the charm of QCD or new physics in $b \to s\ell^+\ell^-$?," arXiv:1406.0566 [hep-ph].

[43] M. Beneke, G. Buchalla, M. Neubert, and C. T. Sachrajda, "Penguins with Charm and Quark-Hadron Duality," *Eur. Phys. J.* **C61** (2009) 439–449, arXiv:0902.4446 [hep-ph].

[44] M. Tanabashi, K. Hagiwara, K. Hikasa, K. Nakamura, Y. Sumino, F. Takahashi, J. Tanaka, K. Agashe, G. Aielli, C. Amsler, *et al.*, "Review of particle physics," *Physical Review D* **98** (2018) no. 3, 030001.

[45] **LHCb** Collaboration, R. Aaij *et al.*, "Measurement of the phase difference between short- and long-distance amplitudes in the $B^+ \to K^+\mu^+\mu^-$ decay," *Eur. Phys. J.* **C77** (2017) no. 3, 161, arXiv:1612.06764 [hep-ex].

[46] G. CERN, "The CERN accelerator complex." CERN-DI-0812015, https://cds.cern.ch/record/2197559?ln=en, 2008.

[47] R. Sahoo, "Relativistic kinematics," *arXiv preprint arXiv:1604.02651* (2016) .

[48] **LHCb** Collaboration, "$b\bar{b}$ production angle plots website." http://lhcb.web.cern.ch/lhcb/speakersbureau/html/bb_ProductionAngles.html.

[49] **LHCb** Collaboration, A. A. Alves, Jr. *et al.*, "The LHCb Detector at the LHC," *JINST* **3** (2008) S08005.

[50] L. Collaboration *et al.*, "LHCb VELO (VErtex LOcator): Technical Design Report." http://lhcb.web.cern.ch/lhcb/speakersbureau/html/bb_ProductionAngles.html, 2001.

[51] R. Aaij, A. Affolder, K. Akiba, M. Alexander, S. Ali, R. Appleby, M. Artuso, A. Bates, A. Bay, O. Behrendt, *et al.*, "Performance of the LHCb vertex locator," *Journal of Instrumentation* **9** (2014) no. 09, P09007.

[52] T. Bellunato, *Development of Ring Imaging Cherenkov Detectors for LHCb.* PhD thesis, Milan U., 2003. `http://inspirehep.net/record/887180/files/CERN-THESIS-2009-038.pdf`.

[53] M. Adinolfi, G. A. Rinella, E. Albrecht, T. Bellunato, S. Benson, T. Blake, C. Blanks, S. Brisbane, N. Brook, M. Calvi, *et al.*, "Performance of the LHCb RICH detector at the LHC," *The European Physical Journal C* **73** (2013) no. 5, 2431.

[54] **LHCb RICH** Collaboration, A. Papanestis and C. D'Ambrosio, "Performance of the LHCb RICH detectors during the LHC Run II," *Nucl. Instrum. Meth.* **A876** (2017) 221–224, `arXiv:1703.08152 [physics.ins-det]`.

[55] T. L. collaboration, "Lhcb rich figures and plots." `https://twiki.cern.ch/twiki/bin/view/LHCb/RICHPicturesAndFigures`.

[56] T. L. collaboration, "Pid plots for conference." `https://twiki.cern.ch/twiki/bin/view/LHCb/PIDConferencePlots`.

[57] **LHCb Silicon Tracker Group** Collaboration, C. Elsasser, "The LHCb Silicon Tracker," *JINST* **9** (2014) no. 01, C01009.

[58] **LHCb** Collaboration, R. Aaij *et al.*, "LHCb Detector Performance," *Int. J. Mod. Phys.* **A30** (2015) no. 07, 1530022, `arXiv:1412.6352 [hep-ex]`.

[59] **LHCb** Collaboration, R. Aaij *et al.*, "Measurement of the track reconstruction efficiency at LHCb," *JINST* **10** (2015) no. 02, P02007, `arXiv:1408.1251 [hep-ex]`.

[60] **LHCb** Collaboration, R. Aaij *et al.*, "LHCb Detector Performance," *Int. J. Mod. Phys.* **A30** (2015) no. 07, 1530022, `arXiv:1412.6352 [hep-ex]`.

[61] R. Antunes Nobrega, *Development of the Experiment Control System and Performance Study of the Muon Chambers for the LHCb Experiment.* PhD thesis, Sapienza, Università di Roma, 2010.

[62] A. A. Alves Jr, L. Anderlini, M. Anelli, R. A. Nobrega, G. Auriemma, W. Baldini, G. Bencivenni, R. Berutti, A. Bizzeti, V. Bocci, *et al.*, "Performance of the LHCb muon system," *Journal of Instrumentation* **8** (2013) no. 02, P02022.

[63] F. Archilli, W. Baldini, G. Bencivenni, N. Bondar, W. Bonivento, S. Cadeddu, P. Campana, A. Cardini, P. Ciambrone, X. C. Vidal, *et al.*, "Performance of the muon identification at lhcb," *Journal of Instrumentation* **8** (2013) no. 10, P10020.

[64] T. Head, "The LHCb trigger system," *Journal of Instrumentation* **9** (2014) no. 09, C09015.

[65] **LHCb** Collaboration, B. Sciascia, "LHCb Run 2 trigger performance," *PoS* **BEAUTY2016** (2016) 029.

[66] R. Aaij, J. Albrecht, F. Alessio, S. Amato, E. Aslanides, I. Belyaev, M. Van Beuzekom, E. Bonaccorsi, R. Bonnefoy, L. Brarda, *et al.*, "The LHCb trigger and its Performance in 2011," *Journal of Instrumentation* **8** (2013) no. 04, P04022.

[67] S. Benson, V. V. Gligorov, M. A. Vesterinen, and J. M. Williams, "The LHCb Turbo Stream," *J. Phys. Conf. Ser.* **664** (2015) no. 8, 082004.

[68] M. Cattaneo *et al.*, "GAUDI LHCb Data Processing Applications Framework User Guide," *LHCb Note* (1999) .

[69] M. Clemencic, G. Corti, S. Easo, C. Jones, S. Miglioranzi, M. Pappagallo, P. Robbe, L. Collaboration, *et al.*, "The LHCb simulation application, Gauss: design, evolution and experience,".

[70] T. Sjöstrand, S. Mrenna, and P. Skands, "Pythia 6.4 physics and manual," *Journal of High Energy Physics* **2006** (2006) no. 05, 026.

[71] D. J. Lange, "The EvtGen particle decay simulation package," *Nuclear Instruments and Methods in Physics Research Section A: Accelerators, Spectrometers, Detectors and Associated Equipment* **462** (2001) no. 1-2, 152–155.

[72] S. Agostinelli, J. Allison, K. a. Amako, J. Apostolakis, H. Araujo, P. Arce, M. Asai, D. Axen, S. Banerjee, G. . Barrand, *et al.*, "Geant4a simulation toolkit," *Nuclear instruments and methods in physics research section A: Accelerators, Spectrometers, Detectors and Associated Equipment* **506** (2003) no. 3, 250–303.

[73] G. Corti, M. Cattaneo, P. Charpentier, M. Frank, P. Koppenburg, P. Mato, F. Ranjard, S. Roiser, I. Belyaev, and G. Barrand, "Software for the LHCb experiment," *IEEE transactions on nuclear science* **53** (2006) no. 3, 1323–1328.

[74] L. collaboration *et al.*, "DaVinci- The LHCb analysis program." `http://lhcbrelease-area.web.cern.ch/LHCb-release-area/DOC/davinci`.

[75] L. Eklund, "The LHCb Upgrade," *arXiv preprint arXiv:1709.04709* (2017) .

[76] **LHCb** Collaboration, M. P. Whitehead, "The upgrade of the LHCb trigger for Run III," *PoS* **EPS-HEP2017** (2018) 528. 5 p. `http://cds.cern.ch/record/2314168`.

[77] M. Tanabashi *et al.*, "Review of Particle Physics," *Phys. Rev.* **D98** (2018) no. 3, 030001.

[78] **LHCb** Collaboration, R. Aaij *et al.*, "Measurement of the polarization amplitudes in $B^0 \to J/\psi K^*(892)^0$ decays," *Phys. Rev.* **D88** (2013) 052002, arXiv:1307.2782 [hep-ex].

[79] **BaBar** Collaboration, B. Aubert *et al.*, "Measurement of decay amplitudes of $B \to J/\psi K^*, \psi(2S)K^*$, and $\chi_{c1}K^*$ with an angular analysis," *Phys. Rev.* **D76** (2007) 031102, arXiv:0704.0522 [hep-ex].

[80] **Belle** Collaboration, K. Chilikin *et al.*, "Experimental constraints on the spin and parity of the $Z(4430)^+$," *Phys. Rev.* **D88** (2013) no. 7, 074026, arXiv:1306.4894 [hep-ex].

[81] **Belle** Collaboration, K. Chilikin *et al.*, "Observation of a new charged charmoniumlike state in $\bar{B}^0 \to J/K^{-+}$ decays," *Phys. Rev.* **D90** (2014) no. 11, 112009, arXiv:1408.6457 [hep-ex].

[82] **LHCb** Collaboration, R. Aaij *et al.*, "Measurement of polarization amplitudes and CP asymmetries in $B^0 \to \phi K^*(892)^0$," *JHEP* **05** (2014) 069, arXiv:1403.2888 [hep-ex].

[83] **Belle** Collaboration, M. Prim *et al.*, "Angular analysis of $B^0 \to \phi K^*$ decays and search for CP violation at Belle," *Phys. Rev.* **D88** (2013) no. 7, 072004, arXiv:1308.1830 [hep-ex].

[84] **BaBar** Collaboration, B. Aubert *et al.*, "Time-Dependent and Time-Integrated Angular Analysis of $B \to \phi K_s \pi^0$ and $B \to \phi K^+ \pi^-$," *Phys. Rev.* **D78** (2008) 092008, arXiv:0808.3586 [hep-ex].

[85] **BaBar** Collaboration, J. P. Lees *et al.*, "B^0 meson decays to $\rho^0 K^{*0}$, $f_0 K^{*0}$, and $\rho^- K^{*+}$, including higher K^* resonances," *Phys. Rev.* **D85** (2012) 072005, arXiv:1112.3896 [hep-ex].

[86] **Belle** Collaboration, S. H. Kyeong *et al.*, "Measurements of Charmless Hadronic $b \to s$ Penguin Decays in the $\pi^+ \pi^- K^+ \pi^-$ Final State and Observation of $B^0 \to \rho^0 K^+ \pi^-$," *Phys. Rev.* **D80** (2009) 051103, arXiv:0905.0763 [hep-ex].

[87] D. Straub, C. Niehoff, P. Stangl, E. Gurler, J. Kumar, S. Reicher, and F. Beaujean, "flav-io/flavio v0.20." Https://doi.org/10.5281/zenodo.375591, 2017.

[88] L.-S. Geng, B. Grinstein, S. Jger, J. Martin Camalich, X.-L. Ren, and R.-X. Shi, "Towards the discovery of new physics with lepton-universality ratios of $b \to s\ell\ell$ decays," *Phys. Rev.* **D96** (2017) no. 9, 093006, arXiv:1704.05446 [hep-ph].

[89] M. Ciuchini, A. M. Coutinho, M. Fedele, E. Franco, A. Paul, L. Silvestrini, and M. Valli, "On Flavourful Easter eggs for New Physics hunger and Lepton

Flavour Universality violation," *Eur. Phys. J.* **C77** (2017) no. 10, 688, arXiv:1704.05447 [hep-ph].

[90] B. P. Roe, H.-J. Yang, J. Zhu, Y. Liu, I. Stancu, and G. McGregor, "Boosted decision trees, an alternative to artificial neural networks," *Nucl. Instrum. Meth.* **A543** (2005) no. 2-3, 577–584, arXiv:physics/0408124 [physics].

[91] Y. Freund and R. E. Schapire, "A Decision-Theoretic Generalization of On-Line Learning and an Application to Boosting," *J. Comput. Syst. Sci.* **55** (1997) no. 1, 119–139.

[92] M. Pivk and F. R. Le Diberder, "SPlot: A Statistical tool to unfold data distributions," *Nucl. Instrum. Meth.* **A555** (2005) 356–369, arXiv:physics/0402083 [physics.data-an].

[93] e. a. M. Chrzaszcz, "The $B^0 \to K^{*0}\mu^+\mu^-$ selection for the 3fb^{-1} of LHCb data." LHCB-INT-2013-058, September, 2014.

[94] CERN, "Tgenphasespace." https://root.cern.ch/root/html530/TGenPhaseSpace.html.

[95] I. Antcheva, M. Ballintijn, B. Bellenot, M. Biskup, R. Brun, N. Buncic, P. Canal, D. Casadei, O. Couet, V. Fine, *et al.*, "Roota c++ framework for petabyte data storage, statistical analysis and visualization," *Computer Physics Communications* **182** (2011) no. 6, 1384–1385.

[96] M. Needham and G. Cowan, "Observation of the decay $\overline{B}{}^0_s \to \psi(2S)K^+\pi^-$,". https://cds.cern.ch/record/1625662.

[97] **LHCb** Collaboration, R. Aaij *et al.*, "Measurements of the S-wave fraction in $B^0 \to K^+\pi^-\mu^+\mu^-$ decays and the $B^0 \to K^*(892)^0\mu^+\mu^-$ differential branching fraction," *JHEP* **11** (2016) 047, arXiv:1606.04731 [hep-ex]. [Erratum: JHEP04,142(2017)].

[98] D. Becirevic and A. Tayduganov, "Impact of $B \to K^{*0}\ell^+\ell^-$ on the New Physics search in $B \to K^*\ell^+\ell^-$ decay," *Nucl. Phys.* **B868** (2013) 368–382, arXiv:1207.4004 [hep-ph].

[99] M. Dring, U.-G. Meiner, and W. Wang, "Chiral Dynamics and S-wave Contributions in Semileptonic B decays," *JHEP* **10** (2013) 011, arXiv:1307.0947 [hep-ph].

[100] D. Aston *et al.*, "A Study of $K^-\pi^+$ Scattering in the Reaction $K^-p \to K^-\pi^+n$ at 11-GeV/c," *Nucl. Phys.* **B296** (1988) 493–526.

[101] S. Descotes-Genon, T. Hurth, J. Matias, and J. Virto, "Optimizing the basis of $B \to K^*ll$ observables in the full kinematic range," *JHEP* **05** (2013) 137, arXiv:1303.5794 [hep-ph].

[102] A. Paul and D. M. Straub, "Constraints on new physics from radiative B decays," *JHEP* **04** (2017) 027, arXiv:1608.02556 [hep-ph].

[103] CERN, "MINOS Errors." http://cmd.inp.nsk.su/old/cmd2/manuals/cernlib/minuit/node14.html.

[104] L. Demortier and L. Lyons, "Everything you always wanted to know about pulls," *CDF note* **43** (2002) .

[105] **Belle** Collaboration, S. K. Choi *et al.*, "Observation of a resonance-like structure in the $\pi^{\pm}\psi'$ mass distribution in exclusive $B \to K\pi^{\pm}\psi'$ decays," *Phys. Rev. Lett.* **100** (2008) 142001, arXiv:0708.1790 [hep-ex].

[106] **Belle** Collaboration, R. Mizuk *et al.*, "Dalitz analysis of $B \to K\pi^{+}\psi'$ decays and the Z(4430)+," *Phys. Rev.* **D80** (2009) 031104, arXiv:0905.2869 [hep-ex].

[107] **LHCb** Collaboration, R. Aaij *et al.*, "Observation of the resonant character of the $Z(4430)^{-}$ state," *Phys. Rev. Lett.* **112** (2014) no. 22, 222002, arXiv:1404.1903 [hep-ex].

[108] J. A. Bailey *et al.*, "$B \to Kl^{+}l^{-}$ Decay Form Factors from Three-Flavor Lattice QCD," *Phys. Rev.* **D93** (2016) no. 2, 025026, arXiv:1509.06235 [hep-lat].

[109] T. Hurth, C. Langenbruch, and F. Mahmoudi, "Direct determination of Wilson coefficients using $B^0 \to K^{*0}\mu^{+}\mu^{-}$ decays," *JHEP* **11** (2017) 176, arXiv:1708.04474 [hep-ph].

[110] R. Aaij and J. Albrecht, "Muon triggers in the High Level Trigger of LHCb," Tech. Rep. LHCb-PUB-2011-017. CERN-LHCb-PUB-2011-017, CERN, Geneva, Sep, 2011. https://cds.cern.ch/record/1384386.

[111] V. V. Gligorov, C. Thomas, and M. Williams, "The HLT inclusive B triggers," Tech. Rep. LHCb-PUB-2011-016. CERN-LHCb-PUB-2011-016. LHCb-INT-2011-030, CERN, Geneva, Sep, 2011. https://cds.cern.ch/record/1384380. LHCb-INT-2011-030.

[112] R. Aaij *et al.*, "The LHCb Trigger and its Performance in 2011," *JINST* **8** (2013) P04022, arXiv:1211.3055 [hep-ex].

[113] C. Sanchez Mayordomo, *Measurement of the mixing-induced and CP-violating parameters of $B_s^0 \to \phi gamma$ decays at LHCb.* PhD thesis, Univ. of Valencia and CSIC (ES), 2018.

[114] M. Williams, V. V. Gligorov, C. Thomas, H. Dijkstra, J. Nardulli, and P. Spradlin, "The HLT2 Topological Lines," Tech. Rep. LHCb-PUB-2011-002. CERN-LHCb-PUB-2011-002, CERN, Geneva, Jan, 2011. http://cds.cern.ch/record/1323557.